Twelve Years of LabEx PRIMES (2012-2024)

Francoise Peyrin, Denis Dauvergne, Olivier Beuf, Jean-François Adam, Olivier Bernard, Michael Beuve, Emmanuel Brun, Sorina Camarasu-Pop, Serge Candéias, Patrick Clarysse, et al.

▶ To cite this version:

Francoise Peyrin, Denis Dauvergne, Olivier Beuf (Dir.). Twelve Years of LabEx PRIMES (2012-2024). Zenodo, 2025, 10.5281/zenodo.14794956 . hal-04928878v2

HAL Id: hal-04928878

https://hal.science/hal-04928878v2

Submitted on 4 Feb 2025

Twelve Years of LabEx PRIMES (2012-2024)

An overview of the research performed in the *Auvergne Rhône Alpes* Region within the *Laboratoire d'Excellence* Physics, Radiobiology, Medical Imaging, and Simulation

February 4, 2025

This work was supported by the LABEX PRIMES (ANR-11-LABX-0063) of Université de Lyon, within the program 'Investissements d'Avenir' operated by the French National Research Agency (ANR).

The following research institutions contribute to the supervision of the LabEx PRIMES : Université de Lyon, CNRS, Inserm, CEA, Université Claude Bernard Lyon 1, Université Grenoble-Alpes, Université Clermont-Auvergne, Université Jean Monnet Saint-Etienne, Université Gustave Eiffel, INSA-Lyon, ENS-Lyon.

Preamble: Twelve years of research, training and transfer at LabEx Physics, Radiobiology, Medical Imaging and Simulation (PRIMES)

Françoise Peyrin[1], **Denis Dauvergne**[2], **Olivier Beuf**[1]

PRIMES scientific coordinators during the 2012-2024 period

Frank Pilleul[1,3]

Coordinator for clinical applications

Béatrice Rayet[1]

Project manager

[1]CREATIS, INSA Lyon, Université Claude Bernard Lyon 1, UJM-Saint Etienne, CNRS UMR 5220, Inserm U1206, 69621 Lyon, France

[2]LPSC, Université Grenoble Alpes, CNRS/IN2P3, Grenoble INP, UMR 5821, Grenoble, France

[3] Centre de lutte contre le cancer Léon Bérard, Department of Radiology, Lyon, France

The prevalence of cancer and age-related diseases is a major public health problem associated with high cost in European countries. Currently, there is still an insufficient level of sensitivity and specificity in diagnosis, as well as a lack of targeted personalized treatments. Quantitative imaging is a central issue for the success of early diagnosis and *in vivo* treatment monitoring. Despite an already large offer of conventional imaging techniques, there are still limitations in terms of contrast, spatial or temporal resolution, radiation dose, and most techniques only provide partial information. Several innovations can be foreseen to increase the diagnostic value of imaging techniques by providing new multi-physics characterization of tissue properties. Cancer radiotherapy, which is one of the most conventional treatments, may be associated to over- or under-dosage, tumor recurrence, radio resistance, and complications. To overcome these issues, nonstandard techniques are considered for catalyzing the effects of treatment. The highly innovative radiotherapy techniques include: particle radiotherapy (offering a better targeting of the tumor), high spatial and temporal fractionation (micro-beams, ultra-high dose rates), nanoparticle- or photo-activated radiotherapy, targeted-alpha therapy. Such techniques are still in an early stage of diffusion due to insufficient fundamental knowledge on the impact of such irradiation on living cells and tissues, as well as the lack of appropriate detection systems to monitor and control these treatments. Thus, there is a need to improve the prediction of benefits and risks for each patient and to propose new efficient, well-prepared, and controlled therapies.

In this context, the PRIMES project gathered expert scientists from renown laboratories from the *Auvergne-Rhône-Alpes* Region to invent, develop, and demonstrate the benefit of new technologies including novel imaging methods for diagnosis, treatment and follow-up, as well as innovative radiotherapy developments supported by state-of-the-art radiobiology. The PRIMES consortium represents about 200 researchers from 16 laboratories. Such breakthrough and scientific progresses relied on the coupling and integration of dedicated instrumentation to advanced numerical processing, the technical developments being strongly coupled to experiments and pre-clinical validation and going towards clinical trials. The final goal of PRIMES is the development of the entire chain from disruptive proof of concept to clinical transfer and clinical demonstration (see Figure 1).

Regarding imaging, the two main pillars of the PRIMES project activities are image formation and image analysis to “see better and see more”. In particular, PRIMES not only works on state-of-the-art imaging equipment such as MR/PET (combination of magnetic resonance imaging and positron emission tomography),

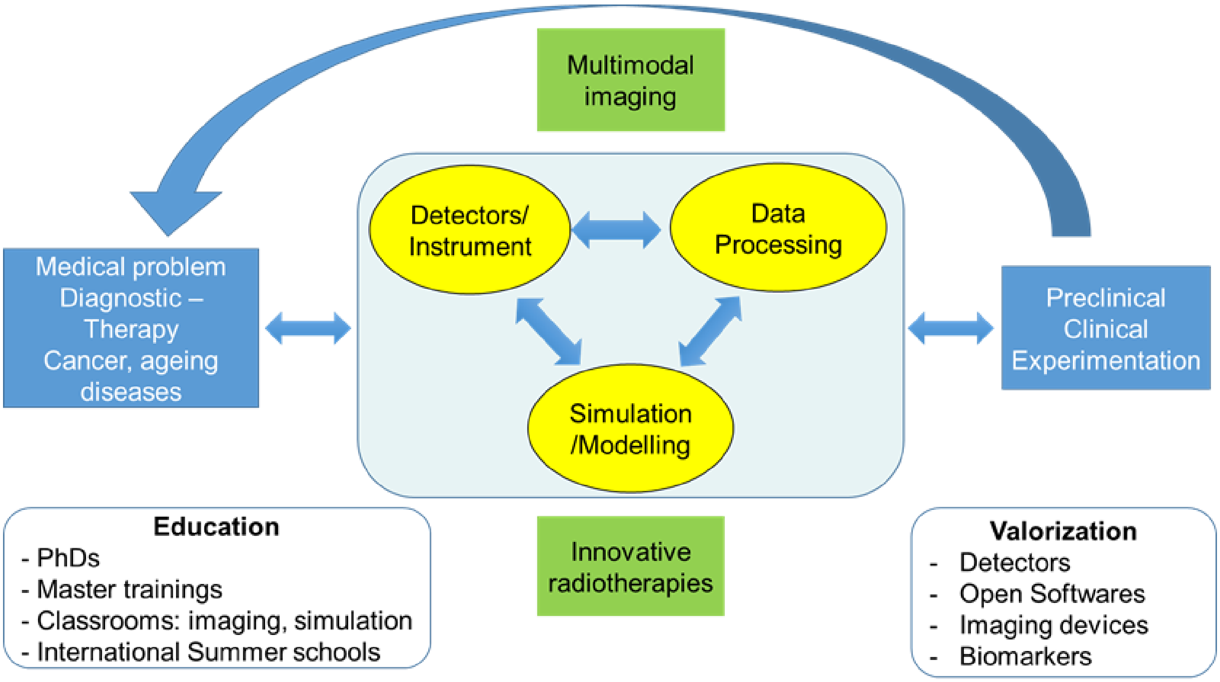

Figure 1: General overview of PRIMES project.

high-field pre-clinical magnetic resonance imaging (MRI) and X-ray spectral CT, but also contributes to the emergence of new devices in multimodality imaging at different levels of the conception chain. Within the multidisciplinary consortium of PRIMES, we have the ability to address the design of new systems in X-ray imaging, MRI, US, optical, and nuclear medicine imaging modalities for targeted radiotherapy or online control of radiotherapy and state of the art X-ray imaging systems with a privilege access to a synchrotron facility at the ESRF (European Synchrotron Radiation Facility). This involved not only instruments, but also data processing, the two components being increasingly entangled to push forward outcomes. This activity involves new physical and computational concepts that have to be integrated within an instrument and also requires the proof of concept of the developed techniques for the given clinical applications considered.

In terms of image analysis, research in machine learning is now evolving towards the exploitation of deep learning approaches. Such approaches also revolutionize the field of medical imaging with an exponential growth of the literature. However, deep learning approaches still raise many challenges regarding the performance that can be achieved with such data driven methods for given applications, the availability of training imaging data and the robustness of the developed techniques with respect to various imaging modalities. It has to be mentioned that, conversely to the mainstream of researches in the area of deep learning dedicated to image segmentation and image analysis, such techniques are more than relevant in the image formation domain, then making a link between image formation and image analysis.

In the field of radiotherapy (RT), PRIMES gathers a unique consortium having the task force to have an integrated approach on various innovative aspects of radiotherapies, namely particle therapy, synchrotron radiation therapy, radiosensitizer-enhanced therapy, targeted alpha therapy, in close connection with conventional radiotherapy centers and coupled to multi scale modeling of biological efficiency. Radiobiological irradiation and analysis platforms are available. This research axis brings together different teams and expertise required for the overall development of innovative radiotherapy techniques, from bench to bedside. This includes instrument development like high-intensity beam monitors or Compton imaging; radiobiological tools including irradiation platforms for data acquisition coupled to multiscale modelling of biological efficiency; simulations for 4D-therapy planning; preclinical studies, with end-to-end studies toward clinical trials on specific cancers. Recent developments foreseen in the project also involve high-risk topics, such as X-ray-induced photodynamic therapy (PDT-X).

Coupling these innovative developments in imaging and radiotherapy places PRIMES in a leading position with few equivalents at the international level, especially when considering applications in cancer and age-related disease. With a strong involvement of the oncology community, from the diagnosis stage to the treatment, including radiobiology studies, PRIMES has an original position with the combination of simulation and modeling to experimental evaluation going from the molecular scale to clinical studies. In this domain, we already achieved several first-in-man studies involving clinicians in cardiovascular and musculoskeletal disease working on unique and well-recognized multiscale/multimodality imaging and biomechanical modeling studies.

This book summarizes main achievements of PRIMES on different scientific topics and their position within the international context. Such achievements were made possible thanks to a continuous effort toward interdisciplinary collaborations between the partner teams. This were done in strong connection with education, by means of master trainings, PhD supports, the organization of practice classes and summer schools.

All the research publications performed within the frame of PRIMES were gathered in an open-based repository: `https://hal.science/PRIMES`.

Contributing laboratories (alphabetic order)

Ampère : Ecole Centrale de Lyon, INSA Lyon, Université Claude Bernard Lyon 1, CNRS, Ampère, UMR5005, 69130 Ecully, France

CEA-LCBM Laboratoire Chimie et Biologie des Métaux, Univ. Grenoble Alpes, CEA, CNRS, IRIG-LCBM-UMR5249, Grenoble, France

CEA-LETI : Laboratoire d'électronique et de technologie de l'information, Université Grenoble Alpes, CEA, LETI, DOPT, F38000 Grenoble, France

CEA-SyMMES : Molecular Systems and nanoMaterials for Energy and Health, UMR 5819 CEA - CNRS – UGA – Grenoble INP, Institut de Recherche Interdisciplinaire de Grenoble, CEA-Grenoble, F-38054 Grenoble, France

CREATIS : Centre de REcherche et d'Acquisition et Traitement de l'Image pour la Santé : INSA Lyon, Université Claude Bernard Lyon 1, UJM-Saint Etienne, CNRS UMR 5220, Inserm U1206, CREATIS, 69621 Lyon, France

CRNL : Centre de Recherche en Neurosciences de Lyon, Université Claude Bernard Lyon 1, UJM-Saint Etienne, CNRS UMR5292, INSERM U1028, Lyon, France

ENS-Lyon : Ecole Normale Supérieure de Lyon (Laboratoire de Chimie), Univ Claude Bernard Lyon 1, CNRS UMR 5182, 46 allée d'Italie, F-69364 Lyon cedex 07, France

ILM : Institut Lumière Matière, Université Claude Bernard Lyon 1, CNRS UMR5306, 10 rue Ada Byron, 69622 Villeurbanne CEDEX, France

INL : Institut des Nanotechnologies de Lyon, Université Claude Bernard Lyon 1, INL, UMR5270, CNRS, INSA Lyon, Ecole Centrale de Lyon, CPE Lyon, Villeurbanne, 69622, France

Institut Pascal : Université Clermont Auvergne, Clermont Auvergne INP, CNRS UMR 6602, Institut Pascal, F-63000 Clermont-Ferrand, France

IP2I : Institut de Physique des 2 Infinis de Lyon : Université Claude Bernard Lyon 1, CNRS-IN2P3 UMR 5822, IP2I, Villeurbanne, France

LabHC : Laboratoire Hubert Curien, University Jean Monnet Saint-Etienne, CNRS, Institut d'Optique Graduate School, UMR 5516, F-42023, Saint-Etienne, France

LBMC : Laboratoire de Biomécanique et Mécanique des Chocs : Univ Lyon, Univ Eiffel, Univ Claude Bernard Lyon 1, LBMC UMR_T9406, 69622, Lyon, France

LIRIS: Laboratoire d'InfoRmatique en Image et Systèmes d'information : Univ Lyon, INSA Lyon, CNRS, Université Claude Bernard Lyon 1, LIRIS, UMR5205, F-69622 Villeurbanne, France

LPC : Laboratoire de Physique de Clermont - UMR6533, CNRS/IN2P3 Université Clermont Auvergne, Aubière, France

LPSC : Laboratoire de Physique Subatomique et de Cosmologie - Université Grenoble Alpes, CNRS/IN2P3, Grenoble INP, LPSC, UMR 5821, Grenoble, France

Neurodis Foundation : Fondation Neurodis, Inserm, Centre hospitalier du Vinatier, Bâtiment 452B, 95 boulevard Pinel, F 69675 Bron Cedex, France

Strobe : Synchrotron Radiation for Biomedicine - Rayonnement SynchroTROn pour la Recherche BiomédicalE : Univ. Grenoble Alpes, INSERM, UA07 STROBE, 38000 Grenoble, France

Contents

Acronyms Index

ACDC automatic cardiac diagnostic challenge. 134, 135
ADMM alternating direction method of multipliers. 83, 165
AI artificial intelligence. 66–68, 133, 173
AIF arterial input function. 139
ANR *Agence Nationale de la Recherche*. 2, 12, 17, 89
ANSM *Agence Nationale de la Sécurité du Médicament et des produits de santé*, `https://ansm.sante.fr/`. 101
ARRONAX *Accélérateur pour la Recherche en Radiochimie et Oncologie à Nantes Atlantique*, `https://www.arronax-nantes.fr/`. 13, 17
ASIC application-specific integrated circuit. 10, 12, 30, 98

BGO bismuth germanate. 3, 4
BNCT boron neutron capture therapy. 34, 59–61
BSC backscatter coefficient. 106–108

CAL Centre Antoine Lacassagne. 1, 4–7, 12, 13, 42
CC Compton camera. 2–4
CEA *Commissariat à l'Énergie Atomique et aux énergies alternatives*, `https://www.cea.fr/`. 33, 34, 53
CEA-LETI *Commissariat à l'Énergie Atomique et aux énergies alternatives - Laboratoire d'Électronique et de Technologie de l'Information*, `https://www.leti-cea.com/cea-tech/leti/english`. 89
CERMEP *Centre d'Etude et de Recherche Multimodal Et Pluridisciplinaire en imagerie du vivant*, `https://www.cermep.fr/`. 84, 110
CERN *Organisation Européenne pour la Recherche Nucléaire*. 18, 63
CFD computational fluid dynamics. 138
CHU *centre hospitalo-universitaire*. 10, 15, 117, 118
CHUGA *Centre Hospitalo-Universitaire Grenoble-Alpes*, `https://www.chu-grenoble.fr/`. 19, 27, 31
CIC-IT *Centre d'Investigation Clinique – Innovation Technologique*, `https://www.cic-it-grenoble.fr/`. 19
CLaRyS *Contrôle en Ligne de l'hadronthérapie par Rayonnements Secondaires*: research collaboration. 1–7, 11, 12
CLaRyS-UFT *Contrôle en Ligne de l'hadronthérapie par Rayonnements Secondaires - Ultra-Fast Timing*: research project . 4, 5, 12
CMA-ES covariance matrix adaptation evolution strategy. 140
CMOS complementary metal-oxyde semiconductor. 18, 20, 29
CMRI cardiac magnetic resonance imaging. 134
CNN convolutional neural network. 144, 157, 158
CNRS *Centre National de la Recherche Scientifique*. 7, 33, 34, 48, 83
CPPM *Centre de Physique des Particules de Marseille*, web site. 1, 2, 5, 12
CREATIS *Centre de Recherche en Acquisition et Traitement de l'Image pour la Santé*, `https://www.creatis.insa-lyon.fr/site/fr`. 1, 2, 5, 12, 18, 56, 63, 81–85, 114, 120
CS compressed sensing or compressive sampling. 156, 157
CT computed tomography. 35, 97–100, 131
cVAE constrained variational auto-encoder. 134, 135
CVD chemical vapor deposition. 12–14

DAS delay and sum. 156
DCC data consistency conditions. 160, 161
DEF dose enhancement factor. 53, 54
DFT density functional theory. 47, 48, 51, 53
DGOS *direction générale de l'offre de soins*, depends on the French Ministry of Health, web site. 31

DH digital holography. 163–165
DSC-MRI dynamic susceptibility contrast magnetic resonance imaging. 139
DW divergent wave. 156–158
DXA dual-energy X-ray absorptiometry. 79

EBS electrical brain stimulation. 101
EBT3 dosimety film developed by the Gafchromic company. 18, 19
EID-CT computed tomography with energy integrating detectors. 98, 99
ENS-Lyon *École Normale Supérieure de Lyon*, `https://www.ens-lyon.fr/`. 51
ERC European Research Council, `https://erc.europa.eu/`. 5
ESRF European Synchrotron Radiation Facility, `https://www.esrf.fr/`. iv, 9, 15, 16, 20–23, 25–27, 30, 31, 33, 36, 53, 80, 81, 89, 92

FBP filtered back-projection. 87, 161, 162
FCN fully-connected network. 157
FDG fluorodeoxyglucose. 100, 141
FDK Feldkamp-Davis-Kress reconstruction algorithm classically used in Cone-Beam CT [1]. 162
FLIRT Oxford Centre for Functional Magnetic Resonance Imaging of the Brain Linear Image Registration Tool. 170
FPGA field programmable gate-array. 14
FSL Oxford Centre for Functional Magnetic Resonance Imaging of the Brain Software Library. 170
FTIR Fourier transform infrared spectroscopy. 125
FWHM full width at half maximum. 12, 108

GAN *generative adversarial network*. 67, 68, 141, 157
GANIL *Grand Accélérateur National d'Ions Lourds*, `https://www.ganil-spiral2.eu/`. 12, 42
GAT graph attention network. 136
GCN graph convolutional network. 136, 137
GdCA gadolinium contrast agent. 53, 54
GdNP gadolinium nanoparticle. 53, 54
GIN *Grenoble Institut des Neurosciences*, `https://neurosciences.univ-grenoble-alpes.fr/fr`. 33
GNN graph neural network. 136
GNP gold nanoparticle. 50, 53, 55, 56
GSURE generalized Stein's unbiased risk estimator. 165

HCL *Hospices Civils de Lyon*, University Hospital of Lyon, `https://www.chu-lyon.fr/`. 18
HU Hounsfield unit, dimensionless unit universally used in computed tomography to express CT numbers in a standardized and convenient form. 100

IAEA TRS technical report series by the International Atomic Energy Agency, web site. 28
ICRU International Commission on Radiation Units and Measurements. 70
IFIC *Instituto de Física Corpuscular*, `https://webific.ific.uv.es/web/`. 4
IJCLab *Laboratoire de Physique des 2 Infinis Irène Joliot-Curie* - Orsay, `https://www.ip2i.in2p3.fr/equipes/prisme/`. 49
ILM *Institut Lumière Matière, Lyon*, `https://ilm.univ-lyon1.fr/`. 33, 34, 46
IMC intima-media complex. 145, 146
IMRT intensity-modulated radiotherapy. 9, 11, 19, 22, 33, 41
IMT intima-media thickness. 145, 146
INCa *Institut National du Cancer*, `https://www.e-cancer.fr/`. 12, 15, 16, 19, 29, 31, 60, 61
INL *Institut des Nanotechnologies de Lyon*, `https://inl.cnrs.fr/`. 15, 18, 19, 29
Inserm *Institut National de la Santé et de la Recherche Médicale*. 33, 82, 85
IP2I *Institut des 2 Infinis de Lyon*, `https://www.ip2i.in2p3.fr/`. 1, 2, 5, 12, 33, 48, 56, 59–61, 63, 77

IRF impulse response function. 139
IRMaGe medical imaging platform at GIN laboratory, Grenoble, `https://irmage.univ-grenoble-alpes.fr/`. 30
IRMAS *Imagerie par Résonance Magnétique de l'Agglomération Stéphanoise*, imaging platform at Saint-Étienne, `http://www.irmas.fr/`. 121
IRSN *Institut de Radioprotection et de Sûreté Nucléaire*, `https://www.irsn.fr/`. 49
ISMRM International Society for Magnetic Resonance in Medicine. 172

LAPD large acceptance pixellated detector. 1, 2
LBMC *Laboratoire de Biomécanique et Mécanique des Chocs*, `https://lbmc.univ-gustave-eiffel.fr/`. 81, 82, 85
LCN lacuna-canaliculi network. viii, 79–81, 86, 92
LEM local effect model. 55, 57–59
LET linear energy transfer. 41, 43, 47, 50, 58, 59, 68
LHE-EPFL *Laboratoire d'Hydraulique Environnementale at Ecole Polytechnique Fédérale de Lausanne* , `https://lhe.epfl.ch/`. 18
LIRIS *Laboratoire d'InfoRmatique en Image et Systèmes d'information*, `https://liris.cnrs.fr/`. 61, 77
LoR line of response, defined by the two interaction vertices of positron annihilation photons in PET detection. 76
LPC *Laboratoire de Physique de Clermont*, `https://lpc-clermont.in2p3.fr`. 1, 2, 34, 56, 60, 61
LPCA *Laboratoire de Physique de Clermont*, `https://lpc-clermont.in2p3.fr`. 63
LPSC *Laboratoire de Physique Subatomique et de Cosmologie - Grenoble*, `https://www.lpsc.in2p3.fr/`. 5, 9, 10, 12–17, 19, 30, 49, 60, 61
LPSC-PNAM *Physique Nucléaire et Applications Médicales* research team at LPSC. 14

MAGICS NMR and Optics, From Measure to Biomarker, research team at CREATIS web site. 114
MAP *maximum a posteriori*. 154
MaPMT matrix photomultiplier tube. 12, 13
MBRT minibeam radiotherapy. 49, 50
MC Monte-Carlo. 4, 5, 16, 30
MD molecular dynamics. 47, 48
MITI *Mission pour les Initiatives Transverses et Interdisciplinaires* from CNRS. 7
MKM microdosimetric kinetic model. 49, 57, 58, 63
ML maximum likelihood: *Maximum de vraisemblance*. 154
MLEM maximum likelihood expectation maximization. 65, 75, 154, 155
MLP most likely path. 161, 162
MoBI modulation based imaging. 92, 93, 95
MR magnetic resonance. iii, ix, x, 113, 114, 121, 122, 126, 128, 129
MRE magnetic resonance elastography. ix, 113–116
MRI magnetic resonance imaging. iv, ix, 27, 41, 45, 89, 97, 100, 101, 108, 109, 113, 115–118, 120, 121, 123, 125–129, 131, 132, 134–137, 139–141, 143–145, 149, 169–172
MRS magnetic resonance spectroscopy. 108, 109, 121, 128, 129, 143, 144, 172
MRSI magnetic resonance spectroscopic imaging. 108–110, 121, 143, 144
MRT microbeam radiotherapy. viii, 9, 15, 16, 20–23, 27–31, 33, 40, 41, 45
MS multiple sclerosis. 136, 142

NMR nuclear magnetic resonance. 108, 126, 172
NP nanoparticle. 50, 53, 55
NTCP normal tissue complication probability. 24, 25, 27
NURBS non-uniform rational basis spline. 72

OC-SVM one-class support vector machine. 140, 141

PA photoacoustic. 104
PAIR *programme d'actions intégrées de recherche*, research program by INCa. 16
PCA principal component analysis. 138
PCD photon counting detector. 98
PCDI phase contrast and dark-field imaging. 90
PCI phase contrast imaging. 92, 125
PCSI *physique, chimie et sciences de l'ingénieur*: research program supported by INCa. 4–6
PDFF proton density fat fraction. 110
PDT photodynamic therapy. vii, 33, 39, 40
PEG polyethylene glycol. 51, 52
PET positron emission tomography. iii, vii, viii, 1, 63–69, 71, 75–77, 100, 117, 141, 149
PG prompt-gamma. vii, 1–6
PGEI prompt-gamma energy integration. 6, 7
PGPI prompt-gamma peak integration. 6
PGS prompt-gamma spectroscopy. 6
PGT prompt-gamma timing. 6
PGTI prompt-gamma timing imaging. 5
PILoT LyonTech multi-modal and experimental imaging platform, https://www.creatis.insa-lyon.fr/site/en/pilot. 104, 110, 126
PMMA poly(methyl metacrylate). 4, 22, 94
PMT photomultiplier tube. 12
PRISME team Physics, Radiobiology, Imaging, Simulation, Modelling and Experimentation at IP2I, https://www.ip2i.in2p3.fr/equipes/prisme/. 60
PSF point spread function: *fonction d'étalement de point*. 155
PTV planned target volume. 27, 41, 70
PW plane wave. 156–158
PWC-Net pyramid, warping and cost volume network. 137

QA quality assurance. 18–20, 22, 29
QCT quantitative computed X-ray tomography. ix, 79, 82–86, 89
QDC charge to digital converter. 10
qMRI quantitative magnetic resonance imaging. 171, 172

RANSAC RANdom SAmple Consensus. 146
RBE relative biological effectiveness. 41, 42, 45, 49, 50, 59, 60
RF radio frequency. 114, 115, 126, 128, 129, 156, 157
RGB red, green and blue (additive primary colors. 101
ROI region of interest. 89, 106–108, 110, 131, 132
ROS reactive oxygen species. 36, 39, 42, 43, 61
RSP relative stopping power. 161

SARRP Small Animal Radiation therapy Platform, product by Xstrahl company, https://xstrahl.com/sarrp/. 30
SATT *société d'accélération de transfert de technologie*. 6
SciFi scintillating fiber. 18, 19
SFRT spatially fractionated radiotherapy. 49
SNR signal to noise ratio. 20, 128, 144
SOLEIL French synchrotron light source, https://www.synchrotron-soleil.fr/. 125
SOTA state of the art. 135
SPCCT spectral photon counting computed tomography. 98–100
SP-CT spectral computed tomography. 84
SPECT single photon emission tomography. 4, 63, 66–68, 154

SPIM selective plane illumination microscopy. 102, 103
SR synchrotron radiation. 14, 80–84
SSM-S spatial and spectral mean-shift. 105, 106
SSRT synchrotron stereotaxic radiotherapy. 26, 27
STROBE *Rayonnement Synchrotron pour la Recherche Biomédicale*, `https://strobe.univ-grenoble-alpes.fr/`. 14, 15, 19, 53
SVD singular value decomposition. 138
SVDD support vector data description. 140
SVM support vector machine. 132, 140

TAT targetted alpha therapy. 59–61
TCP tumour control probability. 24, 25, 27, 59–61
TIMC *Recherche Translationnelle et Innovation en Médecine et Complexité* Laboratory, `https://www.timc.fr/`. 18
TLE track length estimator. 64, 65, 67
ToF time of flight. 4–6, 65
TPS treatment planning system. 26, 30, 57, 59, 64, 75
TV total variation. 154, 155

UAD unsupervized anomaly detection. 141
UCBL *Université Claude Bernard Lyon 1*, `https://www.univ-lyon1.fr/`. 82, 85
UGA *Université Grenoble-Alpes*. 34
US ultrasound. iv, 104, 131, 134, 135, 145, 146, 149

VHEE very high energy electrons, > 70 MeV, used in radiotherapy. 49, 50
VIP virtual imaging platform at Creatis lab, `https://www.creatis.insa-lyon.fr/vip/`. 169
vpg-TLE voxellized prompt-gamma track length estimator. 4, 5

WEPL water equivalent path length. 161

XRF x-ray fluorescence . 125

Gamma imaging: from on-line hadrontherapy monitoring to innovative nuclear medicine

1

Coordinator: Étienne Testa

Contributors: Denis Dauvergne, Jean Michel Létang

1.1 Introduction

Ion-beam therapy (also called hadrontherapy) offers excellent ballistic properties in respect to conventional radiotherapy using γ rays. Indeed, ion energies are adjusted so that the ions stop in the tumor volume with a maximum of energy deposition at the end of their path. However ion ranges are sensitive to treatment uncertainties [2] and the treatment planning systems apply the two following mitigation strategies: they use sub-optimal multi-irradiation fields without organ-at-risk downstream the Bragg peak and safety margins around the tumor volume to ensure the complete irradiation of cancerous cells [3].

Therefore, the online monitoring of ion ranges inside the patient is highly desirable in order to fully benefit from the ballistic properties of ions. The main modalities that have been investigated for 30 years are based on the detection of secondary radiations, mainly annihilation and prompt γ rays but also secondary protons. The CLaRyS collaboration (IP2I Lyon, LPC Clermont-Ferrand, CPPM Marseille and CREATIS) has investigated these 3 monitoring modalities with emphasis on γ-rays detection thanks to the LabEx support.

1.2 PET imaging

One of the possibilities for ballistic control is based on the real-time on-line measurement of the spatial distribution of positron-emitting radionuclides produced by the fragmentation reaction between the projectile and the target and thus on the coincident detection of two photons. The LPC group focused on the development of a large acceptance PET camera prototype (A Rozes & A Bongrand PhDs) that has been eventually transferred to the Centre Antoine Lacassagne (CAL) cancer treatment center in Nice in 2018.

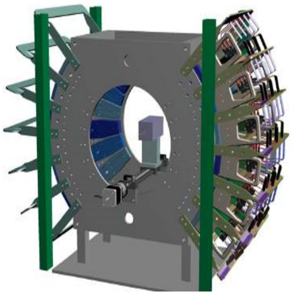

Figure 1.1: CAD view of the complete large acceptance pixellated detector (LAPD) [4].

More specifically, a first prototype called LAPD was designed and built at the Clermont Physics Laboratory. Initially, the PhD work of Arnaud Rozes [5] allowed to compare the predictions of two hadronic models implemented in Geant4 with experimental measurements performed by Dendooven *et al.* [6] at 55 MeV. The focus was then on characterizing the performance of the LAPD and determining its potential when used in a clinical beam. For this purpose, a Monte-Carlo simulation dedicated to understand the associated physics was developed, the detector and the experiments carried out on 65 MeV proton beam at the *Institut Mediterranéen de Protonthérapie* (IMPT) in Nice. Finally, as the LAPD will eventually be coupled with a high-bandwidth acquisition system (µTCA, Micro Telecommunications Computing Architecture) allowing the sending and processing of the measured data in real time, a study of the performances expected on the PROTEUS ONE line of the IMPT at 120 and 230 MeV has been carried out.

1.3 Prompt-gamma imaging

1.3.1 Early studies and projects before LabEx's start

The Prompt Gamma Imaging activity started in IP2I Lyon in late 2000's with the first experimental evidence of the correlation between PG profile as a function of target depth and ion range with carbon ion beams [7]. This promising result led to 'Gamhadron' ANR project (2009-2014) gathering IP2I Lyon, LPC Clermont-Ferrand and CREATIS. This project initiated the investigation of PG imaging with collimated and Compton camera (CC) coupled to a beam hodoscope (Figure 1.2). The European projects ENVISION (2010-2014) and ENTERVISION (2011-2015) as well as the ETOILE project and the IN2P3 institute also supported the LabEx teams involved on PG imaging at this period. The main advances during this period were the following:

- First measurements of PG yields with proton and carbon ion beams and first simulation of collimated cameras
- First evaluation of hadronic models in Geant4 (Monte Carlo simulations for particle transport in matter) [8, 9],
- Optimization of the Compton camera prototype of the CLaRyS collaboration (IP2I Lyon, LPC Clermont-Ferrand, CPPM Marseille and CREATIS) [10, 11],
- Optimization of the collimated camera prototype of the CLaRyS collaboration and publication of a series of PG yields measurements with proton and carbon ion beams [12, 13],
- Assessment and improvement of hadronic models in Geant4 for protons [14] and carbon ion beams [15].

1.3.2 Main LabEx's contributions

The LabEx contribution on this activity started in 2013 with the funding of J.-L. Ley's thesis (2013-2015) followed by the ones of M. Fontana (2016-2018) and O. Allegrini (2020-2022). The first thesis allowed us to perform the first tests of the various detectors, namely (Figure 1.3):

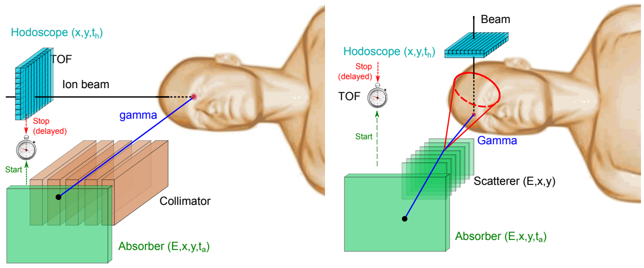

(a) Collimated camera **(b)** Compton camera (CC)

Figure 1.2: Collimated and Compton cameras developed coupled to a beam hodoscope for ion-range verification during hadrontherapy.

- the silicon detectors of the CC scatterer: 7 double-sided silicon strip detector (DSSD) from SINTEF with an active area of $\sim 9 \times 9$ cm^2 to be cooled down in a thermal box at temperatures close to 0°C,
- the bismuth germanate (BGO) scintillators of the CC absorber: 30 blocks of $35 \times 38 \times 30$ mm,
- the beam hodoscope made of squared 1 mm^2 fibers arranged in two perpendicular planes and coupled to multi-anode photomultipliers.

In addition to these instrumentation developments, preliminary results on the evaluation of CC performances during hadrontherapy were obtained by means of Monte Carlo simulations [16].

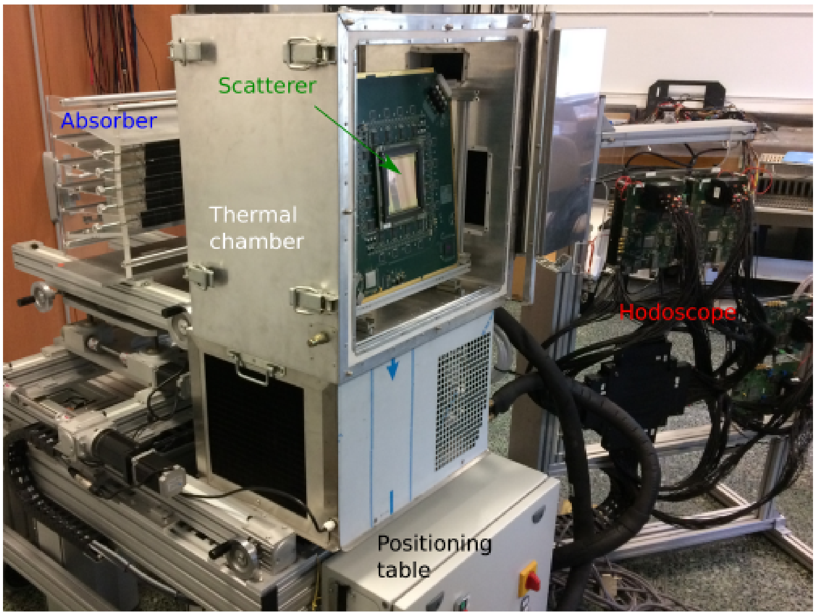

Figure 1.3: Prototype of the Compton camera (CC) and the beam hodoscope developed by the CLaRyS collaboration with the following detectors: BGO scintillators (CC absorber), silicon detectors.

The BGO detectors and the beam hodoscope were characterized during M. Fontana's thesis (2016-2018) and the performances of the CC prototype were evaluated for both hadrontherapy verification and for non-invasive diagnostics in nuclear medicine. Despite their relatively poor energy resolution, the BGO detectors present very good detection efficiency especially to detect high energy γ-rays such as PG [17]. However, the detection efficiency of the CC prototype is actually similar to the one of physically collimated systems. Moreover, CC prototypes have to cope with high counting rates in clinical beam conditions leading to high rates of random coincidences. Further improvement of CC detection efficiency could be considered which could motivate the use of reduced beam intensities at the beginning of the treatments (to limit the rate of random coincidences) in order to perform ion-range verification with a few spots probing the irradiation conditions [18]. Finally the application of CC to nuclear medicine was investigated by comparing CC performances (detection efficiency and spatial resolution) with the ones of a commercial single photon emission tomography (SPECT)-Anger device (the General Electric HealthCare Infinia system with a High Energy General Purpose collimator) for new radio-emitters emitting γ rays of relatively high energies (250 keV– 2.5 MeV). Monte Carlo simulations showed that, with the same dimensions, the CC prototype has a detection efficiency larger than the one of the Anger camera by a factor $\sim$ 20 associated with an enhanced spatial resolution for energies beyond 500 keV [19].

The main results of the last thesis funded by the LabEx on this topic (Allegrini's thesis, 2020-2022) were the following:

- the beam hodoscope with scintillating fibers was finally characterized with in beam tests during O. Allegrini's thesis (2020-2022) (see next chapter);
- the characterization of the silicon detectors (CC scatterer) and their associated electronics unfortunately revealed noise issues in the electronics boards that could not be resolved during the thesis [20]. Further developments could be considered within a collaboration with the IFIC group in Valencia that intends to use such silicon detectors in their CC prototype MACACO (the CLaRyS collaboration and the IFIC group in Valencia (Spain) have collaborated within the IEA project INCONI (2019-2021) on the comparison of CLaRyS and MACACO prototypes);
- the absorber was successfully tested during in-beam tests with a collimated camera composed of the BGO blocks and a tungsten-alloy collimator placed in front of a poly(methyl metacrylate) (PMMA) target irradiated with the 65 MeV proton beam of the CAL-Nice: the measured PG profiles was in very good agreement with the profile simulated with Geant4 [20].
- a new version of the Gate/Geant4 voxellized prompt-gamma track length estimator (vpg-TLE) module was developed within this thesis. The vpg-TLE module is a Monte-Carlo (MC) variance reduction technique developed for the calculation of PG emission in proton therapy. The module provides the PG energy spectra per incident proton in each voxel of the simulated geometry with gains in computing times of the order of 10^3 [21]. In addition to the PG energy spectra, the new module developed during the thesis (vpg-TLE-TT) also provides the PG emission time [20] which is of utmost importance for many PG detection techniques using time of flight (ToF) measurements to retrieve information on ion-range (the PG Timing technique and the PG Time imaging) or to reduce the background induced by secondary neutrons (the ToF gamma cameras, the PG Spectroscopy technique and the PG Peak integral technique) [22].
- the characterization and the in-beam tests of the detectors studied within the PCSI project CLaRyS-UFT (see section 1.3.3);

1.3.3 Projects in close connection with the 'PG imaging' topic

It is worth mentioning the other projects funded by the LabEx in the WP 'MC simulation' in close connections with the topic of hadrontherapy verification by means of PG detection:

- B. Huisman's thesis (2014-2017) on the development in Gate of the aforementioned vpg-TLE module [21] and the development of an analytical model to predict PG collimated cameras performances (multi-parallel slit and knife-edge slit prompt gamma cameras) [23].
- the develoment of another Gate module during the 2-year post-doc of A. Extebeste (2018-2019): the CCmod which is a generic module allowing for simulations and analyses of Compton cameras [**Etxebeste2020**]

This activity has been extended to 'ultra fast timing devices' within the PCSI project CLaRyS-UFT (2017-2021). One of the objectives of this projet was to study the possibility to determine the PG emission point from the 2 points of the line-cone intersection provided by the CLaRyS Compton camera and a beam hodoscope (line and cone correspond respectively to the beam trajectory measured by the hodoscope and the Compton cone). Results show that the PG emission point can be indeed retrieved from the 2 points of the line-cone intersection by means of precise ToF measurement of $\sim$ 200 ps (rms) [**Livingstone2021**]. This study was also supported by the LabEx with a 6-month position of invited researcher for J. Livinstone. In parallel, instrumentation developments were carried out in collaboration with the 'Damavan Imaging' company to couple their Temporal modules composed of $CeBr_3$ scintillators with diamond detectors and estimate the timing resolution that could be achieved between a Compton camera and a beam tagging hodoscope. The characterization of these detectors and the in-beam tests in the CAL-Nice were performed within O. Allegrini's thesis. The preliminary results obtained with the 65 MeV proton beams were quite promising with ToF resolution of about $\sim$ 500 ps (rms) [20].

Another project of ion-range monitoring by means of PG detection has also emerged at LPSC: it consists in PG imaging by the sole time-of flight measurement, between an incident proton and a detected PG. This method, called prompt-gamma timing imaging (prompt-gamma timing imaging (PGTI)) [24], is now investigated in the frame of an ERC-EU project.

1.3.4 Conclusion

In conclusion, a very dynamic research activity has been developed for 15 years around PG imaging within the CLaRyS collaboration gathering 3 laboratories of the LabEx (IP2I Lyon, LPSC Grenoble, CREATIS) and the CPPM Marseille. This activity was strongly supported by the LabEx which allowed us to build an ambitious program from PG cross-section measurements to image reconstruction (see chapter 13), including instrumentation developments and Monte Carlo simulations. This dynamics allowed us to raise other funds such as the PCSI project CLaRyS-UFT with promising results on the Compton camera with precise ToF measurements. The CLaRyS collaboration intends to investigate further the Compton camera application to nuclear medicine initiated in [19, 25]. Another PCSI project carried out by the CLaRyS collaboration is the project 'GammaDosi' (2013-2015) investigating an non-imaging PG detection technique, namely the prompt-gamma peak integration (PGPI) technique recently extended to high intensity beams PGEI with the LabEx's support for the funding of P. Evereare's thesis (next section).

1.4 Prompt-gamma monitoring with non-imaging techniques

In the middle of the 2010's, two non-imaging PG detection techniques were proposed in order to provide ion-range verification with relatively compact devices in respect to the various gamma cameras (collimated and Compton cameras) developed for PG detection: the prompt-gamma timing (PGT) [26] and the prompt-gamma spectroscopy (PGS) techniques [27] using the correlation between ion ranges and the prompt gamma ToF and energy spectra, respectively. With the same objective of compactness and to overcome the limitations of the aforementioned techniques, the CLaRyS collaboration proposed the PGPI that was patented in July 2016 [28] at the end of the PCSI projet 'Gammadosi'. The principle of this technique consists in detecting PG in a few detectors placed around the patient: more specifically, PG generated in the patient are discriminated from background events by means of ToF selection and the various ratios of PG statistics measured in the detectors provide millimetric precision on ion-range on a beam-spot basis (10^8 incident protons). Such results were obtained with both Geant4 simulations and experimental measurements performed with a demonstrator in the CAL cancer treatment center in Nice [29].

In order to valorize this technique, a market study was carried out through PULSALYS (the *société d'accélération de transfert de technologie* (SATT) of the University of Lyon). Its main conclusion was that further developments were required before a potential transfer of technology. Within this context, the CLaRyS collaboration proposed a new thesis project funded in 2020 by the LabEx PRIMES (P. Everaere's thesis, 2020-2023 [30]) to investigate the extension of the PGPI technique (mainly developed for cyclotrons) to the synchro-cyclotrons used in recent protontherapy centers (*e.g.* the Proteus One facility in the CAL treatment center in Nice). The challenge of PG detection with such synchro-cyclotrons arises from the high beam intensity during beam extractions (~ 1 µA) in respect to standard cyclotron beam intensities used in protontherapy centers (~ 1 nA). In order to cope with high PG detection rates while maintaining large detection statistics, we proposed the PGEI technique that consists in measuring the energy deposited during each beam pulse (typically a few 10^7 protons in ~ 10 µs) in the various detectors placed around the patient. As expected, the precision on ion-ranges offered by this technique is slightly degraded in respect to the PGPI technique based on event-by-event detection. However, according to Monte Carlo simulation, this precision is of the order of a few millimeters at the scale of a beam pulse (10^7 incident protons). Moreover we showed experimentally that lead-tungstate scintillators ($PbWO_4$) can cope with the high instantaneous gamma count rates for PGEI at synchro-cyclotrons [31].

These developments will be continued within S. Otmani's thesis (2023-2026) funded by the 'MITI-CNRS' (project call '80 | Prime', collaboration CLaRyS in association with CAL) with the following main objectives: the estimation of the PGEI performances in more realistic conditions (*i.e.* use of anthopomorphic phantoms and treatment plans) and the development of a demonstrator to be tested in the Proteus One facility of the CAL treatment center.

Clinical radiotherapy beam monitoring

2

Coordinator: Denis Dauvergne

Contributors: Marie-Laure Gallin-Martel, Patrick Pittet, Étienne Testa

2.1 Introduction

PRIMES teams in Workpackage 1 'Methods and Instruments for Innovative Radiotherapies' have contributed to several developments for clinical beam monitoring and online dosimetry. These developments are most often undertaken in collaboration with clinical partners. They are based on the teams expertise in particle and nuclear physics instrumentation and modelling, with a strong technical support within the teams laboratories.

Beam monitors have been developped for Intensity Modulated Radiation Therapy, where the photon beams are dynamically shaped by multileaves. Therefore, A 2D-real-time detector is necessary to map the instantaneous flux, and correlate it to the deposited dose.

In particle therapy, an important issue is the need of range verification, which benefits from a 2D beam-trigger in order to perform time-of-flight measurement of secondary radiation (see previous chapter on gamma detection). A first hodoscope made of crossed-scintillating fibers was designed to reach 100 % efficiency for each incident ion or ion bunch. Pushing forward the performance of time-of-flight, a diamond-based hodoscope was developed in order to reach 100 ps timing resolution. With the recent advent of FLASH therapy, a proton beam monitor for high-intensity pulsed beams is under tests.

Then, a diamond stripped detector was developped and tested for portal monitoring of synchrotron microbeam radiotherapy, and used during the veterinary clinical trial held at ESRF-Grenoble.

On-line dosimetry for MRT is presently under study by means of innovative scintillator devices.

2.2 Beam monitoring

2.2.1 TraDeRa beam monitor for Intensity Modulated Radiotherapy

In 2009, the LPSC's Medical Applications group initiated the development of TraDeRa, a gaseous transmission detector for real-time monitoring of photon flux at the accelerator outlet, *i.e.* upstream of the patient. The aim was to develop a detector to monitor conformal IMRT. This highly technical procedure consists of varying the shape of the irradiation beam during the same session to adapt to the shape and volume constraints of the organ to be treated. In this context, TraDeRa scientific objectives were to be able not only to evaluate the dose delivered during the treatment but also to image the shape of the beam in order to provide an effective response to the problem of over- or under-dosing in real time, while being easy to use on a daily basis in a hospital environment. The project involved a collaboration with the radiotherapy department at Grenoble CHU Hospital (Pr J. Balosso and J.-Y. Giraud, members of PRIMES). This detector was designed and characterized during Robin Fabbro's thesis funded by the LabEx PRIMES (2014 – 2017). The main technical objectives that led to TraDeRa development were to set up a detector suitable for quality control that could measure the 2D characteristics of the beam in real time with the emphasis on: transparency (measuring with minimum attenuation of the beam), spatial resolution (of the order of a millimeter at the point where the dose is prescribed), ease of use, resistance over time to intense irradiation.

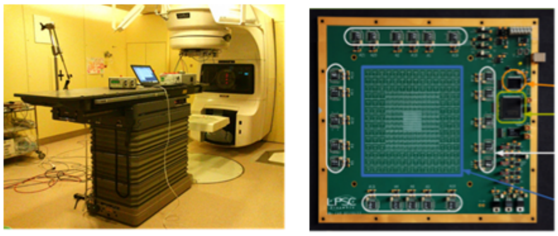

Figure 2.1: The TraDeRa detector positioned on the head of a radiotherapy accelerator at the CHU Michallon. Right: Zoom on the 324-channel, 14×14 cm^2 effective area (blue square) prototype.

Therefore, a 2D matrix of detectors (Figure 2.1) coupled to reading electronics and an acquisition system was designed. The sensitive part of the detector consists of a matrix of anode electrodes (one patent pending Arnoud *et al.*) engraved on a PCB (Printed Circuit Board) capable of withstanding very high dynamics. This PCB is followed by a high-voltage grid, with air simply flowing between the two. When the photons from the beam interact with the PCB (the active zone), secondary electrons are emitted, followed by ionization and the creation of electron-ion pairs that migrate to the anode (the pixels) for the ions and to the cathode (the high-voltage grid) for the electrons. The signal measured on each pixel is proportional to the current induced by the charge drift. The detector supplies current pulses generated by the drift of electrons. These pulses are processed electronically to determine the charge collected by each pixel, which is proportional to the dose in the detector. The electronic devices used are therefore charge amplifier integrator systems. The aim of developing readout electronics for a 1:1 detector with 1600 channels led to the design of the charge to digital converter (QDC) LPSC application-specific integrated circuit (ASIC) [32].

At first, the TraDeRa charge measurement capacity was validated at the CHU Michallon, during R. Fabbro PhD thesis, by comparison with the reference measurement system, which consists of an electrometer coupled to an ionisation chamber. The measurements demonstrate the excellent suitability, within 0.1 %, of three charge measurement systems: the CHU reference (used in clinical mode), the first discrete electronics and finally the ASIC, the two latter being developed at LPSC. Then, the potential of TraDeRa to image, in real time, the movement of the multileaf collimator and detect any positioning error has been evaluated by R. Fabbro Figure 2.2. The results obtained highlight the potential of TraDeRa 324 which is capable, in real time, to reproduce the movement

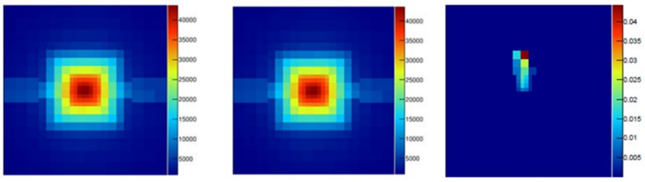

Figure 2.2: Comparison of two successive acquisitions (left) with an error induced on the position of the blades (middle) after image subtraction by TraDeRa (right)

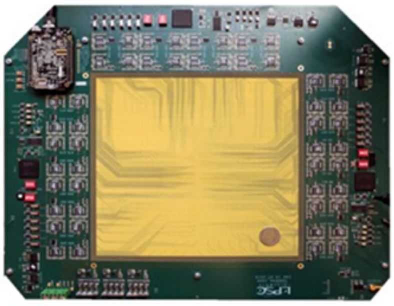

Figure 2.3: TraDeRa 1:1 (1600 channels, 40× 40 cm^2)

of the collimator leaves and to flag a positioning error of the order of 1 millimetre which corresponds to an over-response of 4 %. This also fully meets the requirements of the specifications and consequently validates the prototype, its electronics and the calibration procedure. Indeed, in practice, any overdose greater than 5 % is likely to cause severe clinical complications and any underdose below 95 % can render the treatment ineffective. R. Fabbro's thesis work was concluded with entire caracterization of the 324 channels TraDeRa first prototype and the construction of the 1:1 detector: "TraDeRa 1600" (1600 reading channels) Figure 2.3. In addition, R. Fabbro worked on a Monte Carlo method to evaluate the characteristics of the electron beam of a LINAC accelerator, based on the measurement of depth-dose profiles in a water tank, and adjustment of a minimum number of parameters. A precision of 10 keV at 6 MeV was achieved for the electron energy, much smaller than current values in the literature (~50 keV) [33]. This method is a necessary step to convert the signal from the detector into the measurement of the dose deposit in the patient. This is a key issue to allow the device to be used in clinical IMRT.

2.2.2 Scintillating fiber hodoscope for hadrontherapy

In the context of hadrontherapy, the CLaRyS collaboration has proposed a system for detecting the ion range in the patient based on the detection of secondary prompt gamma (see previous chapter). This system makes use of the time of flight of photons between the patient (the target) and the detector, in order to eliminate the significant background noise induced by neutrons and other scattered radiation. This improves the contrast-to-noise ratio, and therefore the sensitivity of the method. Therefore, an important element in measuring the time of flight is the use of a beam tagging hodoscope. The same hodoscope can also be used for proton radiography (particle tracking). The requirements for such a detector are to be transparent (or at least induce a fixed range shift with minimum scattering), a time resolution ~ 1 ns for prompt-gamma selection, an efficiency >~ 90 % for ToF measurement, and count rate capability of 100 MHz for single carbon detection or single bunch de-

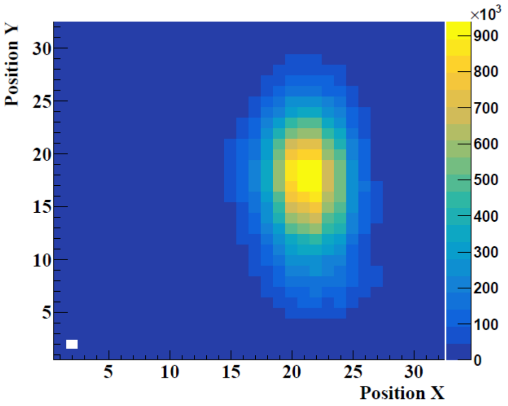

Figure 2.4: 65 MeV proton beam profile, recorded at a counting rate of 20 MHz in coincidence mode (logical AND) between the two fiber-planes

tection with protons. The Scintillating Fiber hodoscope was initiated by the Gamhadron ANR and FP7-ENVISION projects for prompt gamma monitoring (also supported by Rhône-Alpes Region), followed within the CLaRyS collaboration. It consists in two planes of 1 mm^2 squared-shaped scintillating fibers, readout by 64-channel matrix photomultiplier tube (MaPMT)s. A dedicated readout ASIC and acquisition board has been developed at IP2I [34]. The photomultiplier tube (PMT)s were characterized during the PhDs of Jean-Luc Ley[35] [36] [37] and Mattia Fontana [38]. The data acquisition system developed by the CLaRyS collaboration using fast µTCA has been developed for the Compton camera, including the hodoscope acquisition [39] [40]. A 32+32-fiber prototype has been tested first with carbon ions at GANIL, and second with the data acquisition system at CAL-Nice with proton beams, within the PhD of Oreste Allegrini [41]. The scintillating-fibers beam hodoscope was finally characterized in beam tests during O. Allegrini's thesis using 65 MeV proton (in the protontherapy center in Nice, Centre Antoine Lacassagne) as well as 95 MeV/u ^{12}C beams (in GANIL, Caen) at various intensities. This hodoscope successfully provided 2D images of proton beams (Figure 2.4) with a detection efficiency larger than 98 % with logical OR condition between the two fiber planes. Moreover, the timing resolution is around 1.8 ns FWHM. Overall, the performances show that such a technology is viable for beam monitoring during hadrontherapy [42]. A 128 + 128 fibers prototype, read-out with 8 MaPMTs, has also been assembled (Figure 2.5).

2.2.3 Diamond hodoscope for fast timing in hadrontherapy

The CLaRyS-UFT project (LPSC IP2I CPPM CREATIS), funded by the INCa Cancer Plan over the period 2017-2021, supported by *Université Grenoble Alpes* with the funding of S. Curtoni PhD thesis (2017-2020) and by the LabEx PRIMES with the funding of P. Everaere PhD thesis (2020 – 2023), proposed such a very innovative development based on the use of diamond detectors in order to achieve time resolutions of less than 100 ps. Indeed, compared to other semiconductors, chemical vapor deposition (CVD)-diamonds (Chemical Vapor Deposition) exhibit a high resistivity (>10^{13} Ω.m) associated to a large electronic gap (5.48 eV) that

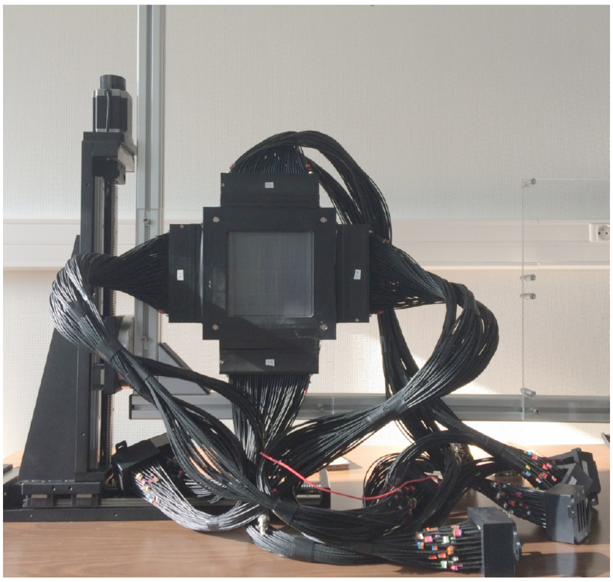

Figure 2.5: Scintillating fiber hodoscope, 2× 128 fibers, read out by 8 MaPMTs

results in an almost negligible leakage current, and thus a low noise level. They are also highly resistant to radiations and, most of all, the high charge carrier mobility (~2000 cm^2 V^{-1} s^{-1}) leads to a very fast response allowing tens of picoseconds time resolution and high count-rate capability. Consequently, diamond is an excellent candidate for such a targeted beam monitoring. Eventually, this diamond beam hodoscope is aimed to be used in a single particle regime, either at clinical intensities for carbon-therapy, or at reduced intensity during proton therapy.

The active part of the hodoscope, built at LPSC, tested and fully characterized in beam conditions (CAL and ARRONAX proton beam facilities) during S. Curtoni and then P. Everaere PhD theses, is made of diamond sensors (Figure 2.6): either single (sCVD) or polycrystalline (pCVD) ones. The choice between the two types of diamond here depends on the signal-to-noise ratio which is closely linked to the purity of the diamond (sCVD is the purest one) and which results from the analysis of the electrical signals generated by the collection of charges in the volume asset. Indeed, the energy deposition of an incident particle in the substrate is 25 times higher for carbon ions of 400 MeV/u than for protons of 70 MeV, allowing the use of pCVD diamonds of lower quality but available with larger surface (optimized coverage of the irradiation field). Then, the diamond read-out is performed by dedicated discrete (eventually integrated) reading electronics (low noise, high counting and timing resolution capacities). This hodoscope is to satisfy the conditions imposed for use in proton therapy and carbon therapy, which implies: counting rate performances at the level of 100 MHz for the entire detector, which results in ~10 MHz per channel, a targeted time resolution of 100 ps and a spatial resolution of about 1 mm and finally, a radiation resistance enabling their functioning at 10^{13} protons/cm^2/year (20 sessions/day). In such an application, the diamonds are used as solid ionisation chambers. Charges are created by the interaction of ionising particles with the material, as in the case of TraDeRa. An electric field causes the carriers to migrate towards the electrodes, where the signal is collected and amplified before being processed by the data acquisition system. To ensure optimum coverage of the hodoscope, the sCVD diamonds are arranged in a mosaic. The metalization for both sCVD and pCVD diamonds is in the form of

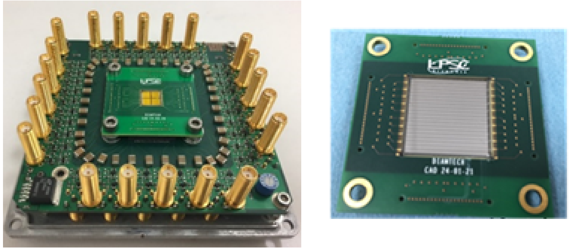

Figure 2.6: Top: the 32 channels diamond beam hodoscope demonstrator equipped with the 4 4.5 × 4.5 mm^2 sCVD diamond mosaic (daughter board) read-out by fast preamplifiers (mother board). Bottom: the 2 × 2 cm^2 pCVD daughter board

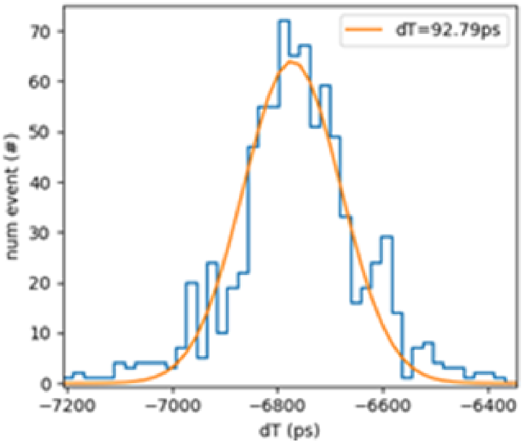

Figure 2.7: Time resolution achieved with the diamond active volume read out by the whole electronic read-out chain. dT is the rms value of the fit function

strips orthogonal on each face (inducing possible X,Y spatial locations). Current preamplifiers were designed [43] using discrete components, at the LPSC, to instrument the diamond strip - by - strip readout. The rest of the electronics chain includes a Constant Fraction Discriminator (CFD), which provides a time measurement independent of fluctuations in the amplitude of the diamond signal at the output of the preamplifiers. And, finally, a Time to Digital converter (TDC) (40 TDC are embedded on a single FPGA) which makes it possible to achieve the temporal resolution between two X and Y strips impacted by the incident ion. S. Curtoni and P. Everaere demonstrated that the expected performance, 93 ps rms time resolution (Figure 2.7), could indeed be achieved by the diamond hodoscope using a 70 MeV proton beam in the single particle regime with 70 MeV protons and sCVD diamonds [44]. Such a result fully validates the developments undertaken and will bring, in a near future, a significative value for the prompt gamma detection for hadrontherapy on-line monitoring.

2.3 On-line dosimetry

2.3.1 Online monitoring of microbeam radiation therapy

The advent of synchrotron radiation (SR) has added a new dimension to the use of X-rays in imaging and therapy. Faced with the complexity of these techniques, clinicians, medical researchers, medical and nuclear physicists are working closely with synchrotron scientists to transfer these developments to clinical trials. The STROBE team and the LPSC-PNAM team collaborate since 2018 within the context of N. Rosuel PhD

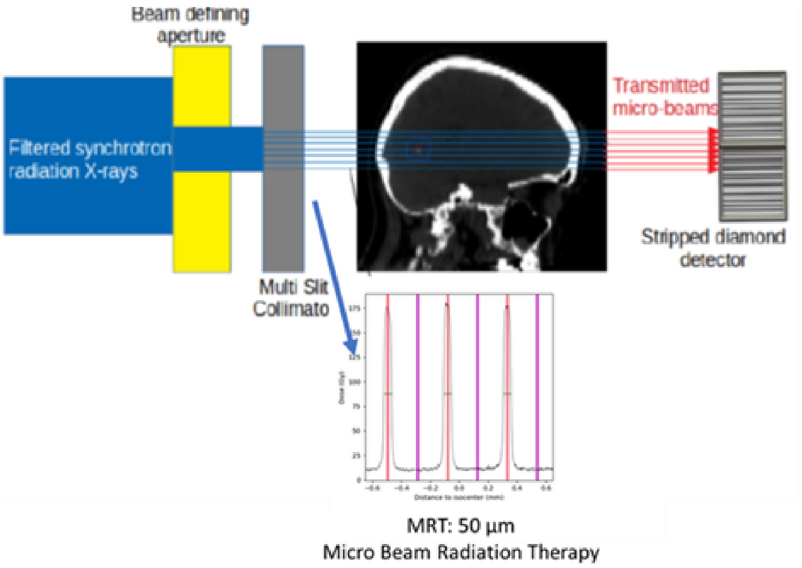

Figure 2.8: The MRT principle and illustration of the diamond portal monitor downstream the patient

thesis (2018-2021) funded by PRIMES, to the development of an on-line monitoring system for MRT using a portal diamond beam monitor (downstream of the patient Figure 2.8), with a spatial resolution enabling each microbeam (~ 50µm width) and each inter-beam space (~ 350µm) to be measured. This work lays the foundations for the veterinary clinical trial in synchrotron microbeam radiotherapy, which started in 2021. Furthermore, in 2023, this research received the support of the INCa Cancer Plan with the funding of the project IODA MASTER which extends until 2027 (STROBE, LPSC, INL, CHU-Grenoble-Alpes).

Spatial fractionation in the context of X-ray radiotherapy is the practice of collimating a beam into an array of smaller beams to provide an inhomogeneous distribution of radiation dose to the target. This principle is particularly well-suited to coherent radiation such as that delivered by a synchrotron (ESRF in Grenoble), allowing high dose deposits to deep tumours while minimising damage to surrounding healthy tissues, thus improving the therapeutic ratio. This spatial fractionation is preserved throughout the patient volume. As this emerging technique is still in its evaluation phase, it obviously requires in-depth methodological and medical development. A further implementation consists in *in vivo* dosimetry, which is the real-time assessment of the actual dose delivered to target volumes (tumor volumes) and surrounding organs during treatment. The question of *in vivo* dosimetry is particularly difficult and has not been addressed so far for this type of therapy. *In vivo* dosimetry in conventional X-ray radiotherapy (in hospitals) is currently performed with diodes or a matrix of silicon diodes: this is the so-called "portal" detector located downstream of the patient. This system is not suitable for synchrotron radiation due to the low energy of the photons (50 – 200 keV) associated to a very high flux (10^4 Gy/s). In this context, the objective that was set with the diamond portal detector was to measure the flux transmitted for each micro-beam, using a multi-channel segmented diamond detector, in order to be able to compare this flux with the predictions resulting from simulations of the treatment plan. In such a design, the diamond must allow a 1D localization, consequently one face of the diamond is metalized in the form of strips, the other is

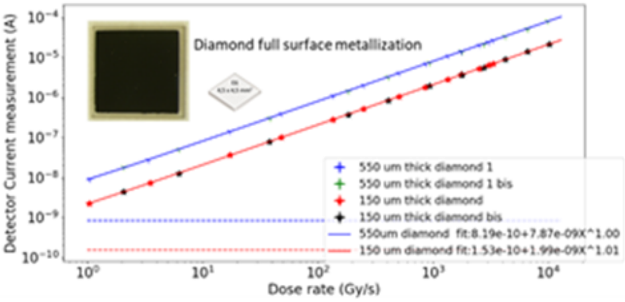

Figure 2.9: Detector current measurement versus dose rate (Gy/s).

uniformly metalized. The size of the strips as well as the space between two consecutive strips have been calculated so that one track measures the charge in the peaks, the next in the valley and this at the distance where the detector is located behind the patient. In addition, MC simulations, conducted by N. Rosuel in his PhD thesis [45], made it possible to estimate an optimized diamond thickness for the detector of 150 μm (Figure 2.9). So, the detector is of sufficient sensitivity not to saturate in the peaks and to be able to also detect the signal in the valley which is two orders of magnitude lower. Experiments carried out at the ESRF also made it possible to test the linearity of the response of the diamond active volume readout by electronics developed at the LPSC (on the model of what was developed for TraDeRa [32]), as a function of the dose rate (intensity for a microbeam) Figure 2.9. This has been validated over the current range provided for MRT measurements. These results led to the design of a first prototype of 32 read channels in discrete electronics then to a second version equipped with integrated electronics, developed at LPSC as well. This 8-channel prototype has demonstrated all its performance and been used in clinical routine on dog veterinary patients as part of the INCa PAIR TUMC project. The data analysis was performed by F. Di Franco during her postdoctoral studies funded by PRIMES in 2023 [46]. It has been proven that the detector was able to measure direct and attenuated microbeams as well as inter beam fluxes with a 1 % precision level. Phantoms' tests (RW3 and anthropomorphic head phantoms) were performed and compared to simulations. A preliminary study showed that absolute differences between simulated and recorded transmitted beams are within <2 %, even with complex geometries. Eventually, a 153-channel detector was built in 2023 on this principle, and tested successfully during the last ID-17 beam-time in July 2003.

2.3.2 Flash therapy - pulsed proton beams: DIAMMONI diamond beam monitoring

Time fractionation makes it possible to deliver doses of the order of Gy in 1 ms, or even 1 μs. In this case, the rapidity with which the dose is delivered makes *in vivo* control more problematic. As we have seen, on-line *in vivo* control of radiotherapy can be done by secondary radiation from nuclear reactions in hadrontherapy. The trend towards increasing the intensity of clinical beams for flash therapy now poses new challenges: adapting the counting capacity of detectors, electronics and data acquisition. On the other hand, the ion accelerators allowing the delivery of such beams create the need for very precise monitoring of the ion flux with fast

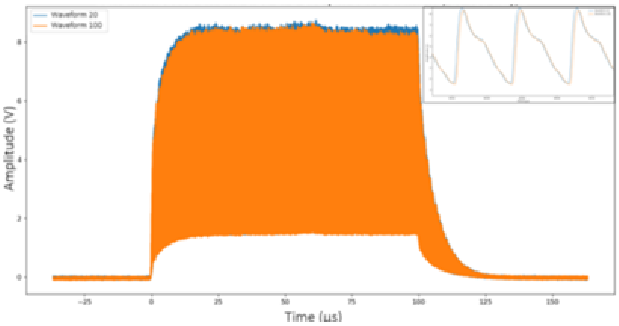

Figure 2.10: Reconstruction by a full metallized diamond detector of a ∼ 100 µs train made of 4 ns proton pulses emitted at 30.45 MHz. During data acquisition performed by a digital sampling oscilloscope, the proton flux was at the level of 410 kGy/s

counting in a strongly radiative environment. An important issue is the adaptation to the temporal beam structures, which vary greatly depending on the type of accelerator (cyclotrons, synchro-cyclotrons or synchrotrons), in terms of useful cycle or peak intensity. The intrinsic qualities of diamond make this semiconductor a perfect candidate, here too, to meet monitoring requirements with such accelerators. This led to the DIAMMONI project funded by ANR (R. Molle PhD thesis 2022-2024 collaboration LPSC, Subatech, ARRONAX) and supported by the LabEx PRIMES (internship R. Molle in 2022).

DIAMMONI proposes the development of a diamond detector for beam monitoring at ARRONAX with an application to proton flash radiotherapy. The beams used are very intense pulsed beams. Key issues in the project are 1) to be able to mark the “start” and “end” of each train of pulses and 2) to integrate the current in each successive train. As in "flash" treatment, the objectives are to increase proton beam intensity of the order of µA which stands for 10^5 to 10^6 particles per single proton pulse, it represents a real challenge. At first, the choice of diamond detector active part is crucial. It implies to use thin diamond (50 µm) highly biased (4 V/µm instead of 1 V/µm which is standard use) in order to avoid charge recombination inducing charge loss. Then it implies the design of a dedicated readout electronics for the current integration. Preliminary experimental studies on the ARRONAX cyclotron have demonstrated that the “start” and “end” train stamp in expected time is well performed Figure 2.10. A zoom on the diamond signal (upper right corner) proves that the pulsation of the signals corresponds to the expected period of 33 ns. Front-end diamond read-out electronics were then developed at the LPSC. It allows the integration of the current in a proton train of variable duration (dt) with an interval between two consecutive trains (dit) also adjustable according to the average beam intensity desired for the delivery of the treatments. The current integration was validated under experimental conditions at the ARRONAX cyclotron under 70 MeV proton beams. In addition, the linearity of the detector’s response under flash therapy conditions has been proven [R. Molle *et al.* article in preparation]. Finally, ageing studies were performed showing that the diamond active part withstands a fluence of 10^{13} Gy/cm^2/year which corresponds to the specifications of the cumulative fluence over one year of such an hadrontherapy treatment.

2.4 Online dosimetry for Small-Field and Microbeam Radiation Therapy using innovative detectors and QA systems

2.4.1 QASys: A novel QA system implementing 2D dose tomography for small-field radiotherapy

Small radiation fields have increasingly been used during external beam radiotherapy, *e.g.* in Stereotactic RadioSurgery for intra-cranial and extra-cranial treatments. Small-field dosimetry and quality assurance (QA) raise some challenging issues due to (i) lack of charged particle equilibrium over most of the radiation field, (ii) partial source occlusion by the LINAC collimation system and (iii) steep dose gradients resulting from important contribution of penumbrae. [47] The detector choice or the system design for small field QA should especially take into consideration the size of the sensitive volumes (volume averaging effect), its water equivalence (energy dependence and dose perturbation) as well as other figures of merits of dosimeters response (dynamic range and linearity, dose rate independence, . . .).

The QASys consortium (INL, CREATIS, TIMC, HCL, LHE-EPFL) in the framework of the project funded by the InCa Cancer Plan over the period (2018-2021) and supported by the LabEx PRIMES (Master Internship A. Zouaoui, 2021) has developed a novel system for small-field QA. It is based on the scintillating fiber (SciFi) detector initially developed for the LHCb experiment at CERN, which is made of tissue-equivalent scintillating plastic fibers with a fiber pitch of 275µm [48].

The first version of the system was focused on the QA of small fields defined by SRS cone collimators. The scintillating signal at the SciFi detector output (which represents the projected field profile along the fibers axis) is read out by a complementary metal-oxyde semiconductor (CMOS) camera and then processed by a specific iterative reconstruction method. System testing for determining beam profiles and collimator output factors has been carried out at Lyon Sud Hospital (HCL) under 6 MV photon beam irradiation. The reconstructed profiles for cone sizes from 4 to 15 mm diameter are coherent with data from EBT3 radiochromic films and micro-TLD [49, 50]. Another version of the system shown in Figure 2.11. is to monitor two-dimensional (2D) dose distributions of small elliptic and rectangular fields.It is based on 6 SciFi detectors stacked with in-plane 30° rotated orientations from each other.

Each detector output is coupled to a linear array of silicon photodiodes. The six acquired projected dose profiles at different orientations are processed by a two-step method (*i.e.* geometric tomography followed by penumbra determination) to perform 2D dose reconstruction [52]. Gamma index analysis using EBT3 films as reference has been performed on data obtained with a 6-MV photon beam, as illustrated in Figure 2.12. It shows that the reconstructed 2D dose distributions have gamma index pass rates higher than 95 % for all the tested configurations with 1 %-Dose-Distance / 1 mm-Distance-To-Agreement criteria [51]. A tomo-

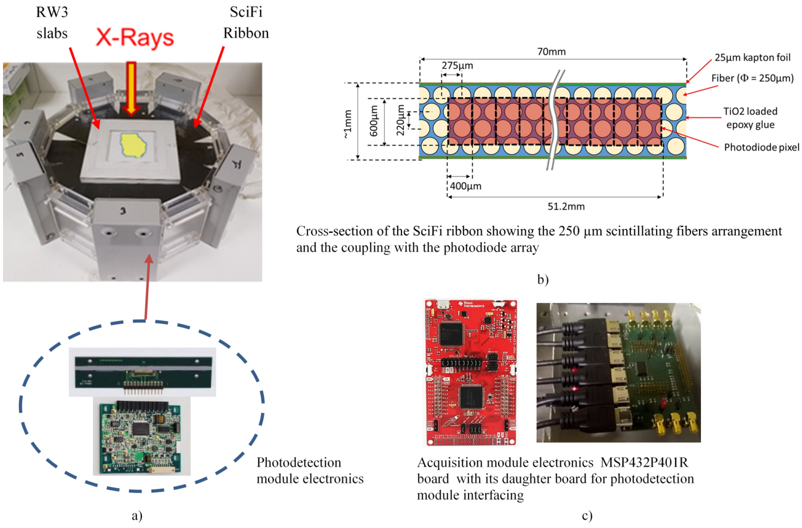

Cross-section of the SciFi ribbon showing the 250 µm scintillating fibers arrangement and the coupling with the photodiode array

b)

Photodetection module electronics

a)

Acquisition module electronics MSP432P401R board with its daughter board for photodetection module interfacing

c)

Figure 2.11: QASys Instrumented phantom prototype for small field QA, implementing a stack of 6 SciFi detectors with in-plane 30° rotated orientations and 768 photodetection channels [51]

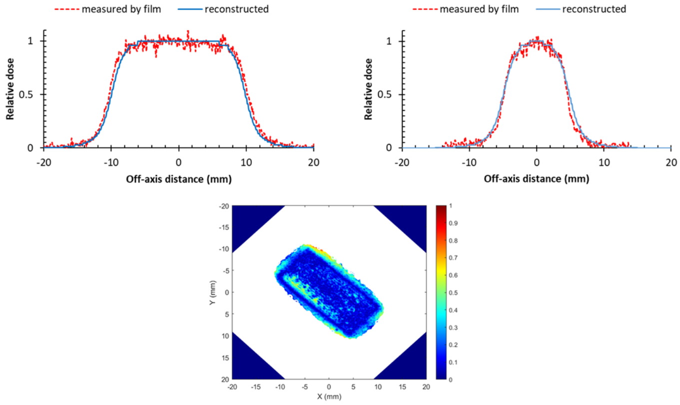

Figure 2.12: Measurement of 2D dose distribution for a 20x10 mm² RT field by QASysy prototype and EBT3 films: Field profiles and Gamma index analysis with 1 %-DD /1mm %-DTA [51]

graphic reconstruction algorithm for cross-sectional imaging of IMRT beams from six projections has also been proposed and experimentally validated [53]. According to the obtained results, such a real-time system could potentially be an alternative to film dosimetry, which is still widely used as reference in clinical practice for small field QA. Moreover, the same system with minor changes could be adopted for a quick and highly resolved Percentage Depth Dose curve (PDD) measurement or check without using a water tank [54]. Its high depth resolution also makes it possible to measure PDD in heterogeneous cavity conditions.

2.4.2 Novel detectors for Synchrotron Microbeam Radiation Therapy dosimetry and QA

Synchrotron Microbeam Radiotherapy, which uses low-energy photon beams at extremely high flux (~10 kGy/s) with submillimeter spatial fractionation, raises multiple challenges for dosimetry and quality assurance, for example in terms of micrometer spatial resolution, dynamics and tissue equivalence of detector response, and radiation hardness. The Ioda-Master project (STROBE, INL, LPSC CIC-IT CHUGA), funded by INCa's Cancer Plan over the period 2023-2026, supported by PRIMES

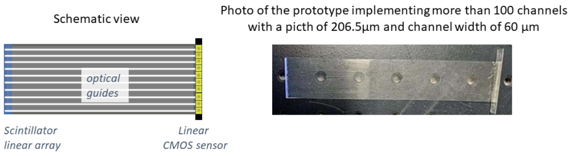

Figure 2.13: MRT dosimetry and QA detector prototype implementing an array of plastic micro-scintillators coupled with a multi-mode multi-core optical guide

(F. Thevenet PhD 2021- 2023 and M. Moussaoui internship in 2023), proposes to meet these challenges using instrumentation based on the use of micro-scintillator arrays.

High resolution PSD detector for synchrotron MRT

Compared with other detection technologies being considered for real-time MRT dosimetry, which use materials with Z and/or densities much higher than the tissue, plastic scintillation detectors (PSD) have a much lower energy dependence of their responses for low-energy photon MRT beams. Archer *et al.* have shown that a point detector, consisting of a 10µm-thin disc of plastic scintillator coupled to an optical fiber, can withstand the extremely high dose rates used in MRT [55].

Based on these interesting properties, we have developed for MRT dosimetry and QA, a novel detector by implementing an array of plastic micro-scintillators coupled to a multi-mode multi-core optical guide. It is worth mentioning that the detector microfabrication process allows self-alignment of each core in the guide with a single micro-scintillator and thus, preserves the full detector resolution. Prototypes with more than 100 channels at half the MRT beams pitch have been built to measure peak and valley doses simultaneously across the full width of the field as shown in Figure 2.13.

The first prototype of the detector allows a full beam coverage (20 mm) with single beam spatial resolution (60 µm). The detector output is read out by a high-resolution linear CMOS sensor. The prototype testing carried out at ESRF under MRT conditions confirm the technology's good radiation hardness, with no observable degradation in detector response after irradiation of 100 kGy carried out at extremely high dose rate (several kGy/s). The detector has a linear dose response with no dose-rate dependence, as shown in Figure 2.14 . These encouraging results validate the undertaken developments. We are currently working on system improvements in terms of SNR optimization and fabrication process for lower inter-channels variation.

Highly-heterogeneous-cavity-based-detector for synchrotron MRT

It is worth mentioning that high-yield PSD are based on a couple of dopants implementing a two-step conversion, *i.e.* (i) scintillation and (ii)

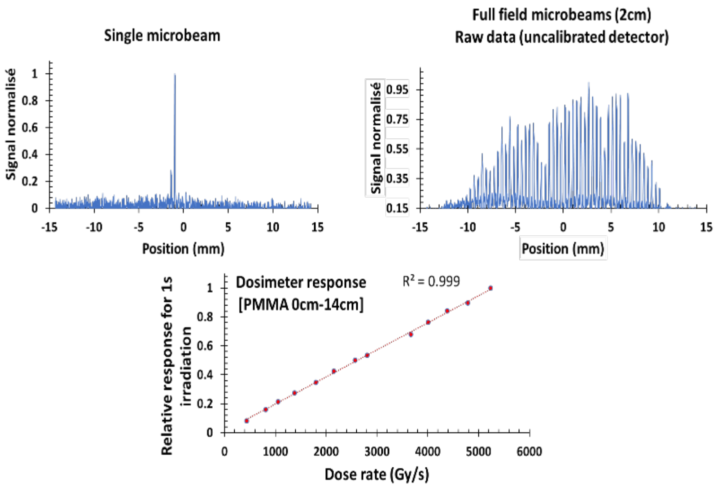

Figure 2.14: Detector response to single microbeam and full MRT field irradiation measured at ESRF

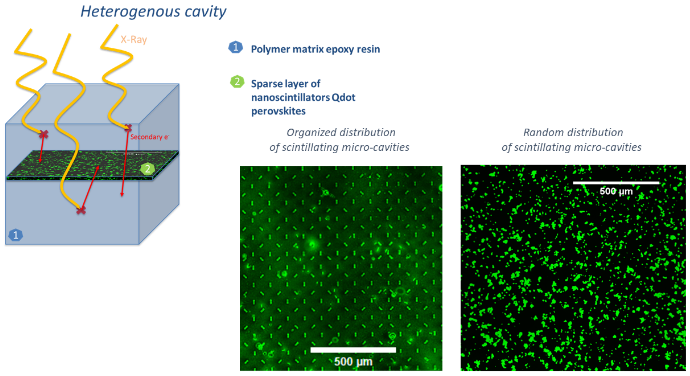

Figure 2.15: Sparse scintillation layer of a few microns thick, based on perovskite QDots

wavelength shifting which limits the miniaturization possibilities of the PSD.

To overcome this difficulty, we are studying an alternative approach based on highly heterogeneous cavities made up of a thin, sparse scintillating layer embedded in a tissue-equivalent polymer matrix. This new type of detector is expected to show low energy dependence of its response because of its principle of operation. Indeed, when such a detector is implemented in a RW3 phantom and thanks to this polymer matrix, it can be considered as a large cavity not disturbing the flux of the primary photons (the charge particle equilibrium is established). Therefore, the collision Kerma gives a good approximation of the absorbed dose in this (large) cavity. The sparse scintillation layer, which comprises high-Z scintillation micro-cavities, mainly detects the electrons resulting from this dose deposition. The response of such a detector can be modeled with a combined use of large and small cavity theories.

To establish the proof of concept for this new detector, we have developed prototypes with a sparse scintillation layer of a few microns thick, based on perovskite QDots. This layer is embedded in an epoxy polymer matrix. Two microfabrication processes have been developed in the framework of M. Moussaoui Master internship (supported by the LabEx Primes) to produce layers with scintillating microcavities that are either organized or randomly distributed. Images of such layers are shown in Figure 2.15. Detectors using an array of highly heterogeneous cavities have been

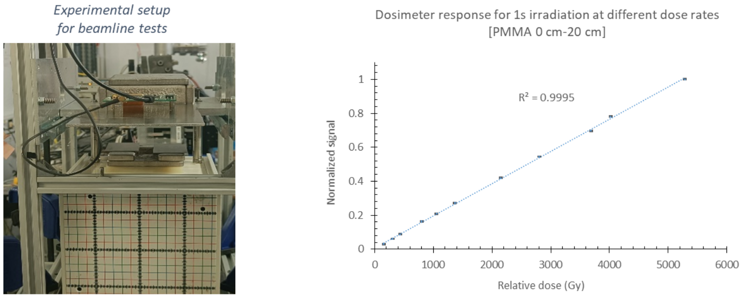

Figure 2.16: Highly-heterogeneous-cavity-based-detector testing at ESRF in MRT conditions

designed, built and tested under synchrotron MRT conditions at ESRF. Figure 2.16 shows the experimental set-up and the measured response of the detector for a 1 s irradiation at different dose rates.

The detector response is linear and does not depend on the dose rate. It exhibits a radiation hardness to be considered for a routine use in synchrotron MRT dosimetry. The detector response shows no energy dependence with the spectrum modification due to the use of PMMA plates (ranging from 0.5 cm to 20 cm) to change the irradiation dose rate. This is in line with predictions from our modelling. Further work is underway to study the energy dependence of this type of detector over a wider range of X-ray photon spectra. Scintillating layers based on other QDots will also be studied as part of the Ioda-Master project.

2.5 Conclusion

Several developments were conducted within the frame of LabEx PRIMES to provide innovative therapeutic beam monitors. In order to be widely used, monitors for IMRT should become mandatory in each treatment facility, which is not yet the case. More focused monitors, such as time- and position-beam hodoscope in particle therapy, and synchrotron-radiation QA and real-time monitoring systems, may have specific applications and deserve forefront research and developments. Such developments are still ongoing.

External beam radiotherapy using synchrotron X-rays

3

Author: Jean-François Adam

3.1 Introduction

The advent of synchrotron radiation (SR) has added a new dimension to the use of x-rays in imaging and therapy [56]; and several beamlines currently have active research programs in medicine using high-flux coherent x-ray beams produced by a synchrotron source. Regarding the complexity of these techniques, clinicians, medical researchers, medical physicists have been collaborating closely with synchrotron scientists to spearhead this development towards clinical trials. The concepts of the two main Synchrotron radiotherapy modalities are summarized on Figure 3.1. The first phase I/II clinical study of synchrotron radiotherapy ever realized has recently been performed at the European Synchrotron Radiation Facility (ESRF), in a dose escalation protocol on 15 patients [57, 58]. Synchrotron Microbeam Radiotherapy (MRT) is now also entering a clinical transfer phase [59] with large animal studies for toxicity studies [60] and a veterinary trial that just started at the European Synchrotron [61] on dogs bearing primary malignant brain tumors. The present chapter introduces the rationale of synchrotron radiotherapy and its high potential in cancer and drug resistant epilepsies management. A focus is made on the synchrotron stereotactic radiation therapy clinical trial and on the translational research in MRT, and related perspectives, to emphasize on the groundbreaking medical physics, clinical and translational research that occured in the frame of the LabEx PRIMES to enable these successful milestones that are definitely game changers in the world of radiotherapy. The radiobiology fundamentals of synchrotron radiotherapy are described in more details in the experimental radiobiology section (cf 4).

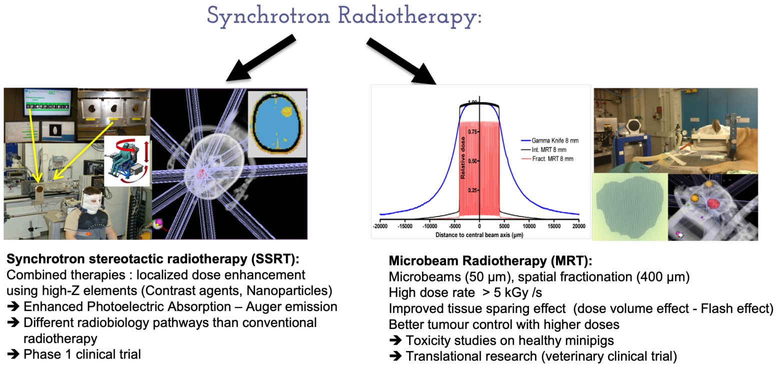

Synchrotron Radiotherapy:

Synchrotron stereotactic radiotherapy (SSRT):
Combined therapies : localized dose enhancement using high-Z elements (Contrast agents, Nanoparticles)
➔ Enhanced Photoelectric Absorption – Auger emission
➔ Different radiobiology pathways than conventional radiotherapy
➔ Phase 1 clinical trial

Microbeam Radiotherapy (MRT):
Microbeams (50 µm), spatial fractionation (400 µm)
High dose rate > 5 kGy /s
Improved tissue sparing effect (dose volume effect - Flash effect)
Better tumour control with higher doses
➔ Toxicity studies on healthy minipigs
➔ Translational research (veterinary clinical trial)

Figure 3.1: Synchrotron Radiotherapy Modalities

3.2 Synchrotron radiation therapy

Radiation therapy (RT) is the use of ionising radiation to treat cancer and some other types of non-cancerous lesions such as drug-resistant epilepsy. Along with surgery and chemotherapy, RT is one of the most effective methods for cancer treatment. Around 50 % of all cancer patients will receive RT at some stage during the course of their illness [62]; and among all patients with malignant brain tumours, almost 85 % had indications for curative- or adjuvant-intent RT [63]. The main challenge of radiotherapy is to deposit a therapeutic radiation dose in the tumour without exceeding the nearby healthy tissue tolerances. For some particularly radio-resistant tumours, RT only offers a palliative option due to the high morbidity of the surrounding healthy tissues. New techniques are under development in order to improve the therapeutic index of radiotherapy *i.e.* the balance between the probability of tumour control (TCP, for Tumour Control Probability) and the risk of normal tissue complications (NTCP, for Normal Tissue Complications Probability). The objective of these new modalities is to widen the so-called therapeutic window. This is achieved when a treatment scheme offers a similar TCP for lower NTCP values, or an improved TCP for similar NTCP values.

The use of low energy x-rays in this context is attractive if the x-ray source can be brought inside or close to the target volume, because of the steep depth-dose curves inherent to these poorly penetrating beam qualities. These techniques are already implemented in clinics with good results in the management of some solid tumours: brachytherapy [64], intrabeam therapy [65] or contact therapy [66] are classical examples. However, the use of low to medium energy x-rays in external beam radiotherapy was almost completely disregarded by the medical community for treating deep seated tumours due to the lack of beam penetration. Several systems have been recently proposed to use kilovoltage x-rays in dynamic arctherapy (kVAT), as a cheaper alternative to linear accelerator-based dynamic treatments [67–69]. These techniques have to be optimised to reach clinical practice, especially by improving the organ at risk doses distributions [68].

Synchrotron radiation can produce high flux (10^5 times higher than a conventional x-ray source), quasi-parallel coherent x-ray beams in the 50-200 keV energy range. The particularities of this x-ray source offer significant advantages in external beam radiotherapy using low to medium energy x-rays. Innovative therapeutic applications of synchrotron radiation have thus been developed in the past 20 years, where the poor beam penetration is compensated by the use of:

- **high-Z elements radiosensitizers for local dose enhancement: the higher the atomic number of the target, the higher the local energy absorption.** The numerous preclinical studies have clearly demonstrated the therapeutic efficacy (significant increase of local energy absorption and of survival time in rodents) of this modality for various radiosensitizing agents: iodinated contrast agents [70]; platinum based chemotherapeutic agents [71, 72]; gold, gadolinium,iron or lathanides nanoparticles [73–77]. An increased differential effect is obtained when irradiating tumors previously loaded with high atomic number elements. If a high-enough radiosensitizer concentration is reached without toxicity, a local increased energy deposition occurs due to the rise of the photoelectric effect cross section on heavy atoms irradiated with low-to-medium energy x-rays and associated secondary particles (photoelectrons, Auger electrons and fluorescence x-rays). These combined treatment modalities benefit from a much greater local dose enhancement at synchrotron beams of low to medium energies, when compared to high-energy photons from a linac [73, 74, 77].

- **high dose rate x-ray beams to take advantage of the so-called flash effect: the higher the dose rate, the higher the healthy tissue tolerance.**The potential of ultrahigh dose-rate single-dose irradiations has been recently shown (< 40 Gy/s, flash, 6 MeV electron beams). In flash irradiations, the occurrence and severity of early and late complications affecting normal tissue is significantly reduced [78, 79] relative to that of conventional irradiations (0.05 Gy/s) at the same dose, with a similar tumor control probability. Medical beamlines in synchrotron facilities can achieve dose rates of 0.1 to 10 kGy/s at 2 cm depth in water (2×2 cm^2 square field), which clearly shows the potential of these sources for exploiting the benefits of the flash effect in external beam radiotherapy using photons sources [80].
- **submillimetric fields for a spatial fractionation of the dose: the smaller the field size, the higher the tolerances of the healthy tissues.** The use of submillimetric field sizes allows to explore the limits of a concept called dose-volume effects: the smaller the field size, the higher the tolerances of the healthy tissues [81, 82]. These tolerances increase dramatically when field sizes smaller than a certain threshold are used [83]. The spatial fractionation of the dose could provide a further gain in tissue sparing due to the biological repair of the microscopic lesions by the minimally irradiated contiguous cells [84]. It has also been recently demonstrated that microbeam radiation therapy significantly improved survival of glioma bearing rats when compared with broad beam radiation therapy delivered at a comparable dose [85, 86]. Therefore, spatial fractionation of the dose using submillimetric field sizes may lead to a simultaneous shift of the TCP and NTCP curves in opposite directions, widening the therapeutic window for radioresistant tumors such as gliomas [87]. The coherent high dose rate synchrotron generated x-ray beams are of particular interest for this technique, with a blurring effect [88] minimised by short irradiations times, and micrometric penumbras [89] due to short electron ranges and high spatial beam coherence.

3.3 Clinical trials in contrast-enhanced synchrotron stereotactic radiotherapy

Clinical therapeutic applications of synchrotron x-rays are thus becoming a reality. Fifteen oligo-brain-metastatic patients have been successfully treated at the European Synchrotron Radiation Facility medical beamline (ESRF-ID17), using 80 keV high-flux quasi-parallel monochromatic x-ray beams, in the presence of iodinated compounds injected immediately before irradiation [57, 58]. These clinical trials have been proposed from the promising *in vitro* and *in vivo* preclinical trials performed in the early 2000's [70, 90, 91]. The medical physics challenges [92] that have been successfully addressed to implement these clinical trials are detailed thereafter. A dedicated treatment room has been built at the ESRF medical beamline [93] together with a irradiation control system interfaced with a state of the art patient safety system (see the left part of Figure 3.1). After a phase of optimisation of the treatment plan parameters (energy, ballistic, etc) performed by Edouard *et al.* [94], a dedicated TPS was adapted to contrast-enhanced synchrotron stereotaxic radiotherapy (SSRT) in which the synchrotron beamline geometry and the transport of low to medium energy polarised photons in presence of high-Z material were modelled [95] (see Figure 3.2).

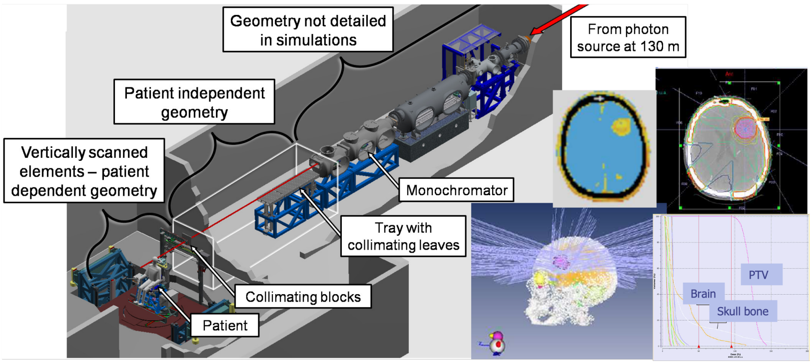

Figure 3.2: Synchrotron Stereotactic Radiotherapy: Beamline model and treatment planning

Dedicated dose prescriptions and absolute dosimetry protocols have also been implemented [96, 97]. Finally a dedicated dosimetry CT protocol including the quantification of the radiosensitizer biodistribution has been proposed, validated and used for treatment planning [98].

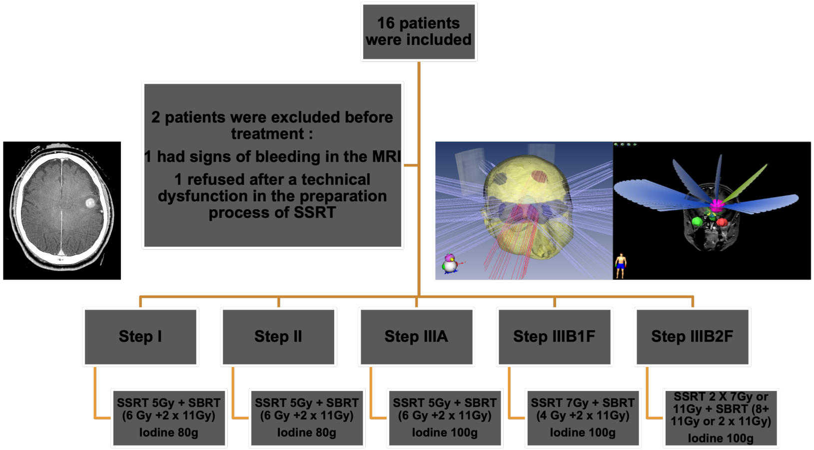

Figure 3.3: Synchrotron Stereotactic Radiotherapy: clinical trial workflow

These interdisciplinary approaches and close collaboration between the Grenoble-Alpes hospital, university team and the ESRF scientists and engineers, lead to the first radiotherapy clinical trial ever performed using synchrotron x-rays. It consisted of a dose escalation protocol to show the feasibility and safety of the technique and 15 patients were successfully treated with an increasing part of their hypo-fractionated stereotactic radiotherapy treatment course being performed using Contrast Enhanced Synchrotron Stereotactic Radiation Therapy (CE-SSRT, see Figure 3.3). In the frame of this clinical trial, our team also presented the very first live human computed tomography (CT) dataset obtained on a synchrotron source with monochromatic x-rays at a clinical radiation dose [99].

This clinical trial has clearly shown the feasibility and safety of this combined treatment technique using iodinated contrast agents. However, due to the limited uptake of iodine (2 mg/mL on average in the planned target volume (PTV) [98]), and the fact that the contrast agent remains extracellular during the irradiation, there is a particular interest for Platinum based chemotherapeutic drugs or Gadolinium nanoparticles to reach a higher therapeutic efficacy in SSRT with molecules that have an approval for being used in the context of combined radiotherapies.

As combined therapies using Carboplatinum [72], or Aguix Gd nanoparticles [74] have shown interesting results under MV irradiations in preclinical trials on rodents, several clinical trails have started using conventional hospital MV Linacs. As a direct consequence of Rousseau *et al.* work [72], a Phase I trial of intracerebral convection-enhanced delivery of carboplatin for treatment of recurrent high-grade gliomas has recently started in the USA [72] for combined radio-chemotherapy using carboplatinum [100]. After years of academic development through collaboration of several French and International laboratories, AGuiX , a sub-5 nm nanoparticle based on a polysiloxane network surrounded by gadolinium chelates has been developed as theranostic agent to be an effective MRI contrast agent and radiosensitizer. This new technology has successfully been transferred in human at Grenoble with the achievement of "First in Man" clinical trial sponsored by CHUGA, the NANORAD trial [101].

These preclinical and clinical trials are paving the way of the future SSRT trials (as for example a Phase II clinical study of SSRT for re-irradiation of local relapsing glioblastoma in presence of Aguix Gd Nanoparticles which has been proposed to the ESRF), using the unique capability of Synchrotron Radiation (SR) tuneable monochromatic x-rays to be produced at clinical dose rate. This achievement allows one to consider, from then on, that the SSRT installation at ESRF combined with the CHUGA expertise to identify, recruit and treat patients at ESRF/ID17, could be an operational platform of SSRT open to external users in collaboration with the radiation-oncology team of the CHUGA. However, the ESRF decided to disregard the continuation of the SSRT program at the end of this first trial. In 2023, the ESRF decided to close ID17 and hence put an end to the feasibility of any *in vivo* medical applications of synchrotron radiation.

3.4 Toward clinical trials in microbeam radiation therapy

There is undoubtedly an improved differential effect (higher TCP with lower NTCP) when using arrays of synchrotron x-rays minibeams (0.5 mm wide beams replicated at a 1 mm pitch [102]) or microbeams (0.05 mm wide beams replicated at a 0.4 mm pitch [85]), in the context of spatially fractionated radiotherapy. In particular, the outstanding improved healthy tissue sparing effect of synchrotron MRT [103] enable to deliver several tenth of Gy in the PTV and hence reach an much higher tumor control with less side effects, when compared to broad beam irradiations [85, 86]. After two decades of preclinical studies, the clinical transfer of MRT in oncology [59] and epilepsy [104, 105] management becomes a reality. Regarding the complexity of these techniques, clinicians, medical researchers, medical physicists had collaborated closely with synchrotron scientists to spearhead this development towards clinical trials. As these high dose rate techniques are still in their conception phase, they obviously had required extensive methodological development for their implementation in transnational research. Rigorous medical physics clinical codes of practice had to be implemented on the beamlines involved. Such protocols are well established in conventional clinical radiotherapy, but they are not directly applicable to synchrotron radiotherapy due to the low to medium energy x-ray spectrum, very high dose rates and radiation detectors and modeling tools limitations if being used for submillimetric beams. The medical physics works, related to the transfer of spatially fractionated beams into transnational research on large animals, is presented thereafter to highlight the strong added value of the LabEx PRIMES collaborative effort to reach these outstanding milestones. A focus is made on theoretical and experimental dosimetry challenges and end to end studies that have been addressed in the preparation of MRT clinical trials.

Several teams from the LabEx PRIMES are collaborating to develop a full medical physics suite (instrumentation, detectors, simulations, treatment planning) for state of the art synchrotron RT programs: MRT and FLASH photon radiotherapy. The final goal of these projects is to propose the contours and methodology of a phase I/II synchrotron radiosurgery clinical trial using these instrumentation and software. Four main research axes have been identified as key challenges to be addressed to that respect: beam characterization, beam monitoring and portal dosimetry; developing instrumented phantoms for dose measurements; modelling the dose distribution and its biological consequences; and providing the adequate methodology for initiating the clinical transfer of MRT.

Measuring the microbeams dose accurately and reliably is a fundamental step towards trials with human patients as precise delivery of the dose prescribed by the oncologist must be ensured. Indeed, the technique is based on the spatial fractionation of the dose using an array of parallel microbeams having a width comparable to that of a human hair (~50 micrometres) and being separated by regions of almost zero radiation (400 micrometres pitch).

An absolute dosimetry protocol has also been proposed, slightly modified from the IAEA TRS 398 code of practice [106], and using a pinpoint chamber in a centimetric square field [107]

Absolute real time dosimetry methods have been successfully benchmarked using a microdiamond detector [108–110], in the framework of a LabEx PRIMES - Australian synchrotron collaborative effort.

Film dosimetry applied to MRT Quality Assurance has been extensively studied by Pellicioli *et al.* [111]. Despite some substantial improvements the method still suffers from large uncertainties, bias due to the reading modality using a single channel microscope and requires lots of post-processing which makes it difficult to be implemented in a clinical workflow. Ocadiz *et al.* developed a patient specific QA based on film dosimetry [112]. This modality has however been set with a limited spatial resolution and with separate outputs for peak and valley doses. It also suffers from high uncertainties due to the noise in the film's readout procedure. An extensive study has been performed as part of a PhD funded by LabEx PRIMES [113], to find the most suitable film type for MRT dose assessment under irradiation conditions that were identical to the treatment.

The INCa has recently granted 3 teams of the LabEx PRIMES with fundings to develop dose calculations algorithm, treatment planning and evaluation tools, beam monitoring devices and *in vivo* dosimetry modalities. Three PhD students were also funded by the LabEx PRIMES in that context.

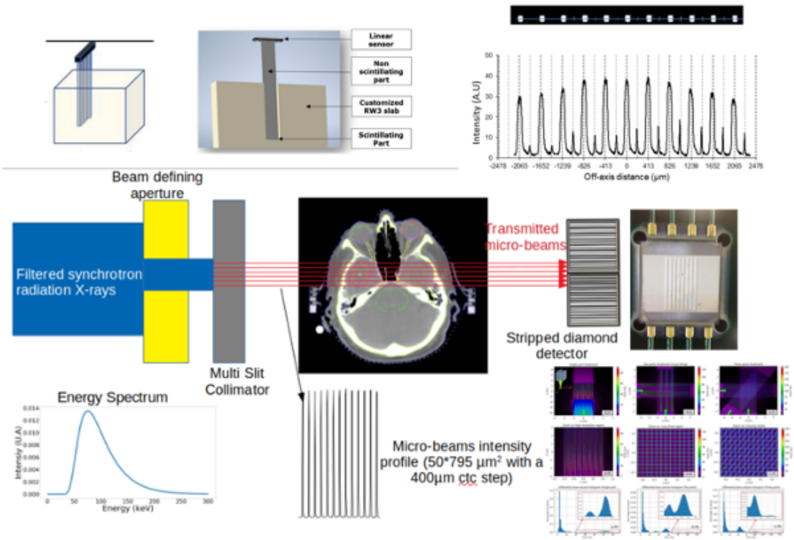

Figure 3.4: Medical Physics suite developed for Microbeam Radiation Therapy (MRT). Top: Patient specific quality assurance based on micro-metric scintillating detectors. Middle : Transmitted beam monitoring using diamond detectors for transit dosimetry.Bottom: high resolution dose calculation Algorithm for treatment plans assessments accounting for the MRT dose distribution complexity.

The developments related to this medical physics suite is represented on Figure 3.4.

The Lyon Institute of Nanotechnology (INL) is currently working on new detectors and methods to address the challenges of patient-specific quality assurance in MRT. Planar scintillating waveguide technology coupled via clear waveguides to linear CMOS camera have been developed in the framework of Florian's Thevenet PhD's project. A new type of detection system using 105 scintillating plastic microstrips has been designed, fabricated and tested under MRT conditions. It exhibits a linear dose response without dose rate dependence. Its radiation hardness makes it suitable for routine use in MRT QA. These preliminary results are very encouraging. Further work is underway to reduce losses in optical guides and increase the signal-to-noise ratio. Alternatives to BC-408 are also being explored to address issues with narrower microstrips [114]. The INL is also working on detectors for orthovoltage small field dosiemtry. These detectors are made base on heterogeneous cavities made of a sparse high-Z scintillation layer (such as perovskites), embedded in a tissue equivalent epoxy resin. To meet the needs of modelling small-sized detectors of orthovoltage X-rays, for spatially fractionated radiotherapy,Thevenet *in vivo* proposed a model to determine the responses of these detectors. The detector model considers that X-ray photons mainly interact with medium surrounding the scintillation layer, and that the output of the detector mainly results from secondary electrons in this layer. This model was compared to measurements performed on the Small Animal Radiation Research Platform SARRP, installed on the IRMaGe platform in Grenoble. Simulations results compared with measurement data were encouraging with differences lower than 16% for beam energies in the 60 kVp to 220 kVp range. These differences could be reduced by refining the model such as with more accurate local secondary particles spectrum modelling [115].

Moreover, within the frame of a treatment, full coverage of the MRT field is required for beam monitoring control, and possibly transit dosimetry. Large area, single crystal diamond detectors developed at LPSC appear as good candidates for this challenge. Recently, during his PhD thesis, N. Rosuel showed the excellent linearity of a diamond detector with dose rate from 1 to 10000 Gy/s [45]. As a proof of concept, a prototype of striped diamond portal detector enabling online microbeam monitoring during synchrotron MRT treatments has been devlopped. The detector, a 550 mm bulk monocrystalline diamond, is an eight-strip device, of height 3 mm, width 178 mm and with 60 mm spaced strips, surrounded by a guard ring. An eight-channel ASIC circuit for charge integration and digitization has been designed and tested. Characterization tests, performed at the ID17 biomedical beamline of the ESRF, showed that the detector can measure direct and attenuated microbeams as well as interbeam fluxes with a precision level of 1%. Tests on phantoms were performed and were compared with Monte Carlo simulations. A 2% difference between experiments and simulations was found for solid water phantoms. In more complex geometries such as the anthropomorphic phantom, a preliminary study showed that the absolute differences between simulated and recorded transmitted beams were within 2%. These results showed the feasibility of performing MRT portal monitoring using a microstriped diamond detector [116]. Online dosimetric measurements have also been performed during preclinical and clinical veterinary trials at ESRF. Two multichannel micro stripped detectors are being developed for this project, including fully integrated electronic readouts. They will be positioned upstream and downstream the patient position and will cover the whole microbeam array extension. The first detector aims at monitoring the incoming flux when the second will measure the transmitted microbeams and be used for transit dosimetry.

Until recently, none of the developed dosimetry tools combined all the requirements for a clinical use in a MRT dedicated TPS: precision, time efficiency and spatial resolution. In her PhD funded by the LabEx PRIMES [113], Sarvenaz Keshmiri recently developed a full high-resolution MC calculation engine based on PENELOPE which is capable of taking into account the 3D conformal MRT fields, to be used as calculation core in a clinical MRT-TPS [117]. This calculation engine named penMRT aims at being reliable, fast enough to ensure dose calculation in a clinical context. It also allows the display of high resolution (5 μm) dose maps and high resolution.This precise micrometric dose calculation engine is a significant added value to understand the underlying radiobiological mechanisms of MRT, when being used as multi-directional treatments. High-resolution 3D dose maps for treatment planning and dose prescription in external beam radiotherapy with spatially fractionated microbeams enable accounting for the dose distribution heterogeneities at the micrometric scale, specific to this disruptive treatment modality. A recent work from Keshmiri *et al.* lead to new dose metrics, not available so far, and adapted to microbeam radiation therapy. These metrics can be used for developing prediction and/or biophysics models in microbeam radiation therapy. A retrospective study was performed on survival data from MRT treatment on rats bearing gliomas and we were able to establish a survival increase prediction model based on peak doses, which is to our knowledge the first correlation ever shown between dose metrics adapted to microbeam radiation therapy and the outcome of a dose escalation study [118].

As proof of principle and cornerstone for the safe clinical transfer of MRT, we conducted the first international therapeutic microbeam irradiation of a spontaneous malignant brain tumor in a veterinary patient [119]. This project was mainly funded by the French National Cancer Institute INCa, the French Healthcare ministry (DGOS) and the LabEx PRIMES. Under the conditions of a clinical trial, we have validated the safe delivery of 3- dimensional conformal MRT as exclusive radiosurgical treatment to a pet dog bearing a malignant brain tumor [120].

3.5 Perspectives

These preclinical and clinical trials are paving the way of the future MRT trials, using the unique capability of Synchrotron Radiation (SR) x-rays to be produced at ultra high dose rates. This achievement allows one to consider, from then on, that the MRT installation at ESRF combined with the CHUGA and LabEx PRIMES teams expertise should be upgraded to a MRT clinical research facility. However, the ESRF decided to disregard the continuation of the MRT program after July 2023. The closure of ID17 has definitely put an end to the feasibility of transferring MRT to clinics in a reasonable time. The only beamline in the world that is pursuing these unique radiotherapy studies on a synchrotron source is the Imaging and Medical Beamline (IMBL) at the Australian Synchrotron. Compact sources such as the line focus source developed in Munich might be an alternative to bring MRT to clinics, however in a mid/long term future [121].

Innovative radiotherapies : experimental radiobiology

4

Coordinator: Claire Rodriguez-Lafrasse

Contributors: Serge Candeias, Hélène Elleaume, Jean-Luc Ravanat, Raphaël Serduc, Patrick Vernet

4.1 Introduction - innovative radiotherapies

In 2012, when the LabEx-1 project began, the field of innovative radiotherapies was more limited compared to today. At that time, radiotherapies mainly relied on improving conventional photonic radiotherapy devices such as Intensity-Modulated Radiation Therapy (IMRT), Stereotactic Body Radiation Therapy (SBRT), Gamma Knife, and CyberKnife. The focus was on better targeting tumor volume. Additionally, there was a growing interest in proton therapy and carbon therapy treatment centres, although scientific validation of their effectiveness through clinical studies was still insufficient. In academic research, there was a focus on developing metal nanoparticles (Au, Pt, Gd, Fe...) used in combination with radiotherapy to increase the dose locally while sparing healthy tissues. There was also interest in using synchrotron light for Stereotaxic Synchrotron Radiation Therapy (clinical trial at ESRF) and Microbeam Radiation Therapy (MRT) studies with pre-clinical models. The five constituent teams of WP3 (Experimental Radiobiology) with complementary skills in radiobiology and chemistry deployed a project around three main areas:

1. Synchrotron irradiation (photo-activation of Z elements and MRT). Two teams of GIN (Inserm U836 - Grenoble), led by Drs Hélène Elleaume and Raphaël Serduc, are leading teams for the development of innovative radiotherapy techniques using synchrotron radiation and CIBEST group from UMR5819 (CEA - Grenoble), led by Dr Jean-Luc Ravanat, is specialized in radiation-induced DNA damage.
2. Combination of metallic nanoparticles with conventional irradiation. The FENNEC team at ILM (CNRS UMR 5620 - Lyon), led by Dr Olivier Tillement, synthesized and developed the AguIX nanoparticles. The RCM team at IP2I (CNRS-IN2P3 UMR5822 - Lyon), led by Pr Claire Rodriguez-Lafrasse, participated in the *in vitro* and *in vivo* proof of concept of the nanoparticles' radiosensitizing effect.
3. Ion irradiation (mainly carbon ions). RCM team of IP2I, led by Pr Claire Rodriguez-Lafrasse, has recognized experience in the molecular mechanisms specifically involved in the response to carbon ion irradiation.

Their goal was to quantify and understand the biological effects induced by these three irradiation modalities, focusing on DNA damage, chromosomal aberrations, oxidative stress, signaling and cell death, and tumor escape, in different models (cellular, preclinical, and clinical). They also aimed to optimize irradiation parameters, evaluate treatment effectiveness, and assess the potential for clinical transfer. Today, the radiation therapy landscape has evolved with the introduction of innovations such as FLASH radiation therapy, which delivers ultra-high doses of radiation at ultra-high dose rates, minimizing damage to healthy tissue. The combination of radiotherapy with sensitizers such as metal nanoparticles and immunotherapy has shown promising results in improving patient survival. Additionally, boron neutron capture therapy (BNCT) and X-ray-induced photodynamic therapy have gained attention for their potential in precise cancer treatment. In response to these advances, the research program for the second phase of LabEx has evolved. The ILM-FENNEC team has transitioned out of the network as the AGuIX nanoparticles have entered an industrial transfer phase. They have been replaced by the Santé team of LPC (CNRS UMR6533 - Clermont-Ferrand), which is working on the development and evaluation of gold nanoparticles. Furthermore, the consortium has been strengthened by the addition of the ProMD team (UMR5249 CEA-CNRS-UGA, CEA - Grenoble), led by Dr. Serge Candéias, focusing on the response of healthy tissues to different types of radiotherapy.

4.2 Photo-activation of high-Z elements (potentially included in nanoparticles) acting as radiation dose-enhancers

Combining radiotherapy with chemotherapeutic agents that sensitize tumors to ionizing radiation has long been considered a promising strategy (*i.e.* radiosensitization). However, when combined, these drugs can increase normal tissue damage and radiation-related side effects due to their inherent cytotoxicity. Another method to improve the therapeutic efficacy of radiotherapy is to increase the dose delivered to tumor cells using high-Z elements that have large photon interaction cross sections, producing a wide variety of secondary emissions such as secondary electrons, Auger electrons, and Compton electrons, leading to reactive oxygen species generation (indirect damages) as well as direct damages. This concept was first introduced in the early '80s by Norman's lab using an iodinated contrast agent as a radiation dose-enhancer [122]. Hainfeld in 2004 [123] proposed the use of nanoparticles containing high Z elements to act as dose enhancers and showed a remarkable survival rate of mice carrying subcutaneous mammary carcinomas, treated with gold nanoparticles. In this domain, various high-Z radiation dose enhancers have been evaluated such as Au, Hf, Gd, Pt, and Fe. Different types of radiosensitizing or radiation dose-enhancer nanoparticles were developed and/or evaluated during the LabEx period.

4.2.1 Contrast-enhanced Synchrotron Stereotactic Radiotherapy (CE-SSRT)

The advent of synchrotron radiation (SR) has added a new dimension to the use of X-rays in imaging and therapy. In addition to conventional X-ray sources, synchrotron radiation has also demonstrated significant

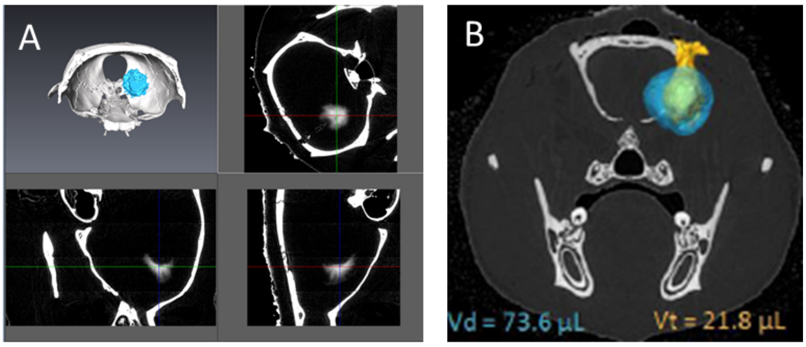

Figure 4.1: Synchrotron-based activation of high-Z elements: A) 3D rendering of the gold distribution using high resolution synchrotron CT imaging (spatial resolution 45 microns, X-ray energy 35 keV). Gold was infused intracerebrally by convection-enhanced delivery (CED) (5 μL at 25 mg/mL Aurovist 15 nm), 10 min before imaging. The blue volume represents the gold surface that encloses more than 1.25 mg/mL of gold (5% of the injected solution concentration). B) Overlap of the distribution of the high Z elements after intra cerebral (blue) injections and the tumor volume (yellow), obtained with K-edge Synchrotron CT.

advantages in external radiotherapy, in particular, the potential of combined therapies using medium-energy synchrotron X-rays to induce photoelectric effect on high-atomic number elements.

The numerous preclinical studies that we have conducted clearly demonstrated the therapeutic efficacy of this modality for various radiation dose-enhancers: iodinated contrast agents [70]; gold, gadolinium, or iron nanoparticles [124–127]. An increased differential effect was obtained when irradiating tumors previously loaded with elements of high atomic number. If a sufficiently high concentration of radiation dose-enhancer is achieved without toxicity, a local increase in energy deposition occurs due to the increased cross-sectional area of the photoelectric effect on heavy atoms irradiated with low- to medium-energy X-rays and associated secondary particles (photoelectrons, Auger electrons, and fluorescence X-rays). These combined treatment modalities benefit from a local dose increase only when using medium-energy synchrotron beams, but not with high-energy photons from a LINAC [124–128]. The absence of local dose enhancement for high-energy photons and gold nanoparticles has been confirmed theoretically (see next chapter).

The biodistribution of the heavy elements (contrast agents or nanoparticles), after intravenous or intra cerebral injections, was studied in a preclinical model of glioblastoma (F98 model) using synchrotron spectral computed tomography (CT). We demonstrated the prime importance of the distribution of the nanoparticles relative to the tumor volume (Figure 4.1).

Iron-based nanoparticles also show great potential despite their much lower atomic number and, consequently, photoelectric cross-section. Indeed, Fe nanoparticles have low toxicity and the ability to accumulate in tumor cells in large quantities and concentrate directly in the target volume [128]. However, these nanoparticles are not as advanced toward clinical trials as Gd nanoparticles and would require a substantial amount of additional preclinical work to reach the clinic, including quantitative biodistribution studies as a function of time and injection modality, precise microdosimetry studies and optimization of preclinical treatment planning.

Close collaborations between the Grenoble-Alpes University Hospital oncologists and European Synchrotron Radiation Facility (ESRF) scientists and engineers have resulted in the first worldwide clinical radiotherapy trial using synchrotron X-rays. This was a dose escalation protocol designed to demonstrate the feasibility and safety of the technique. Fifteen patients were successfully treated, with an increasing proportion of their hypofractionated stereotactic radiotherapy treatment performed using contrast-enhanced synchrotron stereotactic radiotherapy. The patients were treated at the medical beamline of the European Synchrotron Radiation Facility (ESRF-ID17), using 80 keV high-flux quasi-parallel monochromatic X-ray beams, in the presence of an iodinated contrast agent injected immediately before irradiation [129]. The first part of the treatment was delivered at the ESRF (one or two fractions), the other fractions were delivered at the Grenoble-Alpes University Hospital. In this study, we demonstrated the feasibility of this new modality and paved the way for the evaluation of other agents such as nanoparticles to improve the efficacy of radiotherapy.

4.2.2 Gadolinium-based nanoparticles (AGuIX, CuPRiX)

The chemists of one of the LabEx teams have developed an ultrasmall (<5 nm) gadolinium-based nanoparticle (GBN) which presents ideal biodistribution (no uptake of the reticuloendothelial system and a blood half-life of 42 ± 3 min), accumulation in the tumor thanks to increased permeability and retention effect (EPR), and rapid and high renal excretion (96% of GBN eliminated 18 days after intravenous injection) [130]. Thanks to the work of the LabEx teams summarized below and national/international collaborations, AGuIX® (Activation and Guidance of Irradiation by X-Ray) nanoparticles could be produced industrially by the company NHTherAGuIX, under GMP conditions and brought to the clinics in a phase I clinical study by a radiotherapist of the LabEx [131]. Currently, only two nanoparticles are clinically used in the world, in combination with radiotherapy, the AGuIX® and the NBTXR3® hafnium nanoparticles developed by the Nanobiotix company.

In the framework of LabEx, the sensitizing effect of GBNs, associated with photon irradiation at energies between 220 keV and 6 MeV or with carbon ions, was first evaluated in cellular models of tumors known for their low survival rate: squamous cell carcinoma of the head and neck (HNSCC) [132], metastatic melanoma [133] and more recently chondrosarcoma [134]. A radiosensitization factor between 1.2 and 2.1 was obtained, demonstrating the radiosensitizing effectiveness of these GBNs in 2D and 3D cell cultures, even in combination with carbon ions [134, 135]. From a mechanistic point of view, we have shown that GBNs enter cancer cells by passive diffusion and macropinocytosis [136], localize in the cytoplasm, as free particles or trapped in lysosomes, at the immediate proximity of mitochondria [137]. Gadolinium combined with irradiation can produce a wide variety of secondary emissions, such as photo-electrons, Auger and Compton electrons, fluorescence-rays, leading to the production of reactive oxygen species (ROS) that trigger intramitochondrial stress (production of ROS, decrease in transmembrane potential, deletion of mitochondrial DNA (mtDNA) and nuclear DNA damage). Finally, a process of mitotic catastrophe precedes death by late apoptosis [132, 137]. The X-ray interaction probability with the Gd nanoparticles is strongly dependent on the X-ray energy. Using monochromatic X-rays from the synchrotron, we were also able to demonstrate, through experimental clonogenic studies and Monte Carlo simulations, that the AguIX® can act as radiation dose-enhancers when present at 2 mg/mL in the culture medium and irradiated with low energy synchrotron X-rays. As predicted by Monte Carlo simulations, this effect is negligible when using LINAC high-energy irradiation [126]. However, the AGuIX® also have a biological action that is independent of the X-ray energy [125].

The efficacy of AGuIX® has also been demonstrated in xenograft tumor models of HNSCC, metastatic melanoma, and chondrosarcoma as a proof of concept for future clinical transfer [132–134]. Regulatory toxicity studies were carried out in parallel in rats and monkeys. Building on all these results, the first human clinical study was launched by a clinical partner of the LabEx affiliated with the Grenoble-Alpes University Hospital, in patients with multiple brain metastases. The phase 1 dose-escalation study showed that the AGuIX® combination with pan-encephalic radiotherapy specifically targets brain metastases and is retained in tumors for up to 1 week under feasible and safe conditions [131]. A phase II study (NANO-RAD2) is currently underway in Grenoble Hospital (NCT03818386), as well as four other clinical trials around the world in cervical, pancreatic, and lung cancers.

As copper levels in serum and tumor tissues have been directly linked to cancer progression and metastasis formation, a new generation of AGuIX®, called CuPRiX, containing gadolinium atoms and free chelates, has been recently developed to allow: (i) localized copper depletion in tumors to prevent cell dissemination and metastasis, and (ii) increased tumor sensitivity to RT due to the presence of Gd atoms. In cells from three cancer models (lung, breast, head and neck), CuPRiX NPs were able to slow cell migration and invasion, inhibit the activity of the copper-dependent lysyl-oxidase (LOX) enzyme involved in these processes and radiosensitize tumor cells [138]. In a syngeneic mouse model of metastatic breast cancer, combining CuPRiX treatment with fractionated radiotherapy led to a differential gene expression profile (Nanostring® technology), a significant reduction in the tumor growth and number of metastases, as well as an increase in mouse survival (figure 4.2) (Vernos *et al.*, in preparation). This new generation of AGuIX®, CuPRiX, combining radiosensitization and copper chelation, thus appears to be a promising strategy for the treatment of radioresistant and potentially metastatic cancers.

4.2.3 Functionalized gold nanoparticles

Mitochondria, with their own genome, could constitute an alternative target to the nucleus to kill tumor cells. MtDNA alterations can lead to mitochondrial dysfunction but have also been correlated with an increase in the invasive capacity of certain tumor types, such as prostate cancer. Interestingly, irradiation of human cells induces nuclear damage but does not alter the readdressing of repair molecules to the mitochondria, as described with EXD2 [139]. Moreover, mtDNA double-strand breaks led to selective mtDNA degradation in human cell lines (HEK293) [140].

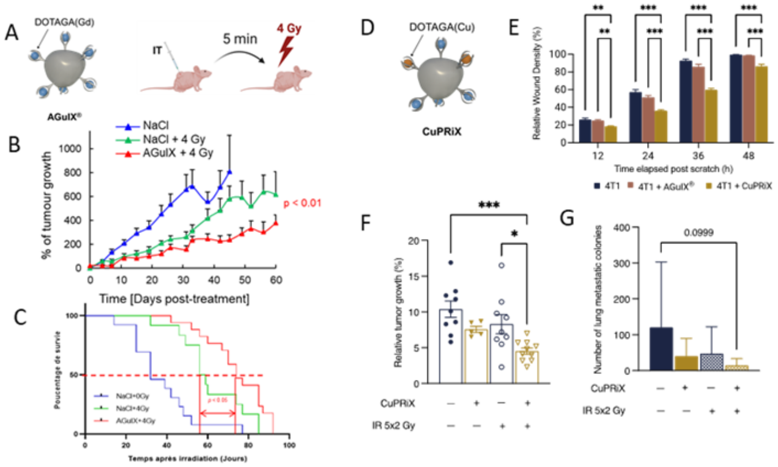

Figure 4.2: Gadolinium-based nanoparticles: A) Schematic representation of AGuIX (adapted from [138]. B,C) *In vivo* evaluation of the efficacy of combined AGuIX (intratumoral injection) and radiotherapy (4 Gy) treatment in HEMC-SS bearing mice (chondrosaroma model) (adapted from [134]. B) Evolution of tumor growth following treatment expressed as mean % of tumor growth ±SEM C) Survival curves (Kaplan-Meier) obtained in response to the different treatments. D) Schematic representation of CuPRiX, a gadolinium- (blue dots) based nanoparticle able to chelate copper (orange dots) (adapted from [138]). E) Effect of CuPRiX and AGuIX on the motility of a breast cancer cell line, 4T1, assessed with the scratch-wound assay. Data are expressed as a percentage of wound confluence (relative density). F,G) *In vivo* evaluation of the efficacy of combined CuPRiX and radiotherapy treatment in an orthotopic syngeneic mouse model of breast cancer. F) Evaluation of the tumor growth following treatment, data are presented as a percentage of tumour growth on day 23 compared with the first day of treatment. G) Number of lung metastatic colonies at the end of the therapeutic sequence.

Targeting mitochondria with metals such as gold in combination with X-irradiation could thus radiosensitive tumor cells, through an increased local dose deposit in relation to the amount of metal and the induction of mitochondrial damage.

In collaboration with the Clermont-Ferrand Chemistry Institute (ICCF), one LabEx team has developed organometallic compounds (N-heterocyclic gold carbenes: gold-NHC complexes) which, thanks to their lipophilic and cationic structure, accumulate in mitochondria. These compounds cause radiosensitization of human prostate tumor cells (PC3) submitted to X-irradiation. Mechanistic studies of the involved processes show (1) mitochondrial depolarization in the presence of these compounds, and (2) modification of mitochondrial respiratory chain proteins, with the loss of some complex III sub-units. These modifications, prior to irradiation, are responsible for the toxic effects of gold-NHC complexes independently of the physical processes of dose enhancement [141]. This first proof of concept to target mitochondria for radiosensitization shows the interest in increasing local gold concentration to induce energy dose deposit enhancement in the vicinity of the mitochondrial network. This first set of experiments led us to develop gold nanoparticles (to increase local gold concentration) functionalized with specific labelling to achieve mitochondrial targeting in prostate tumor cell lines. This was carried out using specific triphenylphosphonium (TPP) moiety combined with gold nanoparticles during synthesis. These TPP@Au NP were internalized in prostate tumor cells and localized in autophagosomes-like structures and mitochondria, even if a low density of internal NP was observed (figure 4.3) [142].

At the same time, rebuilding the mitochondrial network based on deconvolved widefield microscopic images from fibroblast cells was achieved

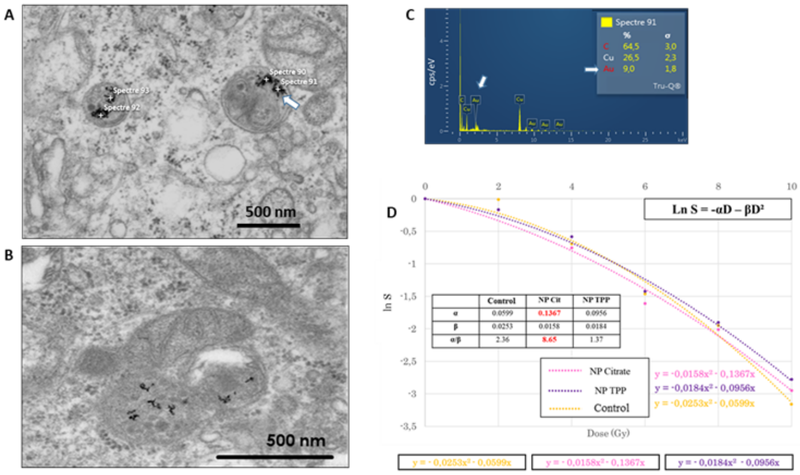

Figure 4.3: Functionalized gold nanoparticles: Electron microscopy (TEM) of A) PC3 cells incubated with AuNP-TPP or B) AuNP citrate showing nanoparticles accumulation in autophagosome-like structures. C) Energy dispersive spectroscopy (EDS) of the AuNP-TPP treated cells showing signals from carbon (C), Copper (Cu) and gold (Au). D) Clonogenicity curves from PC3 cells treated without NP (yellow), with AuNP-citrate (pink) or with AuNP-TPP (purple).

and microdosimetry was performed using irradiation with 250 keV photons [143]. Energy deposition was also evaluated through simulation study of gold nanoparticles (30 nm) nearby mitochondrial network during 120 keV photons irradiation [144].

4.2.4 Nanoscintillators to improve radiotherapy (PDT-X)

Whereas scintillators were originally developed to detect ionizing radiation, the physical characteristics of nanoscintillators give them promising biomedical properties. Nanoscintillators down-convert ionizing radiation into photons with energies ranging from ultraviolet (UV) to near-infrared. It was recently proposed to use nanoscintillators to induce PDT using ionizing radiation. The cytotoxic effects induced by PDT originate mainly from ROS that are specifically generated when tumor-localized photosensitizers are excited by visible light. The optical penetration depth of such photons is only a few mm through the tissues. Therefore, PDT can only be used for superficial and/or fiber-optic accessible tumors. The limited penetration of light in tissues remains the main Achilles' heel of PDT. To overcome this limitation, nanoscintillators (NS) were proposed as intra-tumor light sources that can be activated by X-rays to excite nearby photosensitizers. Because nanoscintillators can be made of high Z elements, they are another promising type of nanoparticles to induce radiation dose-enhancement as previously described. We recently published the first proof that NS induce radiation dose-enhancement in an aggressive preclinical model of glioblastoma (figure 4.4) [145]. Nanoscintillators that emit UV photons, and more specifically UV-C photons that DNA efficiently absorbs, can help control tumor progression by causing specific DNA damage. While X-rays create double-strand breaks, UV-C photons generate pyrimidine dimers and oxidized guanine, both of which can lead to cell death. The use of nanoscintillators to generate UV-C-induced DNA damage instead of X-rays is particularly interesting because it is independent of tumor oxygenation. As hypoxia is a cancer characteristic

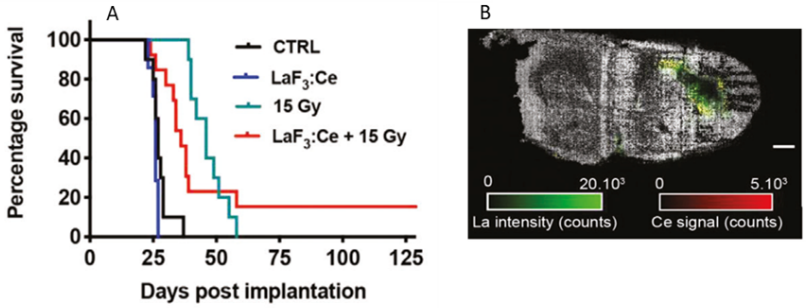

Figure 4.4: Nanoparticles dose-enhancement & X-ray induced photo-dynamic therapy (PDT-X): LaF3:Ce: A) Radiation dose-enhancement by LaF3:Ce leads to a full recovery of 15 % of the animals bearing a F98-brain tumor. Survival curve obtained after treatment when LaF3:Ce nanoparticles are delivered by convection-enhanced delivery (CED) (20 μL of 50 mg mL^{-1}). B) Nanoparticles distribution in the brain by Laser Induced Breakdown Spectroscopy (LIBS). Image of a of a long-term survivor's slice of the brain. LaF3:Ce nanoparticles are still visible in the brain 129 days post tumor implantation. Scale bar = 1 mm. Source: Bulin *et al.* 2020 [145]

often associated with resistance to RT, UV-radioluminescence could be a powerful tool for overcoming hypoxia-related radioresistance. [146].

4.3 Microbeam Radiation Therapy (MRT)

The treatment of aggressive brain tumors remains a therapeutic impasse. A major obstacle is the radiosensitivity of normal brain tissue which limits the dose of radiation. Previous studies highlighted the exceptional tolerance of normal tissues to MRT. The latter is a radically new approach of radiosurgery where X-rays from a synchrotron light source are collimated in a set of parallel planar microbeams, a few tens of microns thick, separated by a few hundred microns. This discontinuous irradiation geometry preserves the normal tissue while delivering considerable doses to the targeted lesion. During the last ten years, MRT research was focused on the clinical transfer of this promising technology by optimizing irradiation efficiency on rodents, by technically moving to large animal exposures, and by treating spontaneous gliomas in dog patients.

Delivery of high-radiation doses to brain tumors via multiple arrays of synchrotron X-ray microbeams permits huge therapeutic advantages. Brain tumor (9LGS)-bearing and normal rats were irradiated using a conventional, homogeneous Broad Beam (BB), or MRT. MRT with a valley dose of 10 Gy deposited between microbeams, delivered by a single port, improved tumor control and median survival time of tumor-bearing rats better than a BB isodose. An increased number of ports and an accumulated valley dose maintained at 10 Gy delayed tumor growth and improved survival. At identical valley isodose, each additional MRT port extended survival, resulting in an exponential correlation between port numbers and animal lifespan. A 10 Gy valley dose, in MRT mode, delivered through 5 ports, achieved the same survival rate as a 25 Gy BB irradiation because of tumor dose hot spots created by intersecting microbeams. Multiport MRT reached exceptional 2.5-fold biological equivalent tumor doses [86]. The unique normal tissue sparing and therapeutic index were eminent prerequisites for clinical translation.

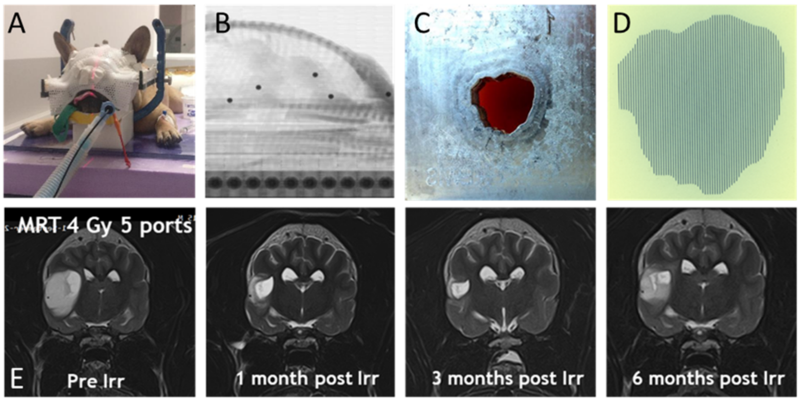

Figure 4.5: Microbeam Radiation Therapy (MRT): A) The dog's head is maintained in a non-invasive stereotactic radiotherapy frame. Metallic beads are positioned on the mask for the MRT treatment positioning. B) One of the two synchrotron beam radiographs, acquired for isocenter positioning using the metallic markers that can be seen on the image. C) Lipowitz alloy mask for conforming the microbeam array to the PTV. D) Gafchromic film showing the conformal microbeam array treatment beam. E) MRI follow-up of the first MRT patient. Axial T2W images acquired before, one, three, and six months after MRT treatment with 4 Gy cumulated valley dose.

The veterinarian trials foreseen by our teams required technological improvements and the transfer of MRT technology to larger animals. We developed a clinical suite in order to perform safe, image guided and TPS-based microbeam irradiations. We applied such methodology to caudate nucleus exposures in pig brains [60]. We were able to study long-term effects of multiport MRT on normal brain tissue at doses up to those that will be delivered in the future vet trial.

As proof of principle and cornerstone for the safe clinical transfer of MRT, a "first in dog" trial was conducted under clinical conditions to evaluate whether 3D conformal MRT can be safely delivered as exclusive radiosurgical treatment in animal patients (figure 4.5). A 17.5 kg French Bulldog received microbeam radiation therapy for his suspected glioma with conformal microbeam arrays of synchrotron-generated X-rays. The dose prescription was adjusted to deliver 2.8 Gy to the PTV. With these parameters, each beam delivered 20-25 Gy to the target as peak doses. Clinical follow-up over 3 months did not indicate radiotoxicity; a significant improvement in the dog's quality of life with the disappearance of tumor-induced seizures. MRI performed 3 months post-irradiation revealed that the mass effect was minimized with normalization of the left lateral ventricle and a tumor volume reduction of 87.4 %. To our knowledge, this neuro-oncologic veterinary trial is the first 3D conformal synchrotron X-ray MRT treatment of spontaneous intracranial tumor in a large animal ever performed. This vet trial is the essential last step before the clinical transfer of MRT in a synchrotron facility in the near future as it will demonstrate the feasibility and safety of treating deep-seated tumors using synchrotron-generated microbeams.

4.4 Hadrontherapy

High-energy ions have the particularity to deposit a maximum of energy at the end of their course. The Bragg peak, characteristic of proton [1H] and carbon ion [^{12}C] beams, clearly enables a dose distribution in patients superior to the most advanced photon radiotherapy modality, such as IMRT (intensity modulated radiotherapy). In addition, the linear energy transfer (linear energy transfer (LET)) of carbon ions, greater than that of protons, gives them a relative biological efficiency (RBE), evaluated between 2 and 3 compared with photons and only 1.1 for protons. The properties of ions permit hypofractionated treatments and lead to better tumor control, increased survival, and better quality of life for patients. Proton therapy is reserved for the treatment of tumors close to organs at risk (ocular tumors, chordomas, and chondrosarcomas of the cranial base. . .) and is particularly attractive for the treatment of paediatric tumors (3 centers in France (Paris, Nice, Caen)). Carbon therapy, more expensive and unavailable in France until 2028, is reserved for radioresistant tumors (soft tissue sarcomas, adenoid cystic carcinomas, mucosal melanomas...) close to organs at risk. Restraint regarding the deployment of carbon ions in the clinic mainly concerns the risk of long-term toxicity and of secondary cancers possibly affording from their higher RBE and fragmentation tail, which have not been clearly proved by randomized studies. In this context and while awaiting the results of such clinical studies, the molecular specificities of the tumor response to carbon ions have been extensively studied in cellular models within the LabEx. Proton irradiation was performed at the Centre Antoine Lacassagne (CAL) in Nice and carbon ion irradiation at the Grand Accélérateur National d'Ions Lourds (GANIL) in Caen, National Institute of Radiological Sciences (NIRS) in Chiba (Japan) and very recently a collaborative contract was signed with the Centro Nazionale di Adroterapia Oncologica (CNAO) at Pavia in Italy.

Monte-Carlo simulations performed within WP3 of the OH° production at 10-12 seconds, in the nuclear volume, after a 2 Gy photon or a 1 Gy carbon ion irradiation revealed two different profiles of distribution. Photon irradiation induces a dense and homogeneous ROS distribution, whereas ROS remain condensed in clusters along the carbon ions tracks. Based on this differential ROS distribution at the nanometric scale and all the biological experimental results, we recently proposed that the higher biological efficacy and specificities of the molecular response to carbon ions rely on a 'stealth-bomber' effect [147].

The "bomber" effect represents most of the deleterious properties of carbon ions on cancer cells at the molecular and cellular levels. It is triggered when the biological targets, such as DNA or organelles, are on the trajectories of carbon ions. In this case, the ROS clustered in the tracks are responsible for: the complex and irreparable DNA damage [148, 149]; the increased level of oxidized proteins (in preparation); the absence of dependency on telomere length [150] and on the intracellular oxygen concentration [135]. The consequence, at an equivalent physical dose of photons, is a higher cell killing effect of carbon ion irradiation [151], specifically on cancer stem cells [152], by a p53-independent and ceramide-dependent mechanism [153].

The "stealth" effect symbolizes the property of carbon ions to deceive the cellular defenses. Thus, the absence of significant ROS production outside the carbon ion tracks does not allow the achievement of a decisive ROS threshold necessary to activate survival pathways and defense mechanisms. This is objectified by: the decrease in the detection of DNA lesions and the activation of their repair [148, 149]; the non-activation of proliferative and invasive pathways [154]; the absence of stabilization of the HIF-1α (hypoxic inhibitory factor) transcription factor [135] and the non-activation of its numerous targets; the specific regulation of key

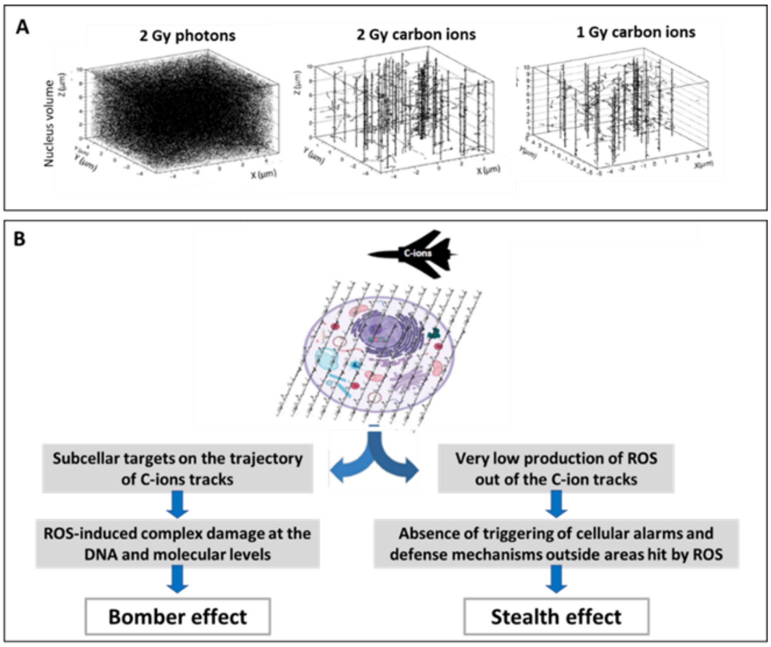

Figure 4.6: The stealth-bomber paradigm: A) Monte Carlo simulations of the OH• radical distribution in water in response to photons and to a mixed radiation field of C-ions (dose-averaged linear energy transfer (LET) 50 keV/μm) at physical and biological equivalent doses of 2 Gy photons and in a volume corresponding to that of a cell nucleus. B) Diagram illustrating the 'stealth-bomber' paradigm. Adapted from [147].

effectors of the proteostasis (Wozny et al in preparation); and the absence of stress granule formation [155].

Altogether, these results led us to propose a new paradigm, setting ROS spatial distribution at the nanometric scale as a highly relevant point, to explain the differential cellular responses to C-ion and X-ray irradiation. It also strongly suggests that hadrontherapy with C-ions will always display a much better efficacy than the most advanced conventional radiotherapy technology.

4.5 Radiobiology of healthy tissues

In addition to radiation-induced tumor cell death, a lot of work has been devoted in recent years to the characterization of the effects of radiation on healthy cells and tissues that are inevitably exposed during radiotherapy. We were more specifically interested in inter-cellular signaling events that may activate - or interfere with - immune responses. Irradiated cells can indeed secrete inflammatory mediators and/or release intracellular molecules that can bind to receptors on surrounding immune cells present in every tissue, or recruited by radiation-induced tissue damage [156, 157]. This form of radiation-induced bystander signals can modify the tissue radiation response and eventually contribute to radiation-induced detrimental effects. These effects are usually thought to be more prominent after low-dose exposure.

We addressed this question *in vitro*, in supernatant transfer experiments. Primary human fibroblasts and keratinocytes obtained from the same donors were exposed to low and high X-ray doses. Their conditioned culture media, harvested one- and two-days post-exposure, were found to reduce the transcription of genes coding for inflammatory cytokines and the inflammatory activation of freshly purified peripheral blood mononuclear cells (PBMCs). These effects were different for fibroblasts and keratinocytes on the one hand, and after low and high dose radiation on the other hand [158]. Additional studies in a tumor model (SW1353 chondrosarcoma) showed that bystander signals elicited after exposure to the same doses of X-rays or carbon ions induce different inflammatory responses in primary endothelial cells [159]. We concluded that soluble signals elicited from irradiated primary and transformed human cells modulate the inflammatory status and response in bystander cells, in relation to the cell type and the radiation type and dose.

In a different approach, the direct effects of radiation exposure on circulating leukocytes were analysed in tumor-free mice after hemi- or whole-brain exposure with X-rays or protons at two different dose rates. Irradiation with protons was found to be more conservative. Exposure of lymph nodes, which are spared during proton exposure, was found to be an important determinant of lymphopenia. Thus, radiation type and parameters have a profound influence on immune cells [160].

4.6 Prediction of the tumor response to radiotherapies

The use of innovative radiotherapies requires understanding tumor response mechanisms at the cellular and molecular levels but also predicting which patient groups are the best responders to each of them. This is essential for an optimized and secure therapeutic management of patients. In order to initiate work addressing this question, predictive biological markers for the response to photon radiotherapy have been studied in the context of three clinical trials. To initiate works addressing this question, predictive biological markers for the response to photon radiotherapy have been studied in the context of two clinical trials focused on oropharyngeal cancers. These are cancers with a poor prognosis, most often diagnosed at an advanced stage, often presenting locoregional recurrences and metastatic extension, and a 5-year survival rate of patients which does not exceed 40 %. Apart from HPV status, there are no biomarkers for early diagnosis, prognosis, and therapeutic choice/monitoring, adapted to the characteristics of the tumor.

As part of the ChemRad clinical study (NCT02714920), we focused on the detection and repair of double-strand breaks via the study of γH2AX foci, the phosphorylation of ATM, and the expression of the stem cell marker CD44 on tumor biopsies slices cultured and irradiated ex vivo. Overexpression of γH2AX, pATM and CD44 in patients who did not respond to treatment was associated with a poor prognosis at baseline. In addition, the ratio of the expression of these three markers at 24 hours after irradiation at 4 Gy versus 0 Gy was also predictive of a poor response to treatment. Finally, the combination of these three markers increased the predictive potential of response to treatment [161]. Furthermore, the morphological and phenotypic analysis of circulating tumor cells (CTCs) on liquid biopsy revealed a correlation between the increase in the number of CTCs between two courses of chemotherapy and a decrease in overall survival [162]. In a second cohort of patients, the expression of NRF2, a transcription factor involved in the response to oxidative stress, was analysed as well as that of peroxiredoxin 6, a protein regulated by NRF2.

Immunohistochemical analysis on tissue microarray (TMA) showed that high expression of NRF2 and peroxiredoxin 6 was a poor prognostic factor for overall and progression-free survival. The association of these two biomarkers reinforced the significance of the results (Philouze *et al.*, submitted). We thus proposed a combination of biomarkers predictive of the response to radio(chemo)therapy in oropharynx cancers. These biomarkers will now be validated in larger cohorts of patients to offer personalized treatments, based on their analysis in initial tumor biopsies before any treatment, and on subsequent liquid biopsies to improve monitoring by identifying resistance to treatment and early recurrences.

4.7 Conclusions and perspectives

The work conducted within the LabEx framework has led to significant advancements in knowledge regarding innovative radiotherapies, ie photo-activation of high-Z elements including nanoparticles, microbeam radiation therapy and hadrontherapy. These cover various fields, ranging from molecular mechanisms at the cellular level to pre-clinical investigations and their translation into clinical practice. The work carried out within the LabEx framework in Experimental and Clinical Radiobiology for Innovative Radiotherapies has led to significant progress in understanding the photo-activation of high-Z elements, including nanoparticles, microbeam radiation therapy, and hadrontherapy. These cover various fields, ranging from molecular mechanisms at the cellular level to pre-clinical investigations and their translation into clinical practice. Without being exhaustive, they have led to several world firsts: - a clinical trial using synchrotron radiation in radiotherapy associated with iodinated contrast agents as dose-enhancers ; - a clinical trial using nanodrug intravenously injected in man for tumor radiosensitization ; - a TPS-based, image-guided, conformal MRT in pigs and pet patients ; - a demonstration of the stealth-bomber paradigm to explain the high RBE of carbon ions. More recently, research has expanded to the effects of radiotherapies on healthy tissues and the prediction of tumor response to radiotherapy, further enhancing the scope of investigation.

The future of innovative radiotherapies is set for significant advancements, focusing on precision improvement, side effect minimization, and combining them with radiosensitizing treatments. Envisaged progress includes personalized therapies tailored to individual patient characteristics (tumor and healthy tissues radiosensitivities), the integration of artificial intelligence for enhanced treatment planning and adaptive radiation delivery, and the synergy between radiotherapy and immunotherapy to enhance the immune response against cancer. The democratization of radiotherapy devices combining imaging tools, such as MRI-LINAC, will allow daily and personalized adjustment of the doses delivered to the tumor, guaranteeing optimal radiation delivery to radioresistant tumor areas with minimal impact on the healthy tissues. Ongoing enhancements in imaging techniques, particularly functional and molecular imaging (radiomic), hold the promise of improved tumor visualization for more precise treatment targeting.

Particle therapies, such as proton- and carbon-therapies, are undergoing refinements to enhance accessibility and efficacy across diverse cancer types. Emerging methods like Boron Neutron Capture Therapy (ILM) and Flash Radiotherapy are gaining recognition for their potential to deliver highly targeted doses with reduced damage to surrounding tissues. The use of nanovectors and nanodrugs, as well as vector-based internal radiotherapy, show potential for targeted drug delivery, improving the therapeutic effect on cancer cells while preserving normal tissues.

In conclusion, the future of innovative radiotherapies holds promising advancements, focusing on further improving the precision of treatment delivery and, consequently, efficacy. This includes decreasing the duration of treatment, reducing side effects, and enhancing the overall quality of life for patients.

Multiscale modeling of physical, chemical, biological and clinical effects of innovative radiotherapies

5

Coordinator: Michaël Beuve

Contributors: Rachel Delorme, Elise Dumont, Jean Michel Létang, David Loffreda, Étienne Testa

5.1 Introduction

Modeling of biological effects of radiotherapy is a huge challenge, considering the complexity and variety of biological systems. The latter may consist of molecules, subcellular entities, cells, assemblies of cells, animals or patients. Moreover, considering the context of innovative radiotherapy, the level of description, at least for the initial mechanisms of radiation interactions, needs to reach the nanoscopic scale. This domain is highly multidisciplinary and requires strong interaction with experimental activity, either to obtain experimental data, or to better understand the mechanisms to be modeled. Another critical constraint to consider is the limit of computer resources. Presently, the only feasible approach is multiscale and multidisciplinary.

This chapter, is organized according to this strategy of modeling. Within the LabEx PRIMES, we chose to combine various modeling at various scales, starting from basic processes and going up to models of tumor control. Moreover, we undertook studies for innovative radiotherapy based on both low and high LET radiation, in parallel to experimental studies undertaken within the LabEx. New collaborations have been successfully created for the real benefit of scientific progress and dynamics.

5.2 Low LET radiations

5.2.1 DNA damage

DFT simulation

The formation of oxidatively-induced DNA lesions is ubiquitous, yet the chemical reaction routes toward a given lesion are not always delineated, and we have sought to rely on density functional theory (DFT) to investigate the formation of several adducts. We have first relied on quantum chemistry, rooted in DFT for the isolated system guanine + 1O2, to delineate a mechanistic pathway that involves a high-lying endoperoxide intermediate. We then rely on DFT/MM-MD (Density Functional Theory/Molecular Mechanics-Molecular Dynamics) simulations combining a quantum chemistry level description to a molecular mechanics description to account for the role of the B-helix environment, which blocks the formation of the spiro derivative of the major product, coupled to a molecular mechanical description of the B-DNA helix. We have probed a marked environment effect as the B-helix tunes the singlet-oxygen addition leading to the formation of 8-oxoguanine in B-DNA, whereas a spiro derivative is obtained if the guanine is isolated [163]. The higher reactivity of guanine over adenine was also traced back to the intramolecular charge transfer between the partially negatively-charged O-O fragment and the guanine fragment, which is more prone to be partly positively-charged [164]. A review paper was also written during the LabEx initiative to sum up our findings concerning $^1O_2$ reactivity.

We also relied on molecular dynamics simulations to investigate the association of polyamine cations with B-DNA, in direct line with the experimental evidences obtained by Jean-Luc Ravanat [165]. Once the reaction is described with an accurate assessment of the free energy barriers into play, we rely on extensive classical molecular dynamics (MD) simulations to probe the structural and dynamic signature of DNA defects within oligonucleotides. We have also studied the formation of lysine-guanine adducts generated upon one-electron oxidation of short oligonucleotides [166].

These two proof-of-concept studies have given rise to a new research line where we situate the chemistry of *nucleosomal* DNA relying on all-atom, explicit-solvent molecular dynamics eventually coupled to tight-binding DFT, which allows to gain 2–3 orders of magnitude on the computational time and thus to explore DNA chemistry exhaustively in its native environment. Dr. Natacha Gillet, recruited at CNRS, will further consolidate this research line of a computational microscope for DNA lesions in Lyon/Grenoble.

Chromosomal aberrations

As part of a collaboration of the PhaBio group at IP2I with Dr. Komowa (Laboratory of Radiation Biology, Joint Institute for Nuclear Research, Russia), a study was undertaken to estimate if a low priming dose of radiation prior to a dose of one Gray could offer a radiation protection effect. Precisely, various values of priming dose in a range covering phenomena of hypersensitivity and enhanced radioresistance were tested. The biological endpoint was chromosomal aberrations, and cells were human blood cells obtained from three donors. The challenging dose was given 24 hours after the priming dose. While hypersensitivity and enhanced radio resistance were observed after the priming dose, no effect was observed after the challenged dose whatever the value of the priming dose [167].

As effects of fluctuations in the deposited dose at the scale of chromosome were suspected, an estimation of these fluctuations was undertaken within the experimental conditions using the Monte-Carlo simulation LPChem [168]. Fluctuations had indeed been observed, quantified and parameterized. However, the establishment of a link between them and the fluctuations in the observed chromosomal aberrations was not obvious. Conversely, the small number of donors (only three) may not be significant to derive a clear conclusion.

Besides, benefiting from the parametrization of energy-deposition fluctuations, a modeling of hyper sensibility and enhanced radiation effects was proposed [167]. The idea was to assume that radio resistance was triggered by the deposition of a sufficient quantity of energy into one or more targets. It has been concluded that a scenario based on the hitting of only one nanotarget gave a prediction of chromosomal aberrations far from the experimental data. Instead, the hitting of numerous nanotargets to trigger radioprotection led to a dose response curve in agreement with experimental data. Alternatively, if the target size was chosen of the order of magnitude of the cell size, the scenario based on one hit led also to a correct behavior.

5.2.2 Mini- and micro- beam radiotherapy

Calculation of RBE and DNA breaks for VHEE - interest in FLASH and MBRT

The LPSC worked in collaboration with the IJCLab, Institut Curie and IRSN, on the development of VHEE (~70-300 MeV) therapy. VHEE beams represent an interesting prospect in external radiotherapy because they have more advantageous dose profiles over photons for treating deep tumors, they can be focused magnetically and are less sensitive to tissue inhomogeneities than proton and photon beams, improving the robustness of treatment plans to uncertainties. In addition, their characteristics would allow combining them with Spatially Fractionated Radiation Therapy (SFRT), such as grid or minibeam (minibeam radiotherapy (MBRT)) therapy, or with FLASH therapy for the treatment of deep tumors, two promising approaches that lead to better tolerance of healthy tissues to irradiation. However, these beams are in technological development and there is currently no VHEE radiobiology platform allowing to study their biological effects, a necessary step before using them in treatment.

Our approach was to characterize theoretically the radiobiological properties of VHEE and optimize their dosimetry for VHEE SFRT approaches to prepare preclinical trials. This project led to 5 published articles, among which 2 studies dedicated to radiobiological modeling are described. A first one aimed at evaluating the direct simple (SSB) and complex DNA damage (SSBcplx or DSB) to compare 3 MBRT approaches with photons, protons and VHEE for the treatment of a human brain tumor. We used a multiscale Geant4 Monte-Carlo approach and the DBSCAN algorithm to determine the mixed field that neuronal cells would see at different depth along peak and valley regions and the number and complexity of DNA breaks that these fields undergone in a full-nucleus DNA geometrical model. We showed that proton MBRTs were the most favorable, allowing to minimize damage in the valleys and obtain the highest rate of complex breaks at the cerebral depth level, but VHEE MBRT would also be a good compromise because it allows to have homogeneous coverage of damage in the tumor, favoring good tumor control, and to maintain a marked spatial fractionation in upstream healthy tissues (indicator of better tissue protection), with machines potentially at a lower cost than protons [169].

A second study aimed to characterize the macro and microdosimetric behavior of the VHEE beams (without SFRT) as well as their relative biological effectiveness (RBE) and corresponding cell survival response, using the GATE code and the microdosimetric kinetic model (MKM) biophysical model. The objective was to compare relatively 100 and

300 MeV VHEE beams among others used in clinics, or of interest for innovative MBRT therapies, as of electron beams of clinical energy (5 and 20 MeV), photons (1.25 MeV, radiobiological reference for an RBE=1) and protons and light ions (^{12}C and ^{20}Ne). This study validated that the RBE of VHEEs should be equivalent to that of clinical electrons ($E \leq 20$ MeV), although presenting a higher LET (see Figure 5.1). No biological effects would have to be considered in treatment planning which gives confidence in the rapid implementation of these beams in clinics for radiotherapy [170]. *In vivo* experiments should be nevertheless undertaken to confirm this conclusion.

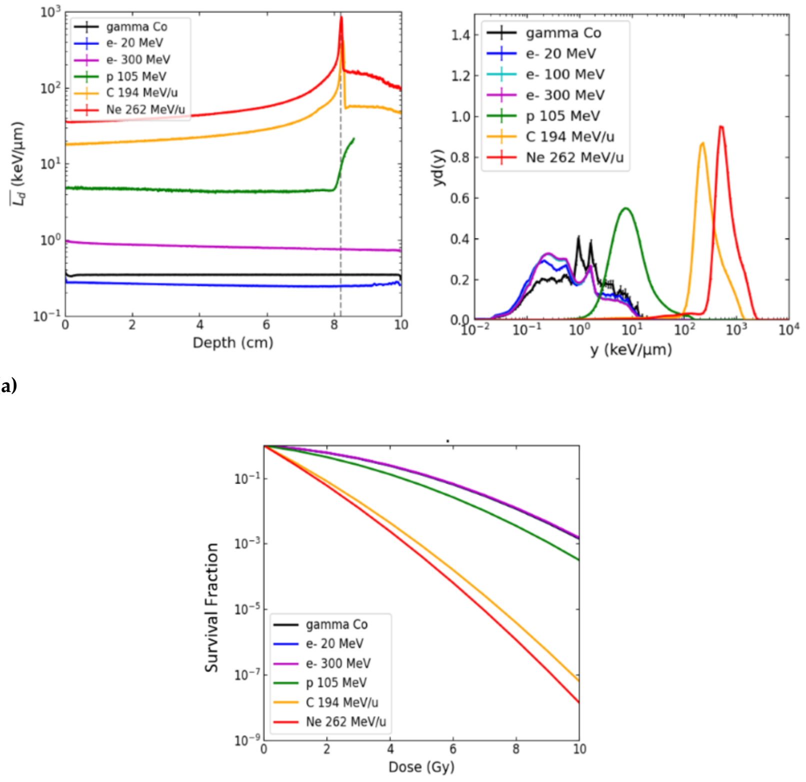

(a)

(b)

Figure 5.1: a) Dose-averaged LET (left), microdosimetric spectra (right) and b) theoretical cell survival curves obtained for VHEE beams compared to clinical electrons, photons and other ion beams of interest in radiotherapy [170].

5.3 Nanoparticles

As mentioned in Chapter 4, experimental data on nanoparticules (NP) were obtained with AGUIX NP, which consist of 10 gadolinium atoms around a silica core. It would have been natural to use these AGUIX NP to perform a theoretical study of the influence of nanoparticles on the physico-chemical processes induced by ionizing radiations. However, gold nanoparticle (GNP)s were chosen as model because:

- they contain a very high concentration of high-Z atoms, while AGUIX NP contain only 10 gadolinium atoms,
- the geometry of GNP is simpler,
- enhancement of biological response had already been observed with GNP in *in vitro* cells.

Simulation work had been started in the context of BIOHYDRA physique Cancer project on gold material and allowed more efficient studies within the LabEx duration. For the development of this strategy, the LabEx has funded 2 PhD students (Floriane Poignant, Chen-Hui Chan) and one-year post-doc (Ricardo Ramos).

5.3.1 Gold nanoparticle structure and Monte-Carlo simulation of electron transport

DFT study of the structure of functionalized gold nanoparticles in aqueous medium

As part of Chen-Hui Chan's PhD thesis, which was defended in July 2019 at Laboratoire de Chimie of ENS-Lyon, a theoretical modeling of functionalized gold nanoparticles was developed in the context of cancer treatment by radiotherapy. Atomistic theoretical models of gold nanoparticles were studied in a size range from 0.9 to 3.6 nm by DFT. The effect of the biological environment was first described by solvating the nanoparticles with explicit water monolayers interacting with the metal surface. The results showed that in the size range 0.9-1.8 nm, water can transform the morphology of some metastable nanoparticles into lower energy solvated structures, although the interaction between gold and water is weak overall [171].

Then, more realistic DFT models of functionalized gold nanoparticles were developed, showing that the role of PEGylation around these nanoparticles is twofold :

1. The organic ligand shell promotes the stellation of certain nanoclusters (regular Au54 decahedron as shown in the figure) in a size range going from 1.1 to 1.3 nm. The greater stability of the polyethylene glycol (PEG) ligands adsorbed on the star decahedral cluster leads to a greater energy cost to desorb them and therefore to a lower propensity for the star nanoparticle to exchange ligands with the cell membrane. This theoretical result was in qualitative agreement with the experiments that were carried out to test the ability of various forms of gold nanoparticles (nano-stars, nano-rods, nano-tips, nano-spheres, etc.) to cross cell membranes.
2. PEGylation promotes the confinement of a few water molecules in the vicinity of the gold nanoparticles, through hydrogen bonds with the PEG ligand chains. This phenomenon was observed in particular for spherical morphologies, which exhibit the greatest capacity to exchange ligands with the membrane and therefore to penetrate the cell. This last result opened the discussion of reactivity, concerning the localization of water molecules around gold nanoparticles at the time of X-irradiation, during radiotherapeutic treatment. The publication of these results [172] was featured on the cover of the journal (see an illustration of the cover art below).

In parallel with this study, other properties such as the electrostatic potential of bulk gold and hydrated gold nanoparticles were calculated by DFT to be used for the development of a Monte-Carlo simulation of electron transport in gold material and nanoparticles.

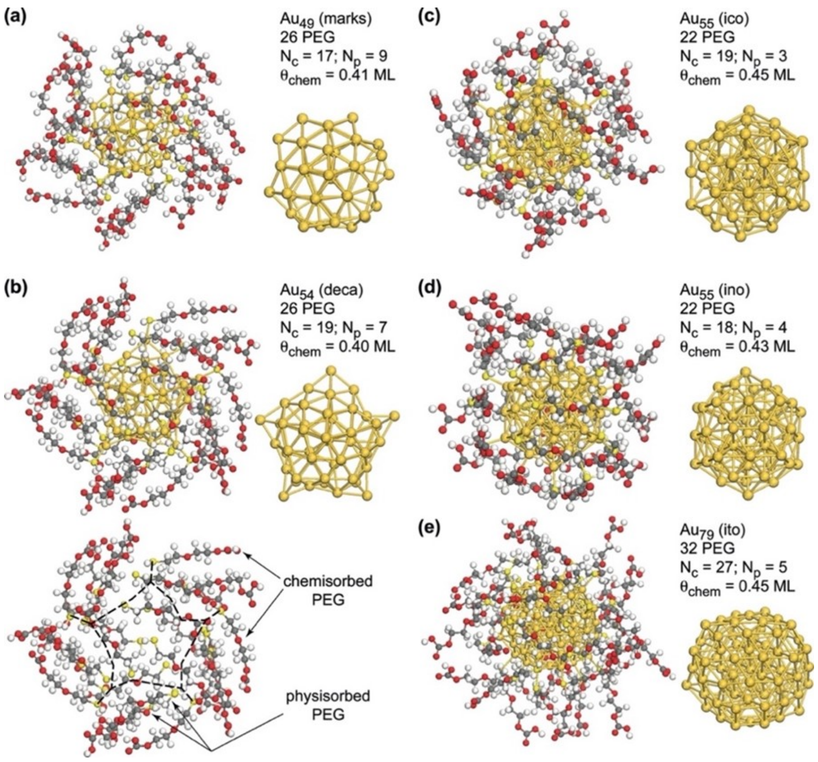

Figure 5.2: Functionalized gold nanoparticles optimized by DFT. (a) Au49 (Marks decahedron), (b) Au54 (regular decahedron), (c) Au55 (icosahedron), (d) Au55 (ino-decahedron), and (e) Au79 (irregular truncated octahedron) are covered with a monolayer of PEG ligands adsorbed on the surface of the nanoparticles and close to saturation. The stellation observed in the Au54 case leads to a more ordered organization of the organic layer (of the "regular brush" type), while the non-symmetric deformations obtained for the other nanoclusters induce a disordered organization (of the "brush" type).

Figure 5.3: Cover of the journal where the results of Chan's work were displayed ([172]).

Development of a Monte-Carlo simulation of electron transport in gold material and nanoparticles

We developed a Monte-Carlo simulation of low-energy electron transport into gold nanoparticles. To allow a comparison with experimental data, the simulation was first developed with bulk gold. This simulation included various mechanisms such as core ionisations, Auger and fluorescence relaxation, surface and bulk plasmons [173]. In line with the work by Beuve *et al.* [174, 175], it included a surface potential through the introduction of a mesoscopic potential. The latter was calculated through DFT calculations described in the previous section [176]. The predictions of the simulation were compared to yields and energy spectra of electron emitted as a consequence of the irradiation of mono-energetic electron beams. A good agreement was observed for electrons emitted with an energy higher than few hundreds of electron Volt. The agreement was less accurate for low-energy electrons, but sufficient for considering the simulation to study the physical-chemical processes modified by the presence of GNP in water irradiated with mono-energetic beams of photons. To this purpose, a calculation of the mesoscopic potential was performed for GNP using DFT. We observed that the change of mesoscopic potential had an influence on the emission of low-energy electrons only. The influence of the value of this mesoscopic potential on the physical-chemical processes induced in water containing GNP was expected therefore at the very surface of GNP and moderate.

5.3.2 Micro and nanodosimetry

Average doses at cellular and nano-scales around gadolinium NP

Work was carried out within the framework of the ANR RAPHAELO in collaboration between the LM2S laboratory at CEA Saclay and the STROBE team at the ESRF in the context of heavy element photoactivation therapy. The objective was to determine the impact of the internalization of Gadolinium nanoparticles (GdNP), in comparison to Gadolinium contrast agents (GdCA), in the experimental cell survival response and characterize them by micro and nanodosimetry. Clonogenicity tests were performed with cells incubated 5h (or not) with GdNPs or GdCA and irradiated in a monoenergetic synchrotron beam of 30 to 90 keV and compared with ^{60}Co irradiation (~1.25 MeV). The experiments showed that GdNP incubated with the cells were particularly effective compared to non-incubated GdNPs and GdCA, reaching sensitization enhancement ratio at 4 Gy (SER_{4Gy}) up to a factor of 3 after the Gd K-edge. The modeling work carried out with PENELOPE and Geant4 permitted to quantify, at the nanometric level, the emission spectra of secondary particles (electron/photon) as a function of the photon irradiation energy and the NP size. According to the most realistic location of GdNP in cells (on membrane or cytoplasm, from microscopy images), we showed that the particles responsible for a possible enhancement of cell nucleus damage were photoelectrons from the K and L shells of Gadolinium and not Auger electrons that had a minor role in the dose enhancement factor (DEF), and were maximized for photon energies 5 to 15 keV above Gd K-edge. Furthermore, simulations carried out at the cellular scale by physically considering the geometry of GdNP or

GdCA allowed to determine the DEF obtained at different other cellular organelles as potential biological critical targets (membrane, cytoplasm or nucleus) according to internalization assumptions (homogeneously distributed in cytoplasm, concentrated in lysosomes or adsorbed on membranes). While non-incubated GdNP or GdCA conditions correlated well with microdosimetry modeling at all energies, incubated cells with GdNPs led to an almost energy-independent sensitization ratio, that was explained by a biological action of GdNP in the cell cellular cycle which blocked them in the more radiosensitive phase G2/M [74]. We showed that the membrane DEF with GdNP adsorbed on it (the closest to the experimental conditions), was the dose increase that could explain the best the important SER observed experimentally after K-edge (see figure 5.4) [177].

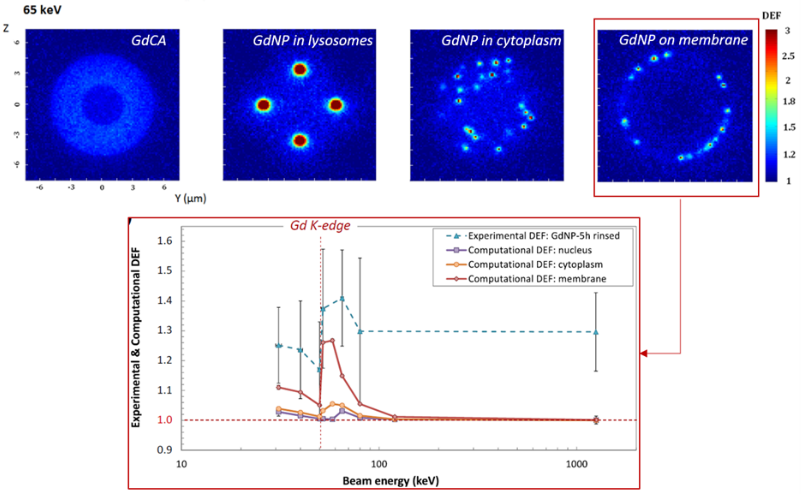

Figure 5.4: Top: Example of Monte-Carlo modeling of dose-enhancement factors (DEF) obtained for a 65 keV photon irradiation at the cellular scale with different hypothesis of gadolinium distributions in a cell considering homogeneously distributed Gd (= GdCA condition) or GdNP of 50 nm radius distributed in cytoplasm, lysosomes or on membrane at the experimental concentration of 2.1 mg Gd/mL. Down: experimental result of cell survival (converted in DEF through linear quadratic model) as a function of photon energy and compared with modeled DEF calculated at nucleus, cytoplasm and membrane for the experimentally verified conditions of GdNP adsorbed on cell membranes [177].

Nanodosimetric spectra around gold NP

While the calculation of mean physical dose gives interesting information for a low cost of calculation, it may lead to artifacts and misunderstandings when energy deposition in targets fluctuates importantly [178]. Alternatively, calculating spectra of specific energy in realistic conditions of irradiation would give information closer to molecular damage. For instance, simulating the irradiation with few grays at charged-particle equilibrium of a large water volume containing a nanoparticle, and calculating a spectrum of energy deposition in a nano-target set close to the nanoparticle, would be useful to estimate realistically the impact of nanoparticle on damage formation. However, this represents a huge challenge to a numerical point of view and had never been done before. Indeed, we estimate that calculating one nanodosimetry spectrum, as show in Figure 5.5, required 500 centuries on one computer. After an important effort of theoretical formalization and algorithm optimization, we reduced the computing time to 24 hours, a world premier [179].

We then could calculate spectra of nanodosimetry, changing the photon energy, the radius of the nanoparticle and the distance separating the nanotarget from the nanoparticle. We observed that the presence of a nanoparticle could increase the probability of depositing high values of specific energy. This probability enhancement varied according to

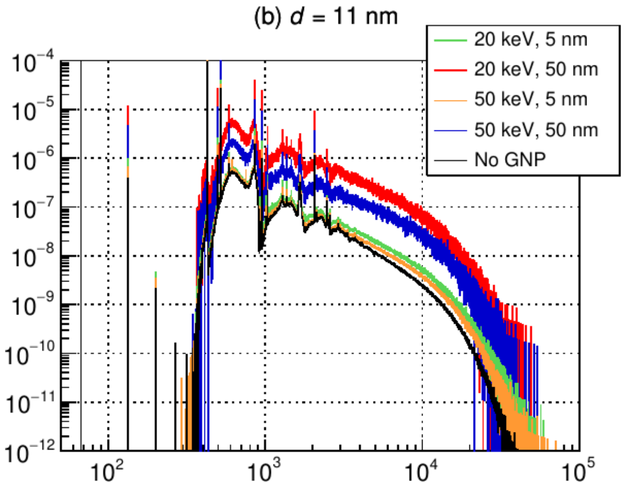

Figure 5.5: Probability density of the restricted specific energy (x-axis in Gy^{-1}) for a 11-mm distance of the nanotarget (10 nm) to the surface of the GNP. The figure shows spectra for 2 photon energies (20 keV and 50 keV), 2 GNP radii (5 and 50 nm) and 1 Gy irradiation [179].

the nanoparticle size and the photon energy. We also observed that the boost was due to Auger cascades and was limited to the proximity of the nanoparticles. Beyond 200 nm, the spectra looked like the one observed in pure water.

To estimate the effect of this boost on a biological point of view, we transferred these spectra to the NanOx model and calculated cell survival assuming the concentration of nanoparticle was homogeneously distributed in cells, including the cell nucleus. Using realistic irradiation dose and nanoparticle concentration, no enhancement of cell killing was observed. This was an outstanding result, knowing that so far the only interpretation of the biological effect enhancement with NP was associated to the boost of physical dose around NP. This interpretation was mainly based on the predictions of the LEM (Local Effect Model) [180–184]. This model was developed initially to predict biological effects associated to hadrontherapy. It assumes that cell survival can be deduced from the mean number of local lethal events generated in the cell nucleus, which may be derived from the radial dose around ion trajectories. In the application of the LEM to NP, the radial dose around the NP was used with nanoparticles homogeneously distributed in cells. However, as already underlined in [178], neglecting dose fluctuations at nanoscale was found critical. Replacing the radial dose by an actual distribution of energy deposition in nanotargets led to the disappearance of the biological effect predicted by the LEM for both hadrontherapy [178] and NP [185]. Finally, these results reinforce the requirement of prudence when interpreting the biological effects in terms of high dose deposition around NP.

5.3.3 Free radical production

While theoretical studies have mostly focused on physical mechanisms and dose enhancement, studies of free radical production were scarce. We investigated the primary yield of free radicals (OH and H_2O_2) induced by 20-90 keV monoenergetic photons, for small GNPs concentrations [186]. Our study was based on a Monte-Carlo approach which enables electron transport down to low energy, both in water and in gold. We obtained, for a gold concentration of 1 mg/mL, an average chemical enhancement varying from 6 to 14%, depending mostly on the photon energy and, to a lesser extent, on the chemical species and size of the GNP. This enhancement was strongly correlated to the dose deposition enhancement, although not strictly proportional. We focused then on the production of radicals around the nanoparticles [187]. In the micrometer range, we obtained an excess of chemical species following GNP ionization, as compared to a reference water nanoparticle (WNP) ionization. This difference came from the dominant processes of photon interaction, *i.e.*, Compton for water and photoelectric for gold, which are characterized by different emitted-electron energy spectra. The overproduction of chemical species could be up to five times higher for GNP, depending on the photon energy. The concentration of chemical species within 100 nm from the GNP surface was higher for GNPs compared to WNPs due to Auger electrons when the nanoparticle radius was equal to 5 nm. On the contrary, it was quite comparable when the nanoparticle radius was equal to 50 nm. This reveals that gold Auger-electrons do not necessarily induce a significant boost of chemical species in the vicinity of GNP, as compared to WNP.

5.4 Hadrontherapy

5.4.1 Monte-Carlo simulations of physico-chemical processes

In hadrontherapy, the variation of the biological effectiveness as a function of ion species and energy must be taken into account. This biological effectiveness can be characterized by cell survival curves described by the well-known linear-quadratic models and its alpha and beta coefficients, usually used in the treatment planning systems. In order to provide such tables of alpha and beta coefficients, biophysical models are required. The input data of these models generally consist of information on nano/micro dosimetric quantities and, concerning some models, reactive species produced in water radiolysis. In order to fully account for the radiation stochastic effects, these input data have to be provided by Monte-Carlo track structure (MCTS) codes allowing to compute physical, physico-chemical, and chemical effects of radiation at the molecular scale. Although the uncertainties associated to these MCTS are very difficult to quantify from a theoretical point of view, they can be estimated through the benchmark of several codes. This was the objective of the study reported in this section and carried out within the PhD thesis of Yasmine Ali funded by the LabEx PRIMES (collaboration IP2I, LPC Clermont-Ferrand, CREATIS). The benchmark proposed in this study dealt with Geant4-DNA (Options 2, 4, and 6) [188] and LPCHEM [189], that are useful codes for estimating the biological effects of ions during radiation therapy treatments [190].

Micro and nanodosimetry

We considered the simulation of specific energy spectra for monoenergetic proton beams (10 MeV), using two codes, LPCHEM and GEANT4-DNA. We compared probability distributions of energy transfer points in cylindrical nanometric targets (10 nm) positioned in a liquid water box. Overall, the specific energy spectra and the chemical yields obtained by the two codes are in good agreement, considering the uncertainties on experimental data used to calibrate the parameters of the MCTS codes. For 10 MeV proton beams, ionization and excitation processes are the major contributors to the specific energy deposition (larger than 90%) while attachment, solvation, and vibration processes are minor contributors.

Radiolysis species production

The radiolysis species production for both electron (1 MeV) and proton (10 MeV) beams were also studied, namely the $^{\bullet}$OH, e^{-}_{aq}, H_3O^+, H_2O_2, H_2, and OH^- yields simulated between 10^{-12} and 10^{-6} s after irradiation. LPCHEM simulates tracks with slightly more concentrated energy depositions than Geant4-DNA which translates into slightly faster recombination than Geant4-DNA. Relative deviations with respect to the average of evolution rates of the radical yields between 10^{-12} and 10^{-6} s remain below 10%.

Computing times

When comparing execution times between the codes, we showed that LPCHEM is faster than Geant4-DNA by a factor of about 4 for 1000 primary particles in all simulation stages (physical, physico-chemical, and chemical). In multi-thread mode (four threads), Geant4-DNA computing times are reduced but remain slower than LPCHEM by ~20% up to ~50%.

5.4.2 Biological dose modelling

Development of the NanOx Model

Two different biophysical models are currently implemented in the treatment planning systems (TPS) of hadrontherapy facilities all over the world: the first version of the local effect model (LEM) [191] and the modified microdosimetric kinetic model (mMKM) [192, 193]. In order to overcome some of their shortcomings, other biophysical models have emerged in recent years proposing alternative frameworks [194–198]. The NanOx biophysical model that we developed and published in 2017 [194] is one of them: its theoretical framework gathered and combined the premises of some of the models proposed in the literature, while fully considering the stochastic nature of energy deposition down to the nanometric scale. It is worth noting that NanOx was developed to predict cell survival in the context of hadrontherapy, but it was designed to be applied to any kind of radiotherapy within a single consistent theoretical framework. This model can indeed be applied for instance to conventional radiotherapy (with gamma ray) and it is currently extended to targeted alpha therapies and boron neutron capture therapy involving low-energy ions. The fully innovative aspects introduced in the NanOx model were the following [199, 200]: the notion of global events that intends to model the lethal effects of the oxidative stress and of the accumulation of sublethal lesions, induced at the scale of the cell sensitive volumes; ii) the notion of chemical specific energy, representing the toxic accumulation of oxidative stress, *i.e.*, the imbalance between the production of reactive oxygen species and antioxidant defenses, or sublethal damage at a cellular level; iii) the construction of the function related to the inactivation of nanotargets. With no *a priori* assumptions on this function except for the monotonic increase, its shape was resolved by means of a linear combination of basis functions and a fit of the weight values of this linear combination to get a good agreement with experimental data. The resulting function presented a threshold and a saturation that were discussed with respect to features of other models [201].

Irradiations with mono-energetic beams

Cell survival prediction in the context of hadrontherapy was the first application of the NanOx model. The meaning and relevance of most of the NanOx parameters were discussed by evaluating their influence on the linear-quadratic coefficient α and on the dose deposited to achieve 10% or 1% of cell survival. The predictions of the model were compared to experimental data obtained with 3 cell lines (HSG, V79 and CHO-K1) irradiated by monoenergetic protons and carbon ions. We conclude that, in the current version of NanOx, the modeling of a specific cell line relies on five parameters, which have to be adjusted to several experimental measurements: the average cellular nuclear radius, the linear-quadratic coefficients describing photon irradiations and the α values associated with two carbon ions of intermediate and high-LET values [202].

Moreover, we also compared the predictions of NanOx with the ones of 5 other biophysical models for HSG, V79 and CHO-K1 cells: the four versions of the local effect model (LEM) and the microdosimetric kinetic model (MKM). Although the LEM IV and the MKM predictions accurately reproduced the trend observed in the data, NanOx predictions were more often more accurate than the ones issued from the other models for the three considered cell lines [203].

Irradiations with Spread-Out Bragg Peak (SOBP)

In order to estimate the biological dose for Spread Out Bragg Peak (SOBP) irradiations, the databases of survival fraction coefficients for several ion types have been implemented into GATE, a Monte-Carlo toolkit. Yasmine Ali conducted these first developments during her PhD thesis, and an article has been published in the Cancers journal on the benchmark of the biological dose estimates with the NanOx and mMKM actors against experimental data [190] with SOBP treament plans coming from a simplified model of the HIBMC 320 MeV/u carbon-ion beam line in Hyogo. This feasablility study paves the way towards the use of the mMKM and NanOx models on clinical beams using patient CT scans.

5.4.3 Modelling of tumor control probability

In the context of the PhD thesis of Marie-Anne Chanrion funded by the Center of hadrontherapy of Marburg (Germany) and co-supervised at IP2I by Prof. Beuve, modeling of Tumor Control Probability (TCP) was undertaken for treatment with carbon ions [204]. The principle of this modeling consisted in assuming that a model of TCP developed for standard radiotherapy could be applied, provided that the physical dose of photons was replaced by the biological dose of ions. For the calculation of the biological dose, the TPS developed at this period by Siemens was considered and the LEM I version was used to calculate the alpha, beta tables.

To test this modeling, prostate cancer was chosen for three reasons. First, clinical data were existing, issued from publications by the first world-wild center of carbon therapy (Japan). Second, the geometry of prostate tumor does not vary too much from one patient to another. It was therefore not required to perform a treatment planning for each patient, which is important since patient images were not available. Third, the center of Marburg had the perspective to treat patients with prostate cancers. We chose as TCP model a Poisson model since such model was based on cell survival probability, consistently with biological dose modeling in hadrontherapy. We studied the influence of the model parameters and tested various TCP models developed for prostate cancer treated by conventional radiotherapy.

While all parameters were found to have an impact on the TCP value, the most critical parameter was the threshold dose of the LEM I model. Then, for three different risks of prostate cancer, we determined the value of the threshold dose by fitting the TCP predictions to the clinical data.

5.5 Radiotherapy with low-energy ions: BNCT and TAT

If hadrontherapy provides a therapeutic solution to increase the biological effectiveness in aggressive and localized cancer treatments, thanks to the high LET of ions, the approach reaches its limits in the case of very infiltrative or metastatic cancers. Promising solutions are proposed by combining a molecular targeting through dedicated vectors and a local emission of very high LET and short-range ions. It is the case in targetted alpha therapy (TAT), where the alpha emitter is directly attached to the chemical vector, or in BNCT where a compound enriched in ^{10}B isotope is first injected, accumulates in tumor and submitted to a neutron field, which capture eventually leads to the emission of very aggressive He and Li ions. Both approaches present common difficulties in dosimetry and treatment planning due to the high heterogeneity of the dose deposition at micrometric scale, depending both on the bio-distribution of the targeting vector and the short range of ions (few cells). In addition, the RBE of ions varies significantly in this short range, a phenomenon that needs to be properly considered in simulation for relevant biological effect predictions.

The LPSC with IP2I team PRISME started a collaboration on this subject in 2016, with two Master students who laid the first foundations for coupling the macroscopic Geant4 simulation of a BNCT treatment with the use of the NanOx model. It allowed to provide a first estimation of the biological dose received by a brain tumor in the approximation of a mixed field algorithm including ion-RBE variation up to their stop (but without micrometric precision). This collaboration demonstrated the feasibility and interest of this coupling for BNCT and led to the PICTURE project (INCa funds), started in 2021, aiming at going further in the predictions by including the microscopic distribution complexity and the consideration of extranuclear damage in the cell survival predictions. The LabEx thesis of Victor Levrague (LPSC/IP2I, 2021-2024) is dedicated to the improvement of biological effect predictions for TAT treatment of microtumors. Mario Alcocer-Ávila, a PICTURE postdoctorant who beneficiates from a grant complement from the LabEx, is working in parallel on the NanOx developments needed for PICTURE's objectives. The project is still ongoing, but two major achievements were accomplished with this work so far:

1. **Adaptation of NanOx algorithm for low-energy (< 10 MeV) ions**: to adapt the NanOx model from the high energies of hadrontherapy, to the low-energies of TAT or BNCT ions, NanOx needed to include the consideration of the energy loss in cell nuclei traversal (*i.e.* the sensitive volume). The estimation of cell survival now integrates the variation of a density function of lethal-event along the ion track that depends on its type and energy at each step. This was accompanied by a narrow-track approximation saving considerable simulation time, valid for low-energy ions, that allowed to neglect the energy deposited outside the sensitive volume due to secondary electrons. The new algorithm was compared with the original implementation of the NanOx model in terms of the inactivation cross-section of HSG cells irradiated by α-particles, and showed consistent predictions above 1 MeV/n. This work is currently the object of an article in submission process.
2. **Determination of heterogeneous distribution of alpha-emitters in dosimetry, cell survival and TCP predictions**: using this new algorithm, we performed a systematic study in order to determine how the micro-distribution and cell internalization of the alpha-emitters impact predictions with different TAT treatment scenarios. To that end, we used the CPOP/Geant4 code to generate realistic 3D multicellular geometries and adapted a new version of this code for TAT in collaboration with LPC-Clermont who developed initially CPOP. Several parameters of influence were studied, such as the size and cancer cell density of the micro-tumor considered, the type (energy) of alpha-radionuclide, the possible diffusion of the radionuclide daughter (in the case of ^{211}At) and the intra-tumoral distribution of the radionuclides, following a uniform or lognormal law. We showed for example that for tumors of radius less than 50 µm, deviations up to 30% could be observed according to the cell internalization of radionuclides, while differences were modest in larger tumors. In regions of low activity, the predicted TCP varied significantly according to the intracellular and for lognormal distributions, and RBE of alphas varied from 2.9 and 3.6. This new calculation chain can be useful in preclinical and clinical trials

to quantify the error made in TAT treatment predictions when intracellular and intratumoral distributions are unknown. This study is also in the process of article submission.

Next steps in the PICTURE project developments include the integration of an extranuclear sensitive volume in the determination of cell survival, to see if considering damage to the cytoplasm organelles can lead to cell survival predictions closer to experiments when BNCT compounds or alpha-emitters are internalized. In addition, developments are ongoing to link the macroscopic dosimetry to these microscopic predictions to provide a full multiscale calculation chain. This is worth mentioning that this project will be pursued beyond the INCa funding and is now a collaboration between five LabEx teams at IP2I, LPSC, LIRIS and LPC-Clermont.

5.6 Conclusion

The LabEx PRIMES has permitted to create a multidisciplinary dynamic of modelling of radiobiological effects. New fruitful collaborations have started, and many are going to continue. Two major and synergetic actions guided the dynamics. One dealing with nanoparticles, in parallel to the experimental chemical and biological activity of the LabEx. This action, supported by 2 PhD and one-year post-doc funded by the LabEx, allowed us to fill the gap between complex quantum computing and biological dose predictions using the NanOx model through the development of Monte-Carlo simulations of radical production and nanodosimetry. The numerical challenge was to perform estimation based on realistic geometry, conditions and nanoparticle concentration. These results questioned the consensual scenario on the role of nanoparticles in the observed enhancement of biological effects, namely the spike of dose in the proximity of the nanoparticles. A second action, supported by two PhD and one-year post-Doc, concerned the development and applications of the NanOx model. This model can predict the probability of cell survival for any ionizing radiation, taking into account all stochastic effects of radiation from the nanoscale and the production of ROS. Through an exhaustive comparison with experimental data and the model considered for Hadrontherapy, we proved this model to be competitive with the other models. These results encouraged the LabEx teams to develop a new actor in the GATE toolkit to predict biological dose for clinical irradiation. Work is in progress to extend these predictions to the probability of tumor control (TCP), which is a quantity closer to clinical objectives. In parallel, the NanOx model application has been extended to innovative radiotherapy, BNCT and TAT, for which the biological effectiveness is due to low-energy ions. This was a new computing and mathematical challenge for the implementation of the NanOx model, since the variation of the ion energy within cells cannot be ignored. Geant4 with a low-energy option was then used, and some cell geometries were determined using confocal microscopy and image analysis. For TAT, predictions of biological dose and TCP were obtained for microtumors. For BNCT, the formalism and algorithms have been designed and need to be implemented. For all these innovative therapies, the research undertaken by the LabEx on radiobiological modeling was intended to go as far as possible toward clinical applications.

GATE modeling: imaging modeling, dosimetry and radiation line modeling

6

Coordinator: David Sarrut

Contributor: Lydia Maigne

6.1 Introduction

The GATE open-source software, developed by the Opengate collaboration, has been available to the scientific community for 20 years, with its first release in 2004 [205–208]. Built on the Geant4 toolkit [209, 210] developed at CERN, GATE provides a versatile platform for conducting Monte Carlo simulations in various medical physics applications. It is widely used for simulating advanced nuclear imaging systems such as PET, SPECT, and Compton Cameras, as well as for predicting dose distributions in radiation therapy, including internal or external beam therapy, brachytherapy, hadrontherapy and more recently in radiation biology. Over the years, members of the LabEx Primes have actively contributed to the development and enhancement of GATE as well as its thorough validation. In the following sections, we describe the major advancements made in the past 10 years.

6.2 Developments around GATE in the past 10 years

6.2.1 GATE for ion beam treatments

Proton beam modeling is crucial in hadrontherapy because of the precise energy deposition at the Bragg peak, enabling targeted tumor treatments while minimizing damage to healthy tissues. Monte Carlo simulations are essential for accurately modeling proton interactions with tissue, accounting for range uncertainties and heterogeneities. However, these simulations are computationally demanding as they need to capture complex physical processes, making efficient and accurate modeling a significant challenge in proton therapy.

Building on earlier developments [211–213], further advancements were made by Grevillot and Elia *et al.*, leading to the implementation of a specific proton beam model in GATE [214–216]. This model allows for precise dose distribution predictions without requiring a detailed description of the entire proton beam head. The work, conducted by LabEx members in collaboration with researchers from the MedAustron therapy center, led to the adoption of GATE as an independent dose calculation tool to evaluate clinical treatment plans. To go further, LPCA, IP2I and CREATIS collaborated on the implementation and validation of biophysical models to estimate the biological dose in ion beam therapy treatments [217]. The modified microdosimetric Kinetic Model (mMKM), preliminary developed by the NIRS in Chiba (Japan) for the treatment planning software (TPS) HIPLAN and, recently available in the latest version of the RayStation treatment planning software by RaySearch Laboratories AB (Stockholm, Sweden), as well as the NanOx model, able to model the local lethal events at the nanometric scales and the non-local events with the production of chemical reactive species at micrometric scale, have been proposed in the BioDoseActor, a new GATE software module, able to predict at the voxel scale biological doses for patient treatments using protons or carbon ions (see previous chapter on radiobiology modeling). Lastly, GATE and Geant4-DNA have been combined and tested to estimate the production of radiolytic species after proton irradiation [218], this study opened the door to the perspective of integrating the entire chemistry module of Geant4-DNA to the GATE platform in the objective to cover the needs in multi-scale applications, from the simulation of sub-cellular damage to the estimation of macroscopic doses to organs.

Additionally, an empirical model for calculating collimator contamination dose in therapeutic proton beams was developed using GATE simulations [219]. This enhanced the accuracy of analytical dose calculations while maintaining reasonable computation times, improving the overall precision of proton therapy treatments.

6.2.2 GATE for Prompt-Gamma and PET-based Dose Monitoring in hadrontherapy

Prompt-gamma imaging has emerged as a key method for real-time dose monitoring in hadrontherapy, particularly in proton and carbon-ion therapy [7]. The ability to track secondary particles generated during treatment provides valuable information for verifying the proton beam range and ensuring accurate dose delivery. GATE has been extensively used to model prompt-gamma emissions and to evaluate the feasibility and accuracy of different monitoring techniques.

In early work, Robert *et al.* [220] conducted a detailed comparison between GATE/Geant4 and FLUKA Monte Carlo codes for the simulation of secondary particle distributions in proton and carbon-ion therapy. This study demonstrated the capacity of GATE to accurately simulate the complex interactions leading to prompt gamma emissions, essential for dose verification in hadrontherapy. Dose monitoring for carbon beam can also be studied with PET imaging: in the study by Jan et al [221], we explored the feasibility of integrating GATE with PET imaging systems for real-time dose monitoring in carbon-ion therapy. Further research [222] assessed the performance of five different PET system designs for proton therapy dose verification, simulating realistic clinical conditions. This study highlighted the potential of GATE to optimize PET-based and prompt gamma monitoring systems.

Gueth *et al.* [223] proposed a machine learning-based approach to patient-specific dose monitoring using GATE simulations, improving the precision of real-time treatment verification. Kanawati *et al.* [224] introduced a Monte Carlo simulation method using a specific track length estimator (TLE) to simulate prompt gamma emissions in proton therapy. To address computational challenges, Huisman *et al.* [21]

developed accelerated prompt-gamma estimation techniques, enabling faster simulations suitable for clinical applications. More recently, [225] expanded on this work, focusing on the analytical modeling and Monte Carlo simulations of multi-parallel slit and knife-edge slit prompt gamma cameras, and [226] introduced an extension of the TLE module that incorporates the prompt-gamma emission time, which is tagged from the proton tracking. Based on these developments, [227] explored the influence of sub-nanosecond time-of-flight (ToF) resolution on online range verification in proton therapy, using the line-cone reconstruction method in Compton imaging. The study demonstrated that achieving sub-nanosecond ToF resolution can enhance the accuracy of proton beam range verification by improving the precision of prompt gamma detection.

In conclusion, GATE has been significantly updated in the last 10 years to allow advanced prompt gamma and PET-based dose monitoring in hadrontherapy. Its simulations have improved the accuracy of dose verification and range estimation through improved modeling, integration with PET systems, and advanced techniques like high-resolution ToF measurements. These developments contributed to the improved design and precision of online dose monitoring systems in proton therapy treatments.

6.2.3 GATE for Compton Camera

Compton cameras, though an old concept [228] with still limited real-world medical applications, still hold significant promise for hadrontherapy monitoring and nuclear imaging. The ability to image gamma radiation without collimation can substantially enhance the efficacy of imaging systems, improving precision in both therapeutic and diagnostic contexts. Despite their potential, designing these systems and developing associated reconstruction algorithms remains complex. Monte Carlo simulations are crucial for studying and optimizing Compton cameras.

In GATE, key advances in Compton camera simulations include the work by Hilaire [229], which explored the impact of the broad energy spectrum of prompt gamma radiation on proton therapy monitoring. This study highlighted challenges and provided solutions to improve imaging accuracy in varying energy conditions. Etxebeste [230] then introduced the CCMod module for GATE, specifically designed to enable detailed simulation of Compton camera imaging, facilitating more accurate modeling and analysis of Compton camera performance. Feng [231] used this GATE model to investigate the influence of Doppler broadening model accuracy on Compton camera list-mode MLEM reconstruction, highlighting the importance of precise modeling in enhancing image quality and diagnostic capability. More recently, Munoz [232] developed techniques based on GATE simulations to image polychromatic sources using Compton spectral reconstruction, improving the ability to visualize complex radiation sources.

These developments collectively enhance our understanding of Compton cameras by providing versatile Monte Carlo simulations tools available to the whole community.

6.2.4 GATE for dosimetry in radiopharmaceutical therapy

Dosimetry for radiopharmaceuticals treatments, such as with ^{177}Lu and ^{90}Y, has seen significant progress in recent years, driven by advances in Monte Carlo simulations and patient-specific methodologies. GATE has played a pivotal role in improving the accuracy and practicality of these techniques.

Sarrut et al [233] developed a 3D voxel-based approach for absorbed dose distribution in radionuclide therapy, applying Monte Carlo methods to model the biodistribution of therapeutic agents such as monoclonal antibodies labeled with ^{90}Y targeting synovial sarcoma. This work introduced more precise modeling techniques for dose estimation, improving treatment planning accuracy. The GATE platform was used for different dosimetry studies in rabbits further extrapolated to humans prior to their use in phase I clinical trials. It has been the case for two radiopharmaceuticals: [131I]ICF01012 used to treat human melanoma [234] and [99mTc]NTP15-5 used in cartilage imaging [235]. In parallel, [236] conducted a first-in-human study targeting FZD10 in metastatic synovial sarcoma, highlighting the importance of accurate dosimetry for safe and effective treatment, using the proposed method.

For *in vitro* applications, the GATE platform aims to integrate the CPOP platform [237], an open source C++ cell POPulation modeler for radiation biology using internal or external radiation beams on spheroids (3D cell populations) using or not nanoparticles.

Further work by [238] utilized digital photon counting PET for quantitative ^{90}Y dosimetry, providing a foundation for more accurate phantom studies. More recently, Vergnaud *et al.* [239, 240] expanded these methods by introducing patient-specific dosimetry approaches, including motion-compensated SPECT reconstructions for selective internal radiation therapy (SIRT) with ^{90}Y and for ^{177}Lu therapies. These improvements allowed better adaptation to variable imaging schedules, reducing the number of SPECT/CT acquisitions needed for ^{177}Lu therapies without compromising dosimetric accuracy. Dosimetry was also performed via specific tools in GATE, via the dose-rate method as an alternative to the conventional MIRD (Medical Internal Radiation Dose) approach.

Other advances include [241], who proposed image-based SPECT calibration methods for more precise activity quantification, and [242], who demonstrated the feasibility of *in vivo* gadolinium nanoparticle quantification using SPECT/CT imaging, together with specific GATE imaging modeling. Together, these developments contribute to improved dosimetry workflows, improving both the precision and efficiency of radiopharmaceutical therapy.

Through these advances, GATE now contains a set of tools dedicated to dosimetry in radionuclide therapies and advanced SPECT imaging capabilities.

6.2.5 GATE and Artificial Intelligence

The integration of artificial intelligence (artificial intelligence (AI)) techniques has brought new possibilities for improving Monte Carlo simulations in medical physics. GATE has been at the forefront of incorporating AI to improve simulation accuracy and efficiency.

A first investigation in this area is the work of Sarrut *et al.* [243], where neural networks were employed to accelerate Monte Carlo simulations by learning the angular response function of SPECT detectors. This approach significantly reduced computation times while maintaining accuracy. Building on the idea of using neural networks to replace part of Monte Carlo simulation, [244] introduced the use of GANs (Generative Adversarial Network) to create compact beam source models, demonstrating their potential to simplify complex source geometries without sacrificing precision in dose distribution predictions. Based on this idea, [245] extended the application of GANs to model complex particle phase spaces for SPECT simulations. In this situation, the neural network is trained from a low-statistics Monte Carlo simulation to generate gammas exiting a patient from a source distribution. Saporta *et al.* [246] expanded on this by using conditional GANs to model families of particle distributions for SPECT simulations, offering enhanced flexibility in representing diverse clinical scenarios with various source distributions. In a more recent study, [247] introduced a GAN-based model for annihilation photon sources in PET simulations. All of these concepts were described in [208], providing a review of AI integration into Monte Carlo methods in medical physics.

These AI-driven advancements have the potential to change the way Monte Carlo simulations are conducted in medical physics, reducing computation times and increasing the adaptability of simulation models while maintaining the high accuracy required in clinical applications. It is still a field in its infancy; further developments are expected in the coming years.

6.2.6 Other Topics

GATE has also been used and developed by LabEx members in a variety of specialized developments beyond the core areas of dosimetry and imaging, including X-ray dose calculations, SPECT simulations...

Baldacci *et al.* [248] introduced a track length estimator (TLE) method for dose calculations in low-energy X-ray irradiations. This method demonstrated improved accuracy in modeling dose deposition for low-energy radiation (gamma below 1 MeV), which is particularly relevant for small animal studies. Building on this, [249] proposed a split-exponential track length estimator (seTLE) tailored for Monte Carlo simulations in small-animal radiation therapy, improving the precision of dose calculations in preclinical research.

In the field of SPECT, [250] developed a fixed forced detection (FFD) technique to accelerate Monte Carlo simulations. This approach significantly reduced simulation times without compromising the accuracy of SPECT image reconstructions, facilitating faster preclinical and clinical assessments. Abbani *et al.* [251] extended the use of Monte Carlo simulations to deep learning-based segmentation for prostate radiation therapy using simulated cone-beam computed tomography (CBCT). This integration of AI with Monte Carlo methods helped enhance the accuracy of segmentation models, potentially improving radiation treatment planning.

Recently, Sarrut *et al.* [252] introduced a photon source model for alpha-emitter radionuclides, expanding the simulation capabilities of GATE for therapies involving these high-LET emitters. Additionally, [253] developed a PET digitization chain within GATE to refine the Monte Carlo simulation of PET imaging systems, further improving image quality and quantitative accuracy.

These diverse developments demonstrate GATE's flexibility and its contributions to various areas of medical physics.

6.2.7 GATE reviews papers

Several comprehensive reviews have highlighted the advancements and growing impact of GATE in medical physics. [207] provided an overview of GATE's use in radiation therapy and dosimetry, emphasizing its role in improving dose calculations and modeling complex therapies. [254], focused on the advancements in emission tomography, particularly in PET and SPECT imaging systems. In 2022, [255] reviewed the broader OpenGATE ecosystem, summarizing its evolution, key tools, and community contributions, reflecting GATE's expanding influence and capabilities in medical imaging and therapy simulations.

6.3 Conclusion

Over the past decade, members of the LabEx Primes collaboration have significantly contributed to the development of GATE. Achievements include advancements in dosimetry for radiopharmaceuticals, enhanced proton beam and prompt gamma modeling, and the integration of AI techniques like GANs to improve simulation accuracy and efficiency. LabEx members also played a key role in expanding GATE's applications to new imaging modalities and therapeutic techniques. However, ongoing challenges remain, particularly in reducing computational demands and refining complex reconstruction algorithms for clinical use.

GATE remains an open-source platform, available to the entire scientific community, and is developed collaboratively. It is available on `https://github.com/OpenGATE/opengate`. Given the collective nature of its development, distinguishing contributions made specifically by LabEx members from those of other researchers can be challenging. In this review, we have chosen to highlight works that were either initiated or actively contributed to by LabEx members.

Looking ahead, LabEx members will continue to contribute to key developments, including the release of GATE 10, which will be Python-based, offering a more user-friendly interface and streamlined workflows. Future research will focus on faster simulations, deeper AI integration, and optimizing imaging systems for emerging therapeutic technologies.

Multi-physics modeling of organs in motion (imaging and therapy)

7

Coordinator: Hamid Ladjal

Contributor: Behzad Shariat

7.1 Introduction: Presentation of the Research Context

In conventional radiation therapy, beams of X rays (high energy photons) are delivered to the patient to destroy tumor cells. Conventional X-ray radiation therapy is characterized by almost exponential attenuation and absorption, delivering a maximum energy near the beam entrance, but continuing to deposit significant energy at distances beyond the targeted volume. Inevitably, some radiation dose is always deposited in the healthy tissues. To optimize the dose deposit within the target, it is then necessary to use several directions of beam delivery.

Hadron Therapy (HT) is an advanced radiotherapy technique for cancer treatment. It offers a better irradiation ballistic than conventional techniques and requires some appropriate quality assurance procedures. Contrary to conventional radiotherapy that uses high-energy photons for tumor irradiation, HT uses charged particles such as protons or carbon ions. The strength of HT lies in the unique physical and radiobiological properties of these particles; they can penetrate the tissues with little diffusion and deposit a maximum of energy just before stopping. This allows a precise definition of the specific region to be irradiated. The peaked shape of the hadron energy deposition is called Bragg peak. With the use of hadrons, the tumor can be irradiated while the damage to healthy tissues is less than with X-rays. Moreover, the radio-biological effectiveness of hadrons could be up to 3 times higher than photons. Thus, they could be used to treat radio-resistant tumors. Radiation therapy as well as hadron therapy requires precise control over the position of tumor volume during treatment to minimize the irradiation of healthy tissue. When the tumor is in a moving organ, the major difficulty is to target the tumor during treatment and to be able to calculate the exact position of the dose deposit. This limiting factor is particularly marked in the case of lung tumors, which explains the still unsatisfactory clinical results. We have also the specific problem of hadrontherapy. As stated before, the beam deposits a maximum of energy in a very localized area corresponding to the Bragg peak. The position of the Bragg peak depends on the density of the matter traversed by the beam. So, in hadrontherapy, we need information about the moving organs density variation that are traversed by the beams because movement and deformation modify densities. Thus, the target motion together with the continuous density variation along the beam path can lead to unexpected dose distributions. In current clinical practice, three main volumes of tissue are defined during the treatment plan design to guide the beam delivery. The first is the gross target volume (GTV), which is the position and the extent of the gross tumor. The second volume includes the GTV and an additional

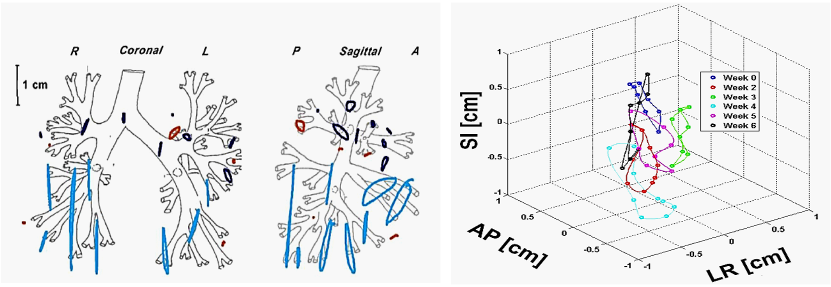

Figure 7.1: Projection of lung tumor trajectories measured with fluoroscopic images, tumor had a mean motion of 24.6±3.8mm. Some trajectories show hysteresis during a complete breathing cycle [260].

margin that takes into account malignant tissue spread that cannot be entirely imaged, and it is called the clinical target volume (CTV). A third volume, named the ITV for Internal Target Volume, was added in the ICRU report 62 to take into account the variations in the size and position of the CTV relative to the patient's reference frame. Last, the planning target volume (PTV) takes into account the geometrical variations. In the case of moving tumors, the PTV is increased so that the tumor lies inside the treatment field at all times and the GTV motion range is about 2 cm [256].

Respiratory-induced organ motion constitutes one of the most difficult challenges to tumor tracking, to treatment planning, as well as to nuclear imaging used for treatment verification. Breathing is an active and complex process where the respiratory motion is non-reproducible [257]. As shown by many studies, the breathing periodicity, amplitude and baseline shifts of patients can vary during a single imaging or treatment session [258, 259]. Lung tumors can even present hysteresis in their trajectories [260], making them more difficult to locate with precision (Figure 7.1).

One of the solutions to calculate tumor position is to use implanted markers. However, this involves an invasive procedure to implant the markers and there are a number of other potential problems, including the possibility of marker migration. Other techniques based on imaging, such as Cone-Beam or deformable image registration, attempt to predict the position of lung tumors [261]. Unfortunately, these methods assume a reproducible motion of the respiratory system. Thus, the complex organ deformations occurring during breathing together with the variability of the patient breathing patterns render existing image-based motion compensation techniques prone to errors. The Cone-Beam technique is invasive and would greatly increase the radiation dose to the patient due to imaging. Generally, it is very difficult or impossible to accurately identify the tumor location and density variability during the treatment. An ideal radiotherapy procedure would continuously adapt the beam to the variation of the tumor's position. Moreover, in the case of HT it would have to adapt to the continuous density changes along the beam path. A full four dimensional continuous imaging of the internal anatomy of the patient during the treatment procedure is yet not feasible. An alternative solution is to use a motion model that tries to find the correspondence between the internal displacements and deformations of the organs and the external respiratory surrogate signals during treatment, taking into account respiratory variability. To overcome these limitations, we have proposed and developed a non-invasive approach for lung tumor tracking based on a biomechanical patient-specific model of the respiratory system, which takes into account the physiology of respiratory motion to simulate the real non-reproducible breathing motion. The developed

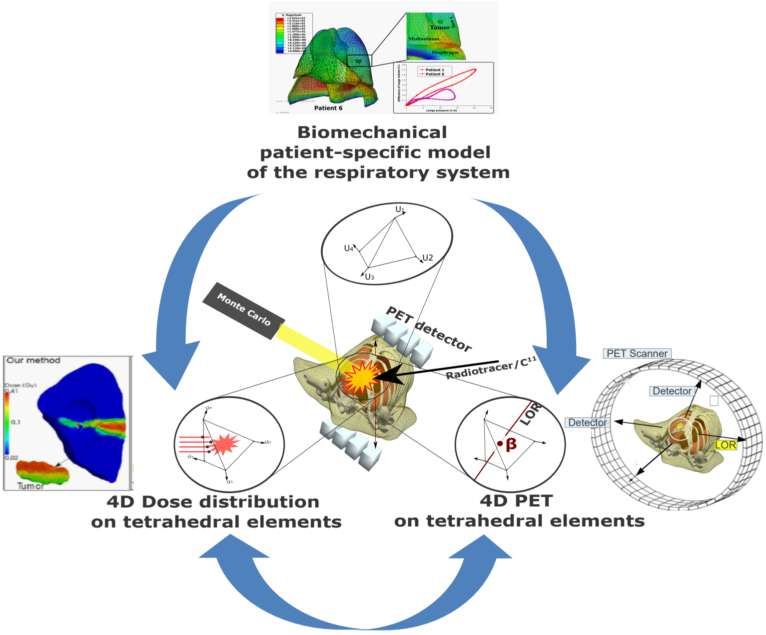

Figure 7.2: Unified patient-specific multi-physics approach, based on same tetrahedral elements. All the physical quantities (deformation of the organs, their densities, deposited dose and nuclear activities for positron emission tomography (PET) imaging) are assigned to the vertices of the tetrahedrons.

model, also takes into account the density variations due to breathing and that can be used during External Beam Radiation Therapy (EBRT). In our works, we chose to use a geometric representation based on tetrahedral geometry, while most models for describing movement are based on hexahedrons. More precisely, we have proposed and implemented a new unified biomechanical patient-specific approach, based on tetrahedral elements, where the transformations (deformations and displacements) are calculated by Finite Element Methods (FEM). In this so-called "multi-physics" approach, all the physical quantities calculated (deformation of the organs, their densities, dose deposit and nuclear activities for positron emission tomography-PET imaging) are as in FEM assigned to the vertices of the tetrahedrons, which represent the organs geometry obtained from CT scan images(Figure 7.2). In this chapter, We focus on some challenges related to organ motion modeling for radiation therapy, specifically, aspects of lung tumor tracking, 4D dose distribution and 4D PET imaging for treatment verification. This research has been carried out within the scope of the European project, ENVISION (co-funded by the European Commission under the FP7 Collaborative Projects Grant Agreement), ETOILE Research Program, France Hadron, ministry funding and supported by the Laboratory of Excellence (LabEx) PRIMES project.

7.2 Patient-specific biomechanical model of the respiratory system

In the context of the PhD of Matthieu Giroux, we have proposed and developed a new 4D biomechanical and physiological model of the respiratory system, permitting the simulation of a full cycle of respiratory motion, to predict with high precision the lung displacement and deformation. Firstly, we have developed a 3D geometric modeling pipeline to build a 3D model of the respiratory system, issued directly from medical image data and adapted for biomechanical simulation. After automatic and semi-automatic segmentation of different respiratory organs (lung, lung tumor, diaphragm and thorax and all skeletal structure) a 3D surface mesh is created for each volume. Due to the excessive number of nodes and large number of bad quality elements, a Computer Aided Design (CAD) based approach has been developed. The segmented anatomic volumes are rebuilt as a solid using non-uniform rational basis spline (NURBS) surface reconstruction. Then a quality 3D mesh with four-node tetrahedral elements is generated. The organs are considered as isotropic, elastic, and hyperelastic materials. The behavior of the lungs is directly driven by simulated actions of the breathing muscles, *i.e.* the diaphragm and the intercostal muscles (the rib cage). The lung model is monitored and controlled by a personalized lung pressure/volume relationship during a whole respiratory cycle. The lung pressure and diaphragmatic forces are patient-specific and calculated by an optimization framework based on inverse finite element analysis.

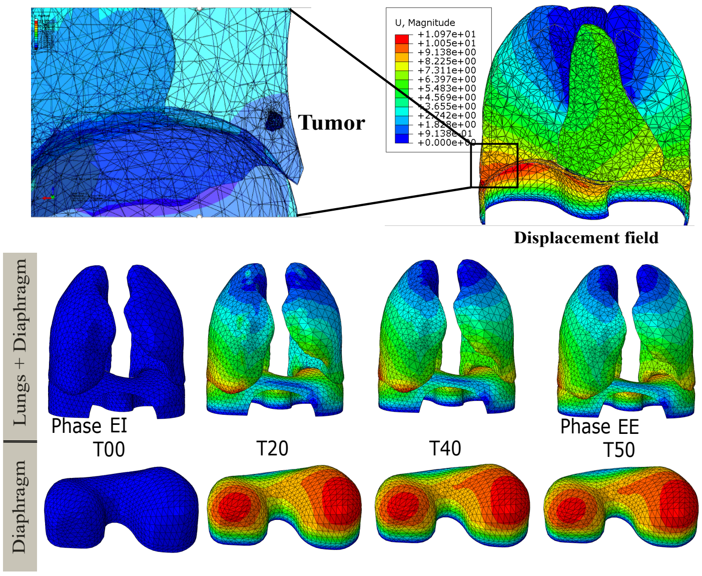

Figure 7.3: Qualitative analysis of patient specific biomechanical simulation; lungs and diaphragm deformations of the respiration between the End Expiration EE (T50) to End Inspiration EI (T90) and intermediate states(T00, T10, T20, T30 and T40

7.2.1 Quantitative and qualitative analysis

In order to demonstrate the validity of our patient specific biomechanical model, quantitative and qualitative analyses of simulations were conducted. We have compared the results of a simulated motion with the experimental data provided directly from the 4D CT scan images DirLab database [262]. We have evaluated the motion estimation accuracy on five selected patients, with small and large breathing amplitudes (Patient 1=10.9 mm, Patient 4=18.1 mm, Patient 6=27.2 mm, Patient 9=15.5 mm and Patient 10=26.06mm). We have also evaluated the lung tumor motion identified in 4D CT scan images and compared it with the trajectory obtained by finite element simulation. The effects of rib kinematics on lung tumor trajectory were investigated.

The Fig.7.3 shows the total deformation and the maximum displacement components of the lungs and diaphragm during breathing. We can observe the maximum displacement of the diaphragm on the right-posterior (RP) and left-posterior (LP) sides. It is also possible to notice a slightly larger (RP) side motion than (LP) side motion, in concordance with the physiological anatomy. For the lungs deformation, the maximum displacement occurs in the posterior region along the superior-inferior (SI) direction (diaphragm direction).

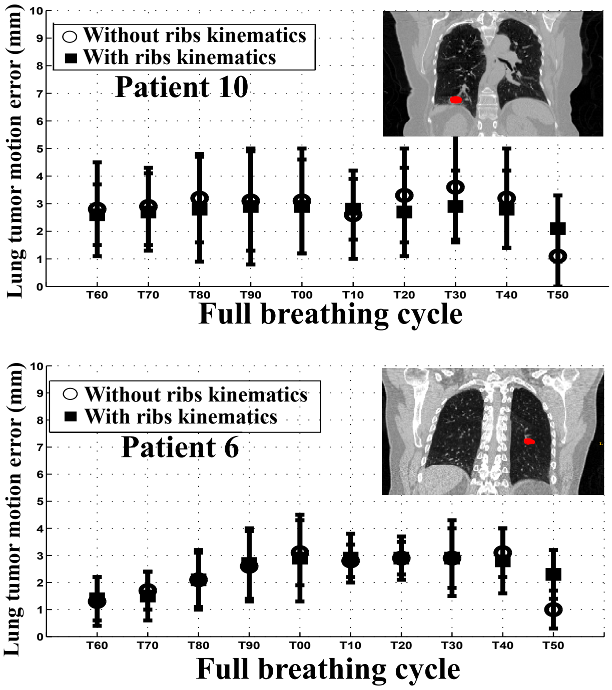

Figure 7.4: Mean errors ± standard deviation of lung tumor position during the whole cycle of breathing (10 phases between the EI and EE) between the trajectory issued from 4D CT images compared to the trajectory calculated by biomechanical finite element simulation coupled with the lung-pressure/diaphragm-force optimization for two patients P6 and P10.

7.2.2 Lung tumor motion

We have compared the finite element simulation results on 300 landmarks, at end inspiration (EI), end expiration (EE) states, and 75 landmarks at each intermediate respiratory state, obtained by manual delineations. The average error for anatomical landmark inside the lung at end inspiration (EI) and end expiration (EE) states as well as the intermediate states, for five patients, is less than $2.5 \pm 1.5mm$ [263].

To evaluate the impact of the rib kinematics on lung tumor motion, we have evaluated also the tumor motion and 3D trajectory identified in 4D CT scan images from the same Dataset DIR-Lab [262], where the tumor location is visible. These trajectories are compared and evaluated with the 3D trajectories obtained by FE simulation, during the whole cycle of breathing (10 phases between the EI and EE). The Fig.7.4 shows the mean errors ± standard deviation of lung tumor position. We have also evaluated the impact of the thoracic respiration on the position of the lung tumor. Thus, in our evaluation we have compared during the whole cycle of the breathing the position-error taking into account the ribs kinematics, generating the thoracic respiration[263, 264]. The figure demonstrates that our patient specific biomechanical model for lung tumor position estimation is very accurate (less than 3 mm).

7.3 4D dose calculation including internal organ motion

The second research area is the estimation of four dimensional dose calculation using deformable tetrahedral geometries. In the context of the PhD of Petru Manescu, the dose distributions are calculated using a time-dependent tetrahedral density map. The internal motion is calculated by patient-specific biomechanical model based on finite element method. Unlike methods based on the conventional voxel-based structures, the deposited energy is accumulated inside each tetrahedron during deformation, thus overcoming the problem of tissue tracking since that the tetrahedron is defined as a part of a tissue whose chemical composition and topology do not change. Thus, in order to obtain a unified model with the process of dose deposition, we replaced the discrete representation of the densities (voxel model) by a continuous approach, as for the finite elements, by placing the densities on the vertices of the tetrahedral meshes. For the internal points, these values are obtained by interpolation. Thus, for each organ, the voxelized attenuation values (CT scanner) are converted into "continuous density" maps and distributed at the vertices of the tetrahedral, respecting the principle of mass conservation. Contrary to voxel-based methods that use image registration algorithms to track individual voxels from one frame to another, our tetrahedral-based method implicitly tracks the tissues as the tetrahedral meshes maintain their topology from one deformation step to another.

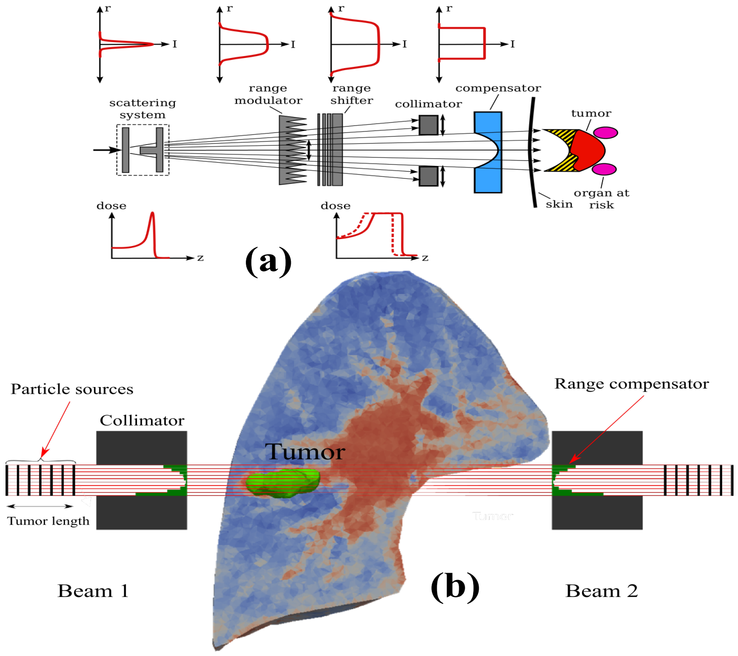

Figure 7.5: (a) Passive scattering technique used in hadron therapy [265]. (b) Treatment planning configuration for lung tumour. Two single-field passive beams were used in opposite directions, each with its own range compensator and collimator

An implementation of the deformable tetrahedral model was done using the Geant4 Monte Carlo code in order to simulate particle-matter interactions and including the deformable tetrahedral geometries together with the passive scattering beam line where the energy of the incident particles is constant (Fig.7.5). We consider our approach to be more accurate, since the deformable image registration methods are based on a series of approximations and interpolations (Fig.7.6). Unfortunately, for Monte Carlo simulations using Geant4, only one density is supported for each tetrahedral element. To overcome these limitations, other density calculation methods have been investigated. We have also studied the impact of the resolution of the tetrahedral mesh on the accuracy of dose distribution[266, 267].

In the context of the PhD of Yazid Touileb, funded by LabEx PRIMES (2014-2018), another problem arose with the relatively excessive number of tetrahedrons. This required considerable time to load the geometries to simulate ion-organ interaction using Monte Carlo simulations. To address this problem, we have defined another dose calculation method that guarantees an accurate dose distribution while reducing the number of elements in the mesh [268, 269]. The new approximation approach takes into account the direction of the beam to minimize the error of the integral of densities, traversed by the beam, converted into water equivalent thickness before the tumor volume. The first results of our simulations are in good agreement with some clinical indicators used in radiotherapy, since the Rigid Body motion and Deformations (RBD) method makes use of a series of approximations. Nevertheless, an experimental validation/comparison within real clinical Treatment Planning System (TPS) is required in order to confirm this statement.

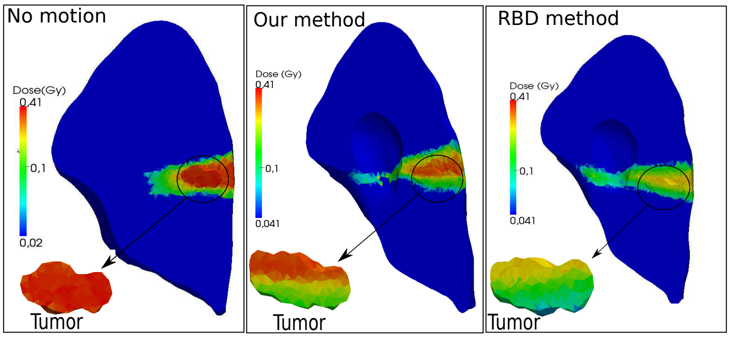

Figure 7.6: 3D tetrahedral dose maps for different scenarios. *Left*: Static simulation. *Center*: Dose distribution taking into account organ motion using the method presented in this study. *Right*: Dose distribution taking into account organ motion using the Rigid Body motion and Deformation RBD method.

7.4 4D PET imaging for treatment verification

In hadron therapy, dose delivery verification is desired to ensure that the treatment was performed as planned. Thus, the objective of treatment verification is to detect and correct the deviations from the treatment plan that compromise the advantages of hadron therapy. To perform such dose verification, the nuclear positron emission tomography (PET) is currently the only method used clinically, a strategy allowing the dose delivery verification [270]. However, the respiratory motion induces displacements and deformation of the organs, which need to be taken into account when reconstructing the spatial radiation activity. As stated before, classical image-based methods that describe motion using Deformable Image Registration (DIR) algorithms cannot fully take into account the non-reproducibility of the respiratory motion nor the tissue volume variations that occur during breathing. In order to overcome these limitations, a new method of correcting motion artifacts in PET image reconstruction based on deformable tetrahedral meshes is proposed. More precisely, the Maximum Likelihood Estimation (MLEM) iterative reconstruction algorithm is adapted to motion estimation models. In contrast with the deformable image registration approaches, the radiation activity was reconstructed on deformable tetrahedral meshes.

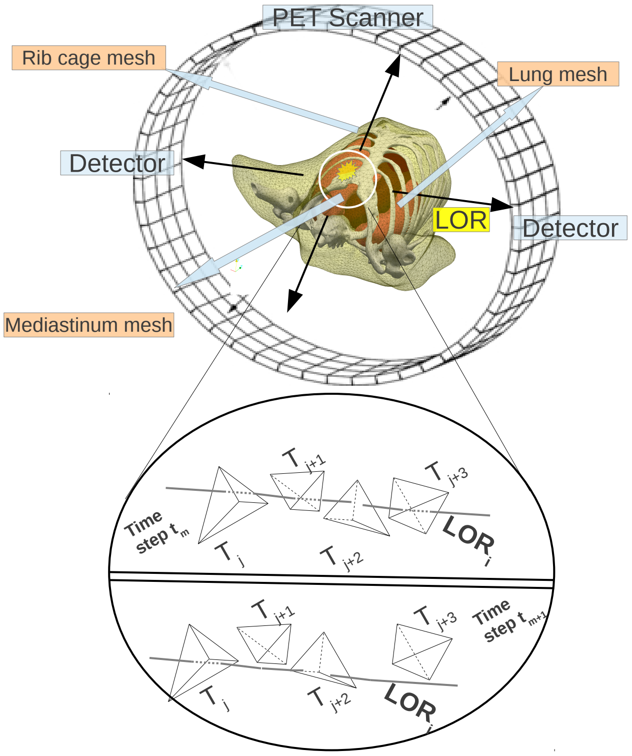

Figure 7.7: Simple time-dependent projection matrix calculation with a deformable tetrahedral geometry using line intersection.

7.4.1 Projection matrix calculation

As opposed to the classical formulation, in the case of a deformable tetrahedral geometry, the projection matrix varies with time, *i.e.* $a_{ik}(t)$ refers to the geometric probability that the source of the coincidence recorded on the LoR i at the time t was inside the tetrahedron T_k. These probabilities are computed by intersecting the grid of tetrahedral with the LoRs during each time step as the tetrahedral elements deform and change their position (Figure 7.7).

7.4.2 Simulation on patient-specific biomechanical lung motion

The deformations were computed using a biomechanical model of the lungs. Five breathing states between End Exhale (EE) and End Inhale (EI) were used. Projection matrices were computed and coincidences were recorded in a list-mode format for each deformation state. Photon attenuation was not taken into account for these simulations. One thousand punctual sources of 1000 Becquerel each were uniformly spread inside the tetrahedral elements of the tumor. Figure 7.9 shows the original CT image of the patient combined with the reconstructed PET images. As a result of the biomechanical motion simulation, the centroid of the tumor is shifted by 1.5 cm in the cranio-caudal direction. This motion severely affects the results of the PET reconstruction. When no motion correction is applied, there is only a Pearson Correlation Coefficient PCC = 75% correlation between the gold standard image and the reconstructed

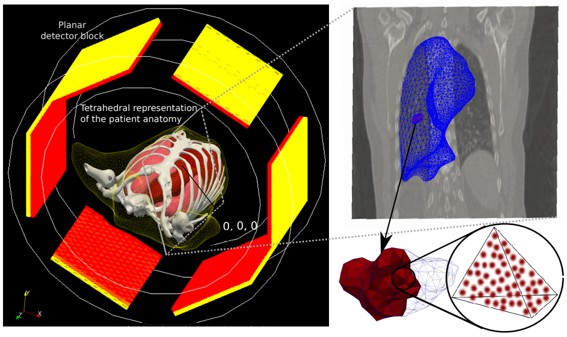

Figure 7.8: Tetrahedral meshes representing the human anatomy placed inside the PET scanner. The radioactivity sources are uniformly spread inside each tetrahedron of the tumor mesh.

one. When motion information is taken into account, there is a good correlation between the reconstructed image and the gold standard with PCC = 92%[271].

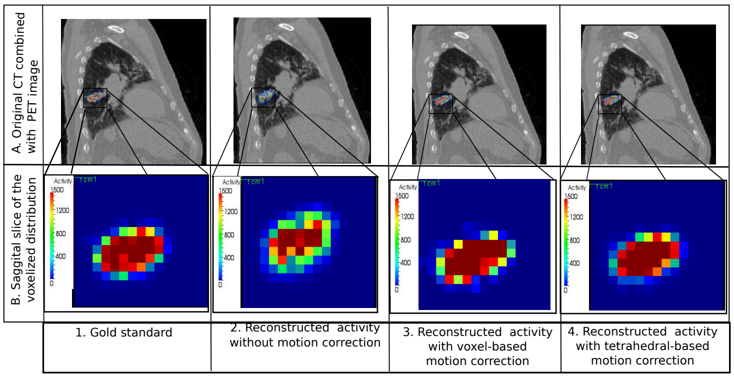

Figure 7.9: Reconstructed activities on patient-specific biomechanical lung motion.

The simulations performed in this study show that the motion compensated reconstruction based on tetrahedral deformable meshes has the capability to correct motion artifacts. Results demonstrate that, in the case of complex deformations, when large volume variations occur, the developed tetrahedral based method is more appropriate than the classical voxel-based one. This method based on patient-specific biomechanical model can correct motion artifacts in PET images and thus reduce the need for additional internal imaging during the acquisition.

7.5 Conclusion

A dynamic research activity has been developed for 15 years around organ motion modeling, gathering 2 laboratories of the LabEx PRIMES (LIRIS and IP2I Lyon). This activity was supported by LabEx PRIMES which allowed us to build an original unified patient-specific approach, based on tetrahedral elements, allowing simultaneous movement quantification of the respiratory system, 4D dose distribution (on-line) and tomographic reconstruction for PET imaging (off-line). In our approach, all the physical quantities: deformation of the organs, their densities, deposited dose and nuclear activities for PET imaging, are assigned to the vertices of the tetrahedrons. We believe that our approach can potentially open interesting perspectives for other imaging techniques.

Bone imaging and associated biomechanical models

8

Coordinator: Françoise Peyrin

Contributor: David Mitton

8.1 Introduction

Bone osteoarticular diseases are increasing in the aged population worldwide. It includes bone fragility disease such as osteoporosis, responsible for fractures and disabilities, and affecting one women over three after the age of fifty years. Osteoarthritis is also a serious public health problem, affecting a large percentage of patients and is expected to increase over the next 10 years, being a major source of pain in aged patients. In the most frequent cancers (*e.g.* breast, lung, prostate), the primary tumor migrates in the bone which is the third most frequent location [272]. These bone metastases which have been poorly studied so far, can induce a risk of fracture.

It is clear that imaging, modeling and biomechanics are playing a major role in research on bone osteoarticular diseases. The LabEx PRIMES has allowed us to gather a multidisciplinary community in these domains, which have been at the heart of many works since 2012. In view of progress in understanding the biological mechanisms but also in diagnosis and treatment, we have conducted works at different levels. We will review results and advances in both more fundamental and patient-oriented research.

8.2 Microscopic imaging and biomechanics of bone

8.2.1 X-ray micro CT

Although osteoporosis is still diagnosed by dual-energy X-ray absorptiometry (DXA), mostly evaluating bone mass, the role of other factors collected under the name of bone quality, including bone micro architecture and bone material properties, has been highlighted since the 1990s [273]. Research on trabecular microarchitecture has been a major driver of the development of X-ray computed tomography (CT)-based techniques like QCT (Quantitative Computed Tomography) and 3D micro-CT [274–277]. These techniques have allowed us to obtain images of the trabecular and cortical bone at spatial resolutions of up to a few micrometers in human and animal models [278–280].

Bone possesses an optimized multiscale hierarchical organization and its biomechanical properties depend on all scales from the microscale to the nanoscale. In the past decade, a new attention has been brought to the osteocytes, the most abundant bone cells, earlier considered to

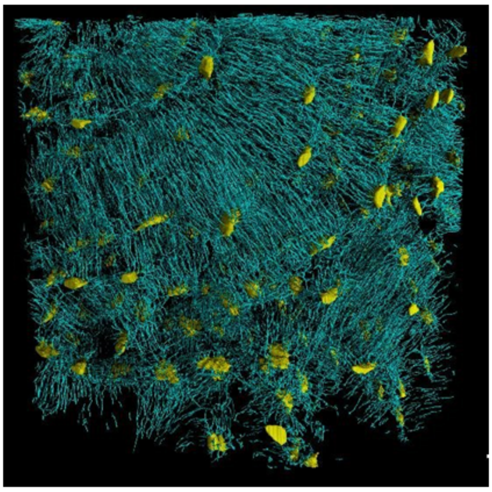

Figure 8.1: Illustration of the 3D lacuno-canalicular network in human femoral cortical bone obtained from phase synchrotron nano-CT imaging (voxel size : 100 nm). The display was obtained after the segmentation of osteocyte lacunae (yellow) and the small canaliculi joining them (green) showing the dense network in an osteon. Scale bar : 40 µm

be passive and rediscovered to be regulators of bone remodeling [281]. They are distributed throughout the bone matrix and interconnected via dendritic processes, and embedded in the so-called LCN. A large part of our research since 2012, has been the development of synchrotron microCT techniques to assess the LCN at the micro or the nano scale, which has been a unique research. Within the activities of the LabEx PRIMES, this work was at the interface of X-ray CT imaging and advanced image processing.

8.2.2 Research on the lacuna-canaliculi network (LCN)

Despite new interest in the osteocyte system, the latter was difficult to assess by using common optical-based microscopy techniques due to its deep inclusion within the mineralized matrix. In a preliminary work, we observed that we could perceive osteocyte lacunae by pushing the spatial resolution of SR micro CT close to the micrometer level [282].

Later on, with spatial resolution at or below the micrometer level, we showed that it was possible to analyze in details bone lacunae from 3D SR micro-CT images. We developed automatic image analysis tools for the segmentation and quantification of osteocyte lacunae and used them to quantify thousands of bone lacunae in human femoral bone [283]. This work had a major impact on our later research during the LabEx PRIMES since it has been applied to many further studies.

Nevertheless, in this work as well as in the literature using X Ray micro-CT, only the osteocytes lacunae were visible and not the canaliculi joining them due to a lack of spatial resolution. By optimizing the 3D SR parallel beam micro CT setup (beamline ID19, ESRF, Grenoble), we could later image the entire LCN including osteocytes lacunae and canaliculi for the first time at a voxel size of at 300 nm [284] (cf Figure 8.1).

We also demonstrated the use of quantitative phase nano-CT at 60 nm [285] to get a better rendering of osteocytes and their junctions (beamline

ID22, ESRF). This later technique is based on propagation phase-contrast imaging involving the acquisition of several scans at different distance acquisitions. The same device was used in the PhD of B Hesse (PhD co-tutored with Univ La Charité, Berlin, Prof K Raum) to study samples from patients suffering from osteonecrosis of the jaw due to bisphosphonate treatment (BRONJ "Bone Related Osteo Necrosis of the Jaw"). We analyzed the osteocyte network architecture at two resolutions (300nm micro-CT and 60nm nano-CT), as well as the mineral variations in the vicinity of lacunae and canaliculi [286, 287]. The work on the LCN was later pursued on a new setup of magnified holographic phase nano-CT system developed at beamline ID16A, at the ESRF (coll P Cloetens). This device exploits a Kirkpatrick-Baez mirror system to reduce the focal spot and reach nanoscale imaging. A phase retrieval algorithm is first applied to the images of the different scans providing a set of phase projections used then to retrieve the 3D phase volumes through tomographic reconstruction. Within the PhD of B Yu, we studied optimal conditions for data acquisition and phase retrieval to recover the LCN with voxels sizes between 120nm down to 30 nm [288].

Such images permit to clearly observe the small canaliculi joining the osteocytes lacunae, nevertheless the 3D binarization of the network remains a challenge. This is due to noise inherent to the image formation problem, dose limitation and the size of canaliculi which can be even smaller than the voxel size. To cope with these problems, we implemented various segmentation methods : a nonlinear filtering associated with a dedicated region growing scheme [289] and an original method based on 3D geodesic path and image tessellation [290]. These methods were later exploited to analyze the properties of LCN in human femoral bone at various resolutions [291, 292].

8.2.3 Research on bone micro cracks

At the tissue level, other important features for understanding the resistance mechanisms of bone are bone microdamage and micro-cracks. These structures are known to be essential in the triggering of bone remodeling but are difficult to assess. Linear microcracks present as very thin gaps in bone, with thicknesses below the µm range, and had mainly ben observed by 2D microscopic techniques. In earlier work, we demonstrated the feasibility of imaging and quantifying them in 3D by SR micro-CT [293, 294].

Within LabEx PRIMES, these methods have been exploited in many collaborative works, in particular to analyze micro-cracks resulting from different modes of mechanical loading [295]. More recently, the goal of the PhD of R Gauthier, in collaboration between the LBMC, the Lyos and CREATIS, was to characterize the toughness of human cortical bone at different sites (femoral shaft, femoral neck, radius) by coupling biomechanical, biochemical measurements and synchrotron imaging. This work led to many results [296–299]. In the postdoc of R Gauthier funded by LabEx PRIMES, we particularly analyzed osteonal and interstitial tissue in human radii cortical bone thanks to the properties of SR micro-CT [298, 299]. These works will be pursued by examining the biomechanical properties of bone tissue in the vicinity of osteocytes lacunae and canaliculi. To this aim, a large collection of LCN from human

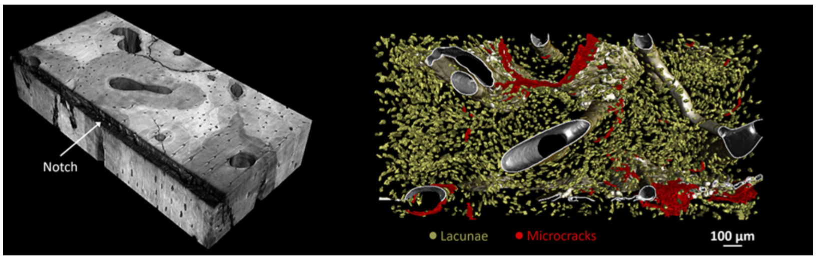

Figure 8.2: Human radius cortical bone sample after a toughness test under quasi-static loading, left : SR micro-CT image (voxel size = 0.7 µm) of the sample, right: 3D rendering after image segmentation showing the Havers/Wolkman network (grey), the osteocyte lacunae (yellow) and the cracks (red). The high toughness of the radius was associated with its capacity to deviate cracks through its complex microarchitecture, as illustrated in the image where the crack follows the cement line

femoral bone samples (n=32) acquired at a voxel size of 100 nm will be further investigated [300].

8.2.4 Research on bone vasculature in oncology

Micro vascularization plays a key role during bone formation but also in the development of cancer tumors. Nevertheless, the structure of microvasculature within bone metastases and its response to treatment is poorly understood. In a collaborative study between the CREATIS, Lyos (UMR 1033, joint research unit between Inserm and UCBL), and Sainbiose labs (Inserm, Ecole des Mines, Saint Etienne), we have studied the vascular system in bone metastases in a mouse model to quantify the efficacy of anti-angiogenic agents used as inhibitors of metastasis development. This work has relied on previous preliminary works in which we had demonstrated the possibility of simultaneously imaging vascularization and bone in pre-clinical rat models [301, 302]. In his PhD, X Hao has proposed new methods to quantify 3D bone vasculature in trabecular and cortical mouse femoral bone. A new segmentation technique, based on a dedicated watershed scheme has been implemented and thoroughly evaluated on simulated and real data [303]. This method has then been exploited to analyze the effect of three treatment protocols in groups of mice (72 samples). It provided unequaled high spatial resolution images and parameters on the bone and vasculature networks simultaneously [304].

8.2.5 Biomechanical models of bone metastases

A doctoral thesis was funded by the LabEx (2016-2019) in collaboration between the LBMC (UMR-T 9406, joint research unit between Univ Eiffel and UCBL) the Lyos (UMR 1033, joint research unit between Inserm and UCBL) and Lyon hospital (Hospices Civils de Lyon) to initiate the validation of the biomechanics models based on QCT images [305]. As a first step, an osteolytic mice model was considered. One group of mice received a subcutaneous injection of tumoral cells. Then, the tumor was resected, characterized by rheology and compared to the mechanical properties of the skin, the fat and the muscles of the same mice. It was

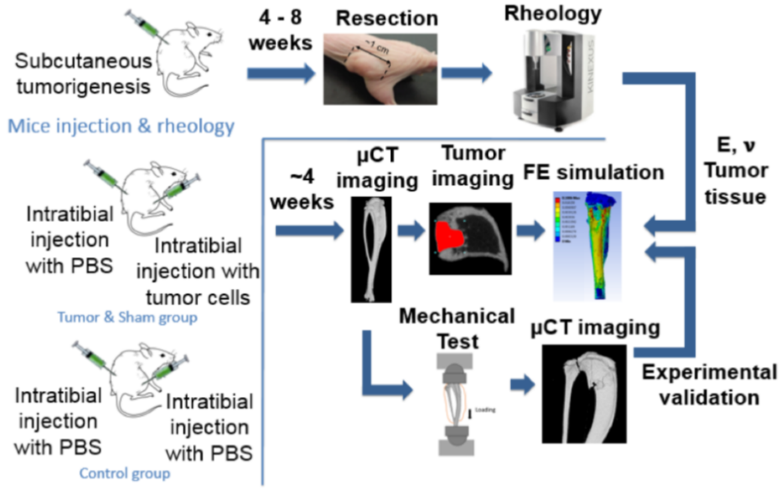

Figure 8.3: Global workflow to assess tumoral properties (upper part) and biomechanics models predicting failure load on a lytic mice model (lower part) from [305].

shown that the multifrequency shear modulus measurements allows to discriminate tumorous from healthy tissues [306]. On other groups of mice, tumoral cells were injected intra-tibially to induce a tumor in the bone. Tomographic (μCT) images were obtained to build subject-specific finite element models. A compression test was performed on each tibia and used to assess the finite element models (Figure 8.3).

8.3 Patient scale imaging and biomechanics of bone

8.3.1 Super resolution in HR-pQCT

While the previous section is related to fundamental studies in bone research, the quantification of bone microarchitecture at the patient scale remains difficult due to the unavoidable compromise between X-ray dose and spatial resolution in X-ray CT. New clinical research devices, named High Resolution peripheral QCT (HR-pQCT), permit to obtain *in vivo* images at peripheric sites (tibia and radius). However, since the spatial resolution of HR-pQCT images is comparable to the mean trabecular thickness, this limits the quantitative analysis of trabecular microarchitecture. In the PhD of A. Toma, funded by LabEx PRIMES, in collaboration between CREATIS and Lab Hubert Curien (CNRS, Saint Etienne), our goal was to improve the quantification of trabecular bone from HR-pQCT images by developing super resolution techniques. The problem was formalized as an ill-posed inverse problem for which we used TV regularization to perform joint super resolution and segmentation. An ADMM based algorithm was implemented and tested on noisy low resolution images obtained by simulation from SR microCT images [307–309]. This work showed that we could recover lost connections between trabeculae and highlighted the improvement in topologic parameters which are particularly biased when the resolution decreases [310].

This work was pursued to move towards real patient data in the PhD of Yufei Li, which poses additional problems, and in particular that of estimating the impulse response of the degradation model. To this aim, several techniques based on optimization methods with specific priors or models were developed [311–313]. We also developed a method based on dictionary-based [313] and carried out preliminary works using deep learning-based methods, yielding to very promising results [314].

Following these pioneer works, the developments based on deep learning applied to HR-pQCT images as part of a collaborative project from Lab Hubert Curien, Sainbiose and CREATIS, thanks to the PhD of Rehan Jhuboo funded by the EUR SLEIGHT. In this work, various state of the art deep learning methods were compared and evaluated to improve the resolution of micro-CT images in mice [315]. Then in order to improve the results, the methods were guided by a new specific bone parameters-based network (work in progress).

8.3.2 Spectral CT for the early diagnosis of osteoarthritis

At the beginning of LabEx PRIMES, the teams in Lyon had been successful to an Equipex project to obtain a state-of-the-art X-ray spectral CT prototype from Philips, unique in Europe, that would be installed at CERMEP Lyon. Compared to standard X-ray CT, this emerging modality has the potential to provide additional information such as the quantitative concentration at a given pixel in several materials (such as bone, soft tissue, contrast agent). Its principle is to acquire energy resolved data thanks to photon-counting detectors. Nevertheless, the processing of such data is more complex than in standard CT and involves non-linearities that require ad'hoc reconstruction methods. This has motivated a number of studies funded by LabEx PRIMES to develop regularize material decomposition methods or one step reconstruction methods.

In the context of osteoarticular diseases, we started one work to study the ability of X-ray spectral (SP-CT) based on photon-counting detectors, to characterize cartilage and meniscus integrity for the early diagnosis of osteoarthritis. This project combined the development of simulation and data processing methods with experimental acquisition of normal and osteoarthritic knees on the SP-CT prototype as well as on SR CT and HR-pQCT. During this work, we showed in particular that the virtual mono-energy images that can also be generated from the spectral CT data were particularly adequate to observe the cartilage simultaneously to bone [316]. The images were compared to SR CT and we could quantity the cartilage thickness [317]. We also developed deep learning methods for material-based spectral decomposition and production of mono energy images [318–320].

8.3.3 Clinical CT for early diagnosis of risk of fracture:

In case of bone metastases, the clinicians need to assess this risk of fracture to choose the best treatment for the patient: either a preventive surgery to avoid the fracture or a chemotherapy or a radiotherapy to treat the cancer. Currently, the clinicians use scores such as the Mirels' score for the femur to assess this fracture risk. However, this score presents a limited sensitivity and specificity [321]. Biomechanical models based on clinical QCT have been proposed at the beginning of the 21st century [322], applied on *ex vivo* human femurs [323] and then on patient data

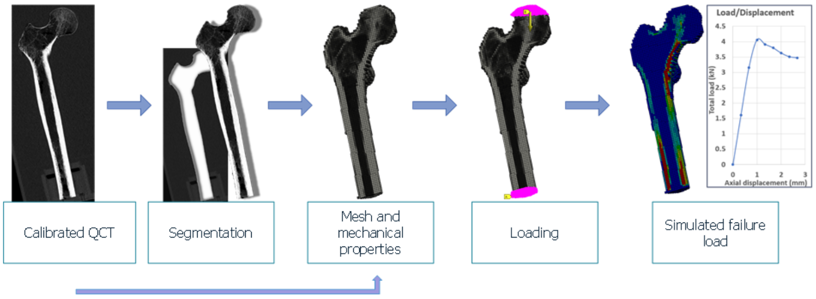

Figure 8.4: Biomechanical model based on Quantitative Computed Tomography (QCT) images to assess femoral failure load

[324]. In 2012, when the LabEx PRIMES was created, very few teams across the world had developed such approach to help clinicians in the assessment of the fracture risk for patients with bone metastases. The validation was limited to few cases, no inter-laboratories studies have been conducted and this approach was at the early stages of the research process.

Our goal in Lyon was to develop tools for the clinicians using our expertise on biomechanical models based on QCT images in the case of osteoporosis. The specific needs were to develop credible models.

Based on the initial work mentioned in paragraph II.5, a doctoral thesis (M Gardegaront) was funded by the LabEx (2020-2023) in collaboration between the LBMC (UMR-T 9406, joint research unit between Univ Eiffel and UCBL), the Lyos (UMR 1033, joint research unit between Inserm and UCBL), CREATIS and Lyon hospital (Hospices Civils de Lyon) to move towards the application of biomechanical models based on QCT images on human femoral bones [325] (Figure 8.4).

Another doctoral thesis (V Allard 2022) was funded by Claude Bernard University to apply this methodology on vertebrae. These researches allowed to improve the credibility of these biomechanical models by a validation on large experimental datasets *ex vivo* considering inter-laboratories studies to assess the reproducibility and the replicability of the models. On the femur, sensitivity studies to evaluate the influence of the operators and those of the input parameters were performed. Key input parameters were identified such as the segmentation. To avoid operator influence, this step is currently automatized (doctoral thesis of E Saillard, collaboration between the Lyos and CREATIS [326]).

8.4 Conclusion and perspectives

The LabEx has allowed to strengthen the research on bone osteoarticular research in the aged propulation. In one hand, it has allowed the Lyon teams to be leaders on research in new X-ray CT imaging modalities including synchrotron micro CT, phase nano CT and spectral CT with applications to bone imaging. We have demonstrated unique results to image the LCN and bone micro cracks joined with biomechanical studies.

In addition, this work has generated various developments in data processing, either for image reconstruction, denoising, image segmentation and quantification. If at the beginning of the LabEx PRIMES, the focus was on compressive sensing methods, the trend has shifted towards deep learning methods receiving increasing interest. Our research on bone super resolution has yield to new collaborations within the Auvergne-Rhones-Alps region (with Lab Hubert Curien, PhD Rehan Julboo, defended Janv 2024.

Concerning applications to biomechanics in cancer, we moved from the initial study on a lytic mice model to the application of the biomechanical models on QCT images from patients with bone metastases. The proof of concept of the clinical application has been done on clinical QCT images collected in a multicentric study in France. The next step will be the application of the methodology in a longitudinal clinical study. A research project at the European level is under discussion to gather the strengths on that topic.

New x-ray imaging modalities | 9

Coordinator: Emmanuel Brun

Contributors: Françoise Peyrin, Simon Rit

9.1 Introduction

The introduction of X-ray tomography (CT) in the 1970s was a major breakthrough as it was the first technique allowing to display sections of the human anatomy non-destructively. X-ray CT has evolved from a 2D to a 3D technique with many improvements in spatial, temporal and contrast resolution and remains the most widely spread medical imaging modality. Its extension to micro and nano-CT now also plays a major role in pre-clinical animal imaging and in microscopic imaging studies. These evolutions have resulted from the combined progresses in X-ray sources and detectors, hardware and reconstruction algorithms. It is expected that medical x-ray imaging will know two major evolutions in the coming years: spectral imaging will be further developed with the advent of photon counting detectors and phase-contrast imaging could be transferred from synchrotrons to clinical applications. The teams of LabEx Primes participated, for the past 10 years, in developing both novel modalities in synchrotrons, laboratory and clinical settings. This chapter aims to summarize the different works performed in this domain.

9.2 Spectral Computed Tomography

9.2.1 Spectral CT reconstruction

X-Ray Spectral CT involves the acquisition of projection data in several energy channels, and thus a specific processing workflow is required to reconstruct spectral CT images. Typically, the object is decomposed in a material basis (like bone, soft tissue and/or contrast agents) or in Compton and photoelectric maps as suggested by Alvarez and Macovski [327]. When including the object model, two approaches have been considered (Figure 9.1): the one-step approach consisting in recovering the object decomposition from the energy-resolved data directly, or the two-step projection-based approach, consisting in first recovering the projected material maps from the energy-resolved data, and then performing the tomographic reconstruction from a standard CT algorithm (like FBP for instance).

Considering the two-step projection-based approach, we first showed that regularized methods led to significantly improved material decomposition on numerical phantom data [329]. This work was pursued in the context of the PhD of Tom Hohweiller, funded by the LabEx (2016-2019). The spectral CT material decomposition problem was formalized as a non-linear inverse problem and solved by minimizing a cost function

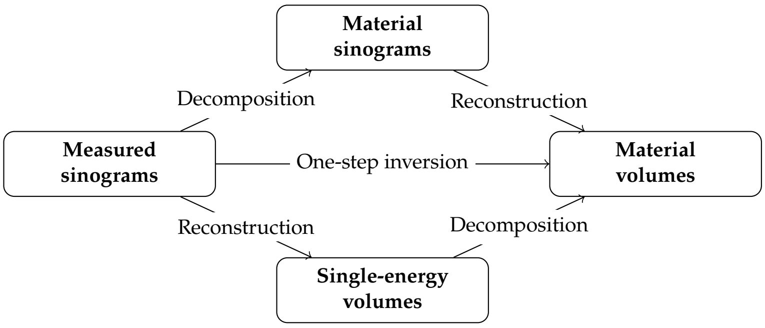

Figure 9.1: The three classes of inversion methods for spectral CT are image-based decomposition (bottom row), projection-based decomposition (top row) and one-step inversion. Figure adapted from [328].

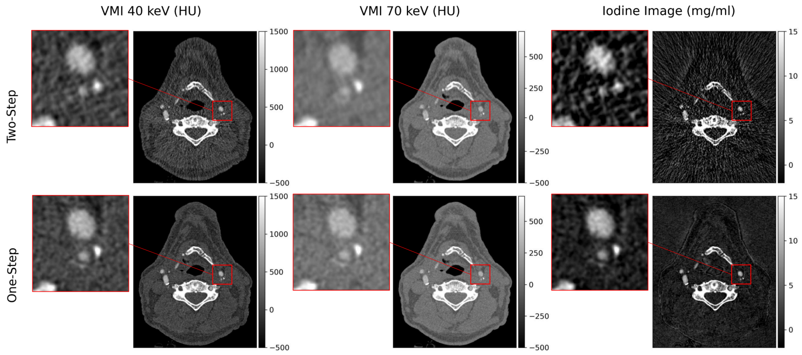

Figure 9.2: Example case of a carotid spectral photon-counting CT angiography in a 68-years-old man using VMIs at 40 keV and 70 keV and iodine images. The one-step spectral images enable a better depiction of a severe carotid stenosis associated with a calcified plaque in comparison to the two-step images (zoomed areas). Figure from [337].

composed of a data fidelity term and a regularisation term embedding a prior knowledge on the projected material maps [330]. First, we implemented a projected Gauss-Newton algorithm that enforces the positivity of the material projections [331]. Second, we implemented a constrained alternating direction method of multipliers (ADMM) enforcing the consistency between the contrast agent projections [332]. We also proposed a method for choosing the hyperparameters in an automated fashion. All the methods were tested on experimental datasets that were acquired by a 5-bin spectral scanner prototype and compared to a state-of-the-art unregularized decomposition algorithm [333].

In parallel, we have also developed a one-step decomposition. Jointly solving the material decomposition and the tomographic reconstruction is far more complex and we first investigated several optimization algorithms for reconstructing two maps for patient tissues and an additional K-edge contrast agent map [334]. The most efficient one used separable quadratic surrogates and was implemented in RTK (Reconstruction ToolKit) [335]. The approach was later improved for uniformizing the convergence in real acquisitions with a helical geometry [336]. The image quality improvement of a one-step approach over a two-step approach was recently demonstrated on several patient images acquired on Lyon's prototype photon counting scanner [337] (Figure 9.2).

9.2.2 Scatter correction in spectral CT

The PhD fellowship of Odran Pivot [338], partly funded by LabEx PRIMES, aimed at correcting for scatter in spectral cone-beam CT images. Scatter is a challenge in single-energy cone-beam CT and the ill-posedness of material decomposition makes it an even more striking issue in spectral CT. This work used a primary modulator mask in front of the source to discriminate primary radiation from scatter assuming a smooth scatter signal. Without scatter, the trace of the mask in the projections can be removed by knowing its impact on each energy bin from calibration measurements. With scatter, the mask is still visible in the projections after correction. Using B-spline basis functions to model the scatter signal, its B-spline parameters can be estimated by minimizing the traces of the mask edges using the gradient at the edge locations. Accurate scatter correction was observed, *e.g.*, on real data of an anthropomorphic phantom acquired on a test bench of the CEA-LETI in Grenoble (Figure 9.3).

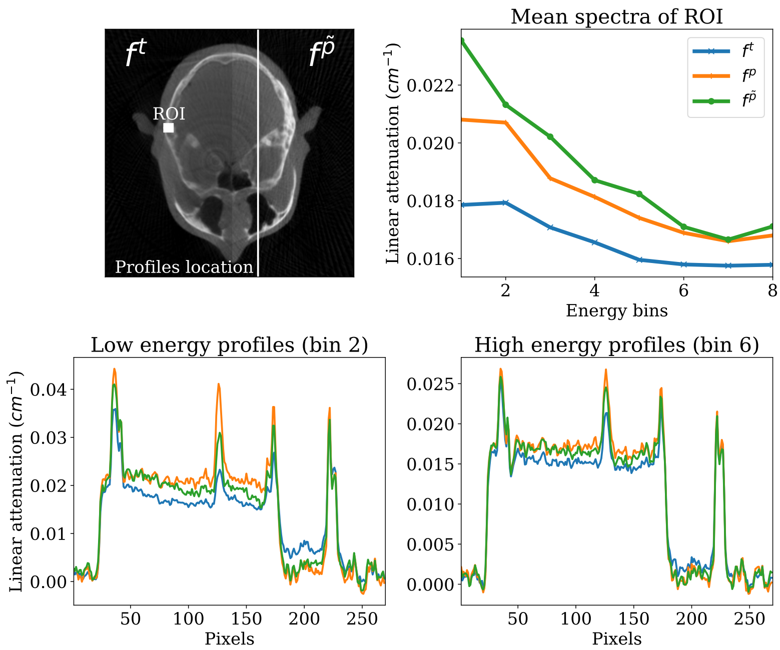

Figure 9.3: Top left: CT slice of the RANDO phantom at bin 41.8 - 52.8 keV of total map on the left against the estimated primary map on the right. Top right: mean spectra of ROI (location on CT slice). Bottom left and bottom right: profiles at bin 41.8 - 52.8 keV and bin 85.8 - 96.8 keV respectively. The color code is the same for all graphs: total map (blue), reference primary map (orange) and estimated primary map (green). Figure from [339].

9.2.3 Spectral CT in the context of knee arthrosis

In the ANR project SALTO (2018-2021), the potential of a X-ray spectral CT device, which was still at the stage of a prototype, was evaluated for the early diagnosis of knee arthrosis. This disease is a serious public health problem affecting a large percentage of the population and is expected to increase over the next 10 years. Conventional imaging methods such as radiography, X-ray CT or MRI have limitations in assessing the integrity of bone and cartilage. Spectral CT should allow to obtain novel quantitative information on the bone and cartilage tissues. SALTO has associated the development of numerical simulation and data processing methods to experimental acquisitions of normal and osteoarthritic knee specimens on state-of-the-art systems (X-ray spectral CT Philips prototype in Lyon, synchrotron CT at ESRF and HR-pQCT, a high-resolution CT system at B3OA, Paris). Regarding data processing, a training knee data basis was generated from monochromatic synchrotron CT images of knee specimen considered as ground truth [340]. We evaluated material decomposition methods based on deep learning neural networks, trained on simulations, and tested both on simulations and experimental data [341]. New numerical methods were proposed for processing spectral data, including material decomposition neural networks for the reconstruction of virtual mono-energy images, as well as denoising methods to improve the quality of the reconstructed images [342–344]. The experimental project allowed us, to evaluate the quality of the images provided by the SP-CT prototype on X-ray spectral CT of the knee specimens showed the interest of using mono-energetic virtual images at some optimal energy for the detection of cartilage [345]. Furthermore, we demonstrated the possibility to extract new information from these images such as the quantification of 3D bone cysts and the 3D cartilage thickness [317].

9.3 Phase Contrast and Dark-Field Imaging

Since the seminal work of Rontgen in 1895, followed by the invention of CT imaging by Hounsfield and Cormack, X-ray imaging is based on the same phenomenon: the attenuation of X-ray photons by matter. Thanks to the advent of third-generation synchrotron sources the wave properties of X-ray could be measured indirectly. Those techniques sensitive to the phase

Over the last three decades, X-ray Phase Contrast and Dark-field Imaging (PCDI) have been proposed to overcome the limitations of conventional absorption-based Imaging: their extremely high sensitivity (up to three orders of magnitude higher than absorption-based imaging) and their capability to obtain high-resolution images for a wide range of application[346] including breast[347, 348], osteoarticular[349–351], brain [352–355] and lung[356] imaging is reported in many studies. Synchrotron Radiation is the gold standard for PCDI because of its high level of beam coherence and photon intensity. However, access to synchrotrons is restricted to a few groups in the world. In-vivo dynamic imaging publications using PCDI are scarce and quasi-exclusively performed at synchrotrons. With limitations, PCDI is also possible using laboratory sources, at the cost of significantly longer acquisition time, which prevents tomographic (3D) application in-vivo at micrometric resolution in 3D.

X-ray Phase Contrast (PC) and Darkfield Imaging (DI) have been demonstrated to outperform conventional 3D imaging modalities based on the sole attenuation [346]. The main aim of PCDI is to decompose the light/matter interactions from a wave perspective. In more details thanks to PCDI technique one can decompose in absorption, refraction (phase contrast) and scattering (or multiple refraction) Figure 9.6 shows an example of decomposition on a fantom.

9.3.1 Physical principles

Unfortunately due to the frequency of X-rays ($\simeq 10^{18} Hz$), the phase aspects of X-rays cannot be sensed directly and undirect techniques have to be used to estimate the phase shifts caused by the samples. Several experimental set-ups

Briefly, Image contrast in PCDI arises from the deviation of X-rays passing through materials with different electron densities [346]. Briefly, these deviations are indicated respectively as a) refracted or b) scattered X-rays depending on the number of traversed interfaces. The so-called "refracted" X-rays deviate within micro- to milli-radians from the original direction; PC refraction images map the distribution of the refraction properties of the sample, defined by the real term of the refraction index. Scattered X-rays deviate instead several dozen or hundreds of milliradians from their original directions; PC images mapping the scattering are indicated as "dark field" images; scattering arises from inhomogeneities in the sample and/or the presence of many interfaces, due to local small porosity (equivalent to, or smaller than the pixel).

9.3.2 Development of micro and nano Phase contrast using free propagation techniques

The phase shift of the incoming X-ray beam induced by an object can be up to three orders of magnitude higher than its attenuation, particularly for soft tissues in the imaging energy range. Phase contrast can be, among other existing techniques, achieved by letting a coherent X-ray beam freely propagate after the sample. In this case, the obtained and recorded signals can be modeled as Fresnel diffraction patterns. The challenge of quantitative phase imaging is to retrieve, from these diffraction patterns, both the attenuation and the phase information of the imaged object, quantities that are non-linearly entangled in the recorded signal.

The PhD of Loriane Weber [357] financed by the LabEx Primes, was focused on the developments and the applications of X-ray phase micro and nano-CT using highly coherent sources such as synchrotron radiation. She mainly worked on iterative tomographic reconstruction techniques on bone material Figure 9.4.

Dr Weber investigated the reconstruction of seeded bone scaffolds using multiple distance phase acquisitions. Phase retrieval is here performed using the mixed approach, based on a linearization of the contrast model, and followed by filtered- back projection. We implemented an automatic version of the phase reconstruction process, to allow for the reconstruction of large sets of samples. The method was applied to bone scaffold data in order to study the influence of different bone cells cultures on bone formation. Then, human bone samples were imaged using phase nano-CT, and the potential of phase nano- imaging to analyze the morphology of the lacuno-canalicular network was shown [358]. We applied existing tools to further characterize the mineralization and the collagen orientation of these samples.

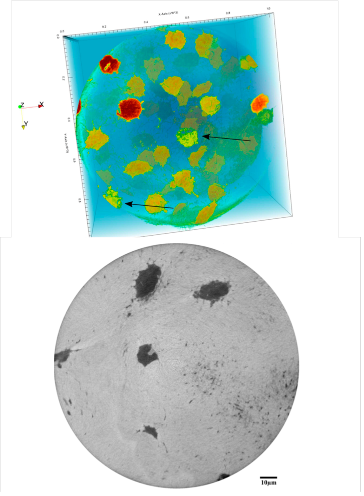

Figure 9.4: Top: 3D rendering of a reconstructed osteoarthritic sample . The black arrows indicate visibly degraded lacunae. The rounded shape of the lacunae is also noticeable. The box is of size 122.88 μm x 122.88 μm x 122.88 μm . Bottom: Reconstructed slice of the osteoarthritic sample. The pixel size is 60nm, and the scale bar represents 10 μm.

Phase retrieval, however, is an ill-posed inverse problem. A general reconstruction method does not exist. Existing methods are either sensitive to low frequency noise, or put stringent requirements on the imaged object. Therefore, Weber *et al.* considered the joint inverse problem of combining both phase retrieval and tomographic reconstruction [359]. They proposed an innovative algorithm for this problem, which combines phase retrieval and tomographic reconstruction into a single iterative regularized loop, where a linear phase contrast model is coupled with an algebraic tomographic reconstruction algorithm. This algorithm is applied to numerical simulated data.

In a later work, we proposed an extended Paganin method suited to multi-distance propagation-based phase contrast CT. The method was compared theoretically and experimentally to the contrast transfer function (CTF) approach for homogeneous objects. The comparison was done in the context of magnified phase nano-CT on the ID16a beamline at the ESRF on bone samples data. Our results showed a gain in image quality in terms of the signal-to-noise ratio and spatial resolution when using four distances instead of one. The extended Paganin's method followed by an iterative refinement step provides the best reconstructions [360]. These images allowed to quantify in 3D the bone lacuna-canalicular network (LCN). This involved the development of specific segmentation and analysis methods to process the large datasets (32-52 GB) [361, 362] (See chapter *Bone Imaging and Associated Biomechanical Models*).

9.3.3 Development of Modulation Based Imaging

Random phase modulation techniques were developed in 2012 [363, 364] at synchrotrons, using the "speckle phenomenon" to create a random intensity pattern which modifications upon introduction of the sample would give its phase information. Beyond its simplicity of implementation, Modulations-Based Imaging (MoBI) is a differential phase technique contrary to free propagation. Moreover, it allows to give access to the Dark-Field signal additionally to the phase and absorption.

Definition: Speckle

In optics, Speckles are random granular patterns that are produced by a very coherent beam when deflected by an element with a rough surface (such as sandpaper).

The experimental set-up of Modulations-Based Imaging (MoBI) is shown in Figure 9.5.

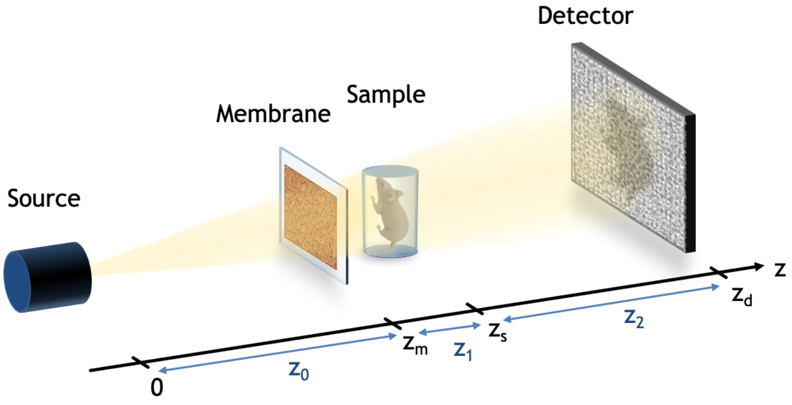

Figure 9.5: Modulations-based imaging set-up. The beam is modulated by a randomly structured membrane before reaching the sample. Then it propagates to the detector distorted by the membrane and the sample. Several images can be acquired with various positions of the membrane.

In MoBI, a structured membrane is introduced after the source (Figure 9.5), which modulates the incoming beam intensity. The distortion of this pattern by refraction and scattering in the imaged object is a PCI modality with the advantage over similar methods that it does not require precise alignment. Further, it can be used with a conventional X-ray setup as well as medical scanners, thus showing substantial promise for clinical use. The experimental complexity of PCI is then transferred to the numerical processing of data. Through the processing of such images, not only the absorption and phase can be retrieved, but also the scattering in two perpendicular directions, known as DFI.

The LabEx Primes played an essential role in the development of MoBI by financing this research with 3 internships, one PhD and experiments at the European Synchrotron Radiation Facility.

9.3.4 Phase Retrieval

Through image analysis method, we can track the modulation distortions caused by the refraction or the scattering of the sample directly in two directions. Phase retrieval is therefore the key process in this technique.

A few algorithms are already available in the literature for tracking the pattern movements between reference and sample images. A first set of methods used an explicit tracking of the modulations by locally comparing, pixel by pixel, the individual displacement of each modulation, using cross-correlation maximization [363–365] or functional minimization [366]. These algorithms are not limited by any specific hypothesis and can be applied to a broad range of samples but are computationally expensive. The second kind of algorithms employs, in contrast, an implicit tracking where the method does not seek the modulations displacement locally but rather assumes total photon flux conservation[367–372]. These methods were developed in part thanks to the LabEx Primes. The starting point of these algorithms is the transport of intensity equation (TIE) that can be used in the Fresnel regime to describe the evolution of intensity due to the insertion of a non-absorbing sample into the beam. This equation can be written as:

$$I_r(x,y) - I_s(x,y) \approx \nabla_\perp \cdot [I_r(x,y) D_\perp(x,y)]. \tag{9.1}$$

The last major contribution to the domain was published by Magnin *et al.* [373] and allows to retrieve the absorption, the refraction and the scattering images on a conventional X-ray source. The

$$\begin{aligned} I_r^{(k)}(x,y) = {} & \frac{1}{I_{obj}(x,y)} I_s^{(k)}(x,y) + D_x(x,y) \frac{\partial I_r^{(k)}(x,y)}{\partial x} \\ & + D_y(x,y) \frac{\partial I_r^{(k)}(x,y)}{\partial y} - z_2 D_f(x,y) \nabla_\perp^2 [I_r^{(k)}(x,y)], \end{aligned} \tag{9.2}$$

Where, $D_\perp = (D_x, D_y)$ is the transverse displacement field and $\nabla_\perp = \partial/\partial x + \partial/\partial y$ is the two dimensional transverse gradient operator. I_{obj} is a sink term introduced to compensate for attenuation that might comprise also the interference fringes, if any. z_2 is the sample-to-detector distance. In order to retrieve the absorption, phase and dark-field signal, we must solve a system with at least 4 membrane positions due to the 4 unknowns (I_{obj}, D_x, D_y, D_f). k is the index of the couple acquisition:

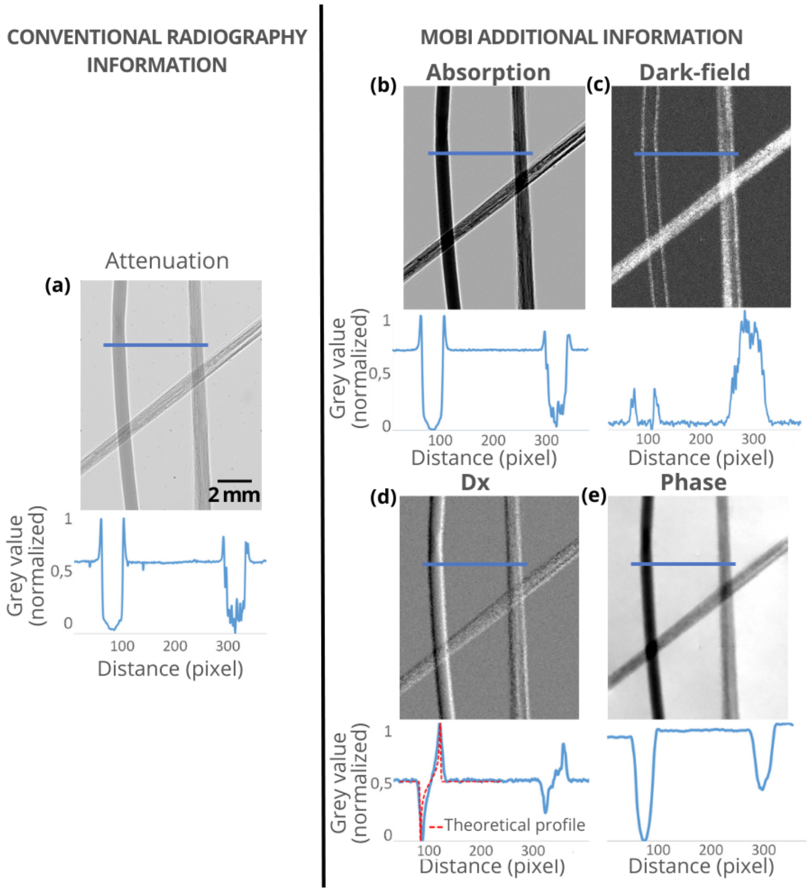

Figure 9.6: Attenuation (a), dark-field (b), dx (c) and phase (d) images of a nylon wire (left) and two bundles of carbon fibers with different orientations. The images are retrieved using the Low Coherence System [373] and 10 pairs of reference and sample images at a sample-detector distance of 3200 mm. Their respective profiles along the blue line are given below each image.

9.3.5 Transfer on laboratory set-ups

On conventional systems, because the speckle phenomenon is difficult to obtain, we fabricate our own membranes with a high Z atomic element (3D printed or using powders) to produce a random intensity modulation. In order to obtain patterns with regular size modulations and high-intensity variations, new membranes were created. This process was patented during Helene Rougé-Labriet PhD thesis [374]. These membranes have different absorption indices and grain sizes. To obtain these membranes, a thin layer of powder is deposited on a self-adhesive surface, which is glued to a thin PMMA plate. Different materials were used and tested (Copper, Iron, TiC) with different granulometries (from 9 to 300 μm).

More recently, in Laurene Quenot PhD & Clara Magnin PhDs, we looked for the optimal geometry of the membrane. In [375] and in a publication to come we indeed compared different geometry such as mesh, honeycomb, spiral and random. The main results of this study is that random geometries we used in the past with sandpaper is not optimal while a quasi-periodic structure was.

Figure 9.6 shows the result extracted from [373]. These images were obtained on a X-ray set-up manufactured by Xenocs (Grenoble, France) with a low coherence source (X-ray focal spot of 50 μm).

9.4 Towards Spectral Multimodal X-ray Imaging

In 2021, the LabEx Primes funded Chris Ninham PhD. The goal of this PhD fellowship is to investigate phase-contrast retrieval from spectral x-ray images with MoBI. Conventional spectral x-ray imaging only considers the attenuation and accounting for the phase requires to model the complex refraction index. Currently, phase contrast images are retrieved by solving a non-linear inverse problem under the assumption that the ratio between the attenuation and the phase is constant or by using several x-ray images acquired at different distances or with different optical configurations. Both the attenuation and the phase depend on the x-ray energy and this PhD assumes that x-ray spectral imaging would provide several measures with a single irradiation to retrieve the phase.

So far we could model the inverse problem and identify adequate acquisition parameters (size and voltage of the x-ray source, speckle pattern, spectral and spatial resolution of the detector, etc.) and perform proof of concepts experiments. More details will be described soon in scientific articles in preparation.

Spectral imaging across modalities

10

Coordinator: Hélène Ratiney

Contributors: Salim Si-Mohamed, Bruno Montcel, Cedric Ray, Nicolas Ducros, François Varray, Pauline Muleki-Seya

10.1 Introduction

Whether it be X-ray imaging, optical imaging, or magnetic resonance or ultrasound imaging, all techniques used in medical imaging result from an interaction between waves and matter. They distinguish themselves from one another by the type (electromagnetic or acoustic) and frequency domain of the waves employed. The exciting wave is characterized by one or more frequencies, and the resulting wave from the material's response to this excitation is itself characterized by a frequency content. This frequency-based decomposition may seem immaterial; indeed, it is rarely naturally available and generally accessible only through a dedicated technique that requires excitation and reception at multiple frequencies. Spectral imaging refers to a technique in various imaging modalities, including X-rays, MRI (Magnetic Resonance Imaging), optics, etc., where not only the spatial distribution of a tissue's response to an excitation is captured but also the characterization of its frequency content at each point in space. In the context of different imaging technologies, this term takes on specific names such as "spectral imaging" for X-rays, "spectroscopic imaging" for MRI, and "hyperspectral imaging" for optical imaging. The goal is to provide a comprehensive understanding of the material or biological sample being imaged by considering its spectral characteristics, allowing for improved analysis and diagnostic capabilities. Living matter is complex, composed of numerous molecules, various contents and multiple compartments. This chapter describes the various research efforts conducted within the labEx PRIMES framework and for the main imaging modalities, illustrating methods for acquiring the spectral dimension and the valuable information it offers. This exploration aims to achieve a more comprehensive description of the complexity of living tissues, thereby providing specific insights to enhance medical diagnostics.

10.2 X-Ray Spectral Imaging

Spectral computed tomography (CT) imaging covers a unique generation of CT systems based on a simple principle that makes use of energy-dependent information. Over the past two decades this principle has been expanded with the introduction of dual-energy CT systems. The first generation of spectral CT devices opened up a new imaging approach in the radiology community with their ability to overcome the limitations of tissue characterization encountered with conventional CT. But recently this technology gives way to a ground-breaking photon-counting CT technology based on a new chain of detection which holds great promise for extending CT towards multi-energy CTimaging

Principles

Spectral Photon Counting Computed Tomography (SPCCT) is a new, emerging technology in the field of spectral imaging [376]. It makes use of energy-resolving detectors, called photon-counting detectors (PCDs), recently integrated into clinical CT platform[377]. PCDs are made of semi-conductive material which makes it possible to convert incoming photons directly into electrical charges which migrate into a counting (application-specific integrated circuit, ASIC). The ASIC shapes a voltage pulse proportional to the incoming photon energy, and each photon can be differentiated in amplitude according to its energy. The transmitted spectrum can thus be characterized into multiple energy bins as defined by their different energy levels. In comparison to dual-energy CT abilities, SPCCT has the potential to provide more complete, accurate sampling of the energy dependence found in the CT images. The second benefit will be that additional materials can be added to the spectral decomposition of the images based on their K-edge energies, *i.e.*, the binding energy between the K-shell and the nucleus. This can be understood as a third unknown factor added to the equation by Alvarez and Macovsky [327]

$$\mu(E) = \alpha_P f_P(E) + \alpha_C f_C(E) + \alpha_{\text{material}} f_{\text{material}}(E)$$

where α_P is the mass coefficient of photoelectric attenuation of the material, $f_P = 1/E^3$ with E the photon energy, α_C is the Compton mass attenuation coefficient of the material , f_C is the Klein-Nishina function, $f_{\text{material}}(E)$ is a mathematical function that characterizes the photoelectric effect of the K-edge material, and α_{material} is the photoelectric absorption coefficient of the material.

This approach, referred to as K-edge imaging, is a real breakthrough in CT post-processing and comes with the promise of being available in the next generation of clinical SPCCT systems. It mainly promises to overcome the limitations of dual-energy CT technology, which cannot specifically or quantitatively separate different materials in the same voxel (or spatially co-registered), such as iodine and calcium.

Current Clinical Applications

SPCCT technology is known to have several benefits over current CT systems that are equipped with energy-integrating detectors (EID-CT). It increases spatial resolution by a factor of 4 with an achievable voxel size of 0.15 to 0.25 mm^3 for all applications, including lung, ear, musculoskeletal, peritoneal, coronary artery, and vessel imaging cite[378, 379]. It decreases the radiation dose by 30-50% while providing a similar noise level to that of EID-CT images by suppressing electronic noise [378, 380–382]. It enhances tissue contrast for a similar energy beam to that of EID-CT images due to the constant weighting of photons, leading to greater weighting of the low-energy photons carrying the photoelectric effect, whereas EID-CT technology uses linear weighting [378]. SPCCT also decreases beam-hardening-like artifacts and blooming artifacts due to higher spatial resolution, despite an increase in CT attenuation of all high-contrast tasks [378, 383]. It enables better energy sampling of the transmitted spectrum than dual-energy CT technology, *i.e.*, more than 2 energies, which enables a greater energy separation between high and low energy photons [384]. As a result, SPCCT may improve the performances of any type of virtual images, such as virtual monochromatic, virtual non-contrast, Z-effective, electronic density, as well as any type of material decomposition process like that of water or iodine imaging [384, 385]. Altogether, these advantages hold great promise for changing the current workflow of CT (Figure 10.1). More importantly, physicians should understand that SPCCT offers all these advantages in just one scan without increasing the dose, changing the technical parameters, or requiring spectral mode prospectively. This key feature should provide great leverage to help spread the use of SPCCT technology.

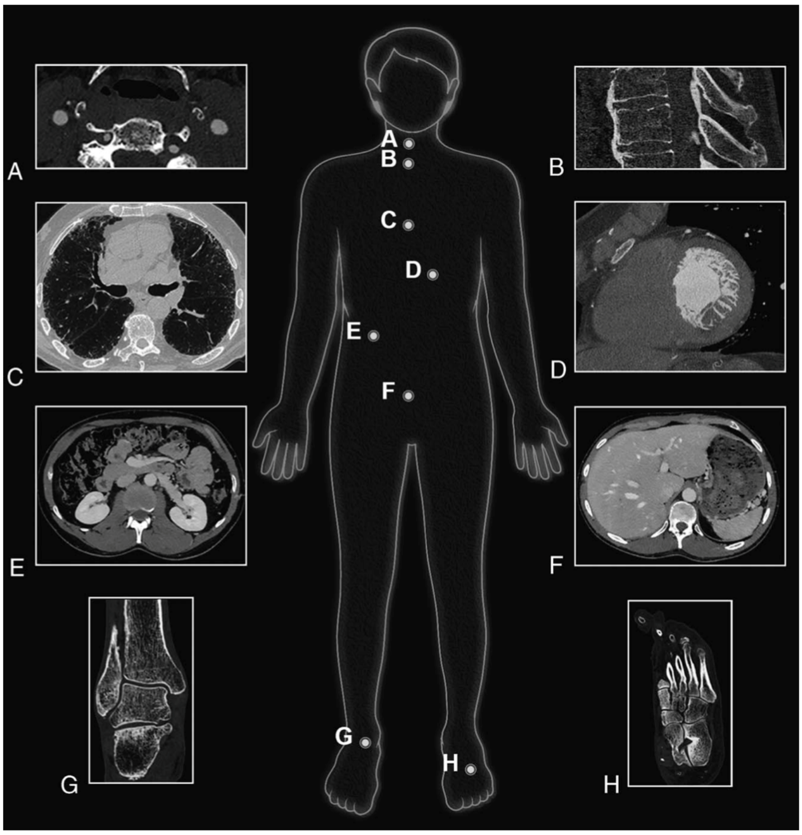

Figure 10.1: Illustration of clinical experience with numerous clinical applications using a whole-body clinical spectral photon-counting CT prototype (Philips Healthcare) on a research platform at the University of Lyon.

Future Color K-edge Clinical Applications

The advantages mentioned above, while illustrating some basic but important advantages of SPCCT over conventional CT imaging, still do not emphasize the most groundbreaking contribution of SPCCT: Color K-edge imaging. Color K-edge imaging places the energy bin boundaries in close proximity to the K-edge energies of elements, defined as the binding energy between the inner electronic layer and the atom. This means that the contrast agent can be identified specifically and quantitatively, allowing concomitant specific imaging of K-edge contrast agents like gold and gadolinium and their differentiation from surrounding tissue and non-K-edge contrast agents such as iodine-based agents [377, 386, 387]. These images will then be offered to radiologists together with the conventional HU-image. K-edge imaging is comparable with the nuclear imaging twin modality of PET-CT where low-resolution functional information on FDG uptake is superimposed on high-resolution anatomical information, opening a completely new CT approach for functional, molecular, or inflammation imaging and many other areas requiring exploration. This new approach may be an advantage for new exploration such as for performing a biphasic organ CT imaging by providing simultaneously a specific enhancement after a consecutive injection of iodine and gadolinium-based contrast agents[388], or for performing a molecular CT imaging by monitoring the macrophage burden within the high-risk atherosclerotic plaques [387]. Despite the multiple pre-clinical studies taking advantage of Color K-edge imaging, translation in humans still has to be developed.

The introduction of spectral photon-counting CT in the clinical field has opened a new chapter for medical imaging. The incremental expectations in term of improved image quality are already being demonstrated for many applications including those most in need of better spatial resolution and contrast, as well as reduced radiation dose. Altogether, SPCCT is expected to provide significant benefits for disease diagnosis, characterization and staging, and also to open to ground breaking approaches that were not previously available in the field of CT.

10.3 Spectral imaging in the visible range

The impact of medical imaging is important for the early diagnostic and for the intervention guidance on pathologies. Medical imaging clinical standards (‘glsmri, nuclear medicine, CT. . .) face limitations in the operative room, due to technical, cost and regulatory constraints. In recent decades, the paradigm of therapeutic interventions has evolved significantly, moving from a linear approach (Decision-Action-Control) to a continuous process of decision optimization based on the steady acquisition and processing of multimodal information. The goal of intraoperative imaging is to provide operating room actors with integrated models for medical decision support that can be optimized in real-time to prevent any obstruction in the course of the surgery. Decision-making thus becomes a permanent feature at the center of the care process, before, during, and after the therapeutic intervention. Ultrasound and optical medical devices are relevant in this intraoperative context because they are easy to handle, reliable, generally low-cost, and allow high acquisition rate. Optics also have the huge advantage of being a non-contact imaging modality and to be close to the current practice in neurosurgery (surgical microscopes is a clinical standard in surgery). However, the diffusion of intraoperative optical devices is still limited because of a lack of reliable intraoperative biomarkers. This impairs their clinical relevance and their ability to correlate with gold-standard pre-operative imaging (MRI, CT. . .), which is mandatory to propose robust integrated models for real-time medical decision support. Gliomas are the most frequent tumors of the central nervous system. They are infiltrative tumors with a

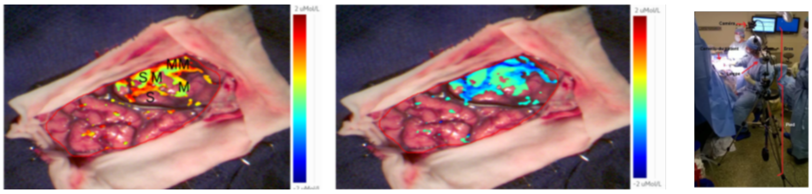

Figure 10.2: Identification of the position of the motor cortex during neurosurgery with optical video. The letters M indicate motor areas and S indicate sensitivity areas (determined with gold standard electrical stimulation). The added false color scale indicates a proposed biomarker after appropriate thresholding and linked to oxy- and deoxy-hemoglobin parameters.

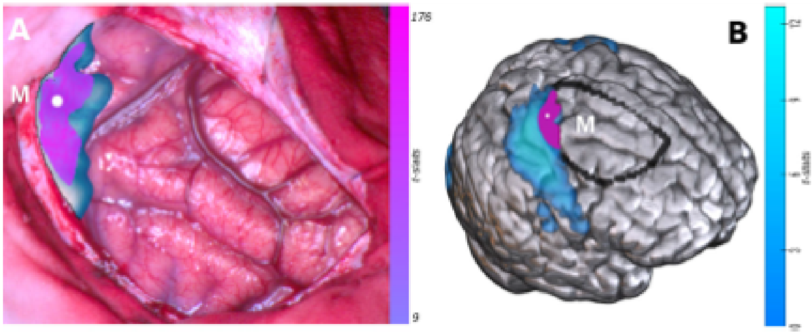

Figure 10.3: Intraoperative optical functional brain maps (purple color scale) superposed to fMRI preoperative functional brain maps (blue color scale). A: In the space of the surgical window, superimposed on the RGB image. A: In the MRI generated 3D head contour. The black contour represents the extent of the surgical window. The letter M indicates the motor cortex area identified by EBS.

solid tumor compound and an infiltrative compound that is very difficult to identify. Their treatment is mainly based on resection as complete as possible. During surgery, the decision to continue or stop resection is a tradeoff between the resection of a maximum of tumor cells and the preservation of functional areas. The gold standard is still the anatomopathological analysis where a biopsy is removed from the brain to identify the tissue nature (tumor / healthy). This procedure takes some time and it is relevant for the surgical procedure to obtain faster information on the biopsy. The intraoperative identification of brain functional areas is tackled by considering the neurovascular coupling which induces variations of local tissue perfusion and oximetry when brain cortical areas are activated. The intraoperative identification of functional brain areas is critical during intracerebral surgical procedures, in order to avoid any postoperative patient deficits. Current clinical standards combine preoperative fMRI and intraoperative electrical brain stimulation (EBS). Hyperspectral optical imaging is used to measure the brain hemodynamics triggered by physiological *stimuli*. Within the labEx PRIMES [389] a fast real-time algorithm was developed and applied, yielding motion-corrected RGB videos of brain during neurosurgery. We proposed a quantification model [390] taking into account the brain heterogeneity in the physical model of biomarkers then produced quantitative maps of functionality biomarkers, see Figure 10.2. We also showed during these works [391] the spatial and temporal correlation of this optical contrast with current clinical standards which combine preoperative fMRI and intraoperative electrical brain stimulation, see Figure 10.3. Concerning tumor localization, the gold standard is still an anatomopathological procedure and is thus time-consuming. An alternative approach could be intraoperative 5-aminolevulinic acid (abbreviated as 5-ALA) Protoporphyrin IX (PpIX) fluorescence imaging but as carried out now, it still lacks sensitivity. The works of Laure Alston showed that *in vitro*, *ex vivo* and *in vivo* studies strongly hints that there exists two close emission spectra of PpIX that are relevant; one peaking at 620 nm and the other at 634 nm [392]. We developed an intraoperative prototype validated by the ANSM and led a clinical trial (NCT02473380) on 10 patients result-

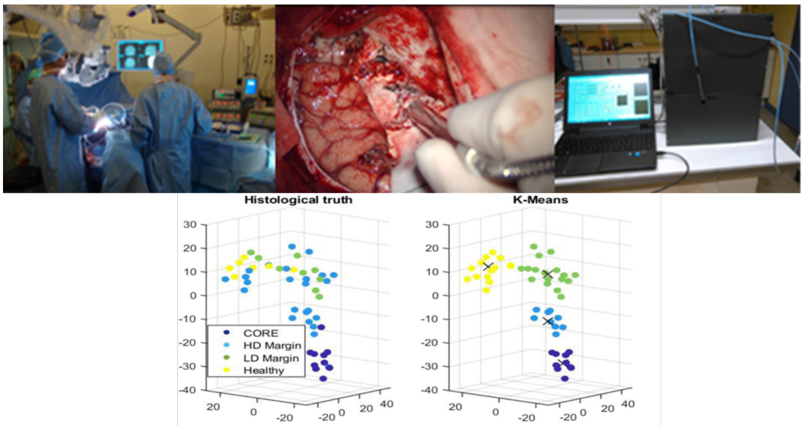

Figure 10.4: Intraoperative system developed and used in a clinical study on 10 patients; Data analysis of the results with unsupervised classification in a t-distributed stochastic neighbor embedding (T-SNE) reduced space. K-means classification with 4 clusters.

ing in the definition of new biomarkers of PpIX fluorescence emission. These results [393], also explored using machine learning approaches [394] suggest that these biomarkers could increase the sensitivity of the 5-ALA induced PpIX fluorescence technique in low-density margins and improve the definition of the boundary between tumor margin and healthy tissues in high and low-grade gliomas, see Figure 10.4. During Arthur Gautheron PhD works funded by the labEx PRIMES, it was also showed that sophisticated fluorescence excitation scheme and *a priori*-free unmixing method can increase the specificity of this method to glioma lesion boundary [395].

10.4 Light sheet fluorescence microscopy

Selective Plane Illumination Microscopy (SPIM) enables rapid three-dimensional (3D) imaging of fluorescent samples across spatial coordinates (x, y, z), significantly reducing photobleaching effects. SPIM captures two-dimensional (2D) slices (x, y) by illuminating the sample with a thin light sheet, while the third dimension z is systematically scanned [396]. The openSPIM initiative has further popularized SPIM by introducing a variety of design modifications, expanding its applicability [397, 398]. Consequently, SPIM has been employed in diverse studies, ranging from the embryonic development of flies and zebrafish to the intricate structures of rat brains and mouse cochleae [399], becoming a cornerstone technique in real-time developmental biology [400].

SPIM harnesses the fluorescence emitted by labeled structures within a specimen. When examining specimens with multiple labels, it becomes crucial to differentiate between the fluorophores. This differentiation often relies on optical filters selected to capture emission spectra at their peak. While filter-based methods are straightforward and effective, they have limitations; for instance, they cannot distinguish between fluorophores with overlapping spectra, resulting in the loss of light outside their pass band [401]. Few techniques have been developed to capture the complete fluorescence spectrum of a sample, or the 4D (x, y, z, λ) hypercube, which could significantly enhance light collection and fluorophore unmixing capabilities.

The pioneering hyperspectral SPIM technique utilized a pair of mirror galvanometers to project an illuminated line onto a spectrometer's

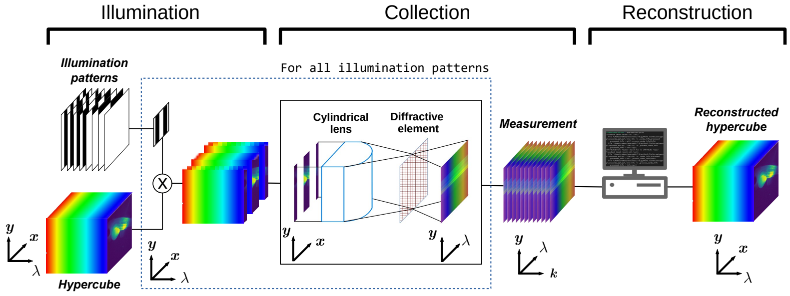

Figure 10.5: Overview of the proposed computational hyperspectral light-sheet microscope. We consider the acquisition of the hyperspectral section $f(x, y, \lambda)$. We use multiple illumination patterns $\{p_k\}_{1\leq k\leq K}$ that are modulated along the x-axis. The fluorescence light emitted by the sample is focused onto the slit of a spectrometer, to provide the raw measurements $\{m_k^\ell(y, \lambda)\}_{1\leq k\leq K}$. Then, the hyperspectral section can be reconstructed numerically from the raw measurements.

entrance slit [402]. Sebastien Crombez's doctoral research (2019-2022) introduces an innovative approach to computational hyperspectral light-sheet microscopy. This method channels the fluorescence signal from the light sheet through a cylindrical lens directly into the spectrometer's slit, leveraging the full spectral resolution of the spectrometer without the need for moving parts, unlike the approach in [402]. By employing a series of spatially encoded light sheets, we can formulate an image reconstruction problem to access the spatial dimension orthogonal to the slit. This concept is encapsulated in Figure 10.5 and has been detailed in [403, 404].

In traditional light-sheet microscopy, the light sheet is uniformly distributed across the (x, y)-plane. Our approach, however, utilizes multiple illumination patterns $\{p_k\}_{1\leq k\leq K}$ modulated along the x-axis. Each pattern, when projected onto the sample, results in raw measurements $\{m_k(y, \lambda)\}_{1\leq k\leq K}$ that are modeled by the equation:

$$m_k(y, \lambda) = \int p_k(x) f(x, y, \lambda)\, dx. \tag{10.1}$$

Here, f denotes the fluorescence hypercube of the imaged slice.

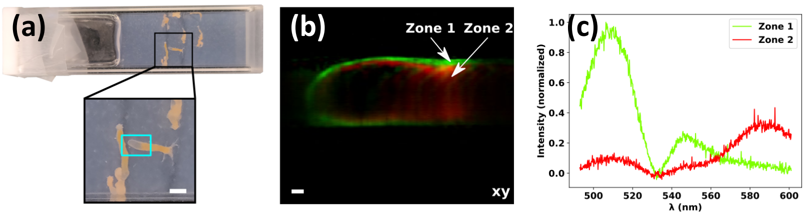

Figure 10.6: Hyperspectral imaging of a two-color hydra specimen labeled with Superfolder Green Fluorescent Protein - GFP ($\lambda^{\text{ex}} = 485$ nm, $\lambda^{\text{em}} = 510$ nm) and DsRed2 ($\lambda^{\text{ex}} = 561$ nm, $\lambda^{\text{em}} = 587$ nm). **(a)** Image of the sample. We show the tail of the hydra that was studied in the cyan box. Scale bar 1 mm. **(b)** Hyperspectral SPIM (green channel range: $[493, 527]$ nm; red channel range: $[576, 601]$ nm). Scale bar, 100 µm. **(c)** Spectra of one element of the shell of the hydra (zone 1) and of one element of the inside of the hydra (zone 2).

Subsequently, we reconstruct the hyperspectral slice from these raw measurements. Assuming the availability of experimental measurements for the light patterns, our reconstruction algorithm can successfully retrieve the encoded spatial dimension. We validated our methodology on a hydra specimen labeled with two distinct fluorophores. The complete spectrum captured at each pixel slice enables the clear differentiation of structures labeled with the two fluorophores, as illustrated in Figure 10.6. The primary constraint of this method is the limited spatial resolution along one axis.

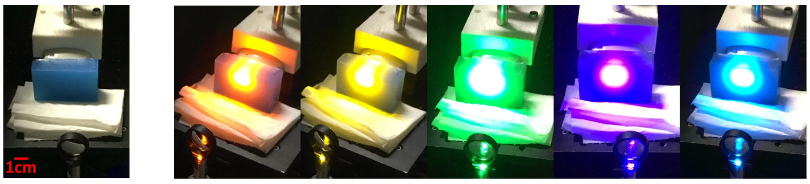

Figure 10.7: Illustration of the multispectral photoacoustic imaging developed on the PILoT platform [409].

10.5 Multi-spectral photoacoustic imaging

The photoacoustic (PA) effect was discovered in 1880 by Alexander Graham Bell, who demonstrated the production of audible sounds by periodically illuminating an object with sunlight [405]. Then, the constant progress that accompanied the development of the laser made it possible to use it as a stable pulsed excitation light source. The first application of the PA effect was the detection of traces of gas in 1971 [406], rapidly followed by establishing a theoretical basis for using the PA effect in solids in 1976 [407]. In the 1990s, the use of the PA effect in diffuse media opened the door to medical applications, and the uses of PA imaging multiplied. Today, the PA effect is used in medical imaging from microscopic (~µm) to macroscopic (~mm) scale. The photoacoustic (PA) effect (also known as the optoacoustic or thermoacoustic effect) corresponds to the production of acoustic waves by an object periodically illuminated by a light wave. The acoustic signals received at the surface of the object or biological tissues by an ultrasound (US) probe are then used to construct what is known as a photoacoustic image of the object. A pulsed optical excitation is required to illuminate the investigated medium to create this effect. Indeed, the optical energy is locally absorbed by the optical absorbers and converted into heat by the photo-thermal effect, which leads to an instantaneous thermoelastic expansion. This sudden and periodic increase in the absorbers causes an acoustic wave. However, the PA effect requires a short-pulsed laser excitation source (<100 ns) so that the expansion/refraction phenomenon can occur. Similarly, the optical energy must be sufficient to create a detectable acoustic signal and can range, depending on the application, from 0.1 mJ/pulse to 100 mJ/pulse while complying with maximum permissible skin exposure safety standards.

Multi-spectral photoacoustic imaging involves exciting the medium with different wavelengths. Biological tissues have an optical absorption that depends on the wavelength of the light excitation [408]. Different photoacoustic images of the same medium can then be used to differentiate between different tissues. Certain major components of living tissue exhibit significant optical absorption in the visible and near-infrared (IR) range, making them the main absorbers of biological tissue. Of the main constituents of biological tissue, haemoglobin has the highest optical absorption in the visible and near-IR range. Moreover, its absorption is strongly linked to its oxygenation level. Typically, it is possible to distinguish between oxyhaemoglobin and deoxyhaemoglobin based on their absorption spectra, which show different patterns, by imaging the biological medium at several wavelengths.

From a signal processing point of view, multi-spectral acquisitions must be processed to estimate the imaged media and/or their concentration. To do so, the classical strategy often uses spectral unmixing, which is based on spectral fitting of the acquired data on reference spectrums [410].

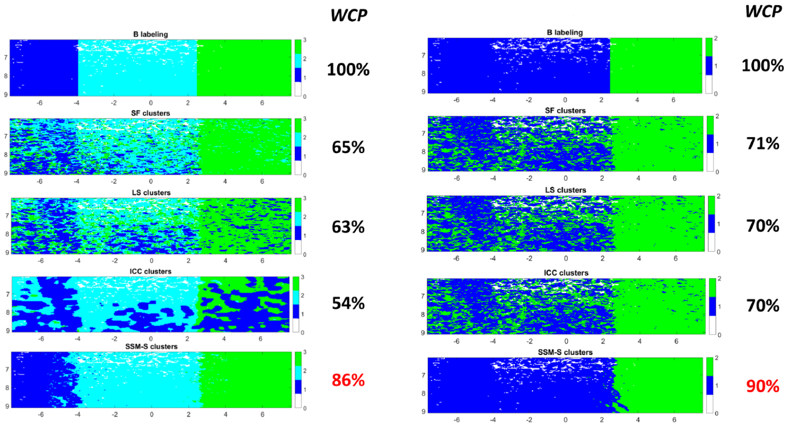

Figure 10.8: Result maps (left) with or (right) without dilution consideration (the diluted blue cluster is represented in cyan). From top to bottom: ground truth, spectral-fitting [410], least-square [413], intra-class correlation [414] and SSM-S. The performances are highlighted by calculating the percentage of well-classified pixels (WCP).

Previous knowledge of the potential imaged medium is necessary for such a strategy. However, in the various published methods of the literature, the spatial information is never considered in the medium extraction, which leads to noisy estimation, and the clustering of close pixels can be affected by different media. For these reasons, a spatial and spectral mean-shift (SSM-S) has been proposed to perform clustering or medium concentration estimation using a spatio-spectral regularization [411, 412]. The formalism is based on an iterative process on the variable $\mathbf{x}_j = \{\mathbf{s}j; \mathbf{A}_j\}$ where $\mathbf{s}_j/\mathbf{A}_j$ is the position/spectrum of the j-th pixel. Then, the iteration process is expressed as:

$$\mathbf{x}_t^{[t+1]} = \frac{\sum_{j=1}^{N} g_s(\mathbf{s}_i^{[t]}, \mathbf{s}_j^{[t]}).g_\lambda(\mathbf{A}_i^{[t]}, \mathbf{A}_j^{[t]}).\mathbf{x}_j^{[t]}}{\sum_{j=1}^{N} g_s(\mathbf{s}_i^{[t]}, \mathbf{s}_j^{[t]}).g_\lambda(\mathbf{A}_i^{[t]}, \mathbf{A}_j^{[t]})} \tag{10.2}$$

with

$$\begin{cases} g_s(\mathbf{s}_i^{[t]}, \mathbf{s}_j^{[t]}) & = \begin{cases} 1 & \text{if } \frac{1}{R_s^2}(\mathbf{s}_i - \mathbf{s}_j)^T(\mathbf{s}_i - \mathbf{s}_j) \leq 1 \\ 0 & \text{otherwise} \end{cases} \\ g_\lambda(\mathbf{A}_i^{[t]}, \mathbf{A}_j^{[t]}) & = \begin{cases} 1 & \text{if } \frac{1}{R_\lambda^2}||\mathbf{A}_i - \mathbf{A}_j||_\infty \leq 1 \\ 0 & \text{otherwise} \end{cases} \end{cases} \tag{10.3}$$

where R_s is a radial distance and R_λ the maximum accepted distance between spectra. The equation (10.3) ensures that the distance between pixel and spectra is conserved during the iterative process. Such process, described in (10.2) is applied to all pixels $\mathbf{x}_i$ of the image region X until convergence of the procedure, *i.e.* stabilization of the featured values throughout the process. Once obtained, pixels can be clustered together [411]. Similar processing can also be extended in order to perform concentration estimation [412].

Using the VevoLazr system, specific experiments have been conducted in order to evaluate the clustering performance of the SSM-S method to separate coloured medium with or without the consideration of its dilution [412]. The results are shown in Figure 10.8. The proposed SSM-S strategy outperforms the state-of-the-art technique without considering a medium's potential dilution.

The proposed SSM-S method improves then the discrimination of multi-spectral photoacoustic datasets. It has been validated on diluted, mixed, and media with particular light attenuation. Moreover, it was highlighted that using the spatial features, in addition to the spectral one, improves the discrimination. Moreover, the method could be extended for 3D multispectral imaging, although it is not yet fully conducted. However, the SSM-S also has some limitations. First, the computation time is longer than simple spectral fitting, where a single matrix inversion is conducted. However, in the context of the clinical application of photoacoustic, the standard extracted parameter is the saturation map (SO_2) based on oxygenated and deoxygenated blood. Also, the proposed SSM-S is not specifically optimized for such an application, and current results did not exhibit a specific improvement in SO_2 map calculation [415]. Last, with the omnipotent presence of deep learning algorithms, the multispectral photoacoustic imaging post-processing may also be revisited with a specific network, as already proposed in [416].

10.6 Ultrasound Spectroscopy

Ultrasound imaging provides an anatomical image of tissues. This grayscale imaging highlights changes in the mechanical properties of tissues where ultrasound is reflected in the ultrasound probe by large structures (organ edges, blood vessels). In areas where the grayscale is homogeneous (speckle), ultrasound is scattered by much smaller structures (cells, muscle fibers...). In these areas, ultrasonic signals are associated with the tissue microstructure they have passed through. The backscatter coefficient (BSC) provides information about the tissue microstructure. To estimate it, the spectra in areas of interest (ROI correspond typically to 10 to 15 wavelengths in both lateral and axial directions) of the measured ultrasonic signals are compensated for tissue attenuation before being normalized by the spectrum of ultrasonic signals from a reference (*e.g.*, a medium whose scatterer characteristics are known). Using an ultrasonic probe with multiple transducers, the reference used is a known reference phantom citeyao1990. In this case, the BSC is expressed as:

$$BSC_s(f) = BSC_{ref}(f)e^{-4z[\alpha_{ref}-\alpha_s]}\frac{|S_s|^2}{\left|S_{ref}\right|^2} \tag{10.4}$$

where z is the depth, BSC_s and α_s are the backscatter and attenuation coefficients of the sample as a function of the frequency f, respectively and BSC_{ref} and α_{ref} those from the reference phantom. S_s and S_{ref} denoted the spectra from the sample and the reference phantom, respectively. Ultrasound scatterer parameters can then be evaluated by comparing the measured BSC with a theoretical BSC estimated using a theoretical ultrasound scattering model.

The ultrasonic scattering structure(s) at the cellular level is(are) still not identified (nucleus, cell or both). Indeed, it is generally difficult to correlate the scatterer parameters to tissue structures from histology. Classically, these models (*e.g.*, the Gaussian model [417]) deal with identical randomly and independently distributed scatterers, making them valid only for diluted medium. A first hypothesis to explain these difficulties may come from the fact that tissue may not be considered a diluted medium. The Structure Factor Model is better adapted for dense media because it also considers the scatterers' interactions using a statistical mechanics structure factor [418]. To gain insight into the cellular structure(s), that is(are) involved in ultrasonic scattering, ultrasound measurements were realized on four cell lines in cell-pellet biophantoms and ex vivo tumors. Ultrasonic scatterer parameters from four cell lines (4T1, JC, LMTK and MAT) of cell-pellet biophantoms and tumors were evaluated using two scattering models (Gaussian and structure factor models). The results of this study highlight that nuclei appear to be the main structure involved in ultrasonic scattering for all the studied tumors; that cells appear to be the structure involved in ultrasonic scattering for LMTK and MAT cell pellets; and that cells and nuclei appear to be the structures involved in ultrasonic scattering for 4T1 and JC cell pellets [419]. Then, another hypothesis to explain the difficulties in correlating scatterer parameters and histological structures is that both cells and nuclei may be involved in ultrasound scattering. We observed that ultrasound scatterer models adapted for nuclei and cell scattering (concentric sphere model [420] and structure factor model adapted for two scatterer types [419]) yield a lower relative error on nucleus and cell radii and volume fractions estimates than the structure factor model for 4T1, JC, LMTK and MAT CP cell-pellet biophantoms [421].

Ultrasonic spectroscopy can be useful for clinical applications involving changes in tissue microstructure [422]: in the presence of fat droplets in the liver for non-alcoholic fatty liver disease patients [423], cell-death changes during anti-cancer therapy [424], comparison between cancerous and healthy tissues [425]. We were interested in cancer characterization. Indeed, the grade of a tumor reflects the tumor's aggressiveness and is assigned based on various criteria, including the cell and the nucleus sizes. The potential of ultrasound spectroscopy to discriminate chondrosarcoma from osteosarcoma was evaluated on *ex vivo* tumors [426]. These models present a lot of differences in terms of cellularity, cells and nuclei size and extracellular matrix composition. The mean BSCs for each sample showed different trends between chondrosarcomas and osteosarcomas. Moreover, the two different osteosarcoma cells lines (MOS-J for OsS1 and OsS2; K7M2 for OsS3 and OsS4) lead to highly contrasted BSCs (Figure 10.9(left)). The differences within the BSCs per ROI are translated into the slope and intercept parameters (using a linear fit of the BSC as a function of frequency) in the scatter plots shown in Figure 10.9 (right). A Wilcoxon rank sum test conducted at a significance level of 5% reveals statistically significant differences in the intercept values between chondrosarcomas and osteosarcomas. Although only ultrasound spectroscopy results are presented here, this study was realized using ultrasound and light backscattering spectroscopy methods to evaluate the complementarity of these two techniques. We were also interested in the evaluation of tumor response to chemotherapy and ultrasound data were acquired and their analysis is in progress.

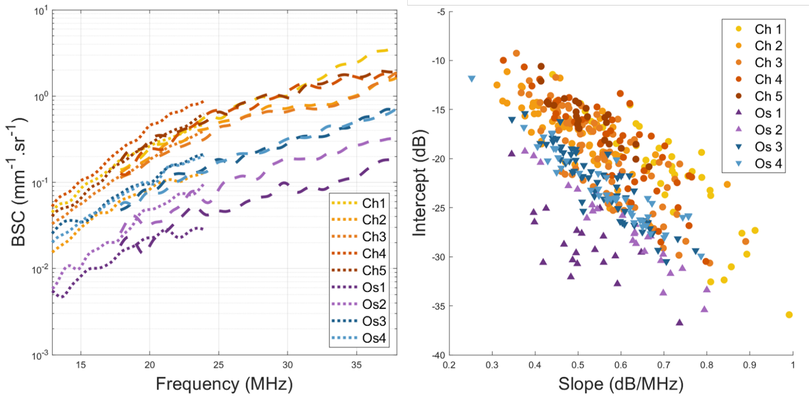

Figure 10.9: Left: Mean BSC b-spline fits obtained with two probes (13-24 MHz and 18-38 MHz) per tumor. Right: Intercept versus slope (BSC linear model over the 18-38 MHz frequency range) for each ROI.

10.7 Magnetic Resonance Spectroscopic Imaging

In the field of magnetic resonance, *in vivo* Magnetic Resonance Spectroscopy (MRS) is a tool for non-invasive measurement of concentrations of biochemical compounds (metabolites, lipids) and provides unique and valuable information for the diagnosis and therapeutic follow-up of a number of brain diseases (epilepsy, multiple sclerosis, stroke, cancer). The combination of MRS and spatial encoding methods derived from Magnetic Resonance Imaging (MRI) enables spectroscopic information to be mapped non-invasively. Although magnetic resonance spectroscopic imaging (MRSI appears far more interesting than single voxel acquisition (Single Voxel spectroscopy), since it provides spectral information in multiple regions within a single acquisition, it still is not widely adopted in clinical routine. This is due to long acquisition times, low spatial resolution and complex- the post-acquisition processing required to extract reliable information. After nearly 30 years of development, spectroscopic imaging techniques have been enriched by advances in MRI (parallel imaging, echo planar and non cartesian sampling, compressive sensing) to speed up acquisition[427].

Thus, MRSI signals consist of spatially distributed one-dimensional spectra, acquired in a two-dimensional k-space (kx, ky). In MRSI, k-space evolves over time with oscillatory functions and exponential decay, reflecting molecular content. A two-dimensional Fourier transform spatially localizes biochemical information, and a one-dimensional Fourier transform along time yields magnetic resonance spectra. Time and k-space domains are separable, with each (kx, ky) point having possibly a bandlimited spectrum (this is the case for phosphorus 31P spectra for example). In *in vivo* MRS, known molecular resonance frequencies and the expected 'full width at half maximum' (FWHM) of resonating peaks could be considered *a priori*.

As part of Jabrane Karkouri's thesis, methodological developments for 31P spectroscopic imaging were carried out in order to reduce acquisition time. The acquisition method we've been working on involves non-cartesian k-space sampling (spiral sampling) coupled with intelligent sub-sampling of the time dimension, or subsampling of the magnetic resonance signal - the NMR spectrum corresponding signal - exploiting *a priori* knowledge of the signal's *a priori* knowledge of the spectral support sparsity and a least-squares estimation for signal reconstruction. Indeed, sparse spectra support allows for faster and simpler signal

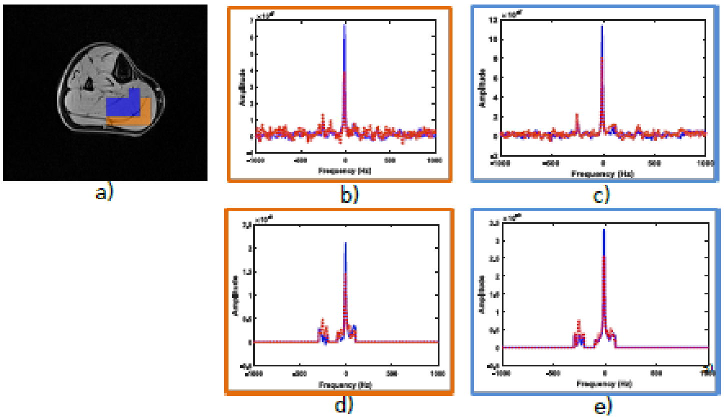

Figure 10.10: The 31P spectra are depicted at the beginning (in blue) and end (in dashed red) of the exercise for both the conventional (full sampling) scenario involving the gastrocnemius muscle (b) and soleus muscle (c), as well as the under-sampled scenario for the gastrocnemius muscle (d) and soleus muscle (e). The regions of interest for spectroscopy voxel averaging are represented in blue and orange on the anatomical image (a). The highlighted voxels in blue correspond to the soleus muscle, while those in orange represent the gastrocnemius muscle. In (a), the anatomical image and highlighted voxels were selected from the zero-filled 16 x 16 Chemical shift Imaging grid and averaged. Notably, in (d) and (e), where the spectra were acquired from under-sampled Free Induction Decay (FID) signal, they are reconstructed solely within the predefined spectral range (as determined by the user special card on the scanner console). This reconstruction is due to the fact that the spectra being derived from under-sampled FID signal, is restricted to the *a priori* known spectral range.

reconstruction, as demonstrated in [428] using the L2 norm for least square (LS) overdetermined solutions. The LS solution is comparable to the final step of the orthogonal matching pursuit algorithm. In a noisy scenario, reconstruction error depends on time sample selection, making optimal choices computationally challenging. The Sequential Backward Selection (SBS) algorithm is introduced as a computationally efficient method, iteratively minimizing Mean Squared Error by removing samples up to the desired number. In [429] we used this sample selection algorithm to undersample the spectrocopic dimension, and we designed a method to design a new sampling strategy taking advantage of the multidimensional characteristic of spiral MRSI. The proof-of-concept for this technique was carried out *in vivo* at 3T on skeletal muscle (Jabrane Karkouri's thesis) 10.10, but suffers from the low signal-to-noise ratio of the data acquired. An application at 7T (which would benefit from the signal gain linked to the use of a more intense magnetic field) is planned for the future.

Also, intrinsically spiral MRSI allows for a faster sampling of k-t space compared to conventional double phase encoding MRSI. This approach can be particularly beneficial in scenarios where a high signal-to-noise ratio is present, such as when assessing contributions like lipid/water content in muscle. Indeed, in muscle 1H MRS enables to identify and quantify extracellular (EMCL) and intramyocellular lipids (IMCL). However, their spatial distribution assessment and quantification remains challenging due to muscle fiber orientation and magnetic susceptibility differences. It is especially difficult for Tibialis Anterior (TA), Gastrocnemius (GM), and Soleus muscles (SM). The characteristics of these muscles, such as fiber type, shape, and orientation, influence IMCL visibility in proton MRS spectra. High-resolution MRSI solution based on spiral sampling to provide a rapid, reliable method for mapping IMCL/EMCL apparent content has been explored. A spiral MRSI sequence was developed on a 3T clinical MRI system, and data were acquired using a

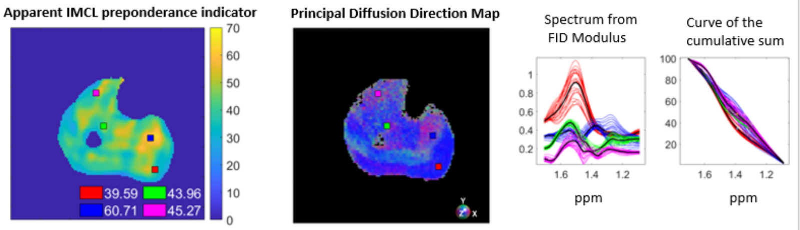

Figure 10.11: Left:Apparent IMCL preponderance indicator map obtained from spiral MRSI acquired on the calf muscle of a volunteer. 4 ROI were drawn in muscles of interest and for which spectra are displayed (right, with a focus on the lipid frequency regions, and curve of the cumulative sum used to compute the IMCL indicator is illustrated) , the map in the middle is the Principal Diffusion Direction Map derived from a fast spin Echo diffusion-weighted/tensor Imaging sequence.

dual resonance 1H/31P transmit/receive coil positioned under the right calf of volunteers. Subsequent sequences included Fast (spin echo-echo-planar-based) diffusion-weighted and T1 vibe Dixon sequences for fiber orientation, high-resolution water, fat, and proton density Fat Fraction (proton density fat fraction (PDFF)) images. Homemade processing tools in Matlab were employed for MRSI data analysis. Automatic phasing and frequency registration were achieved through Fourier transform on the absolute value of the time domain signal and the cumulative sum of amplitudes (CSA) within a defined area was utilized to analyze IMCL and EMCL content. An indicator of preponderance of IMCL over the content IMCL+EMCL was then obtained, see 10.11 [430, 431]. This marker was then studied through simulations and acquisitions on 24 healthy subject and compared to standard spectrum quantification which is subject to multiple difficulties on MRSI data (baseline variations, frequency and phase variations at each voxel). Simulation results confirmed the proposed indicator's ability to generate consistent maps compared to its quantitative counterpart. Significant differences in this indicator as well as for quantitative measurements were observed between GM and SM muscles. A positive correlation existed between the IMCL preponderance indicator and quantitative results. The proposed indicator demonstrated lower coefficient of variation for reproducibility and repeatability compared to quantitative measures.

10.8 Conclusion

The LabEx Primes has supported these works on spectral imaging, on the main medical imaging modalities, by funding PhD theses, providing access to imaging platforms (PILoT, Anican, CERMEP, etc.) and purchasing equipment. In all these modalities, the spectral dimension is an asset for characterizing different tissues, enhancing contrast and measurement specificity. To improve these techniques and to facilitate their application *in vivo* and subsequently in a clinical environment, one needs in-depth expertise in each of these modalities. The journey toward their development and showcasing their enhanced utility compared to existing investigative tools is extensive. Some are still in the proof-of-principle stage, demonstrated on phantoms, cell cultures, or preclinical, while others are actively being employed in clinical settings with elevated expectations and hopes. As these techniques mature, the prospect of conducting integrated, multimodal, and multispectral analyses in both research and, potentially, medical applications will become a tangible prospect. Indeed, each modality contributes a distinct perspective, offering only a partial glimpse into the intricate complexity of living organisms. Nevertheless, integrating or combining multi modalities spectral imaging presents complex challenges, as it will face different scales, different underlying physics, different biological phenomenon probed.

Tissue characterization from multi-modality imaging

11

Coordinator: Olivier Beuf

Contributors: Hélène Ratiney, Pilar Sango Solanas, Benjamin Leporq, Magalie Viallon, Pauline Muleki-Seya, Emmanuel Brun, Maciej Orkiz

11.1 Introduction

Personalized medicine requires the combination of multimodal imaging, new information or signal acquisition strategies and image processing to improve early diagnosis, tissue characterization, and provide quantitative biomarkers for better therapeutic outcomes. PRIMES has developed innovative imaging techniques based on or combining various physical concepts to improve contrast, spatial, or temporal resolution (MRI, optical imaging, X-ray phase CT, X-ray spectral CT, ultrasound). The methods developed have significant applications in cardiac, brain, bone, and cancer imaging. The challenges are to study morphology and physiology, to follow static or dynamic mechanisms, to measure the macroscopic or microscopic properties of tissues on different time scales. Achieving this goal requires the synergy of several imaging modalities pushed to their individual limits. The following sections are some examples of what PRIMES has achieved in this area.

11.2 Biomechanical characterization of viscoelastic properties using MRI

The development of a disease leads, among other things, to morphological and structural changes in the affected organs. The mechanical properties of these tissues undergo changes that can be detected, enabling us to assess the state of the diseased organ. Historically, with palpation, physicians made the first assessments of variations in the rigidity or suppleness of certain organs, as in the case of breast cancer, where the practitioner is able to find anomalies by exerting stress with the fingers. Nowadays, the technique used as the reference examination to assess the pathological state of a tissue is the biopsy. However, it is highly invasive. The search for non-invasive methods is therefore a topical issue, particularly with the help of medical imaging. In particular, the mechanical properties of tissues can be quantified using an imaging technique known as elastography. Here, we take a closer look at Magnetic Resonance Elastography (MRE). MRE was first proposed by Lewa *et al.* [432], [433] in the 1990s, and introduced clinically by a team at the Mayo Clinic [434]. It is performed by generating a shear wave at a given frequency that propagates through the tissue of interest with a certain speed and attenuation that depend on the viscoelastic properties of the medium. Since its introduction, MRE has been investigated to improve

its performance and extend its clinical application [435], [436].
In this context, two PhD thesis carried out in the MAGICS team at CREATIS as part of the LabEx Primes program have focused on the methodological development of MRE. The main contributions are briefly presented below.

11.2.1 MR Elastography: Optimal control for motion encoding at short echo time and simultaneous multi-frequency acquisitions

Magnetic Resonance Elastography (MRE) is used to characterize the viscoelastic properties of biological tissues *in vivo*, based on information about the propagation of an external mechanical wave through the tissue being explored. Typically, a conventional MRE sequence encodes motion through the application of motion-sensitizing gradients (MSGs), which oscillate at the same frequency as the mechanical wave and are placed between excitation and signal readout. However, the presence of these gradients limits the use of the technique when characterizing short T2 tissues. Indeed, their presence lengthens the minimum echo time. In addition, this principle of motion encoding is limited when we are interested in high-frequency excitations, due to the limitations of the gradient amplitude rise time. In addition, the acquisition at multiple frequencies, which are of great interest because they enable more detailed mechanical characterization, is usually achieved by repeating sequentially single-frequency acquisitions. As a result, the examination time required becomes very long. In this context, the aim of our work was to overcome these limitations by proposing innovative multi-frequency acquisition and motion encoding strategies.
During the PhD thesis of P. Sango Solanas, a strategy for the simultaneous encoding of high- and low-frequency movements has been proposed. Using the odd harmonics of trapezoidal GSMs, it is possible to significantly increase the frequency of the shear waves used in MRE without increasing the load on the gradient system [437]. This strategy allows for the simultaneous encoding of waves at multiple frequencies, this latter enabling better tissue characterization. In addition, a sub-sampling method that does not respect Shannon's theorem is proposed, enabling multiple frequency components to be encoded without requiring additional examination time. Experiments carried out on phantoms to compare conventional single-frequency MRE with the proposed simultaneous multi-frequency MRE method showed excellent agreement in viscoelastic parameters.
Next, this work explored the application of optimal control (OC) theory to MRE through the design of optimized radio frequency (RF) pulses [438]. OC pulses are applied with a constant gradient and have the dual role of motion encoding and spatial selectivity. As GSMs are no longer required, signal readout can be performed immediately after the pulse, and the echo time (TE) is greatly reduced. This strategy has been exploited to prove its high potential and extend its fields of application. An initial study demonstrated the use of OC pulses in a radial UTE sequence (ultra short echo time) to encode motion in tissues with very short T2. Experiments on phantoms and then on a bovine tendon sample

showed that viscoelastic parameters can only be characterized with the OC MRE strategy [439] (see Figure 11.1). Finally, a last study combined the multifrequency aspect with the OC strategy. OC RF pulses were adapted to simultaneous multi-frequency MRE and demonstrated its ability to encode multiple frequency pairs *in vitro* [440]. A good match was observed between the viscoelastic parameters obtained with the proposed strategy and with the classical method.
Therefore, this work was an original methodological contribution to the field of MRE, proposing a new OC-based strategy that enables the mechanical properties of tissues with short T2s such as tendons to be characterized for the first time.

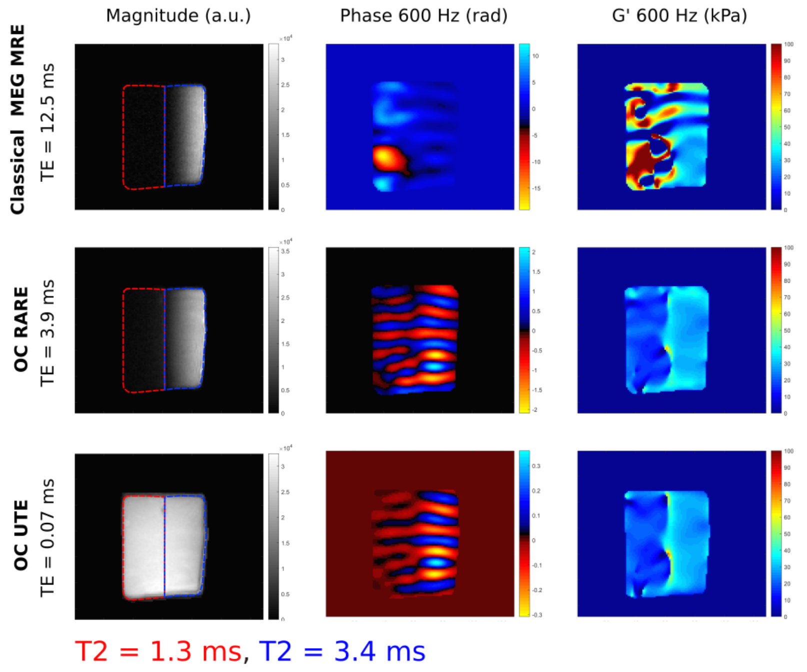

Figure 11.1: Images of magnitude, phase and shear storage modulus G′ obtained at 600 Hz with the different sequences: classical MRE with GSM (classical MEG MRE), OC fast spin echo (OC RARE) and ultra short echo time (OC UTE).

11.2.2 *In vitro* and *ex vivo* multi-frequency MRE for the detection of cerebral fibrillar aggregates in neuro-degenerative diseases

Among the many biological processes involved in dementia, fibrillar aggregation of endogenous proteins with conformational defects is an early feature of neuro-degenerative diseases. MRE has recently been applied to neuro-degenerative diseases. Although mechanical changes associated with these diseases have been detected, the mechanical effect of fibrils has not yet been isolated in clinical or preclinical studies. Therefore, the aim of the work was to exploit the fractal properties of fibrils to differentiate them from non-aggregated proteins. The power law exponent, obtained by fitting multi-frequency MRE data acquired at a macroscopic scale on phantom and on *ex vivo* rat brain, revealed the presence of these microscopic fibrillar aggregates [441].

An MRE bench for imaging *in vitro* and *ex vivo* samples has been developed to carry out a series of multi-frequency MRE measurements (400 to 1200 Hz) on agarose samples containing two types of fibrils, α-Syn and Aβ, and a non-aggregated protein used as a control [442]. The same device was used to characterize *ex vivo* rat brains injected with α-Syn in the striatum using multi-frequency MRE (800 to 1200 Hz). For each rat, the contralateral striatum was injected with saline and used as a control. All MRE data were acquired on a 4.7 T preclinical MRI system using a modified RARE sequence. After direct 3D inversion, the storage modulus, phase angle and wave velocity were extracted from the elastograms. The power-law exponent γ was obtained by fitting the multi-frequency data. In inclusions containing fibrils, γ was significantly higher than in those containing non-aggregated protein (see Figure 11.2). This result is all the more interesting as single-frequency are little affected by the presence of fibrils: multi-frequency MRE provides information on the tissue microstructure and makes it possible to characterize the fibrillar proteins, however small they may be (a few μm).

In rat brains, storage and loss moduli were reduced at all frequencies compared with the contralateral striatum. The γ and ϕ parameters, on the other hand, failed to discriminate fibril injection from control injection. Further experiments would be required to understand this lack of *ex vivo* detection.

This work thus proposed an original methodological contribution to the field of MRE, by isolating *in vitro* for the first time the biomechanical effect of fibrillar structures involved in neurodegenerative diseases such as Alzheimer's and Parkinson's.

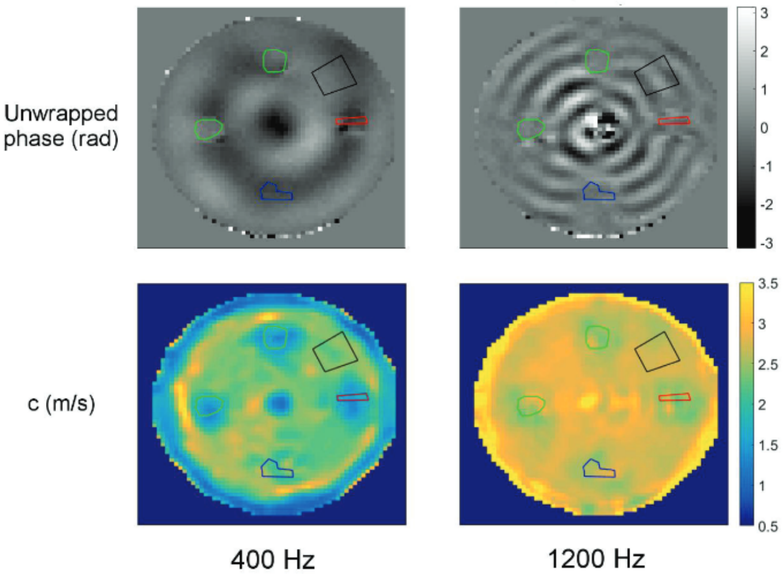

Figure 11.2: Magnetic resonance elastography: unwrapped phase and wave velocity maps obtained at 400 and 1200 Hz (motion-encoding direction orthogonal to the slice). Aβ, α-Syn and bovine serum albumin inclusions and agarose regions of interest are shown in green, red, blue and black, respectively.

11.3 Radiomics : a bridge between medical imaging and precision medicine

The need for personalizing the management of patients has been widely reported [443], [444]. Advances in artificial intelligence applications, combined with those in medical imaging, have led to the gradual conversion of digital medical images into high-dimensional data appropriate for data mining and data science techniques [445]. Meanwhile, computing power and quantitative image analysis techniques have made vast progress, the application of quantitative imaging techniques on medical imaging gained exponential momentum [446]. Currently, radiomics and deep learning are the most researched techniques on medical imaging. This chapter is focused on the radiomic analysis. A brief description of principle, workflow and clinical application examples derived from our experience are provided. Briefly, radiomics refers to the use of computational approaches to extract large numbers of quantitative features from a medical imaging modality, such as computed tomography (CT), magnetic resonance imaging (MRI), and positron emission tomography (PET), to develop predictive models ultimately aiming to enable personalized clinical management [447]. The central aim of radiomic is to uncover, at the macroscopic scale, the tumor characteristics at the microscopic scales (genetic, molecular, cellular, histologic) [448]. The necessary condition is that the image from which the radiomics features are extracted must express the underlying pathological mechanisms. Therefore, radiomic may provide great potential to capture important phenotypic information, such as intra-tumor heterogeneity. In addition, the non-invasive and three-dimensional characterization aspect of radiomics analysis, the availability of vast amounts of medical images, the longitudinal capabilities, and the cost-effectiveness of the method make radiomics a suitable candidate to be incorporated into the body of personalized medicine. The workflow of a radiomic analysis can be summarized as consecutive steps divided into the main categories of data collection, image segmentation, features extraction, development of the signature, and evaluation of the performance. Radiomics can be used for different clinical purpose. For diagnostic/screening purpose, we have demonstrated, from two multicenter cohorts (one including patients from Auvergne-Rhône-Alpes centralized by the Centre Leon Berard for the development of the radiomics signature, and another including patients from Ile de France centralized at CHU Cochin for inference and validation purpose), that MRI radiomics could allow to predict the malignancy of lipomatous soft tissue tumors [449](Figure 11.3), and help to reduce the use of biopsy in a screening context [450].

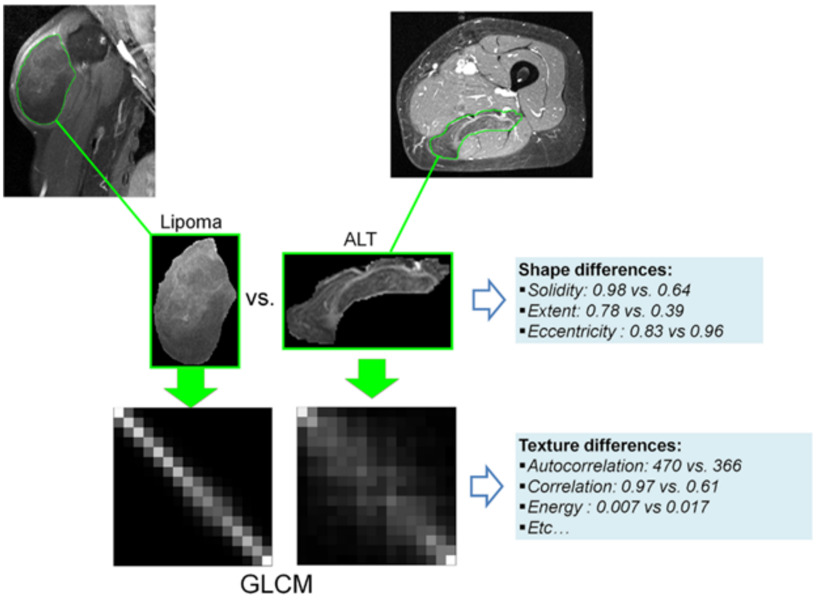

Figure 11.3: Malignant atypical lipomatous tumors display visual differences in shape comparison with lipoma. These differences were quantified by shape radiomics features (such as solidity, extent, and eccentricity). Tumor enhancements display different texture which can be recorded by the GLCM (Gray-level co-occurrence matrix); quantified using GLCM-based descriptors.

In the prediction of medical treatment response, we have developed, from pretherapeutic MRI, a radiomics signature able to predict the pathologic response of neoadjuvant chemotherapy in osteosarcoma (Figure 11.4). Three multicenter cohorts included nearly 200 patients (one from Auvergne-Rhône-Alpes patients centralized by the Leon Bérard center and two external validation cohorts (one including patients from Pays de la Loire centralized by the CHU of Nantes and another including patients from Ile de France centralized by CHU Cochin) were used [451]).

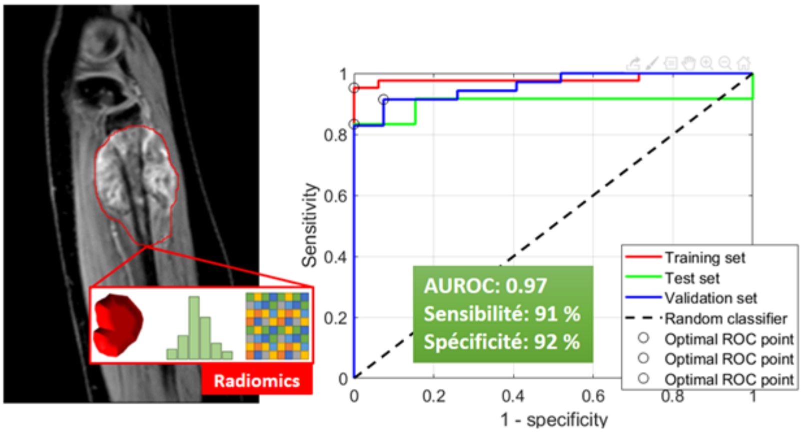

Figure 11.4: Diagnostic performances in the validation cohort of the radiomic signature built from pretherapeutic MRI to predict the histological response of neoadjuvant chemotherapy in Osteosarcomas.

Some of our works have also suggested that the use of different sources of radiomics such as multi-contrast MRI can help to increase model performances. In breast cancer, we have showed that using MRI radiomics derived from T1 perfusion-weighted, diffusion-weighted and T2-weighted, it was possible to predict the response to triple negative breast cancer neoadjuvant chemotherapy from pre therapeutic MRI with better performances in comparison to radiomics extracted from a single contrast images [452] (Figure 11.5). Similarly, we have demonstrated that multicontrast MRI can also allow classifying between breast cancer clinical molecular subtypes, particularly between ER/PR+ and HER2+ or TN and between histological subtype such as intraductal carcinoma vs. intralobular carcinoma [453].

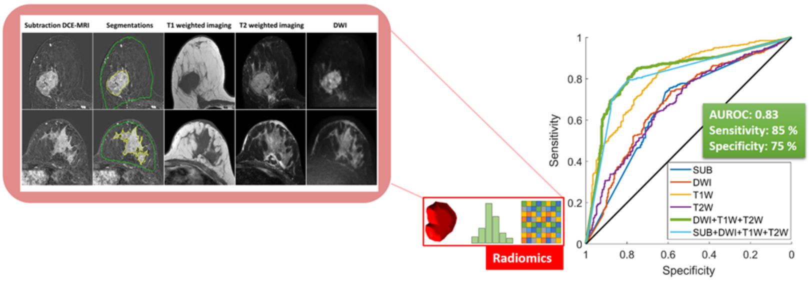

Figure 11.5: Diagnostic performances in the validation set of the radiomic signature built from mutlicontrast pretherapeutic MRI to predict the histological response of neoadjuvant chemotherapy in triple negative breast cancer. The best performances were obtained when radiomics extracted from diffusion-, T2- and T1- weighted were integrated.

In addition to multi-contrast MRI that have demonstrated high interest, we have also evaluated mutliomics approach as sources of data through a radiogenomic study aiming to predict the response of immunotherapy in non-small cell lung cancer. In this study, including patients from NIVOBIO clinical trial (patients from Leon Berard and Georges-François Leclerc comprehensive cancer centers), radiomics extracted from lung CT, genomics, and hot/cold signature will be combined and evaluated. We have shown that the combination or radiomics and genomics increase the prediction performance of radiomics used alone with an AUROC at 0.88 [454].

Such previous work open the way to the early prediction of radiation response by imaging such non-invasive magnetic resonance imaging methods. Recently, intravoxel incoherent motion (IVIM) has gained interest in cancer imaging. IVIM carries both diffusion and perfusion information, making it a promising tool to assess tumor response [455]. Obtaining new radiologic biomarkers of radiotherapy response could lead to a more personalized and biology-guided radiation therapy.

11.4 Quantification of lung aeration with CT scans

Acute respiratory distress syndrome (ARDS) is a severe impairment of gas exchanges in the lungs, resulting in very high mortality ($30 - 50\%$) and requiring artificial ventilation with personalized settings to ensure sufficient oxygenation while minimizing ventilation-induced lung injury. Assessing the patient's lung response to ventilation is crucial to customize these settings. Computed tomography (CT) gives access to local lung aeration *via* tissue density, and can be used to assess changes in aeration induced by different ventilation conditions, provided that lung segmentation and registration are performed in corresponding CT scans. Unfortunately, these tasks are hampered by large opaque regions, which are the radiological hallmark of the syndrome and locally blur the contrasts between lungs and neighboring tissues. Consequently, virtually no automatic methods capable of processing ARDS CT scans had been published at the start of our project, and studies were based on manual segmentation taking several hours per image pair [456].
Our first solutions were oriented towards studies on animal models of ARDS, where a large number of scans per subject are available including easier-to-segment images acquired at high pressure [457]. The easiest image was segmented using a conventional method, and then the segmentation mask thus obtained was deformed to fit the lungs in the remaining images. Deformation was based on image registration involving airway-tree segmentation, skeletonization, and matching [458, 459]. The combination of segmentation and registration was the cornerstone of a method proposed for voxel-wise assessment of lung aeration changes [460] in contrast with existing global or regional approaches. We also applied this combination to assess ventilation indices in a cohort of human patients with a different pathology: chronic obstructive pulmonary disease (COPD) [461]. Unfortunately, initial conventional segmentation usually fails in humans with severe ARDS. Inspired by the first publication reporting successful application of deep learning to lung segmentation in animals with ARDS [462], we trained a 3D U-net model to segment human lungs. The model achieved very good results (inaccuracies of the order of experts' inter- and intra-observer variability), even in patients with very severe ARDS requiring extra-corporeal membrane oxygenation (ECMO) [463]. Another U-net model was trained to segment motion masks, which improved image registration at motion discontinuities between the lungs and ribcage [464].
The number of ARDS cases strongly increased during the COVID-19

pandemic. We developed a prototype software [465], which enabled clinicians to quantitatively characterize COVID-19 ARDS [466, 467], and is now routinely used to choose one of the ventilator settings: tidal volume. It is also used in various studies on animal models of ARDS [468–471].

11.5 Multiparametric multimodality imaging of musculo-skeletal and myocardial muscle damages

The multi-parametric imaging offered by the numerous MRI techniques enables tissue characterization and quantitative assessment of tissue integrity through its magnetic properties. However, the behavior of imaging parameters or markers is not yet sufficiently mastered and understood across pathological situations. Therefore, collaborative efforts among researchers in imaging (CREATIS lab), exercise physiology (Laboratory of Sports Sciences, Lausanne and LIBM), and anesthesia-intensive care in the Auvergne-Rhône-Alpes region focused, using MRI protocols conducted at the University Hospital of Saint Etienne, on developing and validating new imaging biomarkers. This is done to improve our understanding of the behaviors of cardiac and skeletal muscles under stress and to question conventional clinical practices. We have focused on the impact of ultra-endurance on the body, particularly its effects on muscular and cardiac levels. Indeed, during endurance trail races such as the 'Tor des Géants,' muscular and cardiac alterations, along with a significant inflammatory response, occur under conditions of extreme stress for the body. These conditions closely resemble those encountered in critical situations in intensive care patients, poly-trauma cases, or after a myocardial infarction.

11.5.1 Muscular and cardiac alterations during ultra-endurance effort

A longitudinal investigation [472] was performed on athletes engaged in the 2014 "Tor des Géants" Mountain Ultra-Marathon (MUM). Three MRI sessions were conducted: one prior to the race, another immediately upon completion (for finishers), and a third after a 48-hour recovery period. Biological samples were collected at four designated time points, with an additional sample obtained at the midpoint of the race. The study utilized a 3D GRE (Gradient Echo) acquisition with a reconstruction method to calculate PDFF (Proton Density Fat Fraction), χ (magnetic susceptibility), and T2*-values. This method involved two main steps: fat–water separation, yielding parametric T2* and PDFF-maps, and magnetic susceptibility quantification. T2 parametric maps were obtained from meSE (multi echo Spin echo) sequences. Automatic segmentation using external force–driven deformable registration [473] isolated the quadriceps heads in T1-weighted images. Our main finding are that the extensive biomechanical stress experienced during a 330-km MUM significantly led to an evident inflammatory response, as reflected in elevated T2 and T2* relaxation times in the quadriceps muscles of our subjects. These changes are more likely related to water redistribution.

The elevated T2*-values observed might be explained by increased perfusion and/or local fluctuations in oxymyoglobin and oxyhemoglobin levels. This suggests an increase in oxygen suppliers and a decrease in deoxymyoglobin. Conversely, the muscular metabolic and energy storage indicators, represented by fat content (PDFF), remained relatively constant, with a small decrease in PDFF despite the substantial energy expenditure primarily relying on lipids. The magnetic susceptibility χ remained very stable, with only a minimal increase at arrival compared to baseline. Nevertheless, we observed susceptibility variations in the different muscle heads as reported by others. These differences can be attributed to variations in muscle composition (slow-twitch oxidative muscle fibers, capillary density, and myoglobin content). Thus quantitative MRI can monitor, non invasively the effect of exercise challenges and can quantify the effects of training strategies on specific individuals while differentiating the involvement of the different muscle.

11.5.2 MR spectroscopy for skeletal muscle energy metabolism

Compared to the MRI relaxometry techniques mentioned earlier, which are sensitive to inflammatory processes, perfusion effects, and water compartmentalizing in tissues, Magnetic Resonance Spectroscopy, capable of assessing concentrations of metabolites other than water in tissues, provides more specific information. This technique effectively complements MRI for studying muscle disorders, metabolic diseases, or cardiovascular conditions. Specifically, 31P spectroscopy is a non-invasive means to monitor energy metabolism and dynamic concentrations of phosphorylated metabolites during or after exercise, offering insights into the mitochondrial and oxidative capacity of skeletal muscles.

Assessment of energy metabolism through 31P spectroscopy can be done through non-localized spectroscopy, single-voxel spectroscopy, and Magnetic Resonance Spectroscopic Imaging (MRSI). In most cases, non-localized 31P spectroscopy is commonly performed, preventing the measurement of metabolic information from individual muscles. Instead, an average result from the entire muscle is collected at once using the surface coil employed for the experiment. The use of localized 31P spectroscopy would enable spatially resolved information and could drive the development of new sequences incorporating the latest technical advancements (see the Spectral Imaging chapter).

However, despite being explored for over 30 years in academic research, 31P spectroscopy is not yet employed in routine clinical practice. Therefore, we have focused on addressing various obstacles to its integration into routine clinical use. Indeed, developing and implementing a standardized 31P-MRS dynamic acquisition protocol for assessing skeletal muscle energy metabolism and monitoring muscle fatigability in diverse patient cohorts is technically challenging. It requires a high level of expertise, both in conducting the acquisition and processing the data to ensure reliable results. Thus we introduced an advanced quality control approach specifically designed for data obtained through a dynamic 31P-MRS protocol implemented on the 3 T MR scanner of the IRMAS platform [474]. The objective was to offer decision support to operators, aiding in data processing and ensuring reliable results based on objective criteria.

Then we conducted an impact study demonstrating the approach's effectiveness in exploring clinical results from two patient populations experiencing significant fatigue: COVID-19 and multiple sclerosis (MS). The study [475] highlights the positive impact of an advanced quality control pipeline on clinical populations, enhancing statistical power and precision of results. The quality control approach enables the operator to focus on problematic cases, improving data classification for nearly 50 % of subjects in the cohorts. Overall findings indicate altered muscle metabolism in MS and COVID-19 patients compared to controls. Notably, correcting metabolite amplitude by an individual T1 relaxation scale factor significantly influences results, emphasizing the importance of incorporating a resting TR measure into clinical protocols. This study underscores the need for vigilance in the translation of methodological protocols to clinical studies, from acquisition to quantification.

11.6 Micro-vascular and perfusion imaging

Vascular and capillary information can be obtained directly from ultrasound imaging and indirectly from MR imaging.

11.6.1 Ultrasound imaging microvasculature

Ultrasound Localization Microscopy (ULM) is a technique for obtaining ultrasound images of vascular microstructure with micrometric resolution and centimeter depth [476]. This technique, based on the principle of fluorescence photoactivation localization microscopy from optical imaging [477], involves detecting ultrasound contrast agents (microbubbles) in the bloodstream and their tracking during ultrasound imaging. To map the vascular microstructure, several steps are required after ultrasound acquisition: image beamforming, detection and isolation of microbubbles, localization of their centers, and tracking of their displacements [478].

However, the high gain in spatial resolution of this technique comes at the cost of a long acquisition time of the order of a few minutes (5-10 min). A long acquisition time is preferred because it allows a maximum number of microbubbles to travel through a maximum number of vessels, a necessary condition for their detection [478]. To increase the number of microbubbles detected and thus reconstruct a map of micro-vascularization more quickly, we focused on the first stages of the ULM chain: image formation and microbubble detection.

Adaptive ultrasound imaging algorithms can be used to obtain images with higher resolution and/or to limit speckle (textured areas typical of ultrasound images that correspond to the scattering of ultrasound by structures smaller than the ultrasound wavelength) on images to increase the visibility of microbubbles. The advantage of higher image resolution is that it increases the number of individual microbubbles that can be detected. We compared 3 adaptative beamformers, namely pDAS [479], coherence factor [480] and iMAP [481] with the classical delay-and-sum

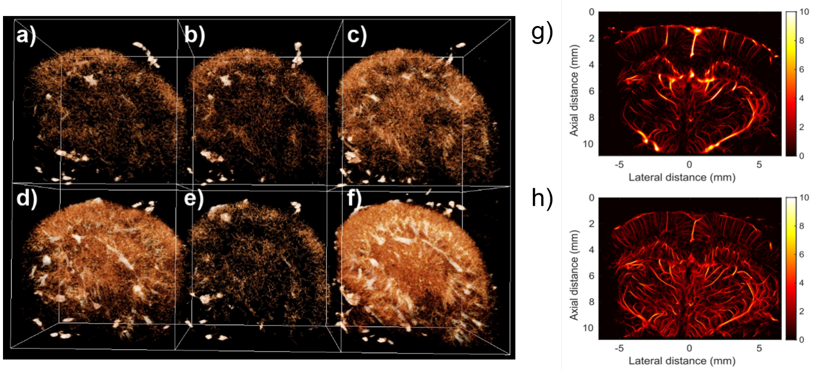

Figure 11.6: Adaptive beamforming for ULM on 3D rat kidney: DAS (a), pDAS (b), coherence factor (c and d), iMAP (e and f). Detection method on 2D rat brains: intensity (g), decision theory with Neyman-Pearson criterion (h).

beamformer (DAS) [482] in a study in collaboration with the LIB laboratory. These adaptive beamformers have the advantage of not being too time-consuming, making them suitable for 3D ultrasound acquisitions. These beamformers have been tested on 3D ultrasound acquisitions of rat kidneys, and the coherence factor and iMAP beamformers allow more microbubbles to be detected (Figure 11.6a-f).

The standard method for detecting micro-bubbles in ULM assumes that contrast agents are the structures with the highest intensities on the ultrasound images. However, the intensity of micro-bubbles may be lower than that of residual tissue or even noise in some cases. Therefore, a detector based on decision theory with the Neyman-Pearson criterion was proposed to facilitate the detection of these micro-bubbles. This new detection method was evaluated on simulated and 2D *in vivo* rat brain and kidney data. It provides a more complete map of micro-vascular structures for an equivalent acquisition time, with more spatially uniform micro-bubble detection than conventional methods [483]. An example of ULM images of rat brain with Neyman-Pearson intensity and detector is shown in Figure 11.6g-h.

11.6.2 Myocardial perfusion quantification by MRI

Cardiovascular diseases and in particular coronary heart disease are the main cause of death worldwide with 17.9 million deaths in 2012. Cardiac MRI is a particularly interesting tool for understanding and evaluating heart disease, including ischemic heart disease. Its diagnostic contribution is often major and it provides information that is not accessible by other imaging modalities. The work carried out focuses more specifically on the so-called myocardium perfusion test, which consists in studying the distribution of a contrast agent within the heart muscle during its first passage. In clinical practice, this examination is often limited to the clinician's visual analysis, allowing him to identify the culprit artery and deduce the impacted territory. However, this technique is relative and does not quantify myocardial blood flow. In recent years, an increasing number of techniques have emerged to enable this quantification at all stages of processing, from acquisition to the measurement itself. We first established a processing pipeline to combine these approaches and evaluate them using a digital phantom and clinical data [484]. We demonstrated that the Bayesian approach is able to quantify myocardium perfusion and its superiority in evaluating the arrival time

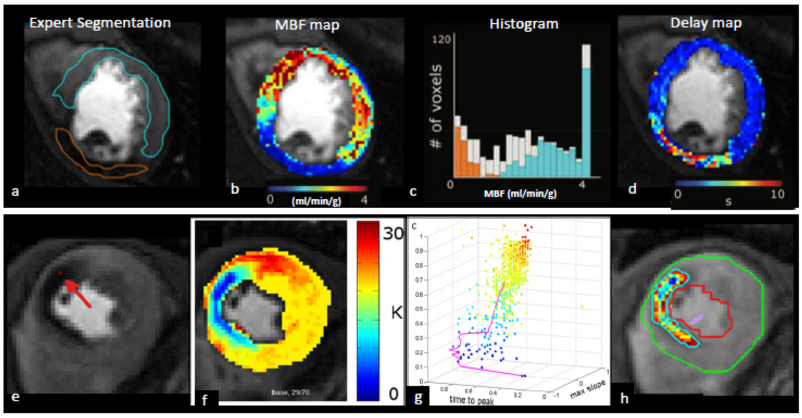

Figure 11.7: a): Peak perfusion image in a patient with an inferior ischemic lesion. Expert segmentation of normal (cyan line) and abnormal (orange) region; b): Myocardial Blood Flow (MBF) map and its respective histogram (c). Overlay cyan and orange colors corresponds to region identified in a); d) Delay map calculated using a bayesian approach. ©Adapted from Daviller *et al.* Front Physiol. 2021 12;12:483714; e) Peak perfusion image in a patient with an infero-lateral ischemic lesion. f-g): Extraction of myocardium voxels time intensity curves features (peak value, time to peak and maximum slope). The map on (f) represents the minimum value of K required to include voxel in the region. (c) Time intensity curves features of each voxel displayed in the 3D features space. Color map of the points is identical to (f). The magenta curve in (g) represents the region growing scheme of the average time intensity curve features evolution of the growing region as a function of iterations. h) K-means and STRG segmentations results. Endo and epicardium borders are defined by the red and green contours. The color map of STRG mask indicates the threshold value for which the voxel has been included to the region. © Adapted from Comput Biol Med. 2019 ;110:108-119.

of the indicator bolus compared to the Fermi model. In addition, the Bayesian approach provides additional interesting information such as the probability density function of the measurement and the uncertainty of the residual function, which makes it possible to know the reliability of the measurement carried out [485]. Finally, we proposed an algorithm for segmentation of myocardial lesions, using the spatial and temporal dimensions of perfusion data. This technique allows an objective and precise segmentation of the hypo-perfused region allowing a myocardial blood flow measurement to detect homogeneous Behavior or increase in the contrast-to-noise ratio (Figure 11.7). In the cohort of 30 patients, the variability of myocardial blood flow measurements performed on voxels detected by this technique was significantly lower than that of measurements performed on voxels in manually defined areas (mean difference=0.14, 95 percent CI[0.07, 0.2]) and those performed on voxels in areas defined using the bullseye method (mean difference=0.25, 95 percent CI[0.17, 0.36]).

11.7 Improve detection and following using imaging in Alzheimer's disease and multiple sclerosis

11.7.1 Virtual histopathology of Alzheimer's disease

Alzheimer's disease is the most frequent dementia among the elderly, as it affects more than 30 million people worldwide. Its pathological pathway involves the aggregation of two abnormal proteins: amyloid-$Beta$ into amyloid-$Beta$ plaques and phosphorylated tau into neuro-fibrillary tangles. Two hypotheses describe Alzheimer's pathology: the amyloid cascade and the metal dysregulation. Its diagnosis is difficult; a few *in vivo* techniques but it is only confirmed at death, upon the analysis of microscope slides: this is histology.

In this work, attempt was to go beyond the proof of concept of seeing the amyloid plaques in X-ray Phase contrast imaging (PCI) (see chapter Novel x-ray imaging). By comparing in 3D the morphology of different transgenic strains, and above all by exploring the source of the plaque signal using PCI, it was demonstrated the role of metals in Alzheimer pathology. This was achieved via an acquisition campaign on 3 light lines at the SOLEIL synchrotron (Gif-sur-Yvette): PCI to measure signal intensity within amyloid plaques, Fourier transform infrared spectroscopy (FTIR) to measure their fibrillar content (ratio of sheets-$Beta$ to helices-$alpha$), XRF to measure their metal content (Zn, Cu, Fe). The aim was to match the biochemical (fibrils) and elemental (metals) composition of the sheets to understand the biological substrate leading to a modification of the refractive index that enables their detection in PCI [486, 487].

11.7.2 MRI contrast optimization by optimal control to study demyelination/remyelination phases in MS rat model

Multiple sclerosis (MS) is a persistent condition affecting the central nervous system, characterized by a combination of inflammatory and neurodegenerative processes. Repeated occurrences of demyelination contribute to varying degrees of neuro-axonal degeneration. Currently, clinical practice lacks sufficient biomarkers to effectively monitor the inflammatory aspects of the disease. As a result, disease activity is often assessed through MRI quantification, which includes measurements of T1/T2 lesion load, the emergence of new T2 lesions, and the presence of Gadolinium. However, conventional MRI metrics, such as lesion burden, location, and type, have limited correlation with disability and offer little long-term prognostic value. There are no established MRI biomarkers for evaluating neurodegenerative processes in clinical practice, hindering our ability to predict disease progression. Furthermore, the underlying pathophysiological mechanisms of demyelination and remyelination, which contribute to neuro-axonal degeneration, remain largely unknown. The formation of focal demyelinated lesions and the failure of remyelination over time result in axonal injury and the loss of neurons. Also these dynamic pathophysiological processes change as the disease progresses. Encouraging myelin repair is crucial as it has the potential to restore normal nerve conduction, facilitate functional recovery, and prevent further axonal and neuronal degeneration. As a result, our research aims to develop novel MRI biomarkers, novel tissue characterization, that can track the changing dynamics of demyelination and remyelination in MS patients throughout the disease's progression. This should make easier the evaluation of innovative, emerging remyelination therapies in clinical settings.

A remarkable and interesting feature of MRI is its ability to produce a wide variety of contrasts, in different anatomical regions, and based on intrinsic soft tissue properties, to distinguish inflammatory, injured, healthy or necrotic tissues. Contrast in MRI relies mainly on the intrinsic magnetic properties of tissues, characterized by relaxation times, and involves either the adjustment of certain acquisition sequence parameters of the MRI sequences (echo time T_E, repetition time T_R, flip angle etc.), or by using *magnetization preparation* sequences placed in front of the detection scheme. These are made up of a sequence of B_1 RF pulses and gradients that enable an interesting contrast-to-noise ratio (CNR) to be achieved between targeted tissues. Bloch's equations model the macroscopic evolution of the acquired nuclear magnetic resonance (NMR) signal and they take into account the static field B_0 and its possible inhomogeneities, the relaxation times T_1 and T_2 intrinsic to the tissues studied, and the excitation radio-frequency field B_1. This RF magnetic field can be seen as a control on the dynamic of the net magnetization at the origin of the NMR signal. Thus to control the evolution of the NMR signal up to its acquisition, the *optimal control* theory could be applied to Bloch's equations and one can find different recent applications, some of which are our contributions, such as robust excitation and refocusing, and more recently for contrast optimization [488], [489], [490]. With this methodology, one can calculate, with a certain degree of optimality, the B_1 field optimizing the contrast between tissues with known relaxation times. In addition, it is possible to calculate the optimal field with respect to a model in which experimental variations are taken into account.

In Benoit Vernier's PhD thesis, we investigated optimal control approaches to improve MRI contrast between two or three specific target tissues within a three-dimensional Magnetization-Prepared Rapid Gradient-Echo (MP-RAGE) framework. The advantage of this approach lies in the utilization of the GRAPE algorithm to fine-tune magnetization preparation in a cyclic sequence without full recovery between cycles. This computational method enables the optimization of magnetization preparation involving any number of radio frequency pulses to enhance contrast while ensuring the establishment of a steady state in the longitudinal magnetization component. We demonstrated the advantages of an optimized T2Prep-IR over a simple inversion for enhancing contrast between white and gray matter [491]. The details of the generic numerical framework are given in , where the versatility of the proposed method is demonstrated through numerical and *in vitro* experiments. *In vivo* experiments were performed on preclinical (11.7 T) and clinical scanner (3 T).

More specifically, we studied in a multiple sclerosis animal model with focal lesion on the left corpus callosum (lysophosphatidylcholine-induced demyelination - LPC), the behavior over time of a MRI contrast obtained with an optimized magnetization preparation designed with optimal control to obtain a hyperintensity signal from short T2 components which are associated with myelin. An advanced image analysis pipeline was developed to analyze this MRI contrast data and to compare it with histological myelin assessment. In details, the MRI system used was the 11.7 T horizontal MR system installed in 2020 on the PILoT imaging platform. The imaging protocol included a T2-weighted axial sequence employing a Rapid Acquisition with Relaxation Enhancement (RARE) sequence. For the examination of short T2 components and myeline signal enhancement, a specific sequence was employed known

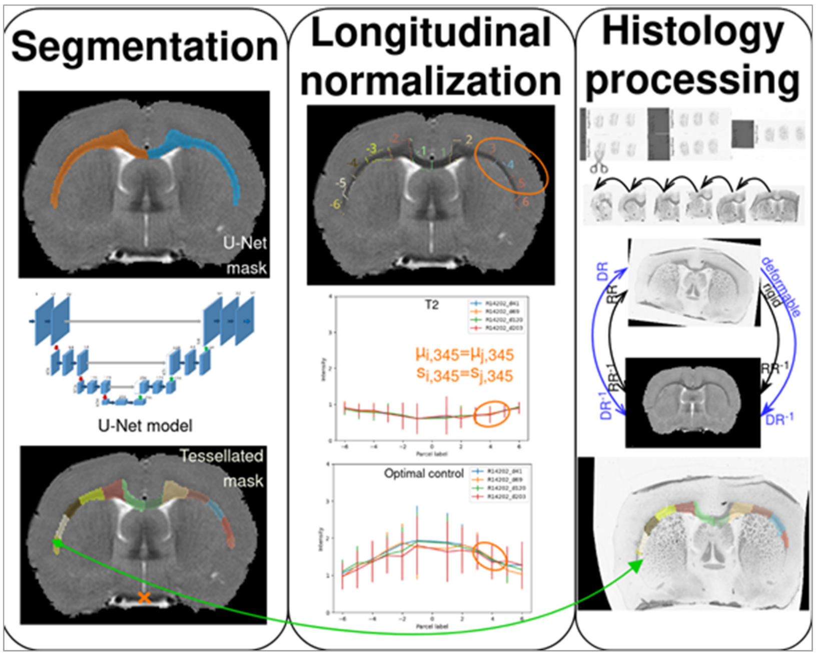

Figure 11.8: Image processing pipeline to compare optimal control MPRAGE and RARE modalities and perfom longitudinal analysis

as Magnetization-Prepared RApid Gradient Echo (MPRAGE), with a magnetization preparation optimized by optimal control (90-degree pulse followed by an 8.5 ms delay, a 180-degree pulse followed by another 8.5 ms delay, a -90-degree pulse, and a subsequent delay of 646 ms). This sequence resulted in an optimized T2 preparation-inversion recovery, contributing to the enhancement of signal characteristics in the imaging process. The image processing pipeline for data analysis (Figure 11.8) involved several critical steps. Initially, preprocessing procedures were applied, including N4 bias filter correction, longitudinal rigid registration on a template rat, and standardization of intensities to establish a uniform basis for subsequent analysis. Automatic segmentation of the corpus callosum in *in vivo* images was performed using a deep learning network (U-Net), with additional sub-segmentation achieved through tessellation, enhancing anatomical delineation. To ensure longitudinal consistency, normalization techniques were implemented, utilizing contralateral corpus callosum sub-regions to account for temporal variations. Deformable registration aligned histology images with MRI T2-weighted images, facilitating accurate spatial correspondence.

Thus, in this study, longitudinal and automated segmentation of the corpus callosum was conducted on a group consisting of 24 LPC-injected rats and 5 healthy rats. In conclusion of the measurements performed, no sustained remyelination was detected in the LPC model over the period spanning from 20 to 200 days post-injection. The optimal control sequence provides an intriguing avenue for signal intensity analysis. T2-weighted imaging demonstrated a closer agreement with observations from Sudan Black B staining than the optimal control sequence when considering corpus callosum volume segmentation. Further refinement of the sequence are needed, to keep the new obtained contrast and improve the resolution of the images.

11.8 Coupling MR and optics modalities

This research axis is motivated by the fact that optical components and devices can provide new functionalities to Magnetic Resonance (MR) systems or complementary information during advanced imaging protocols. This can be done either by using optical sensors within the magnet tunnel; or by including specific optical instruments into multimodal imaging sessions. Indeed, most optical fiber-based systems are fully compatible with MR systems. Consequently, optical transducers or deported sensors are susceptible to bring or extract signals to or from the tissue under investigation, or one component of the MR instrumentation itself. Besides, relatively high temporal or spatial resolution optical techniques can offer valuable analysis parameters to give access to a more precise diagnosis and biomarkers in diverse experimental situations, simultaneously or not. In the LabEx PRIMES, this was investigated in particular in the context of inflammatory bowel disease (IBD) that may lead into colorectal cancer (CRC), this latter being a major public health issue. Currently, conventional endoscopy is used to depict alterations of the intestinal walls and biopsies are performed on suspicious lesions for further analysis (histology). The recent imaging-based diagnosis technic helps to improve patients following-up but also the growth mechanisms. This is potentially the case of high spatial resolution Magnetic Resonance Imaging (MRI) that can be achieved using endoluminal (EC) radiofrequency (RF) coils. In this context, protocols that includes sequentially endoluminal MRI examination with conventional endoscopy, optical spectroscopy and confocal endomicroscopy was evaluated *in vivo* on a mouse model of colitis during longitudinal studies in order to characterization of colorectal tissue lesions. A receive-only radiofrequency single-loop endoluminal coil was designed and built for mice colon wall imaging. The prototype was first characterized *in vitro* on synthetic and organic phantom. Signal-to-Noise Ratio (SNR) profiles were compared with a quadrature volume birdcage coil (QVBC). The SNR measured close to the coil was significantly higher (10 times and up to 3 mm of the EC center) than the SNR measured with the QVBC. The gain in SNR can be used to reduce the in-plane pixel size up to $39 \times 39 \mu\text{m}^2$ (234 μm slice thickness) without time penalty. Consequently, the muscularis propria can be distinguished from the mucosae complex on images acquired with the EC without exogenous contrast agent (11.9) [492]. Beside, Magnetic resonance spectroscopy (MRS) was achieved on colon-wall complex, lumen and visceral fat with voxel sizes ranging from 0.125 μL to 2 μL while keeping acquisition times below 3 min. The acquired spectra show various biochemical contents such as α- and β-methylene but also glycerol backbone and diacyl. Choline was detected in tumoral regions. Visceral fat regions display a high lipid content with no water, whereas colon-wall complex exhibits both high lipid and high water contents. This was the first time that MRS using an EC has been performed for *in vivo* characterization of small local suspicious lesions in the colon walls and surrounding structures and offering alternative solutions to biopsies [493].

Despite certain contraindications linked to the presence of prostheses, pacemakers or recent surgical interventions, MRI presents an excellent benefit/risk ratio. However, the development of MRI systems with ever higher static magnetic fields leads to an increase in the effects of RF electromagnetic fields on patients. These effects result in an increase in

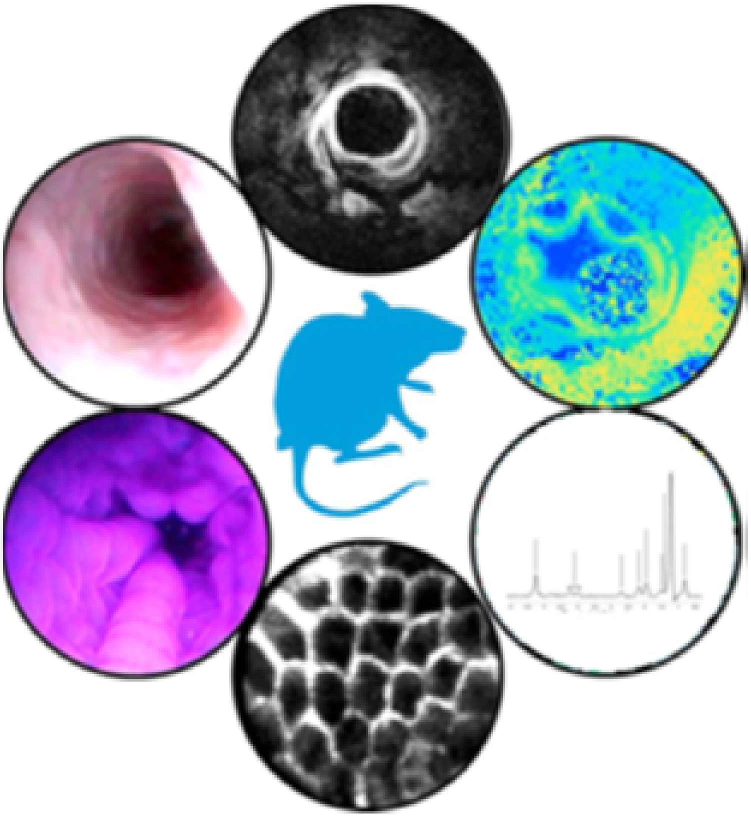

Figure 11.9: Colorectal tissue lesion characterization through a protocol combining imaging and MRS with conventional and confocal endoscopy. A protocol conducted on a chemically induced colitis model in mice. Detection sensitivity and lesion characterization were improved

the specific absorption rate (SAR) which can be locally reinforced by the introduction of conductive elements inside the transmitting coil. This is particularly the case for miniature endoluminal sensors which alone have the capacity to locally access the fine analysis of the digestive walls as it was demonstrated in the previous paragraph.

However, the use of these endoluminal reception sensors entails risks for the patient due to the local SAR induced by the RF electric field in the presence of the cable connecting the coil to the imaging system and which can lead to high local heating. In this context, the project had two objectives:

(1) To carry out an electro-optical (EO) conversion at the MR coil to overcome patient safety problems by replacing the galvanic connections with optical connections; The design and building of an EO then OE conversion chain to characterize all the elements of the conversion and transmission chain and to analyze each element in term of losses. Thus, the key performances to achieve a conversion without degrading the quality of the MRI image were determined [494].

(2) To measure and compare SAR at 7 and 11.7 T in calibrated phantoms, demonstrating the absence of disturbance introduced by the electric field probes developed by the company KAPTEOSs as well as the interest of local and vector measurements of the electric field compared to indirect measurements based on the rise in temperature [495].

11.9 Conclusion

Whether directly or indirectly, the different imaging techniques make it possible to probe tissues at different scales to better characterize their physiological state but also their physio-pathological evolution. Thus, the (macro-)molecular, cellular or vascular composition are accessible through one or the other of the methods developed and addressed in this chapter. Progress in recent years has been significant and demonstrates the need for methodological developments in signal measurement, whether through the development of coils or the implementation of new acquisition strategies which are always inseparable from image analysis techniques for the benefit of progress in imaging of living.

Image analysis 12

Coordinator: Michaël Sdika

Contributors (alphabetical order): Olivier Bernard, Patrick Clarysse, Nicolas Duchateau, Carole Frindel, Thomas Grenier, Carole Lartizien, Odyssée Merveille, Maciej Orkisz, Hélène Ratiney, Michaël Sdika, Antoine Vacavant

12.1 Introduction

Medical image analysis encompasses all the methods dedicated to extracting meaningful information from various types of medical images, such as X-rays, CT scans, MRI, and US images. It plays a crucial role in medical research and clinical practice. For example, it can be used for disease detection and diagnosis, to detect specific patterns, abnormalities, or markers. It is also used for example to automate the delineation of the patient’s anatomical and pathological structure to determine the optimal approach for surgery, radiation therapy, or other interventions. Overall, medical image analysis enhances the accuracy, efficiency, and effectiveness of healthcare by providing valuable insights from medical images, aiding in diagnosis, treatment planning, and patient management. For medical images, different tasks are traditionally tackled: • image segmentation, the partitioning of medical images into meaningful regions or structures, • image registration, that aims to align and spatially match images for motion estimation or comparison, fusion and analysis of the images, • image classification, to automatically classify and recognize specific patterns or abnormalities in medical images, aiding in the diagnosis and characterization of diseases, • image-based modeling and simulation, the creation of synthetic images with given physiological and acquisition parameters, to create infinite datasets with ground truth data.

In the LabEx PRIMES, most of these tasks have been tackled as a result of the large variety of organs and modalities of investigation. In this chapter, the most important results reflecting the work developed since the beginning of the project are presented. The first section is dedicated to image segmentation and registration, including motion estimation. The second section presents our image simulation results. The third section is dedicated to the method developed for diagnosis of prognosis from images. Finally, some clinical application use cases of medical image analysis are presented in the last section.

12.2 Segmentation and Registration

Segmentation aims at delineating regions of interest (ROI) in the images, while image registration seeks the geometric transformation between an image pair. These two tasks are related: given the positions of corresponding ROIs in two images, one can estimate a geometric transformation and if the geometric transformation between two images is known, the segmentation of an image can be mapped onto the other one.

12.2.1 Segmentation

The so-called classical segmentation methods have sought to define mathematically how to extract the structures of interest from the rest of the image using different properties of the segmentation task. For example, level set or active contour methods used the ROI/non-ROI contrast or the fact that image and ROI contours often match. Clustering methods are based on image statistical properties. Atlas-based methods rely on the topological invariance between subjects of the structures to be delineated. Machine learning tools have gradually been used in medical image analysis to improve traditional segmentation methods and deep learning based segmentation methods quickly caught up with, and even surpassed, the performance of conventional methods. The contributions of LabEx PRIMES in segmentation reflect the evolution of the development of image analysis methods in the community.

Atlas-based segmentation Atlas-based segmentation is dedicated to the segmentation of structures having the same relative position from one subject to another such as cerebral structures in brain images or muscle heads in limb images. An image with a ground truth segmentation map, an atlas, is registered to the subject image. The estimated geometric transform is then used to map the atlas segmentation on the subject image. The use of multiple atlases [496] has naturally led to the incorporation of machine learning techniques. In PRIMES several works are based on this approach.

For example in [497], an atlas is defined as an image in which each pixel is associated with a multi-class support vector machine (SVM). To segment a subject, the atlas is registered on the subject images and the label of a pixel is given by the output of the corresponding SVM for a local feature vector as input. The SVM is trained by mimicking this process on a dataset of images with ground truth segmentation. As a result, the segmentation outperformed state-of-the-art multi-atlas segmentation while requiring only one registration procedure.

The use of multi-atlas segmentation was also used for segmenting legs with a few amount of annotated T1-weighted MRI. In [472], a first longitudinal study of quadriceps features extracted from quantitative MRI is performed and correlated to biological biomarkers. The automatic segmentation of the quadriceps was performed using 6 atlases and produced better results than state-of-the-art approaches. The final output segmentation is obtained by weighting each pixel of the 6 output segmentations according to the similarity between the atlas's MRI and the MRI image to segment. Such segmentation allows robust delineation of muscles and enables their longitudinal study. It also generates accurate segmentations of outliers (*i.e.* subjects whose morphology is slightly different from that of other atlases) allowing fine-tuning of deep learning networks to better segment the targeted outlier.

Level Set / active shape models The segmentation of the myocardium plays a crucial role in clinical practice by providing valuable information for cardiac function assessment, ischemia detection, viability evaluation, and intervention planning.

We presented in [498] a level-set based method that allows segmenting the whole myocardium for the four main views used in clinical routine. The heart boundaries are approximated by two hyperquadrics that are then used as a shape prior for the evolving contour. Our method showed good results when compared with expert segmentation on a database composed of 80 images with clinical interest.

In [499], we described a motion prior energy that when minimized imposes a level consistency to the level-set function. This energy is added to a recently proposed framework for the segmentation and tracking of the whole myocardium in multiple orientations. We have also proposed to take advantage of the anatomical and image properties of echocardiographic data to adjust the hyperparameters spatially to make the method more robust. The algorithm was evaluated on a dataset of 15 sequences (around 900 images) where the manual references of two experts are available and compared favorably to state-of-the-art methods.

A book on structure segmentation and cardiac motion estimation in spatiotemporal image sequences was co-edited in 2015 in French (Hermes-Lavoisier, [500]) and English (Hoboken (USA) - London (UK): Wiley-ISTE, [501])

Deep Learning

Datasets One of the main keys in deep learning is the accessibility to annotated datasets. Indeed, supervised deep learning methods are the current state-of-the-art methods in most medical applications and the quality of manual references has a direct impact on the accuracy and generalization of AI methods. In this context, we have set up various international challenges in which we have built databases that we have made available to the community with high-quality expert annotations.

In [502], we introduced one of the largest publicly-available and fully-annotated dataset for 2D echocardiographic assessment. The proposed dataset consists of clinical exams from 500 patients, acquired at the University Hospital of St-Etienne (France) and included in this study within the regulation set by the local ethical committee of the hospital. The acquisitions were optimized to perform left ventricle ejection fraction measurements. To enforce clinical realism, neither prerequisite nor data selection have been performed. Consequently, i) some cases were difficult to trace; ii) the dataset involves a wide variability of acquisition settings; iii) for some patients, parts of the wall were not visible in the images; iv) for some cases, the probe orientation recommendation to acquire a rigorous four-chambers view was simply impossible to follow and a five-chambers view was acquired instead. This produced a highly heterogeneous dataset, both in terms of image quality and pathological cases, which is typical of daily clinical practice data. Manual annotations of the left ventricle endocardium and epicardium as well as the left atrium were done by one cardiologist on the full dataset and from three cardiologists on a fold of 50 patients. This fold was used to measure both the inter- and intra-observer variability. By training on this dataset, we were the first to demonstrate that the nn-UNet method can achieve results comparable to intra-observer variability for the segmentation of echocardiographic images.

In [503], we introduce the automatic cardiac diagnostic challenge (ACDC) dataset, one of the largest publicly-available and fully-annotated dataset for cardiac magnetic resonance imaging (CMRI) assessment. The dataset contains data from 150 multi-equipments CMRI recordings with reference measurements and classification from two medical experts. The overarching objective of this challenge/dataset was to measure how far state-of-the-art deep learning methods can go at assessing CMRI, *i.e.* segmenting the myocardium and the two ventricles as well as classifying pathologies. Results show that state-of-the-art machine learning methods can successfully classify patient data and get highly accurate segmentation results on the order of the expert inter-observer variability.

Using high level prior In PRIMES several works are based on the idea of incorporating high-level prior knowledge into the training of deep segmentation networks of non-pathological structures.

In [504] a patch-based segmentation network is augmented with a branch that adds the location of the patch after affine registration to an atlas. In [505, 506], some localization feature maps are learned and integrated into a Unet segmentation network. In these works, it is assumed that the (normal) brain structures to segment have an expected position in the image and attempts to learn features based on this expected position. The inter-subject variability of the brain structures makes this assumption too restrictive.

In [507, 508], the prior that is enforced is invariant to any invertible geometric transform of the image: only a limited number of structures can be adjacent to a given region. For a given parcellation of the brain, a matrix that indicates the permissible adjacency relationship between structures can be computed. A differentiable adjacency function has been proposed, positive only if any of the adjacency relationship in a given image is violated. A U-net network can then be trained using classical segmentation losses and the constraint that the adjacency function is null. It is also noticed that, as the adjacency function does not require the ground truth segmentation map of the image, semi-supervised training can be used: segmentation losses are used when the ground truth is available, the adjacency loss can be applied on a large non-annotated dataset. As it removes inconsistencies in the segmentation, the effect of this constrained learning is the most visible on the Hausdorff metric.

In [509], we developed a post-processing constrained variational auto-encoder (constrained variational auto-encoder (cVAE)) that converts invalid cardiac shapes into close but correct shapes. This is done by replacing the latent vector of an invalid shape with a close but valid latent vector. Comprehensive tests performed on the output of 18 segmentation methods reveal that our method is effective on both short-axis views from MRI as well as on long-axis views from US as can be seen in Fig. 12.1. Our method relies on a series of anatomical criteria (16 for short-axis

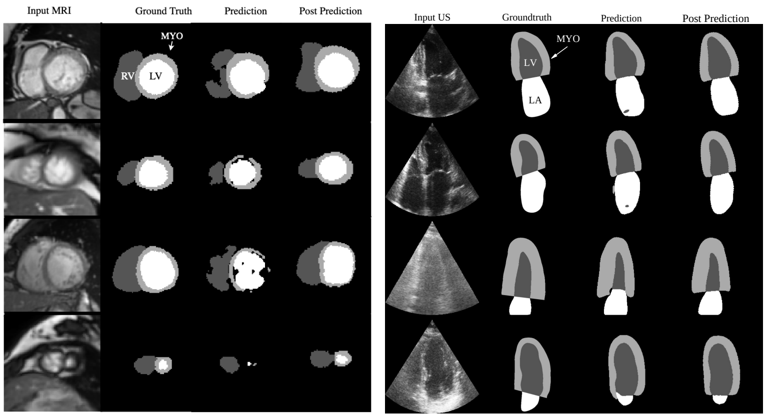

(a) MRI (ACDC) US (CAMUS)

Figure 12.1: Visualisation of the segmentation results from the anatomical post-processing method proposed in [509]. The raw images, manual segmentations by an expert, predictions by automatic methods and post-processed predictions are displayed next to each other. The predictions, even by state-of-the-art segmentation methods, contain multiple anatomical inconsistencies (*e.g.* holes, disconnected components, etc.) that the post-processing corrects using prior anatomical knowledge.

views and 12 for long-axis views) that we use both to detect abnormalities and populate a cVAE latent space. One appealing feature of the proposed framework is that anatomical criteria do not need to be differentiable as they are not included in the loss. Furthermore, it has been shown that the warping of the incorrect segmentation shapes did not change significantly the overall geometrical metrics (Dice score coefficient and Hausdorff distance) nor the clinical metrics (the right ventricle and left ventricle ejection fraction). As such, according to the inter and intra-expert variations reported in the literature, state-of-the-art methods for MRI and US segmentation are within the inter-expert variation and, with our method, are now guaranteed to produce results that follow anatomical guidelines defined by the user.

In [510] we proposed a post-processing pipeline to enforce temporal consistency in 2D+time echocardiography segmentation. The temporal consistency is enforced as a constrained regularization on the curves with respect to time of seven clinically relevant attributes that describe 2D long-axis cardiac shapes. We relied on these attributes to learn an interpretable cardiac shape autoencoder, which is used in the post-processing pipeline to correct the temporal inconsistencies left behind by segmentation methods. We tested our post-processing on five state of the art (SOTA) segmentation methods, both generic and specialized for echocardiography segmentation, and showed systematic improvements in segmentation accuracy metrics, *i.e.* Dice score coefficient and Hausdorff distance, on top of the enforced temporal consistency. Another advantage of our method is that it does not require 2D+time annotated data, since our cardiac shape autoencoder is trained on 2D images. The temporal consistency derives entirely from how we make use of the latent space's interpretability. Finally, from a clinical perspective, automatic tools are currently mainly used to segment the end-diastole and end-systole instants and to provide scalar clinical indices based on these, like the ejection fraction. However, many other indices frequently used, like velocities, strain, or strain rate, require temporally consistent data and can serve to examine the whole cardiac cycle. Thus, temporally consistent segmentation is a necessary step towards automatic image analysis tools that can help to identify and characterize a wider range of cardiovascular diseases.

Learning the Regularization in a Variational Formulation Recently, hybrid variational and deep learning approaches have been studied to keep explicit and explicable models while learning more complex data-driven regularization terms. In [511], we proposed to tackle the problem of disconnected segmentations of blood vessels by learning a regularization term that enforces connectivity. This network, based on a 3D U-Net, was trained to reconnect blood vessels from binary images with artificial disconnections. Once trained, this network is plugged, as a regularization term enforcing the connectivity prior, in a variational scheme to perform blood vessel segmentation. Such a segmentation approach is of high interest, first because it promotes the connectivity of blood vessels, which is a property often lost with state-of-the-art segmentation methods, and second because it does not require annotations on the dataset of interest. The reconnection network is indeed learned on binary synthetic images and can be then applied to any modality and vascular application.

Graph Neural Network Graphs are mathematical structures used to model pairwise relations between objects. They are effective tools for representing and processing data. Since 2009, artificial neural networks have been adapted to graph representation and processing. This particular class of neural networks is named: graph neural network (GNN). Now, all kinds of layers can be used with graphs (*i.e.* graph convolutional network (GCN), graph attention network (GAT),...). In the context of image processing, the image must be first transformed into a graph.

We developed a pipeline able to extract the cortical thickness of brain regions from T1-weighted MRI and create a graph per image (Fig. 12.2). The thickness of brain cortical regions is known to be affected by neurodegenerative diseases such as multiple sclerosis (MS). Therefore, we propose a GCN architecture able to classify healthy subjects from MS patients and also to identify the clinical forms of MS patients (three forms are studied: relapsing-remitting, primary-progressive, and secondary-progressive) [512]. We carefully normalized the graphs from age and gender and studied the impact of the number of cortical regions (using three different brain atlases) and of the complexity of the graph (from complete graphs to simplicial complexes using different thresholds on edges) on the classification performances (assessed using F1-score). The results we obtained from the longitudinal study of 91 MS patients scanned in 7 times on average (leading to 660 scans), highlight the better performance of this GCN compared to state-of-the-art 3D convolutional neural networks. These results open the way for clinical applications such as disability correlation of MRI patients by using T1-weighted MRI available in clinical routine.

12.2.2 Image Registration / Motion Estimation

Motion estimation for cardiac images Motion estimation is highly useful in medical imaging. It can for example be used to compensate motion artifacts that can occur during image acquisition due for example to patient motion. It is essential in cardiac imaging as it allows for the assessment of cardiac function, including measuring parameters such as ejection fraction, wall motion abnormalities, and ventricular volumes. It

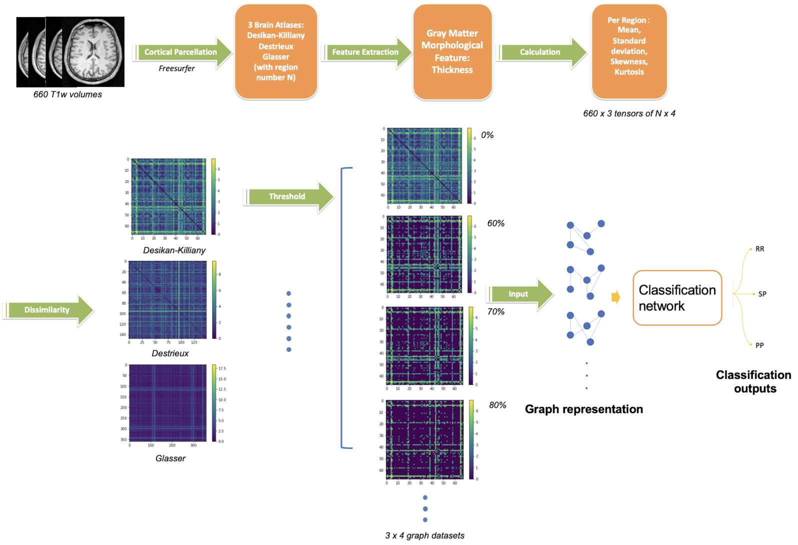

Figure 12.2: Proposed pipeline for GCN classification. The upper steps illustrate the cortical gray matter regions segmentation from T1w-MRI and cortical parcellation using three atlases, the region feature extraction (thickness), and its vector values. The bottom steps describe the graph construction followed by the GCN classification network. Four threshold levels are applied on graphs (0%, 60%, 70%, 80%), leading to four graphs per atlas. In summary, twelve networks are trained separately (3 atlases, 4 threshold levels) on 660 scans.

also aids in the detection and quantification of myocardial diseases, for example in the context of ischemia or scar tissue.

In [513], we developed a deep learning method for motion estimation in echocardiography. Based on the observation that multi-scale analysis has proven to be efficient for motion estimation in ultrasound, we first added a contextual sub-network at each resolution level of the network. In addition, the tracking of speckle patterns whose shapes can evolve between two consecutive frames makes the motion estimation task particularly difficult in ultrasound. For this reason, we decided to reinforce the capacity of the network to extract relevant information by modifying each estimator sub-network. These modifications correspond to skip connections concatenated to the output of each convolutional layer. The interest of these connections is twofold: i) since the pyramid, warping and cost volume network (PWC-Net) architecture is deep, they limit the phenomenon of vanishing gradient; ii) the inputs of each convolutional layer are composed by the concatenation of the input and the outputs of the previous layer, leading to richer information sources. We showed that the combination of a customized version of PWC-Net with the simulated synthetic dataset described in section 12.3 and a dedicated data augmentation strategy outperforms the current state-of-the-art methods, both for the tracking of endocardial borders and the estimation of the global longitudinal strain index. The genericity of our approach was also demonstrated from the first multi-center, multi-vendor and multi-disease study.

Motion Compensation for neurosurgery In [389, 514], we proposed a motion compensation method specially designed to estimate the motion while satisfying the clinical constraints of the surgical room: our method is real-time, robust to large camera motion and occlusions. At time t, our transformation model is the composition of a homography $U(t)$ (for the camera motion) and brain motion T_d:

$$T(x,t) = U(t)T_d(x,t). \tag{12.1}$$

where T_d is decomposed in a linear basis estimated with a principal component analysis (PCA) from the first few frame of the video:

$$T_d(x,t) = x + T_\mu(x) + \sum_{k=1}^{K} \lambda_k(t) p_k(x). \tag{12.2}$$

Only the 11 parameters of the homography and the $K = 5$ λ_k values need to be estimated for each frame instead of thousands or hundreds of thousands of parameters typically used to parameterize deformation fields. The estimation is efficiently done by computing a single singular value decomposition (SVD) using an original extension of the direct linear transform algorithm [515, 516]. The use of iterated re-weighted least squares allows us to robustly estimate the motion parameters. This method, specifically dedicated to motion compensation in the context of brain neurosurgery meets all the constraints for use in a surgical room. It was developed in the context of a larger project within the LabEx PRIMES investigating the detection of functional brain areas with optical imaging (see section 10.3). As such it was concretely used in numerous following works [517–519].

12.3 Simulation

The generation of realistic synthetic medical images provides a valuable resource for developing, testing and validating new algorithms, techniques, and technologies. Synthetic images can be used for example to assess the performance and accuracy of imaging systems, to optimize image analysis or reconstruction algorithms or to train neural networks. In this case, as these images are often generated from the ground truth, supervised learning can be used.

In [513] a solely image-based pipeline was designed to generate realistic 2D synthetic echocardiographic sequences. This allowed to simulate many cases from B-mode template cine loops on which myocardial contours were manually annotated to generate synthetic motion fields. Global deformation ranges obtained with our simulation method match those of real sequences; however, at a finer local scale, disparities can occur. The developed simulation pipeline was employed as a generator for synthetic ultrasound sequences, serving the purpose of data augmentation in deep learning solutions specifically designed for myocardial motion estimation. The generated synthetic dataset consists of 2D apical four chamber view sequences for 100 virtual patients with or without reverberation artifacts and with the corresponding myocardial displacement fields. For open science purposes, the full dataset can be directly accessed at `http://humanheart-project.creatis.insa-lyon.fr/medicaid.html`.

The same pipeline was extended in [520] for the generation of clinical-like ultrasound color Doppler sequences. The proposed pipeline combines state-of-the-art solutions in the fields of computational fluid dynamics and computational ultrasound imaging. The computational fluid dynamics (CFD) model determines the reference value of the blood flow. The ultrasound simulator, in conjunction with scatterer strategies, ensures realistic speckle patterns and Doppler estimates. We evaluated the genericity of our pipeline in four different scenarios. In particular, we showed

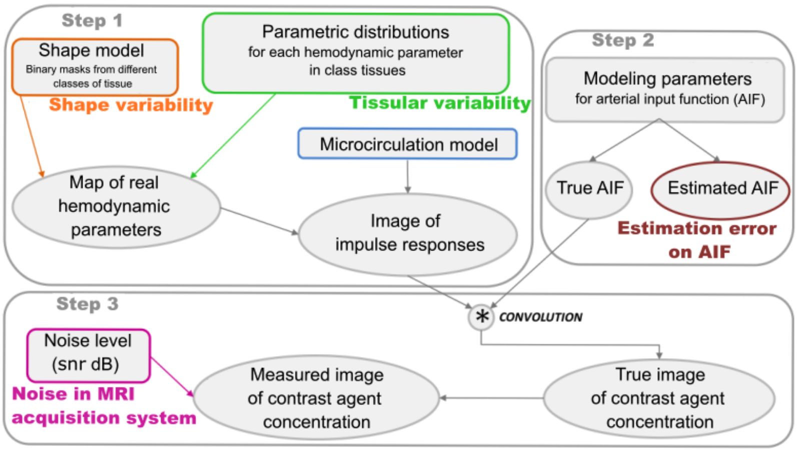

Figure 12.3: Simulation chain developed in [521] for generating concentration images in perfusion MRI. The rectangles represent the modeled sources of variability, and the ellipses the various objects derived from them.

that our pipeline allows the integration of flow acceleration and wall clutter noise. This led to side effects and made Doppler estimation challenging, as in real cases. The pipeline was used to generate an open-access dataset of 20 synthetic sequences available at the following link: `http://humanheart-project.creatis.insa-lyon.fr/duplex.html`

In [521], we created a simulator for digital phantoms in dynamic susceptibility contrast magnetic resonance imaging (DSC-MRI) to evaluate the precision of perfusion analysis software. This simulator, accessible online via the Virtual Imaging Platform at `www.creatis.insa-lyon.fr/vip`, generates – as illustrated in Fig. 12.3 – realistic brain and lesion shapes by simulating the impulse response function (IRF) image, representing tissue temporal responses; the arterial input function (AIF), modeling contrast agent concentration in arterial blood; and the contrast-agent concentration image, simulating the convolved effect of AIF and IRF. This comprehensive approach allows for a thorough evaluation of DSC-MRI analysis algorithms.

Initially used as a ground truth generator for evaluating the robustness of deconvolution algorithms, the simulator is later extended in [522] to address the clinical problem of acute ischemic stroke management. The innovation lies in improving stroke prediction performance using synthetic perfusion MRI produced by the physiologically relevant simulator. Additionally, this second study employs deep learning techniques. Unlike other studies using training datasets based on patient cohorts, this work demonstrates the potential to train on the perfusion MRI data of a single patient in acute stroke to predict the final infarct. This approach, distinct from using synthetic data for perfusion parameter learning, involves working directly on raw (non-deconvolved) data without the need for perfusion parameters. The synthetic data simulated from raw MRI perfusion data serves as a unique form of data augmentation, showcasing its potential benefits for personalized ischemic lesion prediction.

Moreover, as demonstrated in [523], simulations that account for vascular tree information yield the best classification performances on tested patients. This highlights the significance of considering vascular tree details in the simulation process, leading to improved predictive accuracy for final lesion outcomes in stroke patients.

Still in the context of ischemic lesions, but this time for myocardial infarction, we developed an original methodology to perform population-wise personalization of simulations [524] (while personalization is generally done for a given individual's data). This strategy is particularly relevant in case the simulations involve randomness in the model's rules (in our application case, a geometrical model of myocardial infarct may consist of a collection of a random amount of connected spheres of random diameter and somehow random location). It notably involves matching the distributions of real and synthetic cases, and optimization with a gradient-free method (the covariance matrix adaptation evolution strategy (CMA-ES) algorithm), as an analytical formulation of the models is complex or even impossible.

12.4 Diagnostic and Prognosis

12.4.1 Anomaly detection

Advances in machine learning have led to very promising results for the advanced processing and modeling of multimodality medical imaging. The vast majority of architectures for medical image analysis are based on supervised methods requiring the collection of large datasets of annotated examples. Building such annotated datasets is hardly achievable, especially for some specific tasks, including the detection of small and subtle lesions, which are sometimes impossible to visually detect and thus manually outline. This is the case for various brain pathologies including microbleeds, epilepsy or multiple sclerosis lesions as well as Parkinson's disease. One alternative to bypass this obstacle is to treat the lesion localization task as an outlier detection problem in an unsupervised (also called self-supervised) context. It consists in learning a model of representation of normality from the healthy data only, and then to consider as anomalies (outliers) the test samples that deviate too much from normality. We proposed an original analysis framework in this research domain based on one-class support vector machine (OC-SVM) with applications to epileptogenic lesion detection in MRI [525]. The proposed model consists in learning the support of the normative distribution based on a density support estimation algorithm, namely the one-class SVM algorithm. This model was trained in a voxel-wise basis using features extracted from MRI scans of healthy control subjects. This voxelwise analysis allowed both handling the high dimensional nature of neuroimaging data as well as providing an accurate localization of the epileptogenic zone. This model served to ground methodological contributions in outlier detection algorithms accounting for the specificities of neuroimaging data. To handle the presence of noise in the training data, we proposed a reformulation of the support vector data description (SVDD) algorithm by considering an ℓ_0 cost instead of the original Hinge loss [526]. To help with score interpretation, we proposed to convert the outputs of the SVDD algorithm into well calibrated probabilities [527].

Building on the seminal work in [525], we then proposed to replace the manually engineered features with a deep latent representation learned by an autoencoder-like architecture. More specifically, we trained a Siamese autoencoder to reconstruct input paired patches extracted from coregistered normal subjects and used the latent vector as a feature

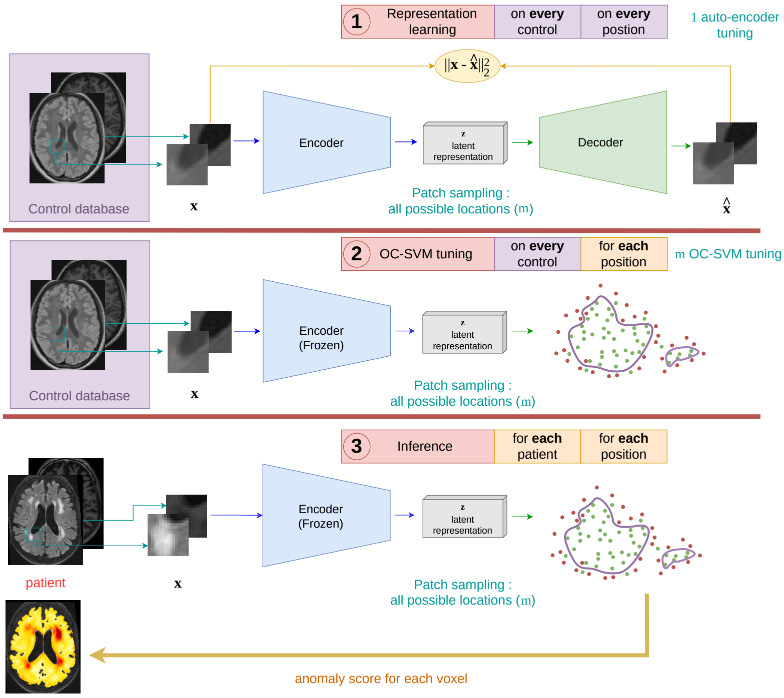

Figure 12.4: UAD pipeline proposed in [530] and consisting of 3 steps : 1) latent representation learning on patches extracted from the whole control database 2)tuning of one OC-SVM model per voxel based on latent representations z extracted at the voxel's location on the whole control database 3) inference on the whole brain using previously tuned OC-SVMs.

vector to train the uniclass density estimation support, as a second step [528]. This approach resembles a recently proposed deep unsupervized anomaly detection (UAD) model type which also trains autoencoder-type models on normal population but performs the detection step by computing the error between the original data and the pseudo-normal data reconstructed by the autoencoder. Such models assume that the AE trained on normal data only will not be able to reconstruct anomalies contained in the patient images. Recent studies have highlighted the limitations of these approaches for the detection of very subtle abnormalities, such as those encountered in many brain pathologies (microhemorrhages, epilepsy, multiple sclerosis, Parkinson's disease. . .). The alternative approach that we propose focuses on performing the detection step in the latent space by coupling the learned representation to a uniclass classifier, *e.g.* OC-SVM. The relevance of this approach has been recently demonstrated for the challenging detection task of subtle epileptogenic lesions in MRI T1 and FLAIR images. Our model indeed detected 65% of lesions that were not visually detected (MRI negative exams) by expert neurologists [528]. We also achieved encouraging performance for the same detection task on T1 and PET data with 71% sensitivity [529]. We recently built on the limits of our model and proposed original methodological contributions to design patient-specific models, relaxing the strong constraint to accurately coregister all control subjects and patients and compare its performance with state-of-the-art UAD models on the open WMH dataset [530]. In a similar smell, we also performed UAD of FDG PET lesion based on generative modeling with GANs of pseudo-normal FDG maps [531].

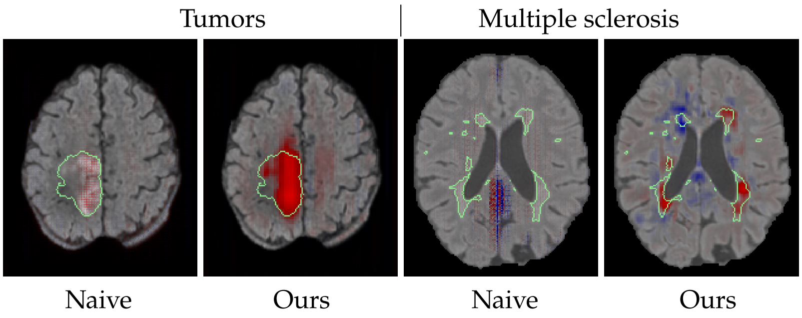

Figure 12.5: Gradient attribution maps for a healthy vs pathological classification for a naive classifier and a classifier trained with our constraint [532]. In red, voxels that drive the decision toward the class "pathology", in blue, voxels that drive the decision toward the class "healthy". The two images on the left are from the tumor experiment, on the right they are from the multiple sclerosis experiment. With our constraint, the decision is more driven by the lesion.

12.4.2 Weakly Supervised Segmentation / Interpretable Deep Learning

Deep learning has enabled a fantastic leap forward in medical image analysis. However, the performance of deep neural networks is offset by a lack of interpretability of their output. Interpretability is of particular importance in a critical field like healthcare: practitioners need to have confidence in the network's decision and ideally understand how the decision was reached. Unfortunately, the decision may be made for the wrong reasons as it can be driven by a bias in the learning database rather than relevant radiological features. We can partially lift the veil on the workings of a network by calculating, during inference, attribution maps [533] indicating the importance of each voxel in the decision. These maps can be used to check that the decision corresponds to clinical a priori. For example, we would like a classification network for healthy vs. pathological images to be based on the presence of lesions. In [534], we propose to use tissue probability maps instead of the raw images and show that MS lesions are more visible on attribution maps. This approach is limited by the quality of the probability maps. In [532], we proposed to constrain the learning of classification such that the attribution maps of healthy subjects are entirely negative, *i.e.* each voxel directs the decision towards the healthy class. Figure 12.5 shows that this constraint, learned on images of healthy subjects only, reveals lesions on images of pathological subject. This enables us to segment them in a weakly supervised way: only the image label (healthy or pathological) is known during training. The results of this method outperform the state of the art on interpretable classification and weakly supervised segmentation.

12.4.3 Representation learning

Representing population data is interesting for several reasons. In some applications, labels are not available or may not be trusted by clinicians (*e.g.* in the case of diseases that are hard to categorize, such as heart failure with preserved ejection fraction), and in such case statistical analyses need to represent the whole population data without using labels, namely in an unsupervised manner. Besides, medical images or descriptors extracted from these images are high-dimensional objects, and estimating an intermediate simplified representation of these data may help to remove irrelevant factors of variation and reduce the computational load for the subsequent application of other algorithms, *e.g.* for diagnosis or prognosis. Representation learning encompasses a family of methods that estimate a simplified latent representation, of reduced dimensionality, into which samples (a sample is often one subject or one acquisition within the population) are organized according to their respective similarities and differences (defined by specific distances between samples). In the context of several medical imaging applications, we first used this family of methods to estimate a relevant latent space onto which performing statistics to characterize the studied population, and plug-in clustering algorithms for phenotyping and risk stratification.

We first focused on manifold learning, which delivers a latent space with dimensions of decreasing importance and associated to specific statistical distances. Within the context of the LabEx PRIMES, we exploited variants of these techniques to handle multi-modal data, either to reach a single latent space associated to different input descriptors (also called manifold fusion [535] [536]), or different latent spaces whose correspondences are controlled (also called manifold alignment [537].

We also relied on (variational) auto-encoders to correct anatomically implausible cardiac segmentations [538]. Additional constraints can be added to order specific latent dimensions according to given variables of interest, which we exploited to reach temporally-consistent segmentations along the cardiac cycle [510], as described more in detail in Sec.12.2.1.

To be more computationally robust and efficient, we are currently developing better data fusion schemes that gradually incorporate the different descriptors or acquisitions and therefore progressively refine the latent representation. We considered a known hierarchy in the data types using manifold learning [536] or a generalization through probabilistic models (Gaussian processes latent variable models, work in progress), and even attempted to automatically learn the optimal hierarchy in the data types using reinforcement learning [539].

Ongoing work is on the addition of specific constraints to estimate more application-relevant latent spaces, better schemes for multi-modal data fusion, and their extension to longitudinal studies.

12.4.4 Parameter Estimation

Magnetic Resonance Spectroscopy Signal Analysis with Deep Neural Network

MRS provides distinctive non-invasive methods, such as mono-voxel spectrum or MRSI, for assessing the concentration of various metabolites within the human body (see Chapter 10). Recent technological advancements have pushed MRS towards closer integration into clinical applications. Numerous studies have demonstrated its value as a supplementary tool to MRI within the same imaging system. This integration offers additional insights into biochemical content, enhancing diagnostic capabilities across various pathologies ([540]). However, despite the progress made in the acquisition of the signal, the implementation of classic signal analysis techniques (pre-processing, reconstruction, formatting and quantification) to estimate the metabolite concentration that we seek, often requires an expertise that limits the application of this technique in a clinical context. Deep learning methods are thought to be able to overcome this obstacle, to enable robust and fully automatic data analysis with the least possible signal analysis expertise for the clinician user. In [541], we proposed, for the first time in the community, a novel approach to metabolite quantification in MRSI using deep learning. A regression framework, leveraging CNN, was introduced to achieve precise estimation of spectral parameters. The model learns spectral features from a comprehensive simulated dataset, encompassing diverse variations in human brain spectra and SNR. Experimental results highlighted the accuracy of the proposed method compared to the current standard quantification method QUEST [542] , showcasing its effectiveness in determining the concentration of 20 metabolites and the macromolecule.

We also propose employing a U-Net architecture to address significant signal artifacts encountered in *in vivo* MRS [543]. This approach relies on a synthetic MRS signal generation framework. Successful implementation of supervised deep learning hinges on having a substantial training dataset with known ground truth. However, creating such a dataset for *in vivo* MRS signals is impractical due to the high cost of acquiring data from human subjects, and ground truth artifact-free spectra for *in vivo* signals are not readily available. This limitation prompted the establishment of a synthetic data generation framework. The resulting dataset, if it accurately replicates the distribution of realistic *in vivo* signals, offers the advantage of being generated at no cost and on a large scale. In addition to the usual combination of metabolite and macromolecule signals (PRESS signals, TE=30ms, simulated using GAMMA [544] / GAVA [545]), along with additional Gaussian noise, various artifacts are introduced. All these diverse signal components are parameterized and varied extensively during the training process. This artifact removal procedure should be useful either for prior standard quantification algorithm or to ease machine learning quantification task. An intense lipid component was supposed to be an artifact coming from subcutaneous lipids and so our procedure could integrate in the future a spatial knowledge or knowledge from other MRI modalities (*e.g.* diffusion MRI) to handle tumor cases.

Personalized modeling of cardiac dynamics and mechanical characterization of the myocardium.

Bio-physical models can bring complementary information on the functional determinants of an organ. Thanks to previously acquired imaging data they can be individualized to the patient leading to patient-specific parameters potentially characterizing disease state and progression. In [546], we developed an individualized modeling approach for the left heart, integrating clinical imaging data for the characterization and longitudinal follow-up of injured myocardium. This approach proceeds in 2 phases based on anatomical and functional cardiac MRI data. 1) Suspect myocardial areas are detected on the basis of deformation parameters. The partitioning thus obtained is a pre-conditioning for the next step, 2) the parameters of a behavioral law of a cardiac biomechanical model are identified from the pressure-volume profile and the deformations derived from the imaging. The approach has been implemented on 21 cases from the MARVEL clinical database (NCT03064503, PI: P. Croisille) and has led to the estimation of a range of myocardial stiffness and contractility parameters that can be compared with the few similar studies in the literature. It is currently being tested on other MRI databases on myocardial ischemia, in order to assess the contribution of these parameters to disease progression.

12.4.5 Study of new transformation representations

Differential geometry and major physics problems are still largely expressed in terms of the operators of classical vector calculus and matrices. New mathematical tools have been developed, notably based on Clifford algebras, producing highly efficient representations of groups of transformations such as the rotation group. In [547], a new representation of n-dimensional Poincaré groups via dual hyperquaternions is developed, with hyperquaternions defined as a tensor product of quaternion algebras endowed with an associative outer product. This formalism leads to a uniquely defined product and simple expressions of the Poincaré generators, with immediate physical meaning, revealing the algebraic structure independently of matrices or operators. An algebraic formulation of the 4D Poincaré group, consisting of space-time rotations and translations, is introduced, together with a numerical application. Finally, the hyperquaternionic representation is compared with that of quantum mechanics. Potential applications include mobile reference frames and computer graphics. Following on from this work, we are investigating the use of these new representations for signal and image processing operators.

12.5 An Example of Translational Study: Quantification of arterial wall kinematics in carotid ultrasound images

Thickening of the intima-media complex (IMC) in the carotid artery wall is a marker of atherosclerosis and many methods have been developed to automate the measurement of intima-media thickness (IMT) *via* IMC segmentation in ultrasound (US) images [548]. Nevertheless, the onset of the disease occurs before the thickening, and early detection likely might be based on changes in bio-mechanical properties of the arterial wall, which requires estimating the two-dimensional (2D) motion of the tissue to infer deformation parameters such as radial compression, longitudinal shear and elongation.

Segmentation of the intima-media complex We have developed a method that segments the intima-media complex (IMC) by an original approach based on dynamic programming and a bank of filters matching the expected shape of radial intensity profiles [549, 550]. The strongest response corresponds to filter locations on a line midway between the IMC contours, with a filter size locally equal to intima-media thickness (IMT), and the dynamic programming scheme is used to ensure continuity and smoothness of the extracted contours. The method proved to be the most accurate among state-of-the-art techniques compared on a large open-access database (CUBS1, 2176 images) [551]. Although its errors were smaller than the inter- and intra-observer variabilities of reference annotations, there is still room for improvement in assessing the IMC radial compression based on IMT values estimated in an image sequence. Therefore, we have developed a new dual-resolution segmentation method based on deep learning: it uses the U-net architecture with one model trained to coarsely localize the IMC center-line and a second model trained to precisely identify the IMC contours in the vicinity of this line [552]. It outperformed the methods compared on CUBS1 database, as well as the methods participating in a comparison on another open-access database (CUBS2, 500 images) [553].

Estimation of the parietal tissue motion While IMC compression may be estimated by accurately segmenting the carotid wall on a sequence of images, estimating other components of tissue deformation requires a different approach. We were among the first teams to propose a method capable of reliably estimating the longitudinal motion of the carotid wall in clinical US image sequences [554]. Unlike other approaches, our method uses a Kalman filter to keep track of the changes in appearance of the speckle pattern of interest. Longitudinal displacement curves thus obtained were used to classify 113 patients into *at risk* and *healthy* groups with promising sensitivity and specificity exceeding 70% [555]. By applying our approach on several points selected along the IMC, we were the first to show and quantify longitudinal cyclic elongation of the artery [556]. A limitation of this approach is the need to manually select speckle patterns perceptible all throughout the sequence. To overcome this limitation, we have developed a fully automatic method combining two tasks: 1) fast detection and matching of salient-point clouds in each image pair, 2) selection of reliable pairs of matched points by means of the RANdom SAmple Consensus (RANSAC) algorithm and a physically plausible deformation model [557]. Although less precise than point tracking, this approach has several advantages: it is fully automatic, more robust, and simultaneously estimates all the components of tissue deformation. In parallel, we were working on identifying biomechanical model parameters from tissue samples in US images [558], as well as on specific US-image forming techniques, which ease motion tracking as compared with clinically available sequences [559]. Our segmentation and motion tracking methods are being made publicly available in the CAROLAB software [560].

12.6 Conclusion

Through its research and development efforts, LabEx PRIMES has advanced the understanding and application of various techniques and algorithms in medical image analysis. Cutting-edge methods in image segmentation, feature extraction, diagnosis, prognosis and image registration were developed, enabling more accurate and efficient processing of medical images. Likewise to the evolution of the field, the works in the LabEx PRIMES have leveraged the power of artificial intelligence and machine learning techniques to enhance medical image analysis. Physically meaningful and highly realistic simulators have also been developed to generate synthetic data to help evaluate algorithms or train deep models on large annotated datasets. To this very purpose, large datasets of real images have also been set up to train robust models. These real datasets are one of the outcomes of the collaboration between physicians and scientists. The unique collaboration between scientists and medical experts in PRIMES enabled to understand clinical needs and the resulting image analysis challenge. This has led to the development of tailored solutions ultimately benefiting patient care and diagnosis.

Image reconstruction 13

Coordinator: Fabien Momey Casella

Contributors: Loïc Denis, Nicolas Ducros, Denis Friboulet, Hervé Liebgott, Voichita Maxim, Fabien Millioz, Simon Rit

13.1 Introduction

Imaging techniques are at the heart of advances in the medical field, with various objectives: studying/understanding diseases, diagnosis, curation. A wide variety of instruments (modalities) - X-ray CT, PET, MRI, Ultrasound (US), Fluorescence, Microscopy - are dedicated to the observation of anatomical and/or physiological phenomenons of the human body, from nanoscopic to macroscopic scale, in a non (or at least as weak as possible) intrusive way. Most of these techniques perform indirect observations, that is to say that the targeted information is not directly acquired by the imaging system. The observation task is a complex process involving a "transformation" of a physical phenomenon, stimulated by the imaging system - or an external - source, into another that can be recorded by dedicated sensors and converted into exploitable data. For example, in ultrasound imaging, the stimulation source takes the form of ultrasonic waves emitted by a probe, that will be reflected and transformed by the sample according to its elastic properties (the targeted information). The echo of these waves are then recorded by the ultrasonic probe and converted into an electrical signal whose properties are related to the characteristics of the source and the sample at several locations. Nowadays, the recorded signal is sampled and digitized to allow computer processing. If this digital signal is spatially dependent, it takes the form of an image. In every imaging technique, the data formation process can be mathematically described, which allows to build a reconstruction procedure, leading to a computer algorithm, to retrieve the initial targeted information, most of the time in the form of a multi-dimensional image of the targeted physical quantity, for example the attenuation coefficient map in X-ray CT or the fluorophore emission activity map in fluorescence imaging. **This reconstruction step is often followed by an image analysis task (see Chapter Image Analysis).**

The problem consisting, in a large sense, in retrieving a targeted information from a set of indirect observations, is called an **inverse problem**. This concept is very widespread in all fields linked to observation, outside the bio-medical field: astrophysics, geology (sismology), biology. The research field of inverse problems modelization and resolution is a "cross-road" between mathematics, physics, computational science, and has benefited, since the 90s, from the advances in signal and image processing and numerical optimization (compressed sensing, deep learning), and computational capabilities (high-performance computing using GPU, distributed computing).

New imaging techniques still emerge, involving more sophisticated acquisition processes, and leading the reconstruction tasks to treat multi-dimensional (up to 3D) and heterogeneous data (spatio-temporal, spatio-spectral, joint processing of combined modalities). The new challenges rising from this increase of complexity is the key action of "image reconstructors" involved in the LabEx PRIMES. In this chapter, we present heterogeneous results obtained in different modalities, highlighting their specificities, showing the richness of approaches and applications, in the field of image reconstruction dedicated to medical imaging. We show how deep learning has become established in recent years in image reconstruction, for example using it to learn more efficient models, with a better reconstruction quality, and how researches involved in the LabEx PRIMES are at the forefront of this breakthrough.

13.2 General formalism of inverse problems

13.2.1 Notations

In each imaging reconstruction problem, we consider the quantities of interest, typically the data and the reconstructed information, as multidimensional signals. The multiple dimensions of these signals can be of heterogeneous nature: spatial (2D, 3D), temporal, spectral.

Moreover, these signals are discretized due to the digitalization process of the recording devices (cameras, sensors, etc.), that leads to a numerical data processing, and thus a discrete representation and restitution of the targeted information.

Discrete quantities are identified by a lowercase bold letter, *e.g.* $\boldsymbol{x}$.

Uppercase letters, *e.g.* $\mathscr{M}$, represents mathematical transformations from a discrete multidimensional space to another.

13.2.2 Data formation model

Whatever the imaging modality, the data formation process can be formulated as follows:

$$\boldsymbol{d} = \mathscr{M}^{(\boldsymbol{\theta})}(\boldsymbol{x}) + \boldsymbol{\eta}\,. \tag{13.1}$$

$\boldsymbol{d}$ stands for the data, $\boldsymbol{x}$ the targeted information. $\mathscr{M}^{(\boldsymbol{\theta})}$ constitutes the numerically implementable model that allows to calculate (an approximation of) $\boldsymbol{d}$ from $\boldsymbol{x}$. This model often depends on a set of calibration parameters $\boldsymbol{\theta}$ (*e.g.* angles of view in tomography, spectral ranges, learned network parameters, etc.). In the following, we simplify the notation of $\mathscr{M}^{(\boldsymbol{\theta})}$ by $\mathscr{M}$. $\boldsymbol{\eta}$ is the noise signal that represents random uncertainties of the measurement process (*e.g.* electronic noise in digital sensors), and modeling errors.

13.2.3 General formulation of the reconstruction problem

The reconstruction problem aims at finding a solution $\boldsymbol{x}^+$ to equation (13.1). If the model $\mathscr{M}$ is invertible and $\mathscr{M}^{-1}$ can be implemented, a natural solution is to apply:

$$\boldsymbol{x}^+ = \mathscr{M}^{-1}(\boldsymbol{d}) \tag{13.2}$$

Most of the time, particularly for advanced imaging modalities, the model $\mathscr{M}$ is not invertible. In the context of inverse problems methodology, a more general way to formulate the resolution of (13.1) writes:

$$\boldsymbol{x}^+ = \underset{x\in\Omega}{\arg\min}\ \mathscr{C}\left(\mathscr{M}(\boldsymbol{x}), \boldsymbol{d}\right) + \mu\,\mathscr{R}\left(\boldsymbol{x}\right) \tag{13.3}$$

The problem hence consists of estimating the optimal signal $\boldsymbol{x}^+$ that "explains" the dataset $\boldsymbol{d}$, considering the model $\mathscr{M}$ parameterized by the set $\boldsymbol{\theta}$. $\mathscr{C}\left(\mathscr{M}(\boldsymbol{x}), \boldsymbol{d}\right)$ is the data-fidelity term, that penalizes the deviation of the model $\mathscr{M}(\boldsymbol{x})$, depending on the current estimate $\boldsymbol{x}$, from the data $\boldsymbol{d}$. This term is often based on statistical considerations on the noise $\boldsymbol{\eta}$, that can be mathematically formulated in the Bayesian framework. For example, under assumption of a Gaussian distribution, the data-fidelity formulation leads to a weighted least-squares criterion. A specificity of inverse problems is to allow the injection of *a priori* knowledge in the resolution process, that takes the form of domain constraints ($\boldsymbol{x} \in \Omega$) or penalties, so-called regularization ($\mathscr{R}$), that will prevent the solution to fall into undesirable minima (*e.g.* noise overfitting). Classical regularization terms favor smoothness by penalizing the ℓ_2-norm of the solution or its gradient, while more sophisticated ones lead to piecewise smooth solutions (edge-preserving with mixed ℓ_2-ℓ_1-norms of the gradient). With the rise of compressed sensing theory, very popular and now widespread priors are based on sparsity enforcement in different spaces: ℓ_1-norm of the image or of its coefficients in a wavelet domain, Total Variation. Injecting regularization terms in the inverse problem criterion lead the solution to a physically relevant image validating a trade-off between the data-fidelity and prior information, that is tuned by weighting the regularizers with a set of hyperparameters μ.

13.2.4 Resolution

Most of the time, the resolution of the inverse problem (13.3) cannot be obtained analytically, and must be treated by numerical optimization. Such resolution methods consists in iterative algorithms mostly based on gradient descent strategies. The optimization process can differ depending on the differentiability of the criterion, leading to so-called "smooth" (conjugated gradients, second-order methods such as quasi-Newton algorithms) and "non-smooth" (proximal algorithms, method of multipliers) optimization algorithms. The latter are based on the assumption that the criterion is convex, with a unique global minimum, which is sometimes not the case particularly when non-linear problems are treated, and then can lead to fall into local minima. To overcome this issue, one can turn to non-convex optimization algorithms (stochastic gradient descent, simulated annealing, greedy algorithm) but at the cost of increased computational burden.

13.2.5 Deep learning based reconstruction

Deep learning brings a new paradigm in the context of inverse problems for image reconstruction. The basic idea is that DL can substitute to model-based iterative methods by directly learning the "reconstructor" given a pair of data and ground truth images. However, such datasets - particularly ground truths - are not easily buildable in practice to ensure its applicability to real data in all its generality and specificity, *i.e.* to avoid overfitting of the learning dataset. Thus, researches in this domain mostly turn into another approach consisting in making model-based and learning methods complementary. Here is a non-exhaustive list of possible strategies:

- learn a reconstructor enforced by physics-based knowledge of the problem ;
- keep the model-based iterative framework and plug a specifically built learned prior ;
- learn more accurate models or some calibration parameters ;
- learn adapted optimization strategies ;
- *etc.*

With this kind of approaches, deep learning is used on specific steps of the inverse problem to leverage inconsistencies of the model-based methods, and appears to be very powerful in this context.

13.3 Compton Camera

13.3.1 Introduction and related work

Compton cameras represent a remarkable advancement in the field of medical imaging and gamma-ray detection. Named after the American physicist Arthur H. Compton, who made groundbreaking contributions to our understanding of photon interactions with matter, these innovative devices have revolutionized our ability to capture and visualize gamma-ray emissions in astrophysics and homeland security. Recent progress made in detector technologies renewed the interest for this imaging modality and motivated number of teams to develop prototypes for different applications. Some of them can be seen in figure 13.1. Foreseen medical applications are on-line monitoring in proton therapy [561], imaging in radionuclide [562] or alpha-therapy [563], multi-modal imaging [564],[565]. First medical acquisitions on humans were made recently [566].

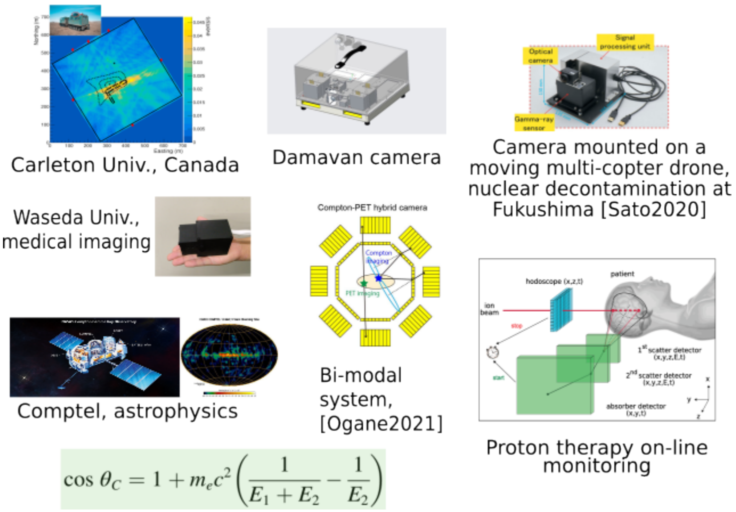

Figure 13.1: Examples of Compton camera prototypes, developed for astrophysics, nuclear decommissioning, homeland security and medical applications.

Image reconstruction is key for the implementation of Compton cameras in medical imaging applications. Since the first algebraic algorithms developed in early 70's, followed by analytical and statistical algorithms in the late 90's, significant progress has been made on modeling the physical phenomena occurring during acquisition, on regularization techniques and on mathematical derivation of new reconstruction formulas. As a result of the Compton angle formula shown in figure 13.1, formula that relates measured energies to the scattering angle θ_C, the projections are integrals on conical surfaces. The forward problem is described by a conical Radon transform. A large effort was put on the inversion of this transform for different camera geometries [567, 568]. In practice, iterative algorithms are however currently the most effective ones as they better account for low statistics, acquisition uncertainties and geometry. The main challenges they face are appropriate modelling, regularization and computing time reduction strategies.

13.3.2 LabEx contributions

Our first contribution concerns the applicability of the Compton camera in prompt-γ imaging [569]. The MEGAlib software originally developed for astrophysics was used both for Monte Carlo data simulation and for iterative image reconstruction [570]. This pioneering study was done in collaboration with A. Zoglauer from the Space Sciences Laboratory at Berkeley, USA. We then realized that mathematical models for three dimensional reconstruction were little investigated in the literature. To remedy this situation, we developed new models and a new analytical reconstruction formula for cameras composed of planar detectors. The first paper we published on this topic [571], associated to breakthrough contributions on Compton scattering tomography [572], have triggered the development of a new branch of the theory of integral operators, aiming to invert various kinds of conical Radon transforms. Inversion of Radon transforms defined on manifolds is nowadays an active research topic on which several conferences, special sessions and workshops have been organized. Our contribution was an inversion formula that allows to exploit projections with arbitrary cone axis direction:

$$f(\mathbf{v}) = 2\pi \int_0^{\pi} \int_0^{\infty} \left(\int_{-\infty}^{\infty} \widehat{\mathscr{P}_{\tau,\delta} f}(\sigma) J_0(2\pi z \tau \sigma) |\sigma|^3 e^{2i\pi\sigma \mathbf{v}.\mathbf{d}_2} d\sigma \right) d\tau d\delta,$$

where the image of the source, f, is reconstructed slice by slice by backprojecting on conical surfaces the projections $\mathscr{P}$ filtered by the ramp and the Bessel functions J_0. Extensions of this work were published in [573],[574]. Although these methods allow to reconstruct a volume in a few seconds, the quality of the images in realistic conditions is not compatible with medical applications. We thus preferred to focus on iterative methods that include a more precise modelling of the physical and statistical properties of the data.

The discrete formulation of the Compton image reconstruction problem is based on the assumption that the data follows a Poisson distribution. Maximum likelihood (ML) and *Maximum A Posteriori* (MAP), formulations then link the data to the volume to reconstruct, with eventually some a priori information. Among the iterative reconstruction methods, the most widespread is list-mode Maximum Likelihood Expectation Maximization (MLEM)[575]. We investigated direct problem modelling [576] and the numerical implementation of the conical surface model [577–579]. A novel MAP-type algorithm with Total Variation (TV) regularization for Poisson distributed data was published in [580]. Regularization allows to largely improve the quality of the images when the number of acquired events is low. A comparative study of analytical and iterative methods was carried in [581], and showcases some advantages of the Compton camera compared to the Anger SPECT camera for limited angle studies (see figure 13.2). In spite of a sensitivity that is one or two orders of magnitude superior compared to Anger cameras, Compton camera might offer only mild gain in image quality at equivalent dose. Yet, at similar reduced covering angle, Compton camera images exhibit inferior limited angle artefacts. All image reconstructions were done in 3D with the home-made software CoReSi, implemented in C++.

Compton cameras are subject to various detector-specific effects, such as energy, spatial and angular resolution limitations. Image reconstruction

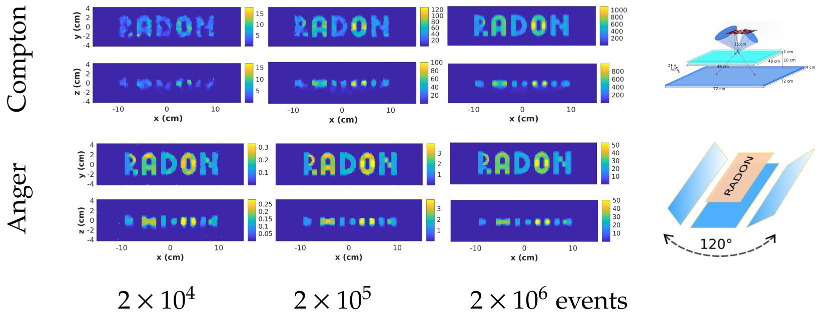

Figure 13.2: Performances of a Compton camera compared to a limited-angle Anger camera on ideal data as function of the number of detected events [581].

algorithms workaround these limitations to improve the reconstructed image's quality. Moreover, a precise model of the physics is of utmost importance in order to obtain qualitative images ([582], [25]). These studies on Doppler broadening and spectral reconstruction are relevant for nuclear medical applications where radionuclides emitting γ photons with multiple wavelengths could thus be employed, in a spectral range where the detectors are subject to important Doppler broadening. Despite the performances demonstrated by these methods on simulated data, the low resolutions currently allowed by the detectors and the low number of acquired events still hamper image quality in real experiments. Post-processing of the resulting images to discard the blur induced by the point spread function (PSF) of the imaging system is therefore necessary. A first attempt was done in the thesis of Y. Feng [583]. We show that, in conjunction with TV regularization, resolution recovery allows to reduce the elongation artefact typical to Compon imaging wth a single detector (see figure 13.3). Images are thus more precise and offer more quantitative information.

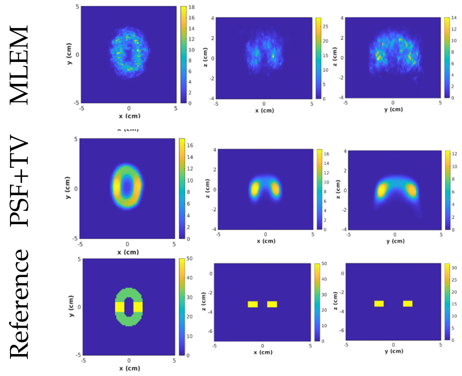

Figure 13.3: MLEM reconstruction without regularization compared to TV-MAP-EM with resolution recovery for a source orthogonal to the detector. The effect of the PSF is very important in this direction and takes the form of an elongation of the source [583].

Deep learning could pave the way towards more powerful image post-processing paradigms, more general than the current iterative methods but still adapted to small datasets. One example is resolution recovery by spatially variant and image-dependent PSFs [580, 584]. However, attention should be paid to the fact that Compton camera image reconstruction is intrinsically three-dimensional. This imposes some limitations on the type of deep-learning methods that can be applied.

13.4 Ultrasons

13.4.1 Introduction and related work

Ultrasound echography allows to non-invasively image human tissues or organs, and can be used for the assessment of many body parts, such as the heart, the vascular system, the skin, the liver, the thyroid, etc. Ultrasonic acquisitions can be used in two ways: either to image the anatomy of organs, or to characterize their function by evaluating, for example, their motion (Doppler modes) or their mechanical properties (elastography).

In ultrasound imaging, the reconstruction process is usually called beamforming. The standard reconstruction/beamforming algorithm described in the literature and widely used in available commercial scanners, called the DAS (Delay And Sum), is a fast, closed-form reconstruction algorithm that computes an image by simply summing the delayed and weighted version of the acquired raw radio frequency (RF) signals. In order to improve image quality, adaptive methods such as minimum variance have been proposed [585–587]. These methods are described as adaptive, in the sense that the weights applied before summation are made signal-dependent. While they indeed yield contrast and resolution enhancement, they are however severely limited by their computational complexity, which hampers any real-time application.

In conventional ultrasound (also coined focused imaging), the image is built line-by-line by insonifying multiple sectors of the entire field of view using sequential narrow beams, which yields frame rates on the order of 30 to 100 images/second. In cardiac imaging, such frame rates are not high enough for applications such as stress echocardiography, all-four-chamber strain imaging, electromechanical wave imaging and myocardial shear wave imaging. While multiline imaging strategies has been described to alleviate this problem [588], another venue based on wide beam imaging is still more promising. Such approach indeed allows imaging the entire field of view with the emission/reception of a single plane wave (PW) or diverging wave (DW), offering the perspective of ultrafast imaging, *i.e.* frame rates as high as several thousands of images per second [589]. However, in PW or DW imaging, the acoustic energy of unfocused beams is spread onto a wider area, resulting in a deterioration of the quality of reconstructed images if no additional processing is performed. To address this problem, coherent compounding of unfocused beams has been proposed [590]. This technique consists in transmitting multiple consecutive beams at different angles and then coherently summing the received signals to improve contrast and resolution. Therefore, a trade-off needs to be made between image quality and frame rate since compounding of more beams produces images of higher quality but decreases the frame rate.

It is only recently that the beamforming/reconstruction step has been formulated as an inverse problem in the form of eq. 13.3. This was initiated in the field of compressed sensing (CS), where several authors expressed the measurement operator corresponding to ultrasound image formation (*i.e.* the forward problem) [591–595]. In such a framework, the DAS is simply a particular solution to the associated inverse problem where the amplitude term linked to propagation and the impulse response of the ultrasound emission/reception system are neglected [591, 592]. CS-based reconstruction of ultrasound images has generated a vast literature, which would require an entire book to cover. Although impressive results have been achieved in terms of image quality and sampling rate reduction (see *e.g.* [596–598]), this approach has not led to routine applications, as solving the associated inverse problem relies on computationally-intensive iterative algorithms, which, as with adaptive methods, precludes any real-time application.

Deep learning was introduced even more recently in the field of ultrasound image reconstruction [599], but it immediately sparked the production of a substantial literature. This rapid development can be explained by the fact that, unlike the aforementioned methods, deep learning-based reconstruction can achieve high image quality while offering reduced computation times, since it is based on elementary operations that are easily and transparently implemented on GPU architectures. The expressivity of deep learning techniques has made it possible to tackle many forms of the reconstruction problem, such as reconstruction from focused, PW or DW imaging, while possibly taking into account the sparsity of the acquired data. Most architectures are based on convolutional neural networks (CNNs) (and in particular the ubiquitous U-Net), but several authors have also implemented generative adversarial networks (GANs), cycle GANs or fully-connected networks (FCNs).

13.4.2 LabEx contributions

We were one of the first teams to propose a CS reconstruction approach for ultrasound imaging in [596, 600]. The originality of this work relies on the fact that its addresses the reconstruction of raw RF signals and proposes to use a wave atoms frame to sparsely representing the oscillatory patterns of these RF data. In particular, it was shown that the wave atoms representation improves the reconstruction error obtained at 90% subsampling by 12 dB and 4 dB compared to the wavelet and Fourier bases, respectively. The CS approach has been extended to the reconstruction of 3D ultrasound images in [597], where we have demonstrated that a specific line wise sampling associated to a representation built using dictionary learning outperforms conventional, deterministic, bases (Fourier and discrete cosine) for the reconstruction of ex-vivo data for subsampling rates as high as 80%. We have then proposed to develop a CS method for functional imaging, *i.e.* accelerating duplex Doppler imaging. We have first shown [601] that randomly interleaving Doppler and imaging emissions, and using a sparse representation in the Fourier domain, allows outperforming conventional interpolation schemes with subsampling rates as high as 60%. We then developed an even more efficient approach by designing a reconstruction scheme based on a block sparse Bayesian learning algorithm [598].

In the field of the reconstruction from wide beam acquisitions, our contributions concern Fourier-based beamforming techniques. As an alternative to previous works described for PW imaging [589, 602], we have proposed an approach based on the Fourier slice theorem (as in computed tomography) to reconstruct the image spectrum [603]. The experiments have shown that the proposed method yields better results in terms of spatial resolution and contrast, when compared to the other Fourier-based methods. A further contribution consisted in extending the Fourier-based techniques to the reconstruction of sectorial images using DW [604]. This approach relies on the design of an explicit transformation, based on the derivation of an isomorphism in terms of travel time between a planar system based on PW and a sectorial one based on DW. The third contribution tackles the image quality/frame rate trade-off linked to the compounding of PW or DW acquisitions and propose to solve this dilemma by using *simultaneous* coded emission of PWs [605]. The obtained in silico and *in vitro* results outperforms the conventional compounding in terms of image quality while yielding a drastic increase of the frame rate. In addition, we made a global contribution to the reconstruction theme among the ultrasound community by organizing the Plane-wave Imaging Challenge in Medical UltraSound (PICMUS) in 2016 as part of the IEEE International Ultrasonics Symposium [606]. The database resulting from this challenge is now a reference in the community for testing and validating plane-wave reconstruction algorithms*.

Our most recent contributions concern image reconstruction based on deep learning, a field in which we produced one of the first published works [599]. The objective of the developed approaches is again to alleviate the image quality/frame rate trade-off linked to the compounding and allow ultrafast imaging. The targeted application is cardiac imaging since ultrafast acquisitions could allow the monitoring of highly transient biological phenomena, such as remotely induced shear waves and electromechanical waves, which are associated to high propagation speed in myocardium (1 to 10 m/s). In this context, we have developed a specific CNN allowing to cope with the specificities induced by the sectorial geometry associated to cardiac DW imaging, *i.e.* an inception model composed of the concatenation of multi-scale convolutional kernels [607, 608]. The obtained results indicates that the proposed method produces high-quality images using only 3 DW, yielding an image quality equivalent to that obtained with the standard compounding of 31 DWs and outperforming more conventional CNN architectures in terms of complexity, inference time and image quality (see figure 13.4).

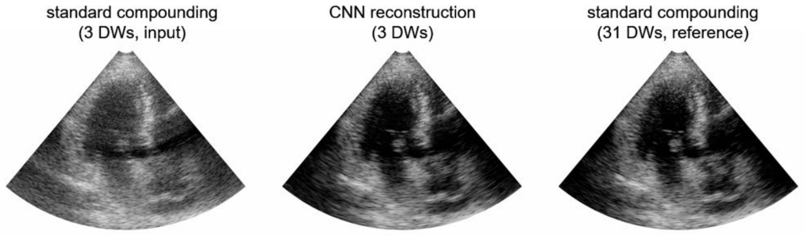

Figure 13.4: Reconstruction of the cardiac structures using standard compounding of 3 DW, the CNN described in [608] using 3 DW and the reference image obtained with the standard compounding of 31 DW.

13.5 Single-Pixel Image reconstruction

Single-pixel imaging is an extreme configuration of computational optics, where a single point detector is used to recover an image. Since the seminal work by Duarte and coworkers [609], single-pixel imaging has

---

* Google Scholar: 199 citations - Web of Science: 154 citations

been successfully applied to fluorescence microscopy, hyperspectral imaging, and short-wave infrared imaging.

Forward problem We model the raw measurement as mixed Poisson-Gaussian noise [610]

$$\mathbf{m}_{+}^{\alpha} \sim g\,\mathcal{P}(\alpha \boldsymbol{S}\boldsymbol{H}_{+}\boldsymbol{f}) + \mathcal{N}(\mu_{\text{dark}}\mathbf{1}, \sigma_{\text{dark}}^{2}\boldsymbol{I}) \tag{13.4a}$$

$$\mathbf{m}_{-}^{\alpha} \sim g\,\mathcal{P}(\alpha \boldsymbol{S}\boldsymbol{H}_{-}\boldsymbol{f}) + \mathcal{N}(\mu_{\text{dark}}\mathbf{1}, \sigma_{\text{dark}}^{2}\boldsymbol{I}) \tag{13.4b}$$

where $\boldsymbol{f}$ represents the image to be retrieved, $\mathcal{P}$ and $\mathcal{N}$ are the Poisson and Gaussian distributions, $\boldsymbol{S} \in \mathbb{R}^{M\times N}$ is a down-sampling matrix (where $M \leq N$), $\boldsymbol{H}_{+,-} \in \mathbb{R}^{N\times N}$ are the (full) measurement matrices, g is a constant that represents the overall system gain (in counts/electron), α is the intensity (in photons) of the image, μ_{dark} is the dark current (in counts), and σ_{dark} is the dark noise (in counts). We further hypothesize that g, μ_{dark} and σ_{dark} are scalars independent of the image intensity α, which can be estimated by calibration. We choose the measurement matrices such that $\boldsymbol{H}_{+} - \boldsymbol{H}_{-} = \boldsymbol{H}$ is a Hadamard matrix.

Rather than working on the raw measurements directly, they are first combined and normalized

$$\mathbf{m}^{\alpha} = (\mathbf{m}_{+}^{\alpha} - \mathbf{m}_{-}^{\alpha})/(\alpha g). \tag{13.5}$$

As the problem now reads $\mathbb{E}\,(\mathbf{m}^{\alpha}) = \boldsymbol{A}\boldsymbol{f}$, where $\boldsymbol{A} = \boldsymbol{S}\boldsymbol{H}$ is a subsampled Hadamard matrix, we will benefit from fast forward and inverse transforms. This will reduce the computational burden of the reconstruction algorithm at the cost of a loss of information that we empirically observed to be limited.

Inverse problem We consider the reconstruction problem as the maximum *a posteriori* estimation

$$\underset{f}{\text{argmax}} \quad \log p(\boldsymbol{m}^{\alpha}|\boldsymbol{f}) + \log p(\boldsymbol{f}) \tag{13.6}$$

where the probability density function $p(\boldsymbol{m}|\boldsymbol{f})$ can be approached using the noise model given in 13.4 while $p(\boldsymbol{f})$ is unknown.

The problem of 13.6 can be solved by considering an expectation-maximisation algorithm. In [611], following the algorithm unfolding approach, we have come up with an iterative algorithm whose iterations are seen as the different layers of a neural network. While some of the parameters of the layer are fixed, others are adjusted during the training phase. The resulting algorithm, which we call EM-Net, takes the following form:

$$\boldsymbol{r}_{k} = \boldsymbol{m}^{\alpha} - \boldsymbol{A}\boldsymbol{f}_{k}, \tag{13.7a}$$

$$\bar{\boldsymbol{f}}_{k} = \boldsymbol{H}^{-1}\boldsymbol{C}_{k}Diag\left(\frac{\boldsymbol{\sigma}_{k}}{\boldsymbol{\sigma}_{k} + \boldsymbol{v}_{k}}\right)\boldsymbol{r}_{k} \tag{13.7b}$$

$$\boldsymbol{f}_{k+1} = \mathcal{G}_{\boldsymbol{\theta}_{k}}(\boldsymbol{f}_{k} + \bar{\boldsymbol{f}}_{k}), \tag{13.7c}$$

where the matrices $\boldsymbol{C}_{k}$ computed before the learning phase, the measurements variances $\boldsymbol{v}_{k}$ are estimated at each iteration, while the variances

$\boldsymbol{\sigma}_k$ are learnt jointly with the parameter $\boldsymbol{\theta}_k$.

13.6 Data consistency conditions

13.6.1 Introduction and related work

Data consistency conditions (DCCs) are mathematical equations characterizing the range of a linear operator. In CT, they are used to describe the redundancies which are expected in the acquired x-ray projections to comply with the model used for tomographic reconstruction. If the DCCs are not verified, a physical effect is not modelled adequately and the DCCs can be used before reconstruction to correct the projections or reconstruction parameters and improve the CT image quality. Among other applications, DCCs have been used for geometric calibration [612, 613], beam hardening correction [614, 615], scatter estimation [616] and motion detection [617, 618].

Each scanner geometry yields a different linear operator and DCCs have been derived for most of them. The 2D parallel geometry is related to the 2D Radon transform and complete (necessary and sufficient) DCCs are known as Helgason-Ludwig conditions. The LabEx PRIMES has investigated DCCs in collaboration with the TIMC laboratory.

13.6.2 LabEx contributions

Two source positions are always on a line and one can derive a set of fan-beam DCCs from two cone-beam projections, whatever the source trajectory. We have shown that other DCCs for a pair of cone-beam conditions based on the Grangeat DCCs [613] can be derived throm these fan-beam DCCs [619]. These *pairwise* DCCs have been used for several applications.

In [620], we used pairwise DCCs to calibrate automatically a cone-beam CT scanner. Seven geometric parameters were automatically estimated prior to reconstruction by optimizing the values that minimized the pairwise inconsistencies. The results demonstrated accurate calibration on both simulated and real data, as can be seen in Figure 13.5 on cone-beam projections acquired on PRIMES' table top scanner for education [621].

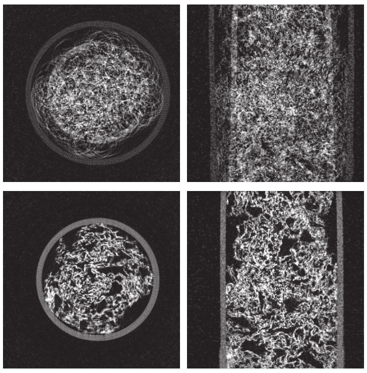

Figure 13.5: Axial (left) and transaxial (right) slices of a sponge sample acquired on a micro CT table top scanner without (top) and with (bottow) automated geometric calibration using DCCs. Figure adapted from [620].

This work has motivated a continuation on breathing motion detection in helical CT, *i.e.*, the geometry of most diagnostic CT scanners. In this geometry, the x-ray detector only images a small volume of the patient and a large CT image is reconstructed by combining the x-ray rotation along a circle by a translation of the patient in a direction orthogonal to the source trajectory plane. In this work, we have derived when pairwise DCCs may be computed and how to use these DCCs to detect breathing motion [622, 623].

More recently, we have investigated the spectral calibration of a dual-energy CT scanner [624]. Spectral calibration is required for material decomposition and this decomposition may be realized prior to image reconstruction. In this work, the spectral model was described by a polynomial which directly converts dual-energy measurements into decomposed material thicknesses. The polynomial coefficients are automatically estimated using pairwise DCCs, thus avoiding calibration measurements.

13.7 Proton computed tomography

13.7.1 Introduction and related work

Proton therapy is the use of ions for external radiotherapy (instead of X-rays in conventional external radiotherapy). The advantage of protons is their limited range since they lose energy continuously while traversing matter until stopping at a characteristic location, the Bragg peak. Accurate planning of proton therapy is crucial to position the Bragg peak in the target. The relative stopping power (RSP) of the patient tissues is the main quantity of interest for proton therapy planning. In clinical practice, the RSP is approximately derived from x-ray CT images.

The development of proton therapy has triggered a renewed interest in proton CT which had been proposed at the same time as x-ray CT [625]. Proton imaging uses protons with sufficient energy to go through the patient. The energy loss, derived from knowledge of the energy before the patient and measurement of the residual energy after the patient, can be used to derive the water equivalent path length (WEPL), *i.e.* the thickness of water which would have caused the same energy loss. The WEPL is also the integral of the RSP along the proton path. One can therefore reconstruct the RSP map by measuring the energy lost by protons, hence the motivation for developing proton CT.

In addition to having a proton beam with sufficient energy, the main challenge of proton CT is that protons are charged particles which are continuously deflected along the proton path due to multiple Coulomb scattering in the patient tissues. These random deflections cause a degradation of the spatial resolution in comparison to conventional x-ray CT. Modern proton CT scanners measure the position and the direction of each proton before and after the scanned object in a list mode fashion to estimate their most likely path (MLP) [626] and maximize the spatial resolution.

With such scanners, ion CT reconstruction is the process of computing the RSP map from the WEPL and MLP of each proton. Until 2012, the problem had been addressed either by iterative reconstruction algorithms which discretize the proton paths to yied a linear inverse problems accounting for the curved path of each proton, or by approximating the curved proton path by straight lines in filtered backprojection (FBP) algorithms.

13.7.2 LabEx contributions

The first PRIMES work was the development of a filtered-backprojection algorithm using curved MLP [627–630]. The algorithm uses an intermediate binning, denominated *distance-driven binning*, because a set of projections is binned for every beam direction, each one for a different distance from the source. A conventional FBP algorithm is then used except for a modified backprojection which uses the projection corresponding to the source-voxel distance. The algorithm improves the spatial resolution with respect to state-of-the-art FBP along straight lines 13.6. The algorithm was later compared to an iterative one [631] and yielded similar image quality. Alternatively, [632] proposed an oblique ramp filter to directly apply the ramp filter of FBP in image space which yielded a slightly better spatial resolution than other algorithms [633]. Deconvolution approaches have also been explored to further improve spatial resolution [634].

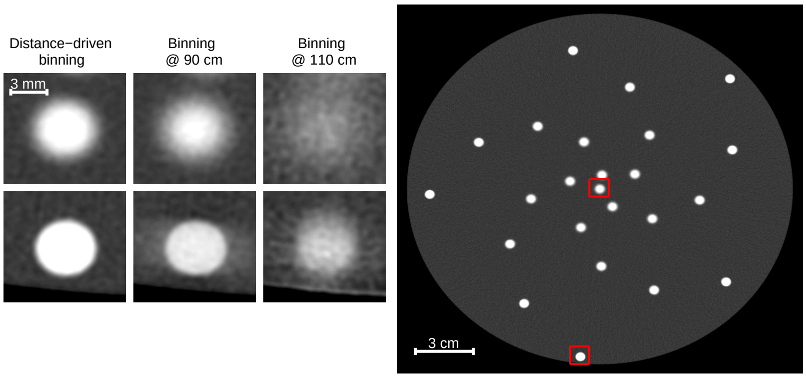

Figure 13.6: Central slice of the proton CT image of a resolution phantom obtained with distance-driven binning (right) and zooms on the central (left, top line) and peripheric (left, bottom line) inserts indicated with red squared boxes. The first column of zoomed images were obtained with distance-driven binning and the second and third columns were obtained with the standard Feldkamp-Davis-Kress (FDK) algorithm [1] using sinograms binned assuming straight line paths according to the position of protons at 90 cm (entrance of the phantom) and 110 cm (exit of the phantom) from the source, respectively. Figure from [628].

The spatial resolution of proton CT images will mainly depend on the accuracy of the MLP estimates. The initial works assumed that the protons traversed water only for estimating the MLP. We have evaluated the effect of this approximation when the traversed object is heterogeneous [635, 636] and found that the effect is minimal and can be accepted. We have also proposed an energy-adaptive version of the MLP estimation [637], *i.e.* the use of the energy knowledge of the proton before and after the patient to better estimate the MLP.

The FBP algorithm along MLP has been adapted to other approaches to proton CT imaging: attenuation [638], which uses the proton fluence before and after the object as x-ray CT, and scattering [639, 640], which uses the average change of direction while traversing the object. Similar resolution improvements were observed with distance-driven binning in comparison to straight line approximation.

All these works were mainly based on Monte Carlo simulations which has a central role in the development of proton imaging [641]. We have used it to demonstrate the clinical benefit for proton therapy planning [642–644]. Our on-going collaboration with the Ludwig Maximilian university, in Munich, has also demonstrated its relevance on real data acquired by a prototype scanner developed by a North-American collaboration [645, 646]. The best setup and technology for a clinical scanner has yet to be developed. We have quantified the spatial resolution attainable with several scanner technologies [647–649]. In collaboration with a group in Vienna (Austria), we have also investigated a new approach to measure the energy loss indirectly with the time-of-flight of protons after [650, 651] or through [652] the object.

13.8 Digital holographic microscopy

13.8.1 Introduction and related work

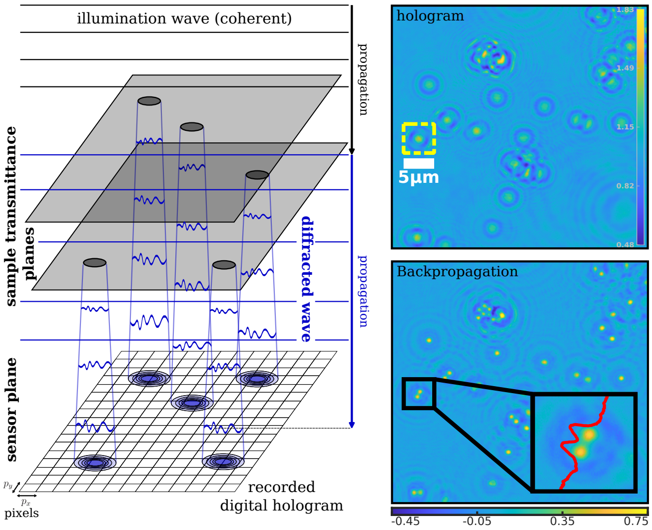

Figure 13.7: Principle of digital holography. Illustration on polystyrene beads DH acquisitions and reconstruction by simple backpropagation.

Digital holography (DH) is an imaging technique that allows to observe microscopic objects located at different distances from the sensor. Hence it is almost 3D, in contrast to conventional microscopy that is only able to produce a crisp 2D image of the objects at the focal plane of the objective. Moreover, the latter only provides an absorption information (attenuation of light intensity by the sample), while DH also gives access to the phase-shift component. In other words, DH allows the observation of both absorbing and partially or fully transparent samples in 3D, classifying it in the family of phase imaging methods [653]. An important property of DH is that it often does not require any labelling of the sample (*i.e.*, chemical processing to increase the absorption of objects of interest). Applications of this technique lay in many fields of research that go from physics (fluid mechanics, materials) to biology (cells, bacteria, viruses).

The principle of DH is schematically depicted in Fig. 13.7. It was first proposed by Gabor in 1948 (Nobel Prize in 1971) [654], from which various techniques and setups have emerged: X-ray microscopy [655], in-line and off-axis DH microscopy, ptychography [656], diffractive tomography [657]. We focus here on the in-line DH configuration that corresponds to Fig. 13.7, which can be implemented through different types of setup: lensfree [658] or mounted on classical microscopes [659]. It consists in interferometric measurements, under coherent or partially coherent illumination, of the light diffracted by the sample. The sensor, located at a given defocused distance, records the intensity of the diffracted wave that has freely propagated after passing through the sample. The measurement is called a hologram. It encodes both the absorbing and phase-shift components of the equivalent transmittance planes where objects of interest are located. These transmittance maps are related to the optical path length difference from the immersion medium n_0 induced by the sample, and constitute the targeted information that can be retrieved after a numerical reconstruction process.

In-line DH reconstruction suffers from the lack of phase information in the recorded intensity hologram. Thus a classical backpropagation (numerical reversing of light illumination) will lead to strong artifacts. To overcome this issue, advanced reconstruction algorithms consist in estimating the missing phase in the data, that is why they are called **phase retrieval** techniques. Such methods were introduced in the 1970s and 1980s with the algorithm first proposed by Gerchberg and Saxton [660] and extended by Fienup [661, 662], both based on alternating propagations and backpropagations between the object and sensor planes, and the application of prior constraints on the object plane. This class of **alternating projections** methods is still widely used today, with improvements to enforce a priori knowledge (support of the objects, admissible values domain, sparsity constraints) [663–665].

Inverse problems approaches take a different point of view from phase retrieval techniques: rather than recovering the phase on the sensor plane (which does not completely solve the sample reconstruction problem), they focus on the reconstruction of the complex-valued transmittance in the object plane. Because of measurement noise and hologram truncation at the borders of the sensor, backpropagating the complex amplitude in the sensor plane does not lead to perfect sample reconstruction, *i.e.*, restoring the sensor phase and reconstructing the complex wave in the sample plane are not strictly equivalent problems.

13.8.2 LabEx contributions

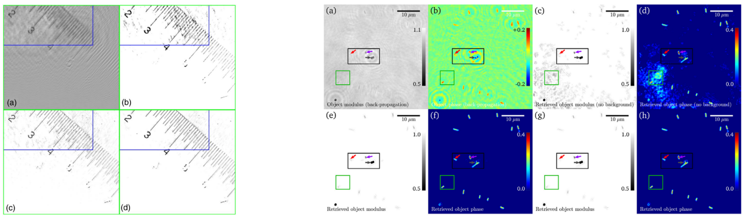

(a) DH reconstruction using numerical super-resolution [Fournier et al., 2017]

(b) Joint estimation of an interferent background and sample reconstruction in DH [Berdeu et al., 20

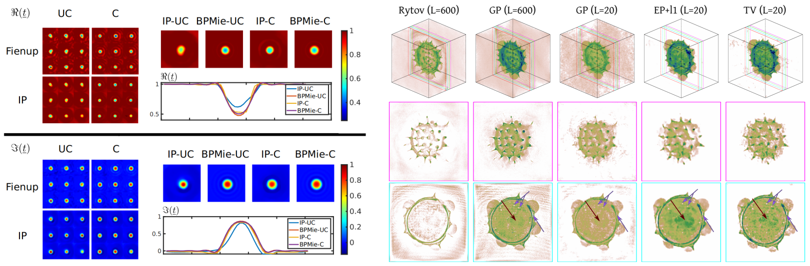

(c) Joint optical aberrations correction and sample reconstruction in DH [Brault et al., 2021]

(d) Unsupervised regullarized reconstruction in tomographic diffractive microscopy [Denneulin et al., 2022]

Figure 13.8: Model-based reconstruction in DH. a) Reconstruction using numerical super-resolution [666]. b) Joint estimation of an interferent background and sample reconstruction [667]. c) Joint optical aberrations correction and sample reconstruction [668]. d) Unsupervised regularized reconstruction in tomographic diffractive microscopy [669].

Our contribution in this domain lies in proposing advanced reconstruction techniques following an inverse problems methodology (model-based iterative reconstruction methods), allowing to better exploit data information and inject relevant prior information. Inverse approaches rely on a direct model of image formation. Compared to the state-of-the-art reconstruction methods, we considered more accurate propagation models and complicated instrumental and experimental effects (digital aperture, field truncation, partial coherence, optical aberrations, etc.). Our works are mainly dedicated to applications in biomedical imaging: bacteria characterization, detection and classification, viral infection studies, etc.

Our expertise in this field was initiated by approaches based on the estimation of morphological and quantitative parameters (position, size, refractive index) of droplets in a 3D scene from hologram measurements [670, 671]. The concept of compressive sensing led to the emergence of new types of regularizers enforcing sparsity in several domains (spatial, gradient, wavelet) that have been successfully adapted to DH reconstruction [672]. In this work, the targeted information is modeled as a stack of 2D transmittance maps. From this work, we have proposed a variety of studies and methods exploiting this inverse problem framework [659] (see Fig. 13.8).

In [666], we have developed a method allowing to perform a numerical super-resolution using a stack of sub-pixel shifted holograms of the same sample. Our algorithm jointly performs the registration and reconstruction steps (see Fig. 13.8(a)). In [673], we have proposed a proximal approach, inspired by the Alternating Direction Method of Multipliers (ADMM), to solve the reconstruction problem considering an accurate non-linear hologram formation model, and regularized by several physically-grounded constraints such as bounds on transmittance values, maximum/minimum phase, spatial smoothness or the absence of any object in parts of the field of view, from which a dedicated proximal operator has been developed (see Fig. 13.8(b)).

In [674], we have successfully combined a model-fitting approach with a regularized inversion to jointly reconstruct parameterized objects (beads) and a complex-valued pixelized transmittance map. In [675], the joint reconstruction of a sample with calibration beads is used as an autofocus process (automatic estimation of the defocus distance of the hologram) to increase the reconstruction quality thanks to a better localisation of the objects of interest. Inverse problems based methods have proven to be powerful for auto-calibration tasks, a critical step in the reconstruction process that we have developed in different settings, for example for color holographic microscopy [676], background estimation [667], or very recently optical aberrations correction [668] (see Fig. 13.8(c)).

We have also extended the 2D DH technique to the 3D reconstruction in tomographic diffractive microscopy. In this context, [669, 677] have proposed an unsupervised regularized reconstruction method that is based on the minimization of the Generalized Stein's Unbiased Risk Estimator (GSURE), that allows to automatically tune the regularization weights (see Fig. 13.8(d)).

Our future works will still deal with the exploitation of the inverse problem framework for DH reconstruction in different contexts: auto-calibration, better quantitative estimations, self-supervised methods, multi-dimensional and multi-variate data processing etc. A key point in the future will be to combine our methods to deep learning based approaches.

13.9 Conclusion

The contributions presented all along this chapter highlight how the LabEx PRIMES has permitted rich advances in the field of image reconstruction for medical and biomedical imaging. The proposed methods and algorithms developed on a wide variety of imaging modalities have benefited each other, thanks to the synergy brought by the LabEx, driven by current issues and challenges brought by imaging as a tool for the exploration, diagnosis and therapy in medical research. As a result, our works are positioned at the forefront of advances in the domain of inverse problems, and prove that there is still a room for improvements.

Reproducibility

14

Coordinator: Sorina Camarasu-Pop

Contributors: Gaël Vila, Hélène Ratiney

14.1 Definitions

As presented in [678], reproducibility can be seen as a spectrum of concerns that starts at a minimum standard of "same data+same methods=same results" to "new data and/or new methods in an independent study=same findings". These two sides of the spectrum correspond to the terms reproducibility and replicability introduced in computational science by [679] and later refined by [680]:

- **Reproducibility:** Authors provide all the necessary data and the computer codes to run the analysis again, re-creating the results.
- **Replicability:** A study that arrives at the same scientific findings as another study, collecting new data (possibly with different methods) and completing new analyses.

The definitions introduced by the Association for Computing Machinery (ACM)[*] are slightly different[†], but also integrate terminology for physical measurements:

- **Repeatability**
  The measurement can be obtained with stated precision by the same team using the same measurement procedure, the same measuring system, under the same operating conditions, in the same location on multiple trials. For computational experiments, this means that a researcher can reliably repeat her own computation.
- **Reproducibility**
  The measurement can be obtained with stated precision by a different team using the same measurement procedure, the same measuring system, under the same operating conditions, in the same or a different location on multiple trials. For computational experiments, this means that an independent group can obtain the same result using the author's own artifacts.
- **Replicability**
  The measurement can be obtained with stated precision by a different team, a different measuring system, in a different location on multiple trials. For computational experiments, this means that an independent group can obtain the same result using artifacts which they develop completely independently.

Beyond these broad definitions, the term "reproducibility" can be regarded differently depending on the research discipline and activity. V Stodden[681] identified three categories :

---

[*] `https://www.acm.org/publications/policies/artifact-review-badging`

[†] ACM has recently harmonized its terminology and definitions with those used in the broader scientific research community

- Computational reproducibility
- Empirical reproducibility
- Statistical reproducibility

The activities within PRIMES are mostly related to the first two categories, that will be presented below.

14.1.1 Computational reproducibility

14.1.2 Introduction and related work

As shown in Figure 14.1 adapted from the Turing Way Community[‡], computational reproducibility means "obtaining the same results when using the same analysis software applied to the same input data". This can be generalized to replicable results when "the same analysis software is applied to different data" and to robust results when "obtaining the same results with different software analysis on the same data". The ultimate goal is to obtain the same scientific conclusions when using different software analysis on different data.

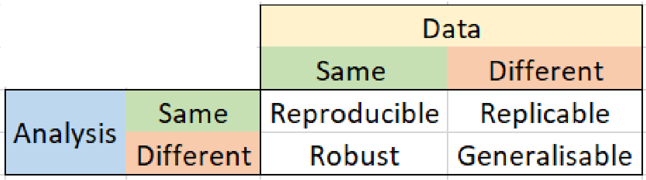

		Data	
		Same	Different
Analysis	Same	Reproducible	Replicable
	Different	Robust	Generalisable

Figure 14.1: Reproducibility matrix.

Computational reproducibility, *i.e.*, obtaining the same results when the same analysis software is applied to the same input data, may seem straightforward. However, even if we provide all the necessary data and the computer codes to run the analysis again, there are a number of issues that may prevent other researchers from re-creating our original results. [682] illustrates them with examples explaining how to make a scientific code re-runnable (R1), repeatable (R2), reproducible (R3), reusable (R4), and replicable (R5).

To begin with, the code itself may not be deterministic. Stochastic models, for example, make use of random variables which introduce variability and uncertainty into the results. These models are very useful for simulating systems that are difficult to model in a deterministic manner. Many optimization problems also use random processes leading to possibly different results. In these cases, it is therefore not possible to reach perfect bitwise reproducibility, but we should at least aim at defining the acceptable uncertainty intervals for considering the result reproducible.

When the code is deterministic, there are other factors that may prevent reproducible results. The execution of a scientific code is dependent on a computational environment comprising an operating system, a compiler, an interpreter or set of libraries. There are a number of different solutions to help improving the reproducibility in such cases. First, it is useful to review the numerical stability of the application [683]. Second, beyond the application itself, there exist different approaches to mitigate the extent of environment-introduced variability. They often rely on package

---

[‡] `https://github.com/the-turing-way/the-turing-way`

managers (such as as Conda[§]), on containerization (most of the time using Docker or Singularity), or on tools such as Guix [684]. We should note however that, in the long term, software and infrastructures cannot be frozen. Variability sources need therefore to be taken into account, evaluated and addressed accordingly.

Some of the best practices to handle our software as a research instrument are provided by [685]: "The first and foremost strategy available to maximize the transparency of research methods is openly sharing the code with the minimal restrictions possible. Complementarily, version control systems, such as Git, are the most basic and effective tool to track how software is developed, and to collaboratively produce code. Beyond open-sourcing the code, software tools implement further transparency strategies by thoroughly documenting their tools and by supporting implementations with scientific publications."

14.1.3 LabEx contributions

Our actions concentrated on the evaluation of the reproducibility of results at the computational environment level, including the code itself and different versions of the same code. The ReproVIP ANR project [ANR-21-CE45-0024-01][¶] in particular focused on evaluating and improving the computational reproducibility of scientific results obtained with the Virtual Imaging Platform (VIP) in the field of medical imaging. ReproVIP aimed at providing an integrated, end to end solution, enabling researchers to launch reproducible executions in a transparent manner.

[686] evaluated the reproducibility of tumor segmentation outcomes produced with a deep segmentation model when MRI images are pre-processed with two different versions of the same pre-processing pipeline. Results showed an important variation of segmentation outcomes between the two versions. Even though on average Dice coefficients were high, values could go down to 0.59. Figure 14.2 shows an example of the differences in outputs when running two different versions of the Brain Tumor Segmentation (BraTS) pipeline on the same input, in this case the UPENN-GMB-00019 subject from the publicly available dataset used in the article (the multiparametric magnetic resonance imaging (mpMRI) scans for de novo Glioblastoma (GBM) patients from the University of Pennsylvania Health System (UPENN-GBM) [687]).

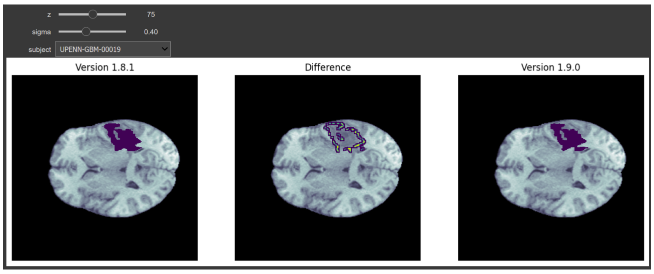

z 75
sigma 0.40
subject UPENN-GBM-00019

Figure 14.2: Differences in outputs when running two different versions of the Brain Tumor Segmentation (BraTS) pipeline on the same input [686]

[688] studied the reproducibility of neuroimaging analyses across operating systems and identified some of the causes of non-reproducibility

---

[§] `https://conda.io/projects/conda/en/latest/user-guide/tasks/manage-environments.html`

[¶] https://anr.fr/Projet-ANR-21-CE45-0024
https://vip.creatis.insa-lyon.fr/home.html

using library and system call interception. The authors found that some of the mathematical functions were based on single-precision floating-point arithmetic whose implementations in operating systems continued to evolve, leading to numerical differences in computational results.

In the last few years, the main approach to avoid software variability in such cases has been to containerize software using Docker or Singularity. However, software containers do not control for hardware heterogeneity. [689] studied the effect of hardware variability on linear registration results produced by the Oxford Centre for Functional Magnetic Resonance Imaging of the Brain Software Library (FSL) Oxford Centre for Functional Magnetic Resonance Imaging of the Brain Linear Image Registration Tool (FLIRT) application packaged with Docker and Guix. Results showed that hardware, software, and numerical variability lead to perturbations of similar magnitudes (although uncorrelated) suggesting that these three types of variability act as independent sources of numerical noise with similar magnitude. The effect of hardware perturbations on linear registration remained moderate, but might impact downstream analyses when linear registration is used as initialization step for other operations.

14.1.4 Experimental reproducibility

When we turn to the notion of reproducibility in experimental fields (imaging data acquisition in our case), we can give reproducibility a slightly different meaning as described above. One definition could be: Repeating the same measurement on a consistent sample, aiming to obtain measurements that are as close as possible, regardless of the experimental conditions. Then the conditions need to be specifically defined and will be a set of factors, such as the operator, location, equipment as well as and the operating system of the computer systems (if experimental data are processed to extract meaningful information), among others. The objective is to achieve consistency in measurements despite variations in these factors, ensuring the reliability and reproducibility of the measurement process. In the following, we showcase the efforts made in MRI to enhance the trustworthiness of measurements, employing approaches that contribute to the reproducibility of results.

Reproducibility in morphologic measurement

In collaboration with Voxcan (Animal Medical Imaging Services, Marcy L'étoile, France), MRI and micro-computed tomography arthrography (µCTA) protocols have been developed to measure cartilage thickness in non-human primate (NHP) models of osteoarthritis [690] . MRI offers clear advantages in terms of exquisite contrast, spatial resolution, 3D anatomical images and non invasive morphometric evaluation. µCTA allows for even greater spatial resolution, facilitating assessment of both cartilage and bone. However, knee cartilage imaging necessitates the injection of a contrast agent beforehand. This injection procedure may potentially cause damage to the cartilage or introduce bias in determining cartilage thickness in the acquired images. Therefore, this aspect needs careful consideration, particularly in an *in vivo* context. The use of non-human primate (NHP) models for osteoarthritis (OA) represents a valuable approach, as NHPs closely mimic the complex conditions of human OA, unlike small animal models. However, the challenge is to measure very thin cartilage thicknesses in NHP compared with those observed in humans, and to ensure that the measurements are reproducible so as to detect pathology-related changes over time. Thus the study demonstrated the reproducibility of the MRI and µCTA acquisition protocol and image processing. To do so, the right knee having received an injection of contrast agent for µCTA, the reproducibility of the mean thicknesses was assessed at different time points on each primate using Bland-Altman analyses comparing the obtained values for the left knee at different time points through MRI. For MRI measurements, key factors in facilitating reproducibility came from the use of homemade receiver coil and of susceptibility-matching foam for precise knee positioning. Finally, both MRI and µCTA were found to be valuable imaging tool for assessing the morphology of cartilage in NHP models, offering insights applicable to studies on osteoarthritis.

The case of quantitative MRI

During the years of the PRIMES labEx, MRI research has focused on the development of quantitative methods. Indeed, the MRI signal is sensitive to numerous bio/physico-chemical and physiological phenomena, and the move from simple "sensitivity" to one or more parameters specific to the (biological) sample studied by means of images is the major challenge that research is setting itself in the development of "quantitative MRI". This quantitative objective is naturally accompanied by a quest for objectivity and standardization of experimental or clinical practices. With this in mind, reproducibility, is an obvious challenge. Moreover, the notion of reproducibility appears at different levels of the development phases, according to the increasing complexity of the sources of "variability" in the results. Indeed, to qualify an MRI method as quantitative, several criteria must be verified during its development. First of all, at the time the technique is developed, the accuracy of the measurement must be characterized. This is done by assessing the reproducibility of the measurement under a number of conditions. The confidence interval here needs also to be characterized, that is performing repeated measurement under the same conditions. Of course, bias assessment, *i.e.* determining whether systematic errors occur (through testing on a calibrated phantom) as well as demonstration of measure linearity need also to be addressed. Then the validation of the technique need to be conducted rigorously with structured reports and should ensured a smooth transition from phantom to patient assessments and here again, should verified reproducibility under varied conditions. Finally the clinical validation is an important step requiring tests on a minimum set of patients (>35), including two measurements per patient (so called repeatability measurement). Ideally the conducted tests should be done across multiple centers to ensure broader applicability. Also tested on machines from different vendors for comprehensive validation constitute a great challenge. These last steps are highly demanding and encompass a long-term process, if the selected method is considered to have a future by MRI manufacturers. Also the setting up of quality assurance measures and adherence to standardized procedures are essential for minimizing uncertainty and improving reproducibility in this validation step. Standardized methods help ensure that measurements are made consistently across different operators and laboratories, contributing to greater reproducibility.

In the specific context of quantitative MRI (qMRI), the ultimate output is not directly derived from the raw measurements of the MRI scanner. Instead, it is obtained after undergoing processing and estimation steps that may introduce sources of variability. Thus a proficient understanding of the acquisition process is essential for the effective implementation of the quantitative method and correctly handle the quantification step (see Fig 14.3); ideally acquisition and quantification should work in synergy.

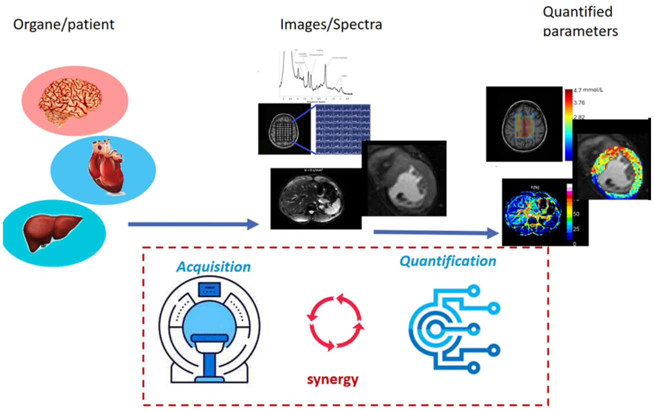

Figure 14.3: Visual summary depicting the complexity inherent in quantitative MRI research, encompassing the entire process from acquisition protocol to parameter estimation—an intricacy that must be considered in qMRI reproducibility studies

In order to obtain "experimental reproducibility", the method should be "robust" to various conditions of the signals/images to process. That is why different challenges are now developed to assess and compare the different developed quantitative methods. For example, in the "MRS fittting challenge" organized by the MRS study group of International Society for Magnetic Resonance in Medicine (ISMRM) and to which one team of the labEx PRIMES participate, significant differences in accuracy and precision between the results were obtained by the different methods/packages [691]. It is also important to establish the experimental conditions under which the results generated can be reproduced. Determining these conditions, which can be verified through quality control, is a key step in conducting reproducibility studies and bringing a given imaging technique from an academic development context to clinical use. As part of A. Naegel's phD thesis [474], quality control was proposed for dynamic 31P NMR spectroscopy (see Tissue Characterization Chapter). In the context of 31P phosphorus MRS acquired during an exercise protocol, it is necessary to check that all MRS acquisitions, consisting of a series of spectra acquired, are acquired under good conditions (checking that the phosphocreatine dynamics follow the expected time evolution and are not tainted by error due to too a late cessation of exercise or patient movement) in order to extract key information on energy metabolism and mitochondrial capacities. The effect of quality control has a direct impact on the reproducibility and reliability of the results obtained in a patient cohort study [475]. Next, Jiqing Huang's PhD research conducted within the labEx PRIMES framework illustrates development of a quantitative MRI method. Indeed, one of the focus was on the investigation of quantitative diffusion MRI for evaluating its potential in assessing liver fibrosis in chronic liver diseases. The initial phase involved the development of techniques for estimating diffusion parameters, necessitating a comparison of various fitting methods such as Nonlinear Least Squares (NLS), Segmented-NLS, and Bayesian approaches. To compare and validate these methods, bias and variance in the estimated parameters were evaluated using Monte Carlo simulations under different signal-to-noise ratio conditions. Subsequently, the methods were applied to actual acquired data, where a gold standard was unavailable, but measurements of biomarkers on liver biopsies were accessible for reference [692].

14.2 Reproducibility event organized by PRIMES

The PRIMES LabEx organized a scientific event around the concept of reproducibility in Lyon: `https://reprod-primes.sciencesconf.org/`. It addressed the reproducibility of a scientific result in the broad sense: experimental reproducibility of a measurement (influence of the acquisition chain, instrumentation, choice of parameters), numerical reproducibility (processing chain) in the AI context, reproducibility of a simulation; as well as everything concerning the statistical analysis that is implemented, the questioning of the sources of uncertainty and error.

14.3 Conclusions and discussions

Reproducibility is important/essential for many aspects, but it is no proof of good research, nor should it be considered as a goal in itself. With the rise of numerous 'computational' techniques, where parameter inference and classification are conducted through computer calculations, the issue of reproducibility in measurements or estimates arises, akin to challenges faced in experimental sciences. Definitions of reproducibility may vary across communities, but the pursuit of reliable and 'valid' results based on objective and documented criteria is a shared goal. Methodological advancements often halt at the proof-of-concept stage, lacking systematic confrontation with the reproducibility phase, which remains a crucial step in the maturation of an imaging technique to gain recognition for its impact in clinical routine.

Bibliography

Here are the references in citation order.

[1] Lee A Feldkamp, Lloyd C Davis, and James W Kress. 'Practical cone-beam algorithm'. In: *Josa a* 1.6 (1984), pp. 612–619. DOI: `10.1364/JOSAA.1.000612` (cited on pages xiv, 162).

[2] Harald Paganetti. 'Range uncertainties in proton therapy and the role of Monte Carlo simulations'. eng. In: *Phys Med Biol* 57.11 (2012), R99–117. DOI: `10.1088/0031-9155/57/11/R99` (cited on page 1).

[3] Antje-Christin Knopf and Antony Lomax. 'In vivo proton range verification: a review'. en. In: *Phys Med Biol* 58.15 (2013), R131. DOI: `10.1088/0031-9155/58/15/R131` (cited on page 1).

[4] Sebastien Binet et al. 'In-beam tests of a PET demonstrator (LAPD) for hadrontherapy beam ballistic control: data comparison to Geant4 Monte-Carlo predictions'. In: *ANIMMA 2019 – Advancements in Nuclear Instrumentation Measurement Methods and their Applications*. Vol. 225. ANIMMA 2019 – Advancements in Nuclear Instrumentation Measurement Methods and their Applications. Portorož, Poland, June 2019, p. 09005. DOI: `10.1051/epjconf/202022509005`. URL: `https://hal.science/hal-02498677` (cited on page 1).

[5] Arnaud Rozes et al. 'Le détecteur pixélisé de grande acceptance: contrôle balistique en ligne en hadronthérapie'. In: *Forum de la recherche en cancérologie Rhône-Alpes Auvergne*. Lyon, France, Apr. 2015. URL: `https://hal.science/hal-01241467` (cited on page 2).

[6] P Dendooven et al. 'Short-lived positron emitters in beam-on PET imaging during proton therapy'. In: *Physics in medicine and biology* 60.23 (2015), p. 8923. DOI: `10.1088/0031-9155/60/23/8923` (cited on page 2).

[7] E. Testa et al. 'Monitoring the Bragg peak location of 73 MeV/u carbon ions by means of prompt gamma-ray measurements'. In: *Applied Physics Letters* 93 (9 2008), pp. 093506-093506–3. DOI: `10.1063/1.2975841`. URL: `http://apl.aip.org/resource/1/applab/v93/i9/p093506_s1?isAuthorized=no` (cited on pages 2, 64).

[8] F. Le Foulher et al. 'Monte Carlo simulations of prompt-gamma emission during carbon ion irradiation'. In: *IEEE Transactions on Nuclear Science* 57 (5 2010), pp. 2768–2772. DOI: `10.1109/TNS.2010.2048042` (cited on page 2).

[9] Fabrice Le Foulher. 'Simulations Monte Carlo et mesures de l'émission de gamma prompts appliquées au contrôle en ligne en hadronthérapie'. Theses. Université Claude Bernard - Lyon I, Oct. 2010. URL: `https://theses.hal.science/tel-00573263` (cited on page 2).

[10] M.-H. Richard et al. 'Design Guidelines for a Double Scattering Compton Camera for Prompt-gamma Imaging During Ion Beam Therapy: A Monte Carlo Simulation Study'. In: *IEEE Transactions on Nuclear Science* 58 (1 2011), pp. 87–94. DOI: `10.1109/TNS.2010.2076303` (cited on page 2).

[11] Marie-Hélène Richard. 'Design study of a Compton camera for prompts-gamma imaging during ion beam therapy'. Theses. Université Claude Bernard - Lyon I, Sept. 2012. URL: `https://theses.hal.science/tel-00934715` (cited on page 2).

[12] M Pinto et al. 'Design optimisation of a TOF-based collimated camera prototype for online hadrontherapy monitoring.' In: *Physics in medicine and biology* 59 (24 Dec. 2014), pp. 7653–7674. DOI: `10.1088/0031-9155/59/24/7653`. URL: `http://www.ncbi.nlm.nih.gov/pubmed/25415207` (cited on page 2).

[13] 'Absolute prompt-gamma yield measurements for ion beam therapy monitoring.' In: *Physics in medicine and biology* 60 (2 Jan. 2015), pp. 565–94. DOI: `10.1088/0031-9155/60/2/565`. URL: `http://www.ncbi.nlm.nih.gov/pubmed/25548833` (cited on page 2).

[14] Marco Pinto et al. 'Assessment of Geant4 Prompt-Gamma Emission Yields in the Context of Proton Therapy Monitoring'. In: *Radiation Oncology* (2016), p. 10. DOI: `10.3389/fonc.2016.00010`. URL: `http://journal.frontiersin.org/article/10.3389/fonc.2016.00010/full` (cited on page 2).

[15] G. Dedes et al. 'Assessment and improvements of Geant4 hadronic models in the context of prompt-gamma hadrontherapy monitoring'. In: *Physics in Medicine and Biology* 59 (7 Apr. 2014), p. 1747. DOI: 10.1088/0031-9155/59/7/1747. URL: http://iopscience.iop.org/0031-9155/59/7/1747 (cited on page 2).

[16] J.-L. Ley et al. *Development of a Time-Of-Flight Compton Camera for Online Control of Ion therapy*. ICTR-PHE 2014. Poster. Feb. 2014. URL: https://hal.science/hal-00945490 (cited on page 3).

[17] M. Fontana et al. 'Large surface gamma cameras for medical imaging: characterization of the bismuth germanate blocks'. In: *Journal of Instrumentation* 13 (08 Aug. 2018), P08018–P08018. DOI: 10.1088/1748-0221/13/08/P08018. URL: http://stacks.iop.org/1748-0221/13/i=08/a=P08018?key=crossref.dde9e4d1c1cfc9a45b490c53402595cc (cited on page 3).

[18] M. Fontana et al. 'Monitoring Ion Beam Therapy With a Compton Camera: Simulation Studies of the Clinical Feasibility'. In: *IEEE Transactions on Radiation and Plasma Medical Sciences* 4 (2 Aug. 2020), pp. 218–232. DOI: 10.1109/TRPMS.2019.2933985 (cited on page 4).

[19] Mattia Fontana et al. 'Compton camera study for high efficiency SPECT and benchmark with Anger system'. In: *Physics in Medicine and Biology* (Oct. 2017). DOI: 10.1088/1361-6560/aa926a. URL: http://iopscience.iop.org/article/10.1088/1361-6560/aa926a (cited on pages 4, 6).

[20] Oreste Allegrini. 'Caractérisation de détecteurs pour des systèmes de monitorage des faisceaux d'ions en hadronthérapie'. Theses. Université Claude Bernard - Lyon I, Nov. 2022. URL: https://theses.hal.science/tel-04458930 (cited on pages 4, 5).

[21] Brent F B Huisman et al. 'Accelerated prompt gamma estimation for clinical proton therapy simulations'. In: *Physics in Medicine and Biology* 61 (21 Nov. 2016), pp. 7725–7743. DOI: 10.1088/0031-9155/61/21/7725. URL: http://stacks.iop.org/0031-9155/61/i=21/a=7725?key=crossref.64d467b892afa202abd156319d625774 (cited on pages 4, 5, 64).

[22] J. Krimmer et al. 'Prompt-gamma monitoring in hadrontherapy: A review'. In: *Nuclear Instruments and Methods in Physics Research Section A: Accelerators, Spectrometers, Detectors and Associated Equipment* (Aug. 2018). DOI: 10.1016/j.nima.2017.07.063. URL: http://linkinghub.elsevier.com/retrieve/pii/S0168900217308380 (cited on page 4).

[23] B F B Huisman et al. 'Analytical modeling and Monte Carlo simulations of multi-parallel slit and knife-edge slit prompt gamma cameras'. In: *Physics in Medicine & Biology* 68.11 (2023), p. 115009. DOI: 10.1088/1361-6560/acd237. URL: https://dx.doi.org/10.1088/1361-6560/acd237 (cited on page 5).

[24] Maxime Jacquet et al. 'A time-of-flight-based reconstruction for real-time prompt-gamma imaging in proton therapy'. In: *Physics in Medicine and Biology* 66.13 (2021), p. 135003. DOI: 10.1088/1361-6560/ac03ca. URL: https://hal.science/hal-03319261 (cited on page 5).

[25] Enrique Muñoz et al. 'Imaging of polychromatic sources through Compton spectral reconstruction'. In: *Physics in Medicine & Biology* 67.19 (2022), p. 195017 (cited on pages 6, 155).

[26] Christian Golnik et al. 'Range assessment in particle therapy based on prompt γ-ray timing measurements'. In: *Physics in Medicine and Biology* 59 (18 Sept. 2014), pp. 5399–5422. DOI: 10.1088/0031-9155/59/18/5399. URL: http://www.ncbi.nlm.nih.gov/pubmed/25157685 (cited on page 6).

[27] Joost M Verburg and Joao Seco. 'Proton range verification through prompt gamma-ray spectroscopy.' In: *Physics in medicine and biology* 59 (23 Dec. 2014), pp. 7089–106. DOI: 10.1088/0031-9155/59/23/7089. URL: http://www.ncbi.nlm.nih.gov/pubmed/25365362 (cited on page 6).

[28] D. Dauvergne, J. Krimmer, and E. Testa. 'Dispositif d'imagerie, appareil d'imagerie le comprenant et procédé d'imagerie'. ICG020479 FR (patent application). 2016 (cited on page 6).

[29] J. Krimmer et al. 'A cost-effective monitoring technique in particle therapy via uncollimated prompt gamma peak integration'. In: *Applied Physics Letters* 110 (15 Apr. 2017), p. 154102. DOI: 10.1063/1.4980103. URL: http://aip.scitation.org/doi/10.1063/1.4980103 (cited on page 6).

[30] Pierre Everaere. ‘Contrôle en ligne en protonthérapie - Conception d’un moniteur de faisceau en technologie diamant et mise en œuvre d’une technique de détection de rayons gamma prompts adaptée aux faisceaux cliniques’. Theses. Université Grenoble Alpes [2020-....], Dec. 2023. URL: `https://theses.hal.science/tel-04592924` (cited on page 6).

[31] Pierre Everaere et al. ‘Energy Integration : a new method for online-range verification in proton therapy with pulsed-beams’. In: *Frontiers in Physics* 12 (2024), p. 1371015. DOI: `10.3389/fphy.2024.1371015t`. URL: `https://hal.science/hal-04589792t` (cited on page 7).

[32] L. Gallin-Martel et al. *Design of a high dynamic range integrated charge to digital converter for online dosimetry in radiotherapy*. IEEE Nuclear Science Symposium & Medical Imaging Conference (2016 IEEE NSS/MIC). Poster. Oct. 2016. DOI: `10.1109/NSSMIC.2016.8069397`. URL: `https://hal.in2p3.fr/in2p3-01390857` (cited on pages 10, 16).

[33] Robin Fabbro. ‘Modélisation d’un accélérateur linéaire clinique en vue de l’exploitation d’un détecteur à transmission dédié au contrôle qualité en radiothérapie’. Theses. Université Grenoble Alpes, Nov. 2017. URL: `https://theses.hal.science/tel-01720776` (cited on page 11).

[34] S. Deng et al. ‘Very fast front end ASIC associated with multi anode PMT for a scintillating-fibre beam hodoscope’. In: *TWEPP 2012 Topical Workshop on Electronics for Particle Physics*. Oxford, United Kingdom, Sept. 2012, pages 2013 JINST 8 C01047. URL: `https://hal.science/hal-00842813` (cited on page 12).

[35] Jean-Luc Ley. ‘Mise en oeuvre d’un démonstrateur de caméra Compton pour l’imagerie en médecine nucléaire et pour le contrôle en temps réel de l’hadronthérapie à l’aide des rayonnements gamma prompts’. Theses. Université Claude Bernard Lyon 1, Dec. 2015. URL: `https://hal.science/tel-01280098` (cited on page 12).

[36] J. Krimmer et al. ‘Development of a Compton camera for medical applications based on silicon strip and scintillation detectors’. In: *Nuclear Instruments and Methods in Physics Research Section A: Accelerators, Spectrometers, Detectors and Associated Equipment* 787 (2015), pp. 98–101. DOI: `10.1016/j.nima.2014.11.042`. URL: `https://hal.science/hal-01101334` (cited on page 12).

[37] J. Krimmer et al. ‘Real-Time Online Monitoring of the Ion Range by Means of Prompt Secondary Radiations’. In: *3rd International Conference On Advancements In Nuclear Instrumentation Measurement Methods And Their Applications (ANIMMA 2013)*. Marseille, France, June 2013, pp. 1–8. DOI: `10.1109/ANIMMA.2013.6728046`. URL: `https://hal.science/hal-00873701` (cited on page 12).

[38] Mattia Fontana. ‘Tests and characterization of gamma cameras for medical applications’. Theses. Université de Lyon, Dec. 2018. URL: `https://hal.science/tel-02017992` (cited on page 12).

[39] X. Chen et al. ‘A Time-Of-Flight Gamma Camera Data Acquisition System for Hadrontherapy Monitoring’. In: *2019 IEEE Nuclear Science Symposium (NSS) and Medical Imaging Conference (MIC)*. Manchester, United Kingdom, Oct. 2019, pp. 1–3. DOI: `10.1109/NSS/MIC42101.2019.9060072`. URL: `https://hal.science/hal-02309735` (cited on page 12).

[40] C. Caplan et al. ‘A μTCA back-end firmware for data acquisition and slow control of the CLaRyS Compton camera’. In: *IEEE MIC 2019*. 2019 IEEE Nuclear Science Symposium and Medical Imaging Conference (NSS/MIC). Manchester, United Kingdom, Oct. 2019. DOI: `10.1109/NSS/MIC42101.2019.9059941`. URL: `https://hal.science/hal-02309672` (cited on page 12).

[41] O V L Allegrini. ‘Caractérisation de détecteurs pour des systèmes de monitorage des faisceaux d’ions en hadronthérapie’. PhD thesis. Université Claude Bernard Lyon 1, 2017 (cited on page 12).

[42] O. Allegrini et al. ‘Characterization of a beam-tagging hodoscope for hadrontherapy monitoring’. In: *Journal of Instrumentation* 16 (2 Feb. 2021), P02028. DOI: `10.1088/1748-0221/16/02/P02028`. URL: `https://iopscience.iop.org/article/10.1088/1748-0221/16/02/P02028` (cited on page 12).

[43] C. Hoarau et al. ‘RF pulse amplifier for CVD-diamond particle detectors’. In: *Journal of Instrumentation* 16.04 (2021), T04005. DOI: `10.1088/1748-0221/16/04/T04005`. URL: `https://dx.doi.org/10.1088/1748-0221/16/04/T04005` (cited on page 14).

[44] S. Curtoni et al. 'Performance of CVD diamond detectors for single ion beam-tagging applications in hadrontherapy monitoring'. In: *Nuclear Instruments and Methods in Physics Research Section A: Accelerators, Spectrometers, Detectors and Associated Equipment* 1015 (2021), p. 165757. DOI: `https://doi.org/10.1016/j.nima.2021.165757`. URL: `https://www.sciencedirect.com/science/article/pii/S0168900221007427` (cited on page 14).

[45] Nicolas Rosuel. 'Monitorage en ligne de la radiothérapie par rayonnement synchrotron à l'aide de détecteurs diamant'. Theses. Université Grenoble Alpes [2020-....], Dec. 2021. URL: `https://theses.hal.science/tel-03943028` (cited on pages 16, 30).

[46] Francesca di Franco et al. 'Monocrystalline diamond detector for online monitoring during synchrotron microbeam radiotherapy'. In: *Journal of Synchrotron Radiation* 30.6 (Oct. 2023), pp. 1076–1085. DOI: `10.1107/s160057752300752x` (cited on page 16).

[47] Hugo Palmans et al. 'Dosimetry of small static fields used in external photon beam radiotherapy: Summary of TRS-483, the IAEA–AAPM international Code of Practice for reference and relative dose determination'. In: *Medical Physics* 45.11 (2018), e1123–e1145. DOI: `https://doi.org/10.1002/mp.13208`. URL: `https://aapm.onlinelibrary.wiley.com/doi/abs/10.1002/mp.13208` (cited on page 18).

[48] C. Joram, G. Haefeli, and B. Leverington. 'Scintillating Fibre Tracking at High Luminosity Colliders'. In: *Journal of Instrumentation* 10.08 (2015), p. C08005. DOI: `10.1088/1748-0221/10/08/C08005`. URL: `https://dx.doi.org/10.1088/1748-0221/10/08/C08005` (cited on page 18).

[49] P. Pittet et al. 'SciFi detector and associated method for real-time determination of profile and output factor for small fields in stereotactic radiotherapy'. In: *Medical Physics* 47.4 (2020), pp. 1930–1939. DOI: `10.1002/mp.14019`. URL: `https://hal.science/hal-02444252` (cited on page 18).

[50] Patrick Pittet et al. 'Assurance Qualité des mini-faisceaux en radiothérapie stéréotaxique avec un détecteur scintillant multicouche et une reconstruction tomographique de champ'. In: *Journée d'étude GDR MI2B - LabEx PRIMES sur les moniteurs faisceaux et contrôle en ligne des irradiations biomédicales*. Lyon, France, Sept. 2020. URL: `https://hal.science/hal-03159227` (cited on page 18).

[51] Josué Esteves et al. 'A novel QA phantom based on scintillating fiber ribbons with implementation of 2D dose tomography for small-field radiotherapy'. In: *Medical Physics* 50.1 (2023), pp. 619–632. DOI: `https://doi.org/10.1002/mp.15902`. URL: `https://aapm.onlinelibrary.wiley.com/doi/abs/10.1002/mp.15902` (cited on pages 18, 19).

[52] Odran Pivot et al. 'Reconstruction of radiotherapy dose fields shaped with a multileaf collimator from six projections'. In: *2020 IEEE Nuclear Science Symposium and Medical Imaging Conference, NSS/MIC*. virtual, United States, Oct. 2020. URL: `https://hal.science/hal-03145322` (cited on page 18).

[53] Odran Pivot et al. 'A tomographic reconstruction algorithm for cross-sectional imaging of IMRT beams from six projections'. In: *Physics in Medicine and Biology* 68.9 (Apr. 2023), p. 095015. DOI: `10.1088/1361-6560/acc925`. URL: `https://hal.science/hal-04061147` (cited on page 19).

[54] P. Pittet et al. 'PO-1570 Instrumented solid-water phantom for quick and high-resolution PDD measurement'. In: *Radiotherapy and Oncology* 170 (2022). ESTRO 2022, 6-10 May 2022, Copenhagen. Onsite in Copenhagen and Online, S1352–S1353. DOI: `https://doi.org/10.1016/S0167-8140(22)03534-4`. URL: `https://www.sciencedirect.com/science/article/pii/S0167814022035344` (cited on page 19).

[55] James Archer et al. 'High spatial resolution scintillator dosimetry of synchrotron microbeams'. In: *Scientific Reports* 9.6873 (2019). DOI: `10.1038/s41598-019-43349-6`. URL: `https://www.nature.com/articles/s41598-019-43349-6` (cited on page 20).

[56] P Suortti and W Thomlinson. 'Medical applications of synchrotron radiation'. In: *Phys Med Biol* 48.13 (July 2003), R1–35. DOI: `10.1088/0031-9155/48/13/201` (cited on page 23).

[57] J. Balosso et al. 'Monoenergetic synchrotron beams: first human experience for therapeutic purpose'. In: *ESTRO 33*. Vol. 111. 1. Vienne, Austria, Apr. 2014, SP–0205. URL: `https://hal.science/hal-01053178` (cited on pages 23, 26).

[58] J.F. Adam et al. 'Synchrotron Stereotactic Radiation Therapy: A Report on Phase 1/2 Clinical Trial Achievements, Ongoing Developments, and Long-Term Prospects'. In: *ASTRO annual meeting*. Vol. 96. International Journal of Radiation Oncology Biology Physics 2. Boston, United States, Sept. 2016, E624–E625. DOI: `10.1016/j.ijrobp.2016.06.2193`. URL: `https://hal.science/hal-01492864` (cited on pages 23, 26).

[59] Laura Eling et al. 'Ultra high dose rate Synchrotron Microbeam Radiation Therapy. Preclinical evidence in view of a clinical transfer'. In: *Radiotherapy & Oncology* 139 (Oct. 2019), pp. 56–61. DOI: `10.1016/j.radonc.2019.06.030`. URL: `https://hal.science/hal-02510707` (cited on pages 23, 28).

[60] Nicolas Coquery et al. 'Locomotion and eating behavior changes in Yucatan minipigs after unilateral radio-induced ablation of the caudate nucleus'. In: *Scientific Reports* 9.1 (Dec. 2019), p. 17082. DOI: `10.1038/s41598-019-53518-2`. URL: `https://hal.science/hal-02376578` (cited on pages 23, 41).

[61] Jean-François Adam et al. 'Toward Neuro-Oncologic Clinical Trials of High-Dose-Rate Synchrotron Microbeam Radiation Therapy: First Treatment of a Spontaneous Canine Brain Tumor'. In: *International Journal of Radiation Oncology* Biology* Physics* 113.5 (2022), pp. 967–973. DOI: `10.1016/j.ijrobp.2022.04.022` (cited on page 23).

[62] T P Hanna et al. 'The population benefit of evidence-based radiotherapy: 5-Year local control and overall survival benefits'. In: *Radiother Oncol* 126.2 (Feb. 2018), pp. 191–197. DOI: `10.1016/j.radonc.2017.11.004` (cited on page 24).

[63] Timothy Paul Hanna, Geoffrey Paul Delaney, and Michael Bernard Barton. 'The Population Benefit of Radiotherapy for Malignant Brain Tumors: Local Control and Survival Estimates for Guideline-Based Use'. In: *J Natl Compr Canc Netw* 14.9 (Sept. 2016), pp. 1111–9. DOI: `10.6004/jnccn.2016.0120` (cited on page 24).

[64] Kari Tanderup et al. 'Advancements in brachytherapy'. In: *Adv Drug Deliv Rev* 109 (Jan. 2017), pp. 15–25. DOI: `10.1016/j.addr.2016.09.002` (cited on page 24).

[65] Jo Picot et al. 'The INTRABEAM® Photon Radiotherapy System for the adjuvant treatment of early breast cancer: a systematic review and economic evaluation'. In: *Health Technol Assess* 19.69 (Aug. 2015), pp. 1–190. DOI: `10.3310/hta19690` (cited on page 24).

[66] Sagar A Patel, Jennifer Y Wo, and Theodore S Hong. 'Advancing Techniques of Radiation Therapy for Rectal Cancer'. In: *Semin Radiat Oncol* 26.3 (July 2016), pp. 220–5. DOI: `10.3310/hta19690` (cited on page 24).

[67] Nicolas D Prionas et al. 'Kilovoltage rotational external beam radiotherapy on a breast computed tomography platform: a feasibility study'. In: *Int J Radiat Oncol Biol Phys* 84.2 (Oct. 2012), pp. 533–9. DOI: `10.1016/j.ijrobp.2011.12.042` (cited on page 24).

[68] Dylan Y Breitkreutz et al. 'Monte Carlo simulations of a kilovoltage external beam radiotherapy system on phantoms and breast patients'. In: *Med Phys* 44.12 (Dec. 2017), pp. 6548–6559. DOI: `10.1002/mp.12619` (cited on page 24).

[69] Magdalena Bazalova-Carter et al. 'Feasibility of external beam radiation therapy to deep-seated targets with kilovoltage x-rays'. In: *Med Phys* 44.2 (Feb. 2017), pp. 597–607. DOI: `10.1002/mp.12047` (cited on page 24).

[70] Jean-François Adam et al. 'Prolonged survival of Fischer rats bearing F98 glioma after iodine-enhanced synchrotron stereotactic radiotherapy'. In: *Int J Radiat Oncol Biol Phys* 64.2 (Feb. 2006), pp. 603–11. DOI: `10.1016/j.ijrobp.2005.09.004`. URL: `https://inserm.hal.science/inserm-00388754v1` (cited on pages 24, 26, 35).

[71] Marie-Claude Biston et al. 'Cure of Fisher rats bearing radioresistant F98 glioma treated with cis-platinum and irradiated with monochromatic synchrotron X-rays'. In: *Cancer Res* 64.7 (Apr. 2004), pp. 2317–23. DOI: `10.1158/0008-5472.can-03-3600` (cited on page 24).

[72] Julia Rousseau et al. 'Efficacy of intracerebral delivery of cisplatin in combination with photon irradiation for treatment of brain tumors'. In: *J Neurooncol* 98.3 (July 2010), pp. 287–95. DOI: `10.1007/s11060-009-0074-3` (cited on pages 24, 27).

[73] L. Bobyk et al. 'Photoactivation of gold nanoparticles for glioma treatment'. In: *Nanomedicine: Nanotechnology, Biology and Medicine* 9.7 (May 2013), pp. 1089–1097. DOI: 10.1016/j.nano.2013.04.007. URL: https://hal.science/hal-00850657 (cited on pages 24, 25).

[74] F. Taupin et al. 'Gadolinium nanoparticles and contrast agent as radiation sensitizers'. In: *Physics in Medicine and Biology* 60.11 (June 2015), pp. 4449–4464. DOI: 10.1088/0031-9155/60/11/4449. URL: https://hal.in2p3.fr/in2p3-01157446 (cited on pages 24, 25, 27, 54).

[75] Gi-Hwan Choi et al. 'Photon activated therapy (PAT) using monochromatic synchrotron X-rays and iron oxide nanoparticles in a mouse tumor model: feasibility study of PAT for the treatment of superficial malignancy'. In: *Radiat Oncol* 7 (Oct. 2012), p. 184. DOI: 10.1186/1748-717X-7-184 (cited on page 24).

[76] Anne-Laure Bulin et al. 'Radiation Dose-Enhancement Is a Potent Radiotherapeutic Effect of Rare-Earth Composite Nanoscintillators in Preclinical Models of Glioblastoma'. In: *Advanced Science* (Sept. 2020), p. 2001675. DOI: 10.1002/advs.202001675. URL: https://hal.science/hal-02939291 (cited on page 24).

[77] Solveig Reymond et al. *Photoactivation of Iron Nanoparticles for the Improvement of Glioma Treatment*. Forum de la recherche en Cancérologie 2018. Poster. Apr. 2018. URL: https://hal.science/hal-01990774 (cited on pages 24, 25).

[78] Vincent Favaudon et al. 'Ultrahigh dose-rate FLASH irradiation increases the differential response between normal and tumor tissue in mice'. In: *Sci Transl Med* 6.245 (July 2014), 245ra93. DOI: 10.1126/scitranslmed.3008973 (cited on page 25).

[79] Pierre Montay-Gruel et al. 'Irradiation in a flash: Unique sparing of memory in mice after whole brain irradiation with dose rates above 100Gy/s'. In: *Radiother Oncol* 124.3 (Sept. 2017), pp. 365–369. DOI: 10.1016/j.radonc.2017.05.003 (cited on page 25).

[80] Marco Durante, Elke Bräuer-Krisch, and Mark Hill. 'Faster and safer? FLASH ultra-high dose rate in radiotherapy'. In: *Br J Radiol* 91.1082 (Feb. 2018), p. 20170628. DOI: 10.1259/bjr.20170628 (cited on page 25).

[81] W Zeman et al. 'Tolerance of mouse-brain tissue to high-energy deuterons'. In: *Science* 130.3391 (Dec. 1959), pp. 1760–1. DOI: 10.1126/science.130.3391.1760-a (cited on page 25).

[82] Yaacov Richard Lawrence et al. 'Radiation dose-volume effects in the brain'. In: *Int J Radiat Oncol Biol Phys* 76.3 Suppl (Mar. 2010), S20–7. DOI: 10.1016/j.ijrobp.2009.02.091 (cited on page 25).

[83] J W Hopewell and K R Trott. 'Volume effects in radiobiology as applied to radiotherapy'. In: *Radiother Oncol* 56.3 (Sept. 2000), pp. 283–8. DOI: 10.1016/s0167-8140(00)00236-x (cited on page 25).

[84] R J Yaes and A Kalend. 'Local stem cell depletion model for radiation myelitis'. In: *Int J Radiat Oncol Biol Phys* 14.6 (June 1988), pp. 1247–59. DOI: 10.1016/0360-3016(88)90404-x (cited on page 25).

[85] Audrey Bouchet et al. 'Better Efficacy of Synchrotron Spatially Microfractionated Radiation Therapy Than Uniform Radiation Therapy on Glioma'. In: *Int J Radiat Oncol Biol Phys* 95.5 (Aug. 2016), pp. 1485–1494. DOI: 10.1016/j.ijrobp.2016.03.040 (cited on pages 25, 27, 28).

[86] Laura Eling et al. 'Unexpected Benefits of Multiport Synchrotron Microbeam Radiation Therapy for Brain Tumors'. In: *Cancers* 13.5 (2021), pp. 936-1-936–15. DOI: 10.3390/cancers13050936. URL: https://hal.science/hal-03326627 (cited on pages 25, 28, 40).

[87] M A Grotzer et al. 'Microbeam radiation therapy: Clinical perspectives'. In: *Phys Med* 31.6 (Sept. 2015), pp. 564–7. DOI: 10.1016/j.ejmp.2015.02.011 (cited on page 25).

[88] B P Poncelet et al. 'Brain parenchyma motion: measurement with cine echo-planar MR imaging'. In: *Radiology* 185.3 (Dec. 1992), pp. 645–51. DOI: 10.1148/radiology.185.3.1438740 (cited on page 25).

[89] Jayde Livingstone et al. 'Experimental optimisation of the X-ray energy in microbeam radiation therapy'. In: *Physica Medica* 45 (Jan. 2018), pp. 156–161. DOI: 10.1016/j.ejmp.2017.12.017. URL: https://hal.science/hal-01680837 (cited on page 25).

[90] Jean François Adam et al. 'Synchrotron radiation therapy of malignant brain glioma loaded with an iodinated contrast agent: first trial on rats bearing F98 gliomas'. In: *Int J Radiat Oncol Biol Phys* 57.5 (Dec. 2003), pp. 1413–26. DOI: `10.1016/j.ijrobp.2003.07.007` (cited on page 26).

[91] S Corde et al. 'Synchrotron radiation-based experimental determination of the optimal energy for cell radiotoxicity enhancement following photoelectric effect on stable iodinated compounds'. In: *Br J Cancer* 91.3 (Aug. 2004), pp. 544–51. DOI: `10.1038/sj.bjc.6601951` (cited on page 26).

[92] Elke Bräuer-Krisch et al. 'Medical physics aspects of the synchrotron radiation therapies: Microbeam radiation therapy (MRT) and synchrotron stereotactic radiotherapy (SSRT)'. In: *Physica Medica* 31.6 (2015), pp. 568–583. DOI: `10.1016/j.ejmp.2015.04.016`. URL: `https://hal.science/hal-01571014` (cited on page 26).

[93] M Renier et al. 'The radiotherapy clinical trials projects at the ESRF: technical aspects'. In: *Eur J Radiol* 68.3 Suppl (Dec. 2008), S147–50. DOI: `10.1016/j.ejrad.2008.04.057` (cited on page 26).

[94] M Edouard et al. 'Treatment plans optimization for contrast-enhanced synchrotron stereotactic radiotherapy'. In: *Med Phys* 37.6 (June 2010), pp. 2445–56. DOI: `10.1118/1.3327455` (cited on page 26).

[95] M Vautrin et al. 'TU-E-BRB-03: A Treatment Planning System for Contrast-Enhanced Stereotactic Synchrotron Radiation Therapy Clinical Trials'. In: *Medical Physics* 38.6Part29 (2011), pp. 3767–3767. DOI: `10.1118/1.3613179` (cited on page 26).

[96] Y Prezado et al. 'Biological equivalent dose studies for dose escalation in the stereotactic synchrotron radiation therapy clinical trials'. In: *Med Phys* 36.3 (Mar. 2009), pp. 725–33. DOI: `10.1118/1.3070538` (cited on page 26).

[97] Y Prezado et al. 'Dosimetry protocol for the forthcoming clinical trials in synchrotron stereotactic radiation therapy (SSRT)'. In: *Med Phys* 38.3 (Mar. 2011), pp. 1709–17. DOI: `10.1118/1.3556561`. URL: `https://hal.univ-grenoble-alpes.fr/inserm-00589299/` (cited on page 26).

[98] Layal Obeid et al. 'Absolute perfusion measurements and associated iodinated contrast agent time course in brain metastasis: a study for contrast-enhanced radiotherapy.' In: *Journal of Cerebral Blood Flow and Metabolism* 34.4 (Apr. 2014), pp. 638–45. DOI: `10.1038/jcbfm.2013.239`. URL: `https://www.hal.inserm.fr/inserm-00964525` (cited on pages 26, 27).

[99] H. Labriet et al. 'Significant dose reduction using synchrotron radiation computed tomography: first clinical case and application to high resolution CT exams'. In: *Scientific Reports* 8.1 (2018), pp. 12491-1-12491–7. DOI: `10.1038/s41598-018-30902-y`. URL: `https://hal.science/hal-02082768` (cited on page 27).

[100] Joshua L. Wang et al. 'Phase I trial of intracerebral convection-enhanced delivery of carboplatin for treatment of recurrent high-grade gliomas'. In: *PLOS ONE* 15.12 (Dec. 2021), pp. 1–12. DOI: `10.1371/journal.pone.0244383` (cited on page 27).

[101] Camille Verry et al. 'Theranostic AGuIX nanoparticles as radiosensitizer: A phase I, dose-escalation study in patients with multiple brain metastases (NANO-RAD trial)'. In: *Radiotherapy and Oncology* 160 (2021), pp. 159–165. DOI: `10.1016/j.radonc.2021.04.021` (cited on page 27).

[102] P. Deman et al. 'Monochromatic minibeams radiotherapy: from healthy tissue-sparing effect studies toward first experimental glioma bearing rats therapy'. In: *International Journal of Radiation Oncology, Biology, Physics* 82.4 (Mar. 2012), e693–e700. DOI: `10.1016/j.ijrobp.2011.09.013`. URL: `https://hal.science/hal-00850697` (cited on page 27).

[103] Lloyd M L Smyth et al. 'The normal tissue effects of microbeam radiotherapy: What do we know, and what do we need to know to plan a human clinical trial?' In: *Int J Radiat Biol* 92.6 (June 2016), pp. 302–11. DOI: `10.3109/09553002.2016.1154217` (cited on page 27).

[104] B. Pouyatos et al. 'Synchrotron X-ray microtransections: a non invasive approach for epileptic seizures arising from eloquent cortical areas'. In: *Scientific Reports* 6 (2016), pp. 27250–27250. DOI: `10.1038/srep27250`. URL: `https://hal.science/hal-01443812` (cited on page 28).

[105] F. Studer et al. 'Synchrotron X-ray microbeams: A promising tool for drug-resistant epilepsy treatment'. In: *Physica Medica* 31.6 (2015), pp. 607–614. DOI: `10.1016/j.ejmp.2015.04.005`. URL: `https://hal.science/hal-01236301` (cited on page 28).

[106] TRS IAEA. '398. Absorbed dose determination in external beam radiotherapy: An International Code of Practice for Dosimetry based on standards of absorbed dose to water'. In: *Vienna International Atomic Energy Agency* (2000). URL: `https://www.iaea.org/publications/5954/absorbed-dose-determination-in-external-beam-radiotherapy` (cited on page 28).

[107] P Fournier et al. 'Absorbed dose-to-water protocol applied to synchrotron-generated x-rays at very high dose rates'. In: *Physics in Medicine & Biology* 61.14 (2016), N349. DOI: `10.1088/0031-9155/61/14/N349` (cited on page 28).

[108] Jayde Livingstone et al. 'Characterization of a synthetic single crystal diamond detector for dosimetry in spatially fractionated synchrotron x-ray fields'. In: *Medical Physics* 43.7 (2016), pp. 4283–4293. DOI: `https://doi.org/10.1118/1.4953833`. URL: `https://aapm.onlinelibrary.wiley.com/doi/abs/10.1118/1.4953833` (cited on page 28).

[109] Jayde Livingstone et al. 'Preclinical radiotherapy at the Australian Synchrotron's Imaging and Medical Beamline: instrumentation, dosimetry and a small-animal feasibility study'. In: *Journal of Synchrotron Radiation* 24.4 (July 2017), pp. 854–865. DOI: `10.1107/S1600577517006233`. URL: `https://doi.org/10.1107/S1600577517006233` (cited on page 28).

[110] Jayde Livingstone et al. 'Experimental optimisation of the X-ray energy in microbeam radiation therapy'. In: *Physica Medica* 45 (2018), pp. 156–161. DOI: `https://doi.org/10.1016/j.ejmp.2017.12.017`. URL: `https://www.sciencedirect.com/science/article/pii/S1120179717306567` (cited on page 28).

[111] Paolo Pellicioli. 'Development of radiochromic film dosimetry at micrometric scale for microbeam radiation therapy'. PhD thesis. Université Grenoble Alpes, 2019. URL: `https://theses.hal.science/tel-03917125v1` (cited on page 28).

[112] Alexandre Ocadiz et al. 'Film dosimetry studies for patient specific quality assurance in microbeam radiation therapy'. In: *Physica Medica* 65 (Sept. 2019), pp. 227–237. DOI: `10.1016/j.ejmp.2019.09.071`. URL: `https://hal.science/hal-02308619` (cited on page 29).

[113] Sarvenaz Keshmiri. 'A multi-scale treatment planning system for microbeam radiation therapy -Validation and biological dosimetry'. Theses. Université Grenoble Alpes [2020-....], Mar. 2023. URL: `https://theses.hal.science/tel-04144657` (cited on pages 29, 30).

[114] Florian Thevenet et al. 'Microstrip plastic scintillating detector system for quality assurance in synchrotron microbeam radiotherapy'. In: *Scientific Reports* (Aug. 2024). DOI: `10.21203/rs.3.rs-4755567/v1`. URL: `http://dx.doi.org/10.21203/rs.3.rs-4755567/v1` (cited on page 29).

[115] F. Thevenet et al. 'A heterogeneous-cavity model for miniaturized detectors of orthovoltage X-rays'. In: *Journal of Physics: Conference Series* 2799.1 (July 2024), p. 012012. DOI: `10.1088/1742-6596/2799/1/012012`. URL: `https://hal.science/hal-04706749v1` (cited on page 30).

[116] Francesca Di Franco et al. 'Monocrystalline diamond detector for online monitoring during synchrotron microbeam radiotherapy'. In: *Journal of Synchrotron Radiation* 30.6 (2023), pp. 1076–1085. DOI: `10.1107/s160057752300752x`. URL: `https://hal.science/hal-04323368` (cited on page 30).

[117] Sarvenaz Keshmiri et al. 'A high resolution dose calculation engine for x-ray microbeams radiation therapy'. In: *Medical Physics* 49.6 (2022), pp. 3999–4017. DOI: `10.1002/mp.15637`. URL: `https://hal.science/hal-03639046` (cited on page 30).

[118] Sarvenaz Keshmiri et al. 'Treatment planning with high-resolution 3D dose maps in preclinical and translational synchrotron microbeam radiation therapy'. In: *Physics and Imaging in Radiation Oncology* 30 (2024), p. 100565. DOI: `10.1016/j.phro.2024.100565` (cited on page 31).

[119] Jean-François Adam et al. 'Toward Neuro-Oncologic Clinical Trials of High-Dose-Rate Synchrotron Microbeam Radiation Therapy: First Treatment of a Spontaneous Canine Brain Tumor'. In: *International Journal of Radiation Oncology*Biology*Physics* 113.5 (2022), pp. 967–973. DOI: `10.1016/j.ijrobp.2022.04.022` (cited on page 31).

[120] Laura Eling et al. 'Neuro-Oncologic Veterinary Trial for the Clinical Transfer of Microbeam Radiation Therapy: Acute to Subacute Radiotolerance after Brain Tumor Irradiation in Pet Dogs'. In: *Cancers* 16.15 (July 2024), p. 2701. DOI: `10.3390/cancers16152701` (cited on page 31).

[121] Johanna Winter et al. 'Clinical microbeam radiation therapy with a compact source: specifications of the line-focus X-ray tube'. In: *Physics and Imaging in Radiation Oncology* 14 (Apr. 2020), pp. 74–81. DOI: `10.1016/j.phro.2020.05.010` (cited on page 31).

[122] Renato Santos Mello et al. 'Radiation dose enhancement in tumors with iodine'. en. In: *Medical Physics* 10.1 (1983). _eprint: https://onlinelibrary.wiley.com/doi/pdf/10.1118/1.595378, pp. 75–78. DOI: `10.1118/1.595378`. URL: `https://onlinelibrary.wiley.com/doi/abs/10.1118/1.595378` (visited on 07/03/2024) (cited on page 34).

[123] James F. Hainfeld, Daniel N. Slatkin, and Henry M. Smilowitz. 'The use of gold nanoparticles to enhance radiotherapy in mice'. en. In: *Physics in Medicine & Biology* 49.18 (Sept. 2004), N309. DOI: `10.1088/0031-9155/49/18/N03`. URL: `https://dx.doi.org/10.1088/0031-9155/49/18/N03` (visited on 07/03/2024) (cited on page 34).

[124] Laure Bobyk et al. 'Photoactivation of gold nanoparticles for glioma treatment'. In: *Nanomedicine: Nanotechnology, Biology and Medicine* 9.7 (Oct. 2013), pp. 1089–1097. DOI: `10.1016/j.nano.2013.04.007`. URL: `https://www.sciencedirect.com/science/article/pii/S1549963413001792` (cited on page 35).

[125] Florence Taupin et al. 'Gadolinium nanoparticles and contrast agent as radiation sensitizers'. en. In: *Physics in Medicine & Biology* 60.11 (May 2015). Publisher: IOP Publishing, p. 4449. DOI: `10.1088/0031-9155/60/11/4449`. URL: `https://dx.doi.org/10.1088/0031-9155/60/11/4449` (visited on 07/03/2024) (cited on pages 35, 37).

[126] Rachel Delorme et al. 'Comparison of gadolinium nanoparticles and molecular contrast agents for radiation therapy-enhancement'. en. In: *Medical Physics* 44.11 (2017), pp. 5949–5960. DOI: `10.1002/mp.12570`. URL: `https://onlinelibrary.wiley.com/doi/abs/10.1002/mp.12570` (cited on pages 35, 37).

[127] A. Ocadiz et al. 'Treatment Planning for Synchrotron Radiotherapy Enhanced with Iron-Oxide Nanoparticles'. In: *Medical Physics*. Vol. 47. Issue: 6. Wiley 111 River St, Hoboken 07030-5774, NJ USA, 2020, E868–E869. URL: `https://scholar.google.com/scholar?cluster=15494504331196388266&hl=en&oi=scholarr` (visited on 07/03/2024) (cited on page 35).

[128] Gi-Hwan Choi et al. 'Photon activated therapy (PAT) using monochromatic Synchrotron x-rays and iron oxide nanoparticles in a mouse tumor model: feasibility study of PAT for the treatment of superficial malignancy'. In: *Radiation Oncology* 7.1 (Oct. 2012), p. 184. DOI: `10.1186/1748-717X-7-184`. URL: `https://doi.org/10.1186/1748-717X-7-184` (cited on page 35).

[129] Layal Obeid et al. 'Absolute Perfusion Measurements and Associated Iodinated Contrast Agent Time Course in Brain Metastasis: A Study for Contrast-Enhanced Radiotherapy'. en. In: *Journal of Cerebral Blood Flow & Metabolism* 34.4 (Apr. 2014). Publisher: SAGE Publications Ltd STM, pp. 638–645. DOI: `10.1038/jcbfm.2013.239`. URL: `https://doi.org/10.1038/jcbfm.2013.239` (visited on 07/03/2024) (cited on page 36).

[130] François Lux et al. 'AGuIX® from bench to bedside—Transfer of an ultrasmall theranostic gadolinium-based nanoparticle to clinical medicine'. In: *British Journal of Radiology* 92.1093 (Jan. 2019), p. 20180365. DOI: `10.1259/bjr.20180365`. URL: `https://doi.org/10.1259/bjr.20180365` (visited on 07/03/2024) (cited on page 36).

[131] Camille Verry et al. 'Theranostic AGuIX nanoparticles as radiosensitizer: A phase I, dose-escalation study in patients with multiple brain metastases (NANO-RAD trial)'. eng. In: *Radiotherapy and Oncology: Journal of the European Society for Therapeutic Radiology and Oncology* 160 (July 2021), pp. 159–165. DOI: `10.1016/j.radonc.2021.04.021` (cited on pages 36, 37).

[132] Imen Miladi et al. 'Combining ultrasmall gadolinium-based nanoparticles with photon irradiation overcomes radioresistance of head and neck squamous cell carcinoma'. In: *Nanomedicine: Nanotechnology, Biology and Medicine* 11.1 (Jan. 2015), pp. 247–257. DOI: `10.1016/j.nano.2014.06.013`. URL: `https://www.sciencedirect.com/science/article/pii/S1549963414003268` (visited on 07/03/2024) (cited on pages 36, 37).

[133] Shady Kotb et al. 'Gadolinium-Based Nanoparticles and Radiation Therapy for Multiple Brain Melanoma Metastases: Proof of Concept before Phase I Trial'. en. In: *Theranostics* 6.3 (Jan. 2016). Publisher: Ivyspring International Publisher, pp. 418–427. DOI: `10.7150/thno.14018`. URL: `https://www.thno.org/v06p0418.htm` (visited on 07/03/2024) (cited on pages 36, 37).

[134] Marie-Thérèse Aloy et al. 'Proof of Concept of the Radiosensitizing Effect of Gadolinium Oxide Nanoparticles in Cell Spheroids and a Tumor-Implanted Murine Model of Chondrosarcoma'. English. In: *International Journal of Nanomedicine* 17 (Dec. 2022). Publisher: Dove Press, pp. 6655–6673. DOI: `10.2147/IJN.S390056`. URL: `https://www.dovepress.com/proof-of-concept-of-the-radiosensitizing-effect-of-gadolinium-oxide-na-peer-reviewed-fulltext-article-IJN` (cited on pages 36–38).

[135] Anne-Sophie Wozny et al. 'Differential pattern of HIF-1α expression in HNSCC cancer stem cells after carbon ion or photon irradiation: one molecular explanation of the oxygen effect'. en. In: *British Journal of Cancer* 116.10 (May 2017). Publisher: Nature Publishing Group, pp. 1340–1349. DOI: `10.1038/bjc.2017.100`. URL: `https://www.nature.com/articles/bjc2017100` (visited on 07/03/2024) (cited on pages 36, 42).

[136] Wael Rima et al. 'Internalization pathways into cancer cells of gadolinium-based radiosensitizing nanoparticles'. In: *Biomaterials* 34.1 (Jan. 2013), pp. 181–195. DOI: `10.1016/j.biomaterials.2012.09.029`. URL: `https://www.sciencedirect.com/science/article/pii/S0142961212010332` (visited on 07/03/2024) (cited on page 36).

[137] S. Simonet et al. 'Gadolinium-Based Nanoparticles Can Overcome the Radioresistance of Head and Neck Squamous Cell Carcinoma Through the Induction of Autophagy'. In: *Journal of Biomedical Nanotechnology* 16.1 (Jan. 2020), pp. 111–124. DOI: `10.1166/jbn.2020.2871` (cited on pages 36, 37).

[138] Paul Rocchi et al. 'A New Generation of Ultrasmall Nanoparticles Inducing Sensitization to Irradiation and Copper Depletion to Overcome Radioresistant and Invasive Cancers'. en. In: *Pharmaceutics* 14.4 (Apr. 2022). Number: 4 Publisher: Multidisciplinary Digital Publishing Institute, p. 814. DOI: `10.3390/pharmaceutics14040814`. URL: `https://www.mdpi.com/1999-4923/14/4/814` (visited on 07/03/2024) (cited on pages 37, 38).

[139] Fenna Hensen et al. 'The mitochondrial outer-membrane location of the EXD2 exonuclease contradicts its direct role in nuclear DNA repair'. en. In: *Scientific Reports* 8.1 (Mar. 2018). Publisher: Nature Publishing Group, p. 5368. DOI: `10.1038/s41598-018-23690-y`. URL: `https://www.nature.com/articles/s41598-018-23690-y` (visited on 07/03/2024) (cited on page 37).

[140] Amandine Moretton et al. 'Selective mitochondrial DNA degradation following double-strand breaks'. en. In: *PLOS ONE* 12.4 (Apr. 2017). Publisher: Public Library of Science, e0176795. DOI: `10.1371/journal.pone.0176795`. URL: `https://journals.plos.org/plosone/article?id=10.1371/journal.pone.0176795` (visited on 07/03/2024) (cited on page 37).

[141] Judith Eguida. 'Approche radiosensibilisatrice de carbènes-Or associés aux irradiations dans des modèles cellulaires humains de tumeur prostatique'. fr. PhD thesis. Université Clermont Auvergne, June 2021. URL: `https://theses.hal.science/tel-04574180` (cited on page 38).

[142] Thibaut Tabanou et al. *Développement et caractérisation de nanoparticules d'or à ciblage mitochondrial*. Published: Meetochondrie. May 2022. URL: `https://hal.science/hal-03648527` (visited on 07/03/2024) (cited on page 38).

[143] S. Zein et al. 'Microdosimetry in 3D realistic mitochondria phantoms: Geant4 Monte Carlo tracking of 250 keV photons in phantoms reconstructed from microscopic images'. English. In: *Physica Medica: European Journal of Medical Physics* 42 (Oct. 2017). Publisher: Elsevier, pp. 7–12. DOI: `10.1016/j.ejmp.2017.08.005`. URL: `https://www.physicamedica.com/article/S1120-1797(17)30247-8/abstract` (visited on 07/03/2024) (cited on page 39).

[144] Z. Francis et al. 'A simulation study of gold nanoparticles localisation effects on radiation enhancement at the mitochondrion scale'. English. In: *Physica Medica: European Journal of Medical Physics* 67 (Nov. 2019). Publisher: Elsevier, pp. 148–154. DOI: `10.1016/j.ejmp.2019.10.038`. URL: `https://www.physicamedica.com/article/S1120-1797(19)30488-0/abstract` (cited on page 39).

[145] Anne-Laure Bulin et al. ‘Radiation Dose-Enhancement Is a Potent Radiotherapeutic Effect of Rare-Earth Composite Nanoscintillators in Preclinical Models of Glioblastoma’. en. In: *Advanced Science* 7.20 (2020). _eprint: https://onlinelibrary.wiley.com/doi/pdf/10.1002/advs.202001675, p. 2001675. DOI: `10.1002/advs.202001675`. URL: `https://onlinelibrary.wiley.com/doi/abs/10.1002/advs.202001675` (cited on pages 39, 40).

[146] Antonia Youssef. ‘L’utilisation de nanoscintillateurs pour augmenter l’efficacité de la radiothérapie’. These de doctorat. Université Grenoble Alpes, Sept. 2022. URL: `https://theses.fr/2022GRALS024` (visited on 07/03/2024) (cited on page 40).

[147] Anne-Sophie Wozny and Claire Rodriguez-Lafrasse. ‘The ‘stealth-bomber’ paradigm for deciphering the tumour response to carbon-ion irradiation’. en. In: *British Journal of Cancer* 128.8 (Apr. 2023). Publisher: Nature Publishing Group, pp. 1429–1438. DOI: `10.1038/s41416-022-02117-6`. URL: `https://www.nature.com/articles/s41416-022-02117-6` (visited on 07/03/2024) (cited on pages 42, 43).

[148] Anne-Sophie Wozny et al. ‘Impact of hypoxia on the double-strand break repair after photon and carbon ion irradiation of radioresistant HNSCC cells’. en. In: *Scientific Reports* 10.1 (Dec. 2020). Publisher: Nature Publishing Group, p. 21357. DOI: `10.1038/s41598-020-78354-7`. URL: `https://www.nature.com/articles/s41598-020-78354-7` (visited on 07/03/2024) (cited on page 42).

[149] Anne-Sophie Wozny et al. ‘Involvement of HIF-1α in the Detection, Signaling, and Repair of DNA Double-Strand Breaks after Photon and Carbon-Ion Irradiation’. en. In: *Cancers* 13.15 (Jan. 2021). Number: 15 Publisher: Multidisciplinary Digital Publishing Institute, p. 3833. DOI: `10.3390/cancers13153833`. URL: `https://www.mdpi.com/2072-6694/13/15/3833` (visited on 07/03/2024) (cited on page 42).

[150] Sylvain Ferrandon et al. ‘Telomere Profiling: Toward Glioblastoma Personalized Medicine’. en. In: *Molecular Neurobiology* 47.1 (Feb. 2013), pp. 64–76. DOI: `10.1007/s12035-012-8363-9`. URL: `https://doi.org/10.1007/s12035-012-8363-9` (cited on page 42).

[151] Mira Maalouf et al. ‘Different Mechanisms of Cell Death in Radiosensitive and Radioresistant P53 Mutated Head and Neck Squamous Cell Carcinoma Cell Lines Exposed to Carbon Ions and X-Rays’. English. In: *International Journal of Radiation Oncology, Biology, Physics* 74.1 (May 2009). Publisher: Elsevier, pp. 200–209. DOI: `10.1016/j.ijrobp.2009.01.012`. URL: `https://www.redjournal.org/article/S0360-3016(09)00086-8/abstract` (visited on 07/03/2024) (cited on page 42).

[152] Gérald Bertrand et al. ‘Targeting Head and Neck Cancer Stem Cells to Overcome Resistance to Photon and Carbon Ion Radiation’. en. In: *Stem Cell Reviews and Reports* 10.1 (Feb. 2014), pp. 114–126. DOI: `10.1007/s12015-013-9467-y`. URL: `https://doi.org/10.1007/s12015-013-9467-y` (cited on page 42).

[153] Gersende Alphonse et al. ‘p53-independent early and late apoptosis is mediated by ceramide after exposure of tumor cells to photon or carbon ion irradiation’. In: *BMC Cancer* 13.1 (Mar. 2013), p. 151. DOI: `10.1186/1471-2407-13-151`. URL: `https://doi.org/10.1186/1471-2407-13-151` (cited on page 42).

[154] Anne-Sophie Wozny et al. ‘ROS Production and Distribution: A New Paradigm to Explain the Differential Effects of X-ray and Carbon Ion Irradiation on Cancer Stem Cell Migration and Invasion’. en. In: *Cancers* 11.4 (Apr. 2019). Number: 4 Publisher: Multidisciplinary Digital Publishing Institute, p. 468. DOI: `10.3390/cancers11040468`. URL: `https://www.mdpi.com/2072-6694/11/4/468` (visited on 07/03/2024) (cited on page 42).

[155] Safa Louati et al. ‘Differential Formation of Stress Granules in Radiosensitive and Radioresistant Head and Neck Squamous Cell Carcinoma Cells’. English. In: *International Journal of Radiation Oncology, Biology, Physics* 118.2 (Feb. 2024). Publisher: Elsevier, pp. 485–497. DOI: `10.1016/j.ijrobp.2023.08.045`. URL: `https://www.redjournal.org/article/S0360-3016(23)07816-1/abstract` (visited on 07/03/2024) (cited on page 43).

[156] Kevin M. Prise and Joe M. O'Sullivan. 'Radiation-induced bystander signalling in cancer therapy'. en. In: *Nature Reviews Cancer* 9.5 (May 2009). Publisher: Nature Publishing Group, pp. 351–360. DOI: `10.1038/nrc2603`. URL: `https://www.nature.com/articles/nrc2603` (visited on 07/03/2024) (cited on page 43).

[157] Grace Y. Chen and Gabriel Nuñez. 'Sterile inflammation: sensing and reacting to damage'. en. In: *Nature Reviews Immunology* 10.12 (Dec. 2010). Publisher: Nature Publishing Group, pp. 826–837. DOI: `10.1038/nri2873`. URL: `https://www.nature.com/articles/nri2873` (cited on page 43).

[158] Isabelle Testard et al. 'Bystander signals from low- and high-dose irradiated human primary fibroblasts and keratinocytes modulate the inflammatory response of peripheral blood mononuclear cells'. In: *Journal of Radiation Research* 64.2 (Mar. 2023), pp. 304–316. DOI: `10.1093/jrr/rrac094`. URL: `https://doi.org/10.1093/jrr/rrac094` (visited on 07/03/2024) (cited on page 44).

[159] Antoine Gilbert et al. 'Label-Free Direct Mass Spectrometry Analysis of the Bystander Effects Induced in Chondrocytes by Chondrosarcoma Cells Irradiated with X-rays and Carbon Ions'. In: *Frontiers in Bioscience-Landmark* 27.9 (Sept. 2022). Number: 9 Publisher: IMR Press, p. 277. DOI: `10.31083/j.fbl2709277`. URL: `https://www.imrpress.com/journal/FBL/27/9/10.31083/j.fbl2709277` (visited on 07/03/2024) (cited on page 44).

[160] Thao-Nguyen Pham et al. 'Beyond lymphopenia, unraveling radiation-induced leucocyte subpopulation kinetics and mechanisms through modeling approaches'. In: *Journal of Experimental & Clinical Cancer Research* 42.1 (Feb. 2023), p. 50. DOI: `10.1186/s13046-023-02621-4`. URL: `https://doi.org/10.1186/s13046-023-02621-4` (visited on 07/03/2024) (cited on page 44).

[161] Pierre Philouze et al. 'CD44, γ-H2AX, and p-ATM Expressions in Short-Term Ex Vivo Culture of Tumour Slices Predict the Treatment Response in Patients with Oral Squamous Cell Carcinoma'. en. In: *International Journal of Molecular Sciences* 23.2 (Jan. 2022). Number: 2 Publisher: Multidisciplinary Digital Publishing Institute, p. 877. DOI: `10.3390/ijms23020877`. URL: `https://www.mdpi.com/1422-0067/23/2/877` (visited on 07/03/2024) (cited on page 44).

[162] Arnaud Gauthier et al. 'Circulating Tumor Cell Detection during Neoadjuvant Chemotherapy to Predict Early Response in Locally Advanced Oropharyngeal Cancers: A Prospective Pilot Study'. en. In: *Journal of Personalized Medicine* 12.3 (Mar. 2022). Number: 3 Publisher: Multidisciplinary Digital Publishing Institute, p. 445. DOI: `10.3390/jpm12030445`. URL: `https://www.mdpi.com/2075-4426/12/3/445` (cited on page 44).

[163] Emmanuelle Bignon et al. 'Molecular Dynamics Insights into Polyamine–DNA Binding Modes: Implications for Cross-Link Selectivity'. In: *Chemistry – A European Journal* 23.52 (), pp. 12845–12852. DOI: `https://doi.org/10.1002/chem.201702065`. URL: `https://chemistry-europe.onlinelibrary.wiley.com/doi/abs/10.1002/chem.201702065` (cited on page 48).

[164] Elise Dumont et al. 'Probing the reactivity of singlet oxygen with purines'. In: *Nucleic Acids Research* 44.1 (Jan. 2016), pp. 56–62. DOI: `10.1093/nar/gkv1364`. URL: `https://hal.science/hal-01271590` (cited on page 48).

[165] Emmanuelle Bignon et al. 'Molecular Dynamics Insights into Polyamine-DNA Binding Modes: Implications for Cross-Link Selectivity'. In: *Chemistry - A European Journal* 23.52 (Sept. 2017). We acknowledge the Pole Scientifique de Modeisation Numerique (PSMN) for computational resources., pp. 12845–12852. DOI: `10.1002/chem.201702065`. URL: `https://hal.science/hal-01646327` (cited on page 48).

[166] Chen-Hui Chan et al. 'Probing interaction of a trilysine peptide with DNA underlying formation of guanine–lysine cross-links: insights from molecular dynamics'. In: *Phys. Chem. Chem. Phys.* 21 (42 2019), pp. 23418–23424. DOI: `10.1039/C9CP04708E`. URL: `http://dx.doi.org/10.1039/C9CP04708E` (cited on page 48).

[167] Micaela Cunha et al. 'Modeling cell response to low doses of photon irradiation: Part 2-application to radiation-induced chromosomal aberrations in human carcinoma cells'. In: *Radiation and Environmental Biophysics* 55 (1 Mar. 2016), pp. 31–40. DOI: `10.1007/s00411-015-0622-5`. URL: `http://www.ncbi.nlm.nih.gov/pubmed/26708100` (cited on page 48).

[168] Micaela Cunha et al. 'Modeling cell response to low doses of photon irradiation-Part 1: on the origin of fluctuations'. In: *Radiation and Environmental Biophysics* (Nov. 2015). DOI: `10.1007/s00411-015-0621-6`. URL: `http://www.ncbi.nlm.nih.gov/pubmed/26590033` (cited on page 48).

[169] M. Dos Santos et al. 'Minibeam radiation therapy: A micro- and nano-dosimetry Monte Carlo study'. In: *Medical Physics* 47.3 (2020), pp. 1379–1390. DOI: `https://doi.org/10.1002/mp.14009`. URL: `https://aapm.onlinelibrary.wiley.com/doi/abs/10.1002/mp.14009` (cited on page 49).

[170] Rachel Delorme et al. 'First theoretical determination of relative biological effectiveness of very high energy electrons'. In: *Scientific Reports* 11.1 (2021), p. 11242. DOI: `10.1038/s41598-021-90805-3`. URL: `https://hal.science/hal-03242669` (cited on page 50).

[171] Chen-Hui Chan et al. 'A Water Solvation Shell Can Transform Gold Metastable Nanoparticles in the Fluxional Regime'. In: *Journal of Physical Chemistry Letters* 10 (Feb. 2019), pp. 1092–1098. DOI: `10.1021/acs.jpclett.8b03822`. URL: `https://hal.science/hal-02057656` (cited on page 51).

[172] Chen-Hui Chan et al. 'Effect of the Ligand Binding Strength on the Morphology of Functionalized Gold Nanoparticles'. In: *Journal of Physical Chemistry Letters* (2020), pp. 2717–2723. DOI: `10.1021/acs.jpclett.0c00300`. URL: `https://hal.science/hal-02519412` (cited on pages 51, 52).

[173] F. Poignant et al. 'Theoretical derivation and benchmarking of cross sections for low-energy electron transport in gold'. In: *European Physical Journal Plus* 135 (4 Apr. 2020), pp. 1–37. DOI: `10.1140/epjp/s13360-020-00354-3`. URL: `https://link.springer.com/article/10.1140/epjp/s13360-020-00354-3` (cited on page 53).

[174] MICHAEL BEUVE. 'Transport et emission d'electrons generes par un ion rapide dans un solide : aspects theoriques et simulations numeriques'. In: *http://www.theses.fr* (Jan. 1999). URL: `http://www.theses.fr/1999CAEN2062` (cited on page 53).

[175] M. Beuve et al. 'Charge dependence of electron emission in swift heavy-ion collisions with carbon'. In: *Physical Review B* 62 (13 Oct. 2000), p. 8818. DOI: `10.1103/PhysRevB.62.8818`. URL: `https://journals.aps.org/prb/abstract/10.1103/PhysRevB.62.8818` (cited on page 53).

[176] Ricardo Ramos et al. 'Low-energy electron transport in gold: mesoscopic potential calculation and its impact on electron emission yields'. In: *Eur.Phys.J.Plus* 136.3 (2021), p. 345. DOI: `10.1140/epjp/s13360-021-01318-x`. URL: `https://hal.science/hal-03186180` (cited on page 53).

[177] R. Delorme et al. 'Comparison of gadolinium nanoparticles and molecular contrast agents for radiation therapy-enhancement'. In: *Medical Physics* 44.11 (Nov. 2017), pp. 5949–5960. DOI: `10.1002/mp.12570`. URL: `https://hal.science/hal-01690606` (cited on page 54).

[178] M. Beuve et al. 'Statistical effects of dose deposition in track-structure modelling of radiobiology efficiency'. In: *Nuclear Instruments and Methods in Physics Research Section B: Beam Interactions with Materials and Atoms* 267 (6 Mar. 2009), pp. 983–988. DOI: `10.1016/j.nimb.2009.02.016`. URL: `http://linkinghub.elsevier.com/retrieve/pii/S0168583X09002444` (cited on pages 54, 55).

[179] Floriane Poignant et al. 'Influence of gold nanoparticles embedded in water on nanodosimetry for keV photon irradiation'. In: *Medical Physics* 48.4 (2020), pp. 1874–1883. DOI: `10.1002/mp.14576`. URL: `https://hal.science/hal-03001810` (cited on pages 54, 55).

[180] 'Biological consequences of nanoscale energy deposition near irradiated heavy atom nanoparticles'. In: *Scientific Reports 2011 1:1* 1 (1 June 2011), pp. 1–10. DOI: `10.1038/srep00018`. URL: `https://www.nature.com/articles/srep00018` (cited on page 55).

[181] Stephen J. McMahon et al. 'Energy dependence of gold nanoparticle radiosensitization in plasmid DNA'. In: *Journal of Physical Chemistry C* 115 (41 Oct. 2011), pp. 20160–20167. DOI: `10.1021/JP206854S/ASSET/IMAGES/MEDIUM/JP-2011-06854S_0007.GIF`. URL: `https://pubs.acs.org/doi/full/10.1021/jp206854s` (cited on page 55).

[182] Stephen J. McMahon et al. 'Nanodosimetric effects of gold nanoparticles in megavoltage radiation therapy'. In: *Radiotherapy and Oncology* 100 (3 Sept. 2011), pp. 412–416. DOI: `10.1016/j.radonc.2011.08.026`. URL: `https://www.qwant.com` (cited on page 55).

[183] Yuting Lin et al. 'Biological modeling of gold nanoparticle enhanced radiotherapy for proton therapy'. In: *Physics in medicine and biology* 60 (10 May 2015), pp. 4149–4168. DOI: 10.1088/0031-9155/60/10/4149. URL: https://pubmed.ncbi.nlm.nih.gov/25953956/ (cited on page 55).

[184] Stephen J. McMahon, Harald Paganetti, and Kevin M. Prise. 'Optimising element choice for nanoparticle radiosensitisers'. In: *Nanoscale* 8 (1 Dec. 2015), pp. 581–589. DOI: 10.1039/C5NR07089A. URL: https://pubs.rsc.org/en/content/articlehtml/2016/nr/c5nr07089a (cited on page 55).

[185] Floriane Poignant. 'Physical, chemical and biological modelling for gold nanoparticle-enhanced radiation therapy : towards a better understanding and optimization of the radiosensitizing effect'. Theses. Université de Lyon, Sept. 2019. URL: https://theses.hal.science/tel-03506229 (cited on page 55).

[186] Floriane Poignant et al. 'Monte Carlo simulation of free radical production under keV photon irradiation of gold nanoparticle aqueous solution. Part I: Global primary chemical boost'. In: *Radiation Physics and Chemistry* 172 (July 2020), p. 108790. DOI: 10.1016/j.radphyschem.2020.108790. URL: https://hal.science/hal-02498384 (cited on page 55).

[187] Floriane Poignant et al. 'Monte Carlo simulation of free radical production under keV photon irradiation of gold nanoparticle aqueous solution. Part II: Local primary chemical boost'. In: *Radiation Physics and Chemistry* 179 (Feb. 2021), p. 109161. DOI: 10.1016/j.radphyschem.2020.109161. URL: https://hal.science/hal-03029595 (cited on page 56).

[188] Ioanna Kyriakou et al. 'Review of the Geant4-DNA Simulation Toolkit for Radiobiological Applications at the Cellular and DNA Level'. In: *Cancers* 14 (1 Jan. 2021). DOI: 10.3390/CANCERS14010035. URL: https://pubmed.ncbi.nlm.nih.gov/35008196/ (cited on page 56).

[189] B Gervais et al. 'Numerical simulation of multiple ionization and high LET effects in liquid water radiolysis'. In: *Radiation Physics and Chemistry* 75 (4 Apr. 2006), pp. 493–513. DOI: 10.1016/j.radphyschem.2005.09.015. URL: http://adsabs.harvard.edu/abs/2006RaPC...75..493G (cited on page 56).

[190] Yasmine Ali et al. 'Monte Carlo simulations of nanodosimetry and radiolytic species production for monoenergetic proton and electron beams. Benchmarking of GEANT4-DNA and LPCHEM codes'. In: *Medical Physics* 49.5 (2022), pp. 3457–3469. DOI: 10.1002/mp.15609. URL: https://hal.science/hal-03622534 (cited on pages 56, 58).

[191] M Scholz et al. 'Computation of cell survival in heavy ion beams for therapy. The model and its approximation'. In: *Radiation and Environmental Biophysics* 36 (1 Feb. 1997), pp. 59–66. URL: http://www.ncbi.nlm.nih.gov/pubmed/9128899 (cited on page 57).

[192] Yuki Kase et al. 'Microdosimetric measurements and estimation of human cell survival for heavy-ion beams'. In: *Radiation research* 166 (4 Oct. 2006), pp. 629–638. DOI: 10.1667/RR0536.1. URL: https://pubmed.ncbi.nlm.nih.gov/17007551/ (cited on page 57).

[193] Taku Inaniwa et al. 'Treatment planning for a scanned carbon beam with a modified microdosimetric kinetic model'. In: *Physics in medicine and biology* 55 (22 Nov. 2010), pp. 6721–6737. DOI: 10.1088/0031-9155/55/22/008. URL: https://pubmed.ncbi.nlm.nih.gov/21030747/ (cited on page 57).

[194] Micaela Cunha et al. 'NanOx, a new model to predict cell survival in the context of particle therapy'. In: *Physics in Medicine and Biology* 62.4 (2017), pp. 1248–1268. DOI: 10.1088/1361-6560/aa54c9. URL: https://hal.science/hal-01446509 (cited on page 57).

[195] F. Cordoni et al. 'Generalized stochastic microdosimetric model: The main formulation'. In: *Physical Review E* 103 (1 Jan. 2021), p. 012412. DOI: 10.1103/PHYSREVE.103.012412/FIGURES/6/MEDIUM. URL: https://journals.aps.org/pre/abstract/10.1103/PhysRevE.103.012412 (cited on page 57).

[196] F. Kamp, D. J. Carlson, and J. J. Wilkens. 'Rapid implementation of the repair-misrepair-fixation (RMF) model facilitating online adaption of radiosensitivity parameters in ion therapy'. In: *Physics in Medicine & Biology* 62 (13 May 2017), N285. DOI: 10.1088/1361-6560/AA716B. URL: https://iopscience.iop.org/article/10.1088/1361-6560/aa716b (cited on page 57).

[197] Francesca Ballarini and Mario P. Carante. 'Chromosome aberrations and cell death by ionizing radiation: Evolution of a biophysical model'. In: *Radiation Physics and Chemistry* 128 (Nov. 2016), pp. 18–25. DOI: `10.1016/J.RADPHYSCHEM.2016.06.009` (cited on page 57).

[198] V. Conte et al. 'NANODOSIMETRY: TOWARDS A NEW CONCEPT OF RADIATION QUALITY'. In: *Radiation Protection Dosimetry* 180 (1-4 Aug. 2018), pp. 150–156. DOI: `10.1093/RPD/NCX175`. URL: `https://dx.doi.org/10.1093/rpd/ncx175` (cited on page 57).

[199] Mario Alcocer-Ávila et al. 'Formalism of the NanOx biophysical model for radiotherapy applications'. In: *Frontiers in Physics* 11 (2023). DOI: `10.3389/fphy.2023.1011062`. URL: `https://www.frontiersin.org/articles/10.3389/fphy.2023.1011062` (cited on page 57).

[200] Mario Alcocer-Ávila et al. 'Cell survival prediction in hadrontherapy with the NanOx biophysical model'. In: *Frontiers in Physics* 10 (2022). DOI: `10.3389/fphy.2022.1011063`. URL: `https://www.frontiersin.org/articles/10.3389/fphy.2022.1011063` (cited on page 57).

[201] Caterina Monini et al. 'Determination of the Effective Local Lethal Function for the NanOx Model'. In: *Rad.Res.* 193.4 (2020), pp. 331–340. DOI: `10.1667/rr15463.1`. URL: `https://hal.science/hal-02571523` (cited on page 58).

[202] Caterina Monini et al. 'Study of the Influence of NanOx Parameters'. In: *Cancers* 10.4 (Apr. 2018). DOI: `10.3390/cancers10040087`. URL: `https://hal.science/hal-01919767` (cited on page 58).

[203] Caterina Monini et al. 'Comparison of biophysical models with experimental data for three cell lines in response to irradiation with monoenergetic ions'. In: *Physics and Imaging in Radiation Oncology* 12 (Oct. 2019), pp. 17–21. DOI: `10.1016/j.phro.2019.10.004`. URL: `https://hal.science/hal-02543068` (cited on page 58).

[204] M.-A. Chanrion et al. 'The influence of the local effect model parameters on the prediction of the tumor control probability for prostate cancer'. In: *Physics in Medicine and Biology* 59 (2014), pp. 3019–3040. DOI: `10.1088/0031-9155/59/12/3019`. URL: `https://hal.science/hal-00990873` (cited on page 59).

[205] S Jan et al. 'GATE: A Simulation Toolkit for PET and SPECT'. In: *Physics in Medicine and Biology* 49.19 (Oct. 2004), pp. 4543–4561. DOI: `10/dz8473` (cited on page 63).

[206] S. Jan et al. 'GATE V6: A Major Enhancement of the GATE Simulation Platform Enabling Modelling of CT and Radiotherapy.' In: *Phys Med Biol* 56.4 (Feb. 2011), pp. 881–901. DOI: `10.1088/0031-9155/56/4/001` (cited on page 63).

[207] David Sarrut et al. 'A Review of the Use and Potential of the GATE Monte Carlo Simulation Code for Radiation Therapy and Dosimetry Applications'. In: *Medical physics* 41.6Part1 (June 2014), p. 064301. DOI: `10.1118/1.4871617` (cited on pages 63, 68).

[208] David Sarrut et al. 'Advanced Monte Carlo Simulations of Emission Tomography Imaging Systems with GATE'. In: *Physics in Medicine and Biology* 66.10 (May 2021), 10TR03. DOI: `10/gj6rkh` (cited on pages 63, 67).

[209] J. Allison et al. 'Recent Developments in GEANT4'. In: *Nuclear Instruments and Methods in Physics Research Section A: Accelerators, Spectrometers, Detectors and Associated Equipment* 835 (2016), pp. 186–225 (cited on page 63).

[210] J. Allison et al. 'Geant4 Developments and Applications'. In: *IEEE Transactions on Nuclear Science* 53.1 (Feb. 2006), pp. 270–278. DOI: `10.1109/TNS.2006.869826` (cited on page 63).

[211] L. Grevillot et al. 'GATE as a GEANT4-based Monte Carlo Platform for the Evaluation of Proton Pencil Beam Scanning Treatment Plans.' In: *Phys Med Biol* 57.13 (July 2012), pp. 4223–4244. DOI: `10.1088/0031-9155/57/13/4223` (cited on page 63).

[212] L Grevillot et al. 'A Monte Carlo Pencil Beam Scanning Model for Proton Treatment Plan Simulation Using GATE/GEANT4'. In: *Physics in Medicine and Biology* 56.16 (Aug. 2011), pp. 5203–5219. DOI: `10/b5nhwv` (cited on page 63).

[213] Loïc Grevillot et al. 'Optimization of GEANT4 Settings for Proton Pencil Beam Scanning Simulations Using GATE'. In: *Nuclear Instruments and Methods in Physics Research Section B: Beam Interactions with Materials and Atoms* 268.20 (Oct. 2010), pp. 3295–3305. DOI: `10/chnqct` (cited on page 63).

[214] L. Grevillot et al. 'The GATE-RTion/IDEAL Independent Dose Calculation System for Light Ion Beam Therapy'. In: *Frontiers in Physics* 9 (2021). DOI: `10.3389/fphy.2021.704760` (cited on page 63).

[215] Alessio Elia et al. 'A GATE/Geant4 Beam Model for the MedAustron Non-Isocentric Proton Treatment Plans Quality Assurance'. In: *Physica Medica* 71 (Mar. 2020), pp. 115–123. DOI: `10/ggw5vd` (cited on page 63).

[216] Carla Winterhalter et al. 'Evaluation of GATE-RTion (GATE/Geant4) Monte Carlo Simulation Settings for Proton Pencil Beam Scanning Quality Assurance'. In: *Medical Physics* 47.11 (Nov. 2020), pp. 5817–5828. DOI: `10.1002/mp.14481` (cited on page 63).

[217] Yasmine Ali et al. 'Estimate of the Biological Dose in Hadrontherapy Using GATE'. In: *Cancers* 14.7 (2022). DOI: `10.3390/cancers14071667`. URL: `https://www.mdpi.com/2072-6694/14/7/1667` (cited on page 63).

[218] Giovanna Rosa Fois et al. 'Monte Carlo simulations of microdosimetry and radiolytic species production at long time post proton irradiation using GATE and Geant4-DNA'. In: *Medical Physics* (2024). DOI: `10.1002/MP.17281`. URL: `https://onlinelibrary.wiley.com/doi/full/10.1002/mp.17281` (cited on page 64).

[219] M Vidal et al. 'An Empirical Model for Calculation of the Collimator Contamination Dose in Therapeutic Proton Beams.' In: *Physics in medicine and biology* 61.4 (Feb. 2016), pp. 1532–1545. DOI: `10.1088/0031-9155/61/4/1532` (cited on page 64).

[220] Charlotte Robert et al. 'PET-based Dose Delivery Verification in Proton Therapy: A GATE Based Simulation Study of Five PET System Designs in Clinical Conditions'. In: *Physics in Medicine and Biology* 58.19 (Oct. 2013), pp. 6867–6885. DOI: `10/ggjtb4` (cited on page 64).

[221] Sebastien Jan, Thibault Frisson, and David Sarrut. 'GATE Simulation of 12C Hadrontherapy Treatment Combined with a PET Imaging System for Dose Monitoring: A Feasibility Study'. In: *IEEE Transactions on Nuclear Science* 60 (2013), p. 423. DOI: `10.1109/TNS.2012.2233496` (cited on page 64).

[222] C. Robert et al. 'Distributions of Secondary Particles in Proton and Carbon-Ion Therapy: A Comparison between GATE/Geant4 and FLUKA Monte Carlo Codes.' In: *Phys Med Biol* 58.9 (May 2013), pp. 2879–2899. DOI: `10.1088/0031-9155/58/9/2879` (cited on page 64).

[223] P. Gueth et al. 'Machine Learning-Based Patient Specific Prompt-Gamma Dose Monitoring in Proton Therapy.' In: *Physics in Medicine & Biology* 58.13 (July 2013), pp. 4563–4577. DOI: `10.1088/0031-9155/58/13/4563` (cited on page 64).

[224] W. El Kanawati et al. 'Monte Carlo Simulation of Prompt γ-Ray Emission in Proton Therapy Using a Specific Track Length Estimator.' In: *Phys Med Biol* 60.20 (Oct. 2015), pp. 8067–8086. DOI: `10.1088/0031-9155/60/20/8067` (cited on page 64).

[225] B. F. B. Huisman et al. 'Analytical Modeling and Monte Carlo Simulations of Multi-Parallel Slit and Knife-Edge Slit Prompt Gamma Cameras'. In: *Physics in Medicine and Biology* 68.11 (May 2023). DOI: `10.1088/1361-6560/acd237` (cited on page 65).

[226] J M Létang, O Allegrini, and É Testa. 'Prompt-gamma track-length estimator with time tagging from proton tracking'. In: *Physics in Medicine & Biology* 69.11 (2024), 115052:1–10. DOI: `10.1088/1361-6560/ad4a01` (cited on page 65).

[227] Jayde Livingstone et al. 'Influence of sub-nanosecond time of flight resolution for online range verification in proton therapy using the line-cone reconstruction in Compton imaging'. In: *Physics in Medicine & Biology* (May 2021). DOI: `10.1088/1361-6560/ac03cb`. URL: `https://iopscience.iop.org/article/10.1088/1361-6560/ac03cb` (cited on page 65).

[228] D. B. Everett et al. 'Gamma-Radiation Imaging System Based on the Compton Effect'. In: *Proceedings of the Institution of Electrical Engineers* 124.11 (Nov. 1977), pp. 995–1000. DOI: `10/d9ggh2` (cited on page 65).

[229] Estelle Hilaire et al. 'Proton Therapy Monitoring by Compton Imaging: Influence of the Large Energy Spectrum of the Prompt-γ Radiation'. In: *Physics in Medicine & Biology* 61.8 (Apr. 2016), p. 3127. DOI: `10.1088/0031-9155/61/8/3127` (cited on page 65).

[230] A Etxebeste et al. 'CCMod: a GATE module for Compton camera imaging simulation.' In: *Physics in medicine and biology* 65 (5 Feb. 2020), p. 055004. DOI: `10.1088/1361-6560/ab6529`. URL: `http://www.ncbi.nlm.nih.gov/pubmed/31869822` (cited on page 65).

[231] Yuemeng Feng et al. 'Influence of Doppler Broadening Model Accuracy in Compton Camera List-Mode MLEM Reconstruction'. In: *Inverse Problems in Science and Engineering* 29.13 (Dec. 2021), pp. 3509–3529. DOI: `10.1080/17415977.2021.2011863` (cited on page 65).

[232] Enrique Muñoz et al. 'Imaging of polychromatic sources through Compton spectral reconstruction'. In: *Physics in medicine and biology* 67 (19 Oct. 2022). DOI: `10.1088/1361-6560/AC92B9`. URL: `https://pubmed.ncbi.nlm.nih.gov/36113437/` (cited on page 65).

[233] David Sarrut et al. '3D Absorbed Dose Distribution Estimated by Monte Carlo Simulation in Radionuclide Therapy with a Monoclonal Antibody Targeting Synovial Sarcoma'. In: *EJNMMI Physics* 4.1 (Dec. 2017), p. 6. DOI: `10/ggjtkg` (cited on page 66).

[234] Elodie Jouberton et al. 'Radiation dosimetry of [131I]ICF01012 in rabbits: Application to targeted radionuclide therapy for human melanoma treatment'. In: *Medical Physics* 45.11 (2018), pp. 5251–5262. DOI: `10.1002/MP.13165`. URL: `https://onlinelibrary.wiley.com/doi/full/10.1002/mp.13165` (cited on page 66).

[235] Giovanna Rosa Fois et al. 'Internal dosimetry of [99mTc]NTP15-5 radiotracer for cartilage imaging in preclinical and clinical models using the GATE Monte Carlo platform'. In: *Medical Physics* 48.1 (2021), pp. 477–487. DOI: `10.1002/MP.14603`. URL: `https://onlinelibrary.wiley.com/doi/full/10.1002/mp.14603%20https://onlinelibrary.wiley.com/doi/abs/10.1002/mp.14603%20https://aapm.onlinelibrary.wiley.com/doi/10.1002/mp.14603` (cited on page 66).

[236] Anne-Laure Giraudet et al. 'A First-in-Human Study Investigating Biodistribution, Safety and Recommended Dose of a New Radiolabeled MAb Targeting FZD10 in Metastatic Synovial Sarcoma Patients'. In: *BMC Cancer* 18.1 (Dec. 2018), p. 646. DOI: `10/gdqsxr` (cited on page 66).

[237] L. Maigne et al. 'CPOP: An open source C++ cell POPulation modeler for radiation biology applications'. In: *Physica Medica* 89 (2021), pp. 41–50. DOI: `10.1016/j.ejmp.2021.07.016`. URL: `http://www.physicamedica.com/article/S112017972100260X/fulltext` (cited on page 66).

[238] Joey Labour et al. 'Yttrium-90 Quantitative Phantom Study Using Digital Photon Counting PET'. In: *EJNMMI Physics* 8.1 (July 2021), p. 56. DOI: `10.1186/s40658-021-00402-6` (cited on page 66).

[239] Laure Vergnaud et al. 'Patient-Specific Dosimetry Adapted to Variable Number of SPECT/CT Time-Points per Cycle for ^{177}Lu-DOTATATE Therapy'. In: *EJNMMI Physics* 9.1 (Dec. 2022), p. 37. DOI: `10.1186/s40658-022-00462-2` (cited on page 66).

[240] Laure Vergnaud et al. 'Dosimetric Impact of 3D Motion-Compensated SPECT Reconstruction for SIRT Planning'. In: *EJNMMI Physics* 10.1 (Feb. 2023), p. 8. DOI: `10.1186/s40658-023-00525-y` (cited on page 66).

[241] Adrien Halty et al. 'Image-Based SPECT Calibration Based on the Evaluation of the Fraction of Activity in the Field of View'. In: *EJNMMI physics* 5.1 (2018), p. 11. DOI: `10.1186/s40658-018-0209-8` (cited on page 66).

[242] Olga Kochebina et al. 'In Vivo Gadolinium Nanoparticle Quantification with SPECT/CT'. In: *EJNMMI Physics* 6.1 (Dec. 2019), p. 9. DOI: `10/gf446v` (cited on page 66).

[243] D Sarrut et al. 'Learning SPECT Detector Angular Response Function with Neural Network for Accelerating Monte-Carlo Simulations'. In: *Physics in Medicine & Biology* 63.20 (Oct. 2018), p. 205013. DOI: `10/ggjtkb` (cited on page 67).

[244] D. Sarrut, N. Krah, and J. M. Létang. 'Generative Adversarial Networks (GAN) for Compact Beam Source Modelling in Monte Carlo Simulations'. In: *Physics in Medicine and Biology* 64.21 (Oct. 2019), p. 215004. DOI: `10/gf82xv` (cited on page 67).

[245] David Sarrut et al. 'Artificial Intelligence for Monte Carlo Simulation in Medical Physics'. In: *Frontiers in Physics* 9 (2021), p. 601. DOI: `10.3389/fphy.2021.738112` (cited on page 67).

[246] Albert Saporta et al. 'Modeling Families of Particle Distributions with Conditional GAN for Monte Carlo SPECT Simulations'. In: *Physics in Medicine & Biology* 67.23 (Dec. 2022), p. 234001. DOI: `10.1088/1361-6560/aca068` (cited on page 67).

[247] D Sarrut et al. 'Annihilation Photon GAN Source Model for PET Monte Carlo Simulation'. In: *Physics in Medicine & Biology* 68.13 (July 2023), p. 135018. DOI: `10.1088/1361-6560/acdfb1` (cited on page 67).

[248] F. Baldacci et al. 'A Track Length Estimator Method for Dose Calculations in Low-Energy x-Ray Irradiations: Implementation, Properties and Performance.' In: *Z Med Phys* (June 2014). DOI: `10.1016/j.zemedi.2014.04.001` (cited on page 67).

[249] F. Smekens et al. 'Split Exponential Track Length Estimator for Monte-Carlo Simulations of Small-Animal Radiation Therapy'. In: *Physics in Medicine & Biology* 59.24 (Nov. 2014), p. 7703. DOI: `10.1088/0031-9155/59/24/7703` (cited on page 67).

[250] Thomas Cajgfinger et al. 'Fixed Forced Detection for Fast SPECT Monte-Carlo Simulation'. In: *Physics in Medicine & Biology* 63.5 (2018), p. 055011. DOI: `10.1088/1361-6560/aa9e32` (cited on page 67).

[251] Nelly Abbani et al. 'Deep Learning-Based Segmentation in Prostate Radiation Therapy Using Monte Carlo Simulated Cone-Beam Computed Tomography'. In: *Medical Physics* n/a.n/a (2022). DOI: `10.1002/mp.15946` (cited on page 67).

[252] D. Sarrut, A. Etxebeste, and J. M. Létang. 'A Photon Source Model for Alpha-Emitter Radionuclides'. In: *Physics in Medicine & Biology* 69.9 (Apr. 2024), p. 095009. DOI: `10.1088/1361-6560/ad3881` (cited on page 68).

[253] Julien Salvadori et al. 'PET Digitization Chain for Monte Carlo Simulation in GATE'. In: *Physics in Medicine & Biology* 69.16 (2024). DOI: `10.1088/1361-6560/ad638c` (cited on page 68).

[254] David Sarrut et al. 'Modeling Complex Particles Phase Space with GAN for Monte Carlo SPECT Simulations: A Proof of Concept'. In: *Physics in Medicine and Biology* 66.5 (2021). DOI: `10.1088/1361-6560/abde9a` (cited on page 68).

[255] David Sarrut et al. 'The OpenGATE Ecosystem for Monte Carlo Simulation in Medical Physics'. In: *Physics in Medicine and Biology* 67.18 (Sept. 2022). DOI: `10.1088/1361-6560/ac8c83` (cited on page 68).

[256] Soo Lee et al. 'Gross tumor volume dependency on phase sorting methods of four-dimensional computed tomography images for lung cancer'. In: *Radiation Oncology Journal* 35 (Sept. 2017), pp. 274–280. DOI: `10.3857/roj.2017.00444` (cited on page 70).

[257] H. Shirato et al. 'Speed and amplitude of lung tumor motion precisely detected in four-dimensional setup and in real-time tumor-tracking radiotherapy'. In: *Int. Journal of Radiation Oncology, Biology and Physics* 64.4 (2006). DOI: `10.1016/j.ijrobp.2005.11.016` (cited on page 70).

[258] S. S. Vedam et al. 'Acquiring a four-dimensional computed tomography dataset using an external respiratory signal'. In: *Physics in medicine and biology* 48 (2003), pp. 45–62. DOI: `10.1088/0031-9155/48/1/304` (cited on page 70).

[259] R. George et al. 'The application of the sinusoidal model to lung cancer patient respiratory motion. Sinusoidal model for respiratory motion'. In: *Medical Physics* 32 (2005), pp. 2850–2861. DOI: `10.1118/1.2001220` (cited on page 70).

[260] Yvette Seppenwoolde et al. 'Precise and real-time measurement of 3D tumor motion in lung due to breathing and heartbeat, measured during radiotherapy'. In: *International Journal of Radiation Oncology* Biology* Physics* 53.4 (2002), pp. 822–834. DOI: `10.1016/s0360-3016(02)02803-1` (cited on page 70).

[261] W Kilby et al. 'The CyberKnife Robotic Radiosurgery System in 2010.' In: *Technology in cancer research & treatment* 9.5 (2010), pp. 433–452 (cited on page 70).

[262] Richard Castillo et al. 'A framework for evaluation of deformable image registration spatial accuracy using large landmark point sets'. In: *Physics in Medicine and Biology* 54.7 (2009), pp. 1849–1870. DOI: `10.1088/0031-9155/54/7/001` (cited on pages 72, 73).

[263] Hamid Ladjal et al. 'Towards Non-Invasive Lung Tumor Tracking Based on Patient Specific Model of Respiratory System'. In: *IEEE Trans. Biomed. Eng.* 68.9 (2021), pp. 2730–2740. DOI: `10.1109/TBME.2021.3053321` (cited on page 73).

[264] Matthieu Giroux et al. 'Biomechanical Patient-Specific Model of the Respiratory System Based on 4D CT Scans and Controlled by Personalized Physiological Compliance'. In: *Medical Image Computing and Computer-Assisted Intervention MICCAI 2017*. Ed. by Maxime Descoteaux et al. Vol. 10434. DOI: 10.1007/978-3-319-66185-8_25. Cham: Springer International Publishing, 2017, pp. 216–223. URL: http://link.springer.com/10.1007/978-3-319-66185-8_25 (visited on 01/23/2018) (cited on page 73).

[265] Daniel Richter. 'Treatment planning for tumors with residual motion in scanned ion beam therapy'. In: *Thesis* (2012). URL: http://tuprints.ulb.tu-darmstadt.de/id/eprint/3071 (cited on page 74).

[266] Petru Manescu et al. 'Four-dimensional radiotherapeutic dose calculation using biomechanical respiratory motion description'. In: *International Journal of Computer Assisted Radiology and Surgery* (2013), pp. 1–9 (cited on page 75).

[267] Petru Manescu et al. 'Four-dimensional radiotherapeutic dose calculation using biomechanical respiratory motion description'. In: *Int. J. Comput. Assist. Radiol. Surg.* 9.3 (2014), pp. 449–457. DOI: 10.1007/s11548-013-0935-2 (cited on page 75).

[268] Yazid Touileb et al. 'Motion-induced Monte Carlo dose calculation using deformable tetrahedral meshes'. In: *2016 IEEE 13th International Symposium on Biomedical Imaging (ISBI)*. 2016, pp. 1257–1260. DOI: 10.1109/ISBI.2016.7493495 (cited on page 75).

[269] Yazid Touileb et al. 'Particle-beam-dependent optimization for Monte Carlo simulation in hadrontherapy using tetrahedral geometries'. In: *Physics in Medicine and Biology* 63.13 (2018). DOI: 10.1088/1361-6560/aacbe5. URL: https://iopscience.iop.org/article/10.1088/1361-6560/aacbe5/meta (cited on page 75).

[270] Katia Parodi et al. 'PET imaging for treatment verification of ion therapy: Implementation and experience at GSI Darmstadt and MGH Boston'. In: *Nuclear Instruments and Methods in Physics Research Section A: Accelerators, Spectrometers, Detectors and Associated Equipment* 591.1 (2008), pp. 282–286. DOI: 10.1016/j.nima.2008.03.075 (cited on page 75).

[271] Petru Manescu et al. '4D positron emission tomography image reconstruction based on biomechanical respiratory motion'. In: *2016 IEEE 13th International Symposium on Biomedical Imaging (ISBI)*. 2016, pp. 99–102. DOI: 10.1109/ISBI.2016.7493220 (cited on page 77).

[272] Cyrille B. Confavreux et al. 'Fracture Risk Evaluation of Bone Metastases: A Burning Issue'. eng. In: *Cancers* 13.22 (Nov. 2021), p. 5711. DOI: 10.3390/cancers13225711 (cited on page 79).

[273] Ego Seeman and Pierre D Delmas. 'Bone quality–the material and structural basis of bone strength and fragility.' In: *The New England journal of medicine* 354.21 (May 2006), pp. 2250–61. DOI: 10.1056/NEJMra053077 (cited on page 79).

[274] Lee A. Feldkamp et al. 'The direct examination of three-dimensional bone architecture in vitro by computed tomography'. en. In: *Journal of Bone and Mineral Research* 4.1 (Feb. 1989), pp. 3–11. DOI: 10.1002/jbmr.5650040103. URL: http://onlinelibrary.wiley.com/doi/10.1002/jbmr.5650040103/abstract (visited on 11/25/2015) (cited on page 79).

[275] K. Engelke et al. 'High spatial resolution imaging of bone mineral using computed microtomography. Comparison with microradiography and undecalcified histologic sections'. In: *Investigative Radiology* 28.4 (Apr. 1993), pp. 341–9. URL: http://www.ncbi.nlm.nih.gov/pubmed/7683009 (cited on page 79).

[276] P. Rüegsegger, B. Koller, and R. Müller. 'A microtomographic system for the nondestructive evaluation of bone architecture'. en. In: *Calcified Tissue International* 58.1 (Jan. 1996), pp. 24–29. DOI: 10.1007/BF02509542. URL: http://link.springer.com/article/10.1007/BF02509542 (visited on 11/25/2015) (cited on page 79).

[277] Murielle Salomé et al. 'A synchrotron radiation microtomography system for the analysis of trabecular bone samples'. en. In: *Medical Physics* 26.10 (1999), p. 2194. DOI: 10.1118/1.598736. URL: http://scitation.aip.org/content/aapm/journal/medphys/26/10/10.1118/1.598736 (visited on 07/29/2016) (cited on page 79).

[278] Tor Hildebrand et al. 'Direct Three-Dimensional Morphometric Analysis of Human Cancellous Bone: Microstructural Data from Spine, Femur, Iliac Crest, and Calcaneus'. en. In: *Journal of Bone and Mineral Research* 14.7 (July 1999), pp. 1167–1174. DOI: `10.1359/jbmr.1999.14.7.1167`. URL: `http://onlinelibrary.wiley.com/doi/10.1359/jbmr.1999.14.7.1167/abstract` (visited on 01/24/2016) (cited on page 79).

[279] Estela Martín-Badosa et al. 'Excised bone structures in mice: imaging at three-dimensional synchrotron radiation micro CT.' en. In: *Radiology* 229.3 (Dec. 2003), pp. 921–8. DOI: `10.1148/radiol.2293020558`. URL: `http://pubs.rsna.org/doi/abs/10.1148/radiol.2293020558` (cited on page 79).

[280] Valérie Bousson et al. 'Cortical bone in the human femoral neck: three-dimensional appearance and porosity using synchrotron radiation'. eng. In: *Journal of Bone and Mineral Research: The Official Journal of the American Society for Bone and Mineral Research* 19.5 (May 2004), pp. 794–801. DOI: `10.1359/JBMR.040124` (cited on page 79).

[281] Lynda F Bonewald. 'The amazing osteocyte.' In: *Journal of bone and mineral research : the official journal of the American Society for Bone and Mineral Research* 26.2 (Feb. 2011), pp. 229–38. DOI: `10.1002/jbmr.320` (cited on page 80).

[282] F. Peyrin et al. 'Micro-CT examinations of trabecular bone samples at different resolutions: 14, 7 and 2 micron level'. eng. In: *Technology and Health Care: Official Journal of the European Society for Engineering and Medicine* 6.5-6 (Dec. 1998), pp. 391–401. URL: `https://hal.science/hal-02159351` (cited on page 80).

[283] Pei Dong et al. '3D osteocyte lacunar morphometric properties and distributions in human femoral cortical bone using synchrotron radiation micro-CT images'. en. In: *Bone* 60 (Mar. 2014), pp. 172–185. DOI: `10.1016/j.bone.2013.12.008`. URL: `http://linkinghub.elsevier.com/retrieve/pii/S8756328213004961` (visited on 01/11/2017) (cited on page 80).

[284] Alexandra Pacureanu et al. 'Nanoscale imaging of the bone cell network with synchrotron X-ray tomography: optimization of acquisition setup: Synchrotron x-ray tomography reveals the bone cell network'. en. In: *Medical Physics* 39.4 (Apr. 2012), pp. 2229–2238. DOI: `10.1118/1.3697525`. URL: `http://doi.wiley.com/10.1118/1.3697525` (visited on 07/05/2017) (cited on page 80).

[285] Max Langer et al. 'X-ray phase nanotomography resolves the 3D human bone ultrastructure.' In: *PloS one* 7.8 (Jan. 2012). Ed. by Xi-Nian Zuo, e35691. DOI: `10.1371/journal.pone.0035691`. URL: `http://dx.plos.org/10.1371/journal.pone.0035691` (cited on page 80).

[286] Bernhard Hesse et al. 'Alterations of mass density and 3D osteocyte lacunar properties in bisphosphonate-related osteonecrotic human jaw bone, a synchrotron µCT study'. eng. In: *PloS One* 9.2 (2014), e88481. DOI: `10.1371/journal.pone.0088481` (cited on page 81).

[287] Bernhard Hesse et al. 'Canalicular network morphology is the major determinant of the spatial distribution of mass density in human bone tissue: evidence by means of synchrotron radiation phase-contrast nano-CT.' In: *Journal of bone and mineral research : the official journal of the American Society for Bone and Mineral Research* 30.2 (Feb. 2015), pp. 346–56. DOI: `10.1002/jbmr.2324`. URL: `http://www.ncbi.nlm.nih.gov/pubmed/25130720` (cited on page 81).

[288] Boliang Yu et al. 'Evaluation of phase retrieval approaches in magnified X-ray phase nano computerized tomography applied to bone tissue'. eng. In: *Optics Express* 26.9 (Apr. 2018), pp. 11110–11124. DOI: `10.1364/OE.26.011110` (cited on page 81).

[289] A. Pacureanu et al. 'Segmentation of 3D cellular networks from SR-micro-CT images'. English. In: *2011 IEEE International Symposium on Biomedical Imaging: From Nano to Macro*. IEEE, Mar. 2011, pp. 1970–1973. DOI: `10.1109/ISBI.2011.5872796` (cited on page 81).

[290] Maria A Zuluaga et al. 'Bone canalicular network segmentation in 3D nano-CT images through geodesic voting and image tessellation'. In: *Physics in Medicine & Biology* 59.9 (2014), p. 2155. DOI: `10.1088/0031-9155/59/9/2155`. URL: `https://dx.doi.org/10.1088/0031-9155/59/9/2155` (cited on page 81).

[291] Boliang Yu et al. 'Assessment of the human bone lacuno-canalicular network at the nanoscale and impact of spatial resolution'. eng. In: *Scientific Reports* 10.1 (Mar. 2020), p. 4567. DOI: `10.1038/s41598-020-61269-8` (cited on page 81).

[292] Boliang Yu et al. 'Quantification of the bone lacunocanalicular network from 3D X-ray phase nanotomography images'. eng. In: *Journal of Microscopy* 282.1 (Apr. 2021), pp. 30–44. DOI: `10.1111/jmi.12973` (cited on page 81).

[293] A. Larrue et al. 'Denoising of Synchrotron Radiation Micro-Ct Images of Trabecular Bone for the Extraction of 3d Quantitative Data on Micro-Cracks'. In: *IEEE MIC*. Dresden, Germany, Oct. 2008 (cited on page 81).

[294] Aymeric Larrue et al. 'Synchrotron Radiation Micro-CT at the Micrometer Scale for the Analysis of the Three-Dimensional Morphology of Microcracks in Human Trabecular Bone'. en. In: *PLOS ONE* 6.7 (July 2011). Publisher: Public Library of Science, e21297. DOI: `10.1371/journal.pone.0021297`. URL: `https://journals.plos.org/plosone/article?id=10.1371/journal.pone.0021297` (visited on 07/04/2024) (cited on page 81).

[295] U. Wolfram et al. 'Characterizing microcrack orientation distribution functions in osteonal bone samples'. eng. In: *Journal of Microscopy* 264.3 (Dec. 2016), pp. 268–281. DOI: `10.1111/jmi.12440` (cited on page 81).

[296] Rémy Gauthier et al. 'Strain rate influence on human cortical bone toughness: A comparative study of four paired anatomical sites'. eng. In: *Journal of the Mechanical Behavior of Biomedical Materials* 71 (July 2017), pp. 223–230. DOI: `10.1016/j.jmbbm.2017.03.015` (cited on page 81).

[297] Rémy Gauthier et al. '3D micro structural analysis of human cortical bone in paired femoral diaphysis, femoral neck and radial diaphysis'. eng. In: *Journal of Structural Biology* 204.2 (2018), pp. 182–190. DOI: `10.1016/j.jsb.2018.08.006` (cited on page 81).

[298] Rémy Gauthier et al. '3D analysis of the osteonal and interstitial tissue in human radii cortical bone'. eng. In: *Bone* 127 (Oct. 2019), pp. 526–536. DOI: `10.1016/j.bone.2019.07.028` (cited on page 81).

[299] Rémy Gauthier et al. 'Influence of loading condition and anatomical location on human cortical bone linear micro-cracks'. eng. In: *Journal of Biomechanics* 85 (Mar. 2019), pp. 59–66. DOI: `10.1016/j.jbiomech.2019.01.008` (cited on page 81).

[300] R Gauthier et al. 'Human femoral lacuno-canalicular network by X-ray nano-CT'. In: *Computer Methods in Biomechanics and Biomedical Engineering*. Vol. 26. S1. Grenoble, 2023, S1–S338. URL: `https://hal.science/hal-04289439v1` (cited on page 82).

[301] Max Langer et al. 'Simultaneous 3D Imaging of Bone and Vessel Microstructure in a Rat Model'. In: *IEEE Transactions on Nuclear Science* 58.1 (Feb. 2011). Conference Name: IEEE Transactions on Nuclear Science, pp. 139–145. DOI: `10.1109/TNS.2010.2091282`. URL: `https://ieeexplore.ieee.org/document/5677452` (visited on 07/04/2024) (cited on page 82).

[302] Rhonda Prisby et al. 'Intermittent PTH(1-84) is osteoanabolic but not osteoangiogenic and relocates bone marrow blood vessels closer to bone-forming sites'. eng. In: *Journal of Bone and Mineral Research: The Official Journal of the American Society for Bone and Mineral Research* 26.11 (Nov. 2011), pp. 2583–2596. DOI: `10.1002/jbmr.459` (cited on page 82).

[303] Hao Xu, Max Langer, and Françoise Peyrin. 'Quantitative analysis of bone microvasculature in a mouse model using the monogenic signal phase asymmetry and marker-controlled watershed'. In: *Physics in Medicine & Biology* 66.12 (2021), p. 125005. DOI: `10.1088/1361-6560/ac047d`. URL: `https://dx.doi.org/10.1088/1361-6560/ac047d` (cited on page 82).

[304] Hao Xu et al. 'Impact of Anti-Angiogenic Treatment on Bone Vascularization in a Murine Model of Breast Cancer Bone Metastasis Using Synchrotron Radiation Micro-CT'. eng. In: *Cancers* 14.14 (July 2022), p. 3443. DOI: `10.3390/cancers14143443` (cited on page 82).

[305] B Delpuech et al. 'Failure Prediction of Tumoral Bone with Osteolytic Lesion in Mice'. In: *Developments and Novel Approaches in Biomechanics and Metamaterials*. Vol. 132. Advanced Structured Materials. 2020. URL: `https://doi.org/10.1007/978-3-030-50464-9_2` (cited on pages 82, 83).

[306] S. Nicolle et al. 'Multi-frequency shear modulus measurements discriminate tumorous from healthy tissues'. eng. In: *Journal of the Mechanical Behavior of Biomedical Materials* 140 (Apr. 2023), p. 105721. DOI: `10.1016/j.jmbbm.2023.105721` (cited on page 83).

[307] A. Toma et al. 'Higher order total variation super-resolution from a single trabecular bone image'. In: *2014 IEEE 11th International Symposium on Biomedical Imaging (ISBI)*. Apr. 2014, pp. 1152–1155. DOI: `10.1109/ISBI.2014.6868079` (cited on page 83).

[308] A. Toma et al. 'Total variation super-resolution for 3D trabecular bone micro-structure segmentation'. In: *2014 22nd European Signal Processing Conference (EUSIPCO)*. Sept. 2014, pp. 2220–2224. URL: `URL%20=%20%7Bhttps://hal.science/hal-01076159%20,%20%7D` (cited on page 83).

[309] Alina Toma, Bruno Sixou, and Françoise Peyrin. 'Iterative choice of the optimal regularization parameter in TV image restoration'. en. In: *Inverse Problems and Imaging* 9.4 (Oct. 2015), pp. 1171–1191. DOI: `10.3934/ipi.2015.9.1171`. URL: `http://www.aimsciences.org/journals/displayArticlesnew.jsp?paperID=11747` (visited on 07/28/2016) (cited on page 83).

[310] Françoise Peyrin et al. 'Semi-blind joint super-resolution/segmentation of 3D trabecular bone images by a TV box approach'. In: *2015 23rd European Signal Processing Conference (EUSIPCO)*. ISSN: 2076-1465. Aug. 2015, pp. 2811–2815. DOI: `10.1109/EUSIPCO.2015.7362897`. URL: `https://ieeexplore.ieee.org/document/7362897` (visited on 12/14/2023) (cited on page 83).

[311] Y. Li et al. 'Super-resolution/segmentation of 2D trabecular bone images by a Mumford-Shah approach and comparison to total variation'. In: *2016 24th European Signal Processing Conference (EUSIPCO)*. ISSN: 2076-1465. Aug. 2016, pp. 1693–1697. DOI: `10.1109/EUSIPCO.2016.7760537`. URL: `https://ieeexplore.ieee.org/document/7760537` (visited on 12/14/2023) (cited on page 84).

[312] Y. Li, B. Sixou, and F. Peyrin. 'Nonconvex Mixed TV/Cahn–Hilliard Functional for Super-Resolution/Segmentation of 3D Trabecular Bone Images'. en. In: *Journal of Mathematical Imaging and Vision* 61.4 (May 2019), pp. 504–514. DOI: `10.1007/s10851-018-0858-1`. URL: `https://doi.org/10.1007/s10851-018-0858-1` (visited on 12/14/2023) (cited on page 84).

[313] Yufei Li et al. 'Investigation Of Semi-coupled Dictionary Learning In 3D Super Resolution HR-pQCT Imaging'. In: *IEEE Transactions on Radiation and Plasma Medical Sciences* 3.2 (2019), pp. 129–136. DOI: `10.1109/TRPMS.2018.2881488`. URL: `https://hal.science/hal-01996993` (cited on page 84).

[314] Y. Li, B. Sixou, and F. Peyrin. 'A Review of the Deep Learning Methods for Medical Images Super Resolution Problems'. In: *IRBM* 42.2 (Apr. 2021), pp. 120–133. DOI: `10.1016/j.irbm.2020.08.004`. URL: `https://www.sciencedirect.com/science/article/pii/S1959031820301408` (visited on 12/14/2023) (cited on page 84).

[315] Rehan Jhuboo et al. 'Why do State-of-the-art Super-Resolution Methods not work well for Bone Microstructure CT Imaging?' In: *2022 30th European Signal Processing Conference (EUSIPCO)*. ISSN: 2076-1465. Aug. 2022, pp. 1283–1287. DOI: `10.23919/EUSIPCO55093.2022.9909945`. URL: `https://ieeexplore.ieee.org/document/9909945/` (visited on 12/14/2023) (cited on page 84).

[316] Christine Chappard et al. 'Virtual monoenergetic images from photon-counting spectral computed tomography to assess knee osteoarthritis'. eng. In: *European Radiology Experimental* 6.1 (Feb. 2022), p. 10. DOI: `10.1186/s41747-021-00261-x` (cited on page 84).

[317] Célestin Garcelon et al. 'Quantification of cartilage and subchondral bone cysts on knee specimens based on a spectral photon-counting computed tomography'. eng. In: *Scientific Reports* 13.1 (July 2023), p. 11080. DOI: `10.1038/s41598-023-38238-y` (cited on pages 84, 90).

[318] Juan F. P. J. Abascal et al. 'Material Decomposition in Spectral CT Using Deep Learning: A Sim2Real Transfer Approach'. In: *IEEE Access* 9 (2021), pp. 25632–25647. DOI: `10.1109/ACCESS.2021.3056150` (cited on page 84).

[319] Juan FPJ Abascal et al. 'A residual U-Net network with image prior for 3D image denoising'. In: *2020 28th European Signal Processing Conference (EUSIPCO)*. IEEE, 2021, pp. 1264–1268. URL: `https://ieeexplore.ieee.org/abstract/document/9287607/` (visited on 08/23/2024) (cited on page 84).

[320] S. Bussod et al. 'Human Knee Phantom for Spectral CT: Validation of a Material Decomposition Algorithm'. In: *2019 IEEE 16th International Symposium on Biomedical Imaging (ISBI 2019)*. ISSN: 1945-8452. Apr. 2019, pp. 1170–1173. DOI: 10.1109/ISBI.2019.8759192. URL: https://ieeexplore.ieee.org/document/8759192/ (visited on 12/14/2023) (cited on page 84).

[321] Timothy A. Damron et al. 'CT-based Structural Rigidity Analysis Is More Accurate Than Mirels Scoring for Fracture Prediction in Metastatic Femoral Lesions'. eng. In: *Clinical Orthopaedics and Related Research* 474.3 (Mar. 2016), pp. 643–651. DOI: 10.1007/s11999-015-4453-0 (cited on page 84).

[322] Joyce H. Keyak et al. 'Predicting the strength of femoral shafts with and without metastatic lesions'. eng. In: *Clinical Orthopaedics and Related Research* 439 (Oct. 2005), pp. 161–170. DOI: 10.1097/01.blo.0000174736.50964.3b (cited on page 84).

[323] Esther Tanck et al. 'Pathological fracture prediction in patients with metastatic lesions can be improved with quantitative computed tomography based computer models'. eng. In: *Bone* 45.4 (Oct. 2009), pp. 777–783. DOI: 10.1016/j.bone.2009.06.009 (cited on page 84).

[324] L. C. Derikx et al. 'The assessment of the risk of fracture in femora with metastatic lesions: comparing case-specific finite element analyses with predictions by clinical experts'. eng. In: *The Journal of Bone and Joint Surgery. British Volume* 94.8 (Aug. 2012), pp. 1135–1142. DOI: 10.1302/0301-620X.94B8.28449 (cited on page 85).

[325] Marc Gardegaront et al. 'Inter-laboratory reproduction and sensitivity study of a finite element model to quantify human femur failure load: Case of metastases'. eng. In: *Journal of the Mechanical Behavior of Biomedical Materials* 158 (Oct. 2024), p. 106676. DOI: 10.1016/j.jmbbm.2024.106676 (cited on page 85).

[326] Emile Saillard et al. 'Finite element models with automatic computed tomography bone segmentation for failure load computation'. eng. In: *Scientific Reports* 14.1 (July 2024), p. 16576. DOI: 10.1038/s41598-024-66934-w (cited on page 85).

[327] Robert E. Alvarez and Albert Macovski. 'Energy-selective reconstructions in X-ray computerized tomography'. In: *Phys. Med. Biol.* 21.5 (1976), pp. 733–744. DOI: 10.1088/0031-9155/21/5/003 (cited on pages 87, 98).

[328] Simon Rit, Cyril Mory, and Peter B Noël. 'Image Formation in Spectral Computed Tomography'. In: *Spectral, Photon Counting Computed Tomography*. 1. CRC Press, July 2020, pp. 355–372. DOI: 10.1201/9780429486111-19. URL: https://hal.science/hal-02956555 (cited on page 88).

[329] Nicolas Ducros et al. 'Regularization of Nonlinear Decomposition of Spectral X-ray Projection Images'. In: *Medical Physics* 44.9 (2017), e174–e187. DOI: 10.1002/mp.12283. URL: https://hal.science/hal-01391538 (cited on page 87).

[330] Tom Hohweiller et al. 'Spectral CT material decomposition in the presence of poisson noise: A Kullback-Leibler approach'. In: *Innovation and Research in BioMedical engineering* 38.4 (2017), pp. 214–218. DOI: 10.1016/j.irbm.2017.06.002. URL: https://hal.science/hal-01557367 (cited on page 88).

[331] Tom Hohweiller et al. 'A Constrained Gauss-Newton Algorithm for Material Decomposition in Spectral Computed Tomography'. In: *ISBI 2018 IEEE International Symposium on Biomedical Imaging*. IEEE. Washington, United States, Apr. 2018. DOI: 10.1109/ISBI.2018.8363587. URL: https://hal.science/hal-01825613 (cited on page 88).

[332] Tom Hohweiller et al. 'An ADMM Algorithm for Constrained Material Decomposition in Spectral CT'. In: *EUSIPCO*. Rome, Italy, Sept. 2018. URL: https://hal.science/hal-01909643 (cited on page 88).

[333] J. P. Schlomka et al. 'Experimental feasibility of multi-energy photon-counting K-edge imaging in pre-clinical computed tomography'. In: *Physics in Medicine and Biology* 53.15 (2008), p. 4031. URL: http://stacks.iop.org/0031-9155/53/i=15/a=002 (cited on page 88).

[334] Cyril Mory et al. 'Comparison of five one-step reconstruction algorithms for spectral CT'. In: *Physics in Medicine and Biology* 63.23 (2018), p. 235001. DOI: 10.1088/1361-6560/aaeaf2. URL: https://hal.science/hal-01760845 (cited on page 88).

[335] S. Rit et al. 'The Reconstruction Toolkit (RTK), an open-source cone-beam CT reconstruction toolkit based on the Insight Toolkit (ITK)'. In: *International Conference on the Use of Computers in Radiation Therapy (ICCR) 2013*. Vol. 489. 1. Melbourne, Australia, May 2013, p. 012079. DOI: `10.1088/1742-6596/489/1/012079`. URL: `https://hal.science/hal-00847373` (cited on page 88).

[336] Pierre-Antoine Rodesch, Si-Mohamed Salim, and Simon Rit. 'Spatially varying regularization weights for one-step spectral CT with SQS'. In: *Sixth international conference on image formation in X-ray computed tomography*. Regensburg, Germany, Aug. 2020, pp. 58–61. URL: `https://hal.science/hal-03014176` (cited on page 88).

[337] P.-A. Rodesch et al. 'Image quality improvement of a one-step spectral CT reconstruction on a prototype photon-counting scanner'. In: *Phys Med Biol* (2023). DOI: `10.1088/1361-6560/ad11a3` (cited on page 88).

[338] Odran Pivot. 'Scatter correction for spectral computed tomography'. Theses. Université de Lyon, Nov. 2019. URL: `https://theses.hal.science/tel-02902108` (cited on page 88).

[339] Odran Pivot et al. 'Scatter correction for spectral CT using a primary modulator mask'. In: *IEEE Transactions on Medical Imaging* 39.6 (June 2020), pp. 2267–2276. DOI: `10.1109/TMI.2020.2970296`. URL: `https://hal.science/hal-02461992` (cited on page 89).

[340] S Bussod et al. 'Human Knee Phantom for Spectral CT: Validation of a Material Decomposition Algorithm'. In: *ISBI IEEE International Symposium on Biomedical Imaging*. Venise, Italy, Apr. 2019. URL: `https://hal.science/hal-02068517` (cited on page 89).

[341] Juan F P J Abascal et al. 'Material Decomposition in Spectral CT using deep learning: A Sim2Real transfer approach'. In: *IEEE Access* (2021). DOI: `10.1109/ACCESS.2021.3056150`. URL: `https://hal.science/hal-02952707` (cited on page 89).

[342] J. F. P. J. Abascal et al. 'A sparse and prior based method for 3D image denoising'. In: *2019 27th European Signal Processing Conference (EUSIPCO)*. ISSN: 2076-1465. Sept. 2019, pp. 1–5. DOI: `10.23919/EUSIPCO.2019.8902564` (cited on page 90).

[343] Juan F P J Abascal et al. 'A residual U-Net network with image prior for 3D image denoising'. In: *28th European Signal Processing Conference (EUSIPCO)*. Amsterdam, Netherlands, Jan. 2021. DOI: `10.23919/Eusipco47968.2020.9287607`. URL: `https://hal.science/hal-02500664` (cited on page 90).

[344] Suzanne Bussod et al. 'Convolutional Neural Network for Material Decomposition in Spectral CT Scans'. In: *2020 28th European Signal Processing Conference (EUSIPCO)*. ISSN: 2076-1465. Jan. 2021, pp. 1259–1263. DOI: `10.23919/Eusipco47968.2020.9287781`. URL: `https://ieeexplore.ieee.org/document/9287781/` (cited on page 90).

[345] Christine Chappard et al. 'Virtual monoenergetic images from photon-counting spectral computed tomography to assess knee osteoarthritis'. In: *European Radiology Experimental* 6.1 (Dec. 2022), p. 10. DOI: `10.1186/s41747-021-00261-x`. URL: `https://hal.science/hal-03705076` (cited on page 90).

[346] Alberto Bravin, Paola Coan, and Pekka Suortti. 'X-ray phase-contrast imaging: from pre-clinical applications towards clinics'. In: *Physics in Medicine & Biology* 58.58 (2013), R1–R35. DOI: `10.1088/0031-9155/58/1/R1`. URL: `http://stacks.iop.org/0031-9155/58/i=1/a=R1` (cited on page 90).

[347] Yunzhe Zhao et al. 'High-resolution, low-dose phase contrast X-ray tomography for 3D diagnosis of human breast cancers'. In: *Proceedings of the National Academy of Sciences* 109.45 (2012), pp. 18290–18294. DOI: `10.1073/pnas.1204460109` (cited on page 90).

[348] Susanne Grandl et al. 'Detection of post-therapeutic effects in breast carcinoma using hard x-ray index of refraction computed tomography–a feasibility study'. In: *PloS one* 11.6 (2016). DOI: `10.1371/journal.pone.0158306` (cited on page 90).

[349] Ludovic Broche et al. 'Calcified cartilage revealed in whole joint by X-ray Phase contrast imaging'. In: *Osteoarthritis and Cartilage Open* (2021), p. 100168. DOI: `10.1016/j.ocarto.2021.100168` (cited on page 90).

[350] Annie Horng et al. 'Cartilage and soft tissue imaging using X-rays: propagation-based phase-contrast computed tomography of the human knee in comparison with clinical imaging techniques and histology'. In: *Investigative radiology* 49.9 (2014), pp. 627–634. DOI: `10.1097/RLI.0000000000000063` (cited on page 90).

[351] Hélène Rougé-Labriet et al. 'X-ray Phase Contrast osteo-articular imaging: a pilot study on cadaveric human hands'. In: *Scientific reports* 10.1 (2020), pp. 1–8. DOI: `https://doi.org/10.1038/s41598-020-58168-3` (cited on page 90).

[352] Franz Pfeiffer et al. 'Phase retrieval and differential phase-contrast imaging with low-brilliance X-ray sources'. In: *Nature physics* 2.4 (2006), pp. 258–261. DOI: `https://doi.org/10.1038/nphys265` (cited on page 90).

[353] Mareike Töpperwien et al. 'Three-dimensional virtual histology of human cerebellum by X-ray phase-contrast tomography'. In: *Proceedings of the National Academy of Sciences* 115.27 (2018), pp. 6940–6945. DOI: `https://doi.org/10.1073/pnas.1801678115` (cited on page 90).

[354] Matthieu Chourrout et al. 'Brain virtual histology with X-ray phase-contrast tomography Part I: whole-brain myelin mapping in white-matter injury models'. In: *bioRxiv* (2021). DOI: `https://doi.org/10.1364/BOE.438832` (cited on page 90).

[355] Matthieu Chourrout et al. 'Brain virtual histology with X-ray phase-contrast tomography Part II: 3D morphologies of amyloid-β plaques in Alzheimer's disease models'. In: *bioRxiv* (2021). URL: `https://hal.science/hal-03451419v1` (cited on page 90).

[356] Liisa Porra et al. 'Synchrotron imaging shows effect of ventilator settings on intrabreath cyclic changes in pulmonary blood volume'. In: *American journal of respiratory cell and molecular biology* 57.4 (2017), pp. 459–467. DOI: `10.1165/rcmb.2017-0007OC`. URL: `https://u-picardie.hal.science/hal-03558223v1` (cited on page 90).

[357] Loriane Weber. 'Iterative tomographic X-Ray phase reconstruction'. Theses. Université de Lyon, Sept. 2016. URL: `https://hal.science/tel-01455376` (cited on page 91).

[358] Loriane Weber et al. *In-line phase nano-tomography of human femoral bone in osteoporosis and osteoarthritis*. Materials Science and Engineering – MSE2014 Congress and Exhibition. Poster. Sept. 2014. URL: `https://hal.science/hal-01922717` (cited on page 91).

[359] Loriane Weber, Max Langer, and Françoise Peyrin. *Refractive index retrieval by combining the contrast transfer function and SART in X-ray in-line phase tomography*. XXVème Colloque GRETSI. Poster. Sept. 2015. URL: `https://hal.science/hal-01288073` (cited on page 91).

[360] Boliang Yu et al. 'Evaluation of phase retrieval approaches in magnified X-ray phase nano computerized tomography applied to bone tissue'. In: *Optics Express* 26.9 (2018), pp. 11110–11124. DOI: `10.1364/OE.26.011110`. URL: `https://hal.science/hal-01812632` (cited on page 92).

[361] Boliang Yu et al. 'Assessment of the human bone lacuno-canalicular network at the nanoscale and impact of spatial resolution'. In: *Scientific Reports* 10.1 (Mar. 2020), p. 4567. DOI: `10.1038/s41598-020-61269-8`. URL: `https://www.hal.inserm.fr/inserm-02510928` (cited on page 92).

[362] Boliang Yu et al. 'Quantification of the bone lacunocanalicular network from 3D X-ray phase nanotomography images'. In: *Journal of Microscopy* 282.1 (Apr. 2021), pp. 30–44. DOI: `10.1111/jmi.12973`. URL: `https://hal.science/hal-03705692` (cited on page 92).

[363] Sebastien Berujon, Hongchang Wang, and Kawal Sawhney. 'X-ray multimodal imaging using a random-phase object'. In: *Physical Review A* 86.6 (2012), p. 063813. DOI: `https://doi.org/10.1103/PhysRevA.86.063813` (cited on pages 92, 93).

[364] Kaye S Morgan, David M Paganin, and Karen KW Siu. 'X-ray phase imaging with a paper analyzer'. In: *Applied Physics Letters* 100.12 (2012), p. 124102. DOI: `https://doi.org/10.1063/1.3694918` (cited on pages 92, 93).

[365] Sebastien Berujon and Eric Ziegler. 'Near-field speckle-scanning-based x-ray imaging'. In: *Physical Review A* 92.1 (2015), p. 013837 (cited on page 93).

[366] Marie-Christine Zdora et al. 'X-ray Phase-Contrast Imaging and Metrology through Unified Modulated Pattern Analysis'. In: *Physical Review Letters* 118.20 (2017), p. 203903. DOI: `10.1103/PhysRevLett.118.203903` (cited on page 93).

[367] David M. Paganin et al. 'Single-image geometric-flow x-ray speckle tracking'. In: *Physical Review A* 98.5 (2018), p. 053813. DOI: `10.1103/PhysRevA.98.053813` (cited on page 93).

[368] Konstantin M Pavlov et al. 'Single-shot x-ray speckle-based imaging of a single-material object'. In: *Physical Review Applied* 13.5 (2020), p. 054023. DOI: `10.1103/PhysRevApplied.13.054023` (cited on page 93).

[369] Konstantin M Pavlov et al. 'X-ray multi-modal intrinsic-speckle-tracking'. In: *Journal of Optics* 22.12 (2020), p. 125604. DOI: `10.1088/2040-8986/abc313` (cited on page 93).

[370] Laurene Quenot et al. 'Evaluation of simulators for x-ray speckle-based phase contrast imaging'. In: *Physics in Medicine and Biology* 66.17 (Sept. 2021), pp. 1–12. DOI: `10.1088/1361-6560/ac1f38`. URL: `https://hal.science/hal-03329939` (cited on page 93).

[371] Helene Rouge-Labriet et al. 'Comparison of X-ray speckle-based imaging deflection retrieval algorithms for the optimization of radiation dose'. In: *Physics in Medicine and Biology* 66.6 (Mar. 2021), p. 065005. DOI: `10.1088/1361-6560/ab87f7`. URL: `https://hal.science/hal-03600465` (cited on page 93).

[372] Laurène Quénot et al. 'Implicit tracking approach for X-ray phase-contrast imaging with a random mask and a conventional system'. In: *Optica* 8.11 (2021), p. 1412. DOI: `10.1364/OPTICA.434954`. URL: `https://hal.science/hal-03555222` (cited on page 93).

[373] Clara Magnin et al. 'Dark-field and directional dark-field on low-coherence x ray sources with random mask modulations: validation with SAXS anisotropy measurements'. In: *Opt. Lett.* 48.22 (2023), pp. 5839–5842. DOI: `10.1364/OL.501716`. URL: `https://opg.optica.org/ol/abstract.cfm?URI=ol-48-22-5839` (cited on pages 93, 94).

[374] Hélène Rougé Labriet, Sébastien Berujon, and Emmanuel Brun. 'DISPOSITIF D'IMAGERIE PAR RAYONS X ET PROCEDE D'IMAGERIE ASSOCIE'. BNT226114PC00. 2021 (cited on page 94).

[375] Clara Magnin et al. 'Dispositif d'imagerie, appareil d'imagerie le comprenant et procédé d'imagerie'. FR2312651. 2023 (cited on page 94).

[376] J Greffier et al. 'Spectral CT imaging: Technical principles of dual-energy CT and multi-energy photon-counting CT'. In: *Diagn. Interv. Imaging.* 104.4 (2023), pp. 167–177. DOI: `10.1016/j.diii.2022.11.009` (cited on page 98).

[377] Salim Si-Mohamed et al. 'Review of an initial experience with an experimental spectral photon-counting computed tomography system'. In: *Nucl. Instrum. Methods Phys. Res. Sect. Accel. Spectrometers Detect. Assoc. Equip.* 873 (2017), pp. 27–35. DOI: `10.1016/j.nima.2017.08.053` (cited on pages 98, 100).

[378] Salim A. Si-Mohamed et al. 'Coronary CT Angiography with Photon-counting CT: First-In-Human Results'. In: *Radiology* 303.2 (2022), pp. 303–313. DOI: `10.1148/radiol.2022202432` (cited on pages 98, 99).

[379] Salah Al Si-Mohamed, Sara Boccalini, Marjorie Villien, et al. 'First experience with a whole-body spectral photon-counting CT clinical prototype'. In: *Investigative Radiology* (2023). DOI: `10.1097/RLI.0000000000000965` (cited on page 98).

[380] Salah Al Si-Mohamed, Sara Boccalini, Pierre-Adrien Rodesch, et al. 'Feasibility of lung imaging with a large field-of-view spectral photon-counting CT system'. In: *Diagnostic and Interventional Imaging* 102.5 (2021), pp. 305–312. DOI: `10.1016/j.diii.2021.01.001` (cited on page 98).

[381] Amir Pourmorteza, Rebecca Symons, Andreas Henning, et al. 'Dose Efficiency of Quarter-Millimeter Photon-Counting Computed Tomography: First-in-Human Results'. In: *Investigative Radiology* 53.6 (2018), pp. 365–372. DOI: `10.1097/RLI.0000000000000463` (cited on page 98).

[382] Shuai Leng, Kuppusamy Rajendran, Hui Gong, et al. '150-um Spatial Resolution Using Photon-Counting Detector Computed Tomography Technology: Technical Performance and First Patient Images'. In: *Investigative Radiology* 53.11 (2018), pp. 655–662. DOI: `10.1097/RLI.0000000000000488` (cited on page 98).

[383] Sara Boccalini et al. 'Feasibility of human vascular imaging of the neck with a large field-of-view spectral photon-counting CT system'. In: *Diagnostic and interventional imaging* 102.5 (2021), pp. 329–332. DOI: `10.1016/j.diii.2020.12.004` (cited on page 99).

[384] Robert E Alvarez. 'Estimator for photon counting energy selective x-ray imaging with multibin pulse height analysis'. In: *Medical physics* 38.5 (2011), pp. 2324–2334. DOI: `10.1118/1.3570658` (cited on page 99).

[385] Joel Greffier et al. 'Virtual monochromatic images for coronary artery imaging with a spectral photon-counting CT in comparison to dual-layer CT systems: a phantom and a preliminary human study'. In: *European Radiology* (2023), pp. 1–13. DOI: `10.1007/s00330-023-09529-9` (cited on page 99).

[386] Salim Si-Mohamed et al. 'Multicolour imaging with spectral photon-counting CT: a phantom study'. In: *European radiology experimental* 2.1 (2018), pp. 1–10. DOI: `10.1186/s41747-018-0063-4` (cited on page 100).

[387] Salim A Si-Mohamed et al. 'In vivo molecular K-edge imaging of atherosclerotic plaque using photon-counting CT'. In: *Radiology* 300.1 (2021), pp. 98–107. DOI: `10.1148/radiol.2021203968` (cited on page 100).

[388] Salim Si-Mohamed et al. 'Spectral photon-counting computed tomography (SPCCT): in-vivo single-acquisition multi-phase liver imaging with a dual contrast agent protocol'. In: *Scientific reports* 9.1 (2019), p. 8458. DOI: `10.1038/s41598-019-44821-z` (cited on page 100).

[389] Michaël Sdika et al. 'Repetitive Motion Compensation for Real Time Intraoperative Video Processing'. In: *Medical Image Analysis* 53 (2019), pp. 1–10. DOI: `10.1016/j.media.2018.12.005`. URL: `https://hal.science/hal-01974104` (cited on pages 101, 137).

[390] Charly Caredda et al. 'Intraoperative quantitative functional brain mapping using an RGB camera'. In: *Neurophotonics* 6.04 (Dec. 2019), p. 1. DOI: `10.1117/1.NPh.6.4.045015`. URL: `https://hal.science/hal-02425832` (cited on page 101).

[391] Charly Caredda et al. 'Intraoperative identification of functional brain areas with RGB imaging using statistical parametric mapping: Simulation and clinical studies'. In: *NeuroImage* (July 2023), p. 120286. DOI: `10.1016/j.neuroimage.2023.120286`. URL: `https://hal.science/hal-04170059` (cited on page 101).

[392] Laure Alston et al. 'Nonlinear relation between concentration and fluorescence emission of protoporphyrin IX in calibrated phantoms'. In: *Journal of Biomedical Optics* 23.09 (Sept. 2018). DOI: `10.1117/1.JBO.23.9.097002`. URL: `https://hal.science/hal-01890753` (cited on page 101).

[393] L. Alston et al. 'Spectral complexity of 5-ALA induced PpIX fluorescence in guided surgery: a clinical study towards the discrimination of healthy tissue and margin boundaries in high and low grade gliomas'. In: *Biomedical optics express* 10.5 (2019), p. 2478. DOI: `10.1364/BOE.10.002478`. URL: `https://hal.science/hal-02109250` (cited on page 102).

[394] Pierre Leclerc et al. 'Machine learning-based prediction of glioma margin from 5-ALA induced PpIX fluorescence spectroscopy'. In: *Scientific Reports* 10.1 (Jan. 2020), 1462 et suiv. DOI: `10.1038/s41598-020-58299-7`. URL: `https://hal.science/hal-02440653` (cited on page 102).

[395] Arthur Gautheron et al. 'An explicit Estimated Baseline Model for Robust Estimation of Fluorophores using Multiple-Wavelength Excitation Fluorescence Spectroscopy'. In: *IEEE Transactions on Biomedical Engineering* (2023). DOI: `10.1109/TBME.2023.3299689`. URL: `https://hal.science/hal-04188757` (cited on page 102).

[396] Jan Huisken et al. 'Optical Sectioning Deep Inside Live Embryos by Selective Plane Illumination Microscopy'. In: *Science* 305.5686 (Aug. 2004), pp. 1007–1009. DOI: `10.1126/science.1100035`. (Visited on 04/10/2021) (cited on page 102).

[397] Peter G Pitrone et al. 'OpenSPIM: An Open-Access Light-Sheet Microscopy Platform'. In: *Nature Methods* 10.7 (July 2013), pp. 598–599. DOI: `10.1038/nmeth.2507`. (Visited on 10/03/2023) (cited on page 102).

[398] Omar E. Olarte et al. 'Light-Sheet Microscopy: A Tutorial'. In: *Advances in Optics and Photonics* 10.1 (Mar. 2018), p. 111. DOI: `10.1364/AOP.10.000111`. (Visited on 10/03/2023) (cited on page 102).

[399] Peter A. Santi. 'Light Sheet Fluorescence Microscopy: A Review'. In: *Journal of Histochemistry & Cytochemistry* 59.2 (Feb. 2011), pp. 129–138. DOI: 10.1369/0022155410394857. (Visited on 10/03/2023) (cited on page 102).

[400] Michael Weber and Jan Huisken. 'Light Sheet Microscopy for Real-Time Developmental Biology'. In: *Current Opinion in Genetics & Development* 21.5 (Oct. 2011), pp. 566–572. DOI: 10.1016/j.gde.2011.09.009. (Visited on 10/03/2023) (cited on page 102).

[401] M.E. Dickinson et al. 'Multi-Spectral Imaging and Linear Unmixing Add a Whole New Dimension to Laser Scanning Fluorescence Microscopy'. In: *BioTechniques* 31.6 (Dec. 2001), pp. 1272–1278. DOI: 10.2144/01316bt01. (Visited on 10/03/2023) (cited on page 102).

[402] Wiebke Jahr et al. 'Hyperspectral Light Sheet Microscopy'. In: *Nature Communications* 6 (Sept. 2015), p. 7990. DOI: 10.1038/ncomms8990. (Visited on 06/07/2017) (cited on page 103).

[403] Sébastien Crombez et al. 'A computational hyperspectral structured light sheet microscope'. In: *2021 OSA Imaging and Applied Optics Congress*. Vancouver (virtual), Canada, July 2021. URL: https://hal.science/hal-03212864 (cited on page 103).

[404] Sébastien Crombez et al. 'A computational hyperspectral structured light sheet microscope'. working paper or preprint. Oct. 2021. URL: https://hal.science/hal-03363493 (cited on page 103).

[405] Alexander Graham Bell. 'On the production and reproduction of sound by light'. In: *American Journal of Science* s3-20.118 (1880), pp. 305–324. DOI: 10.2475/ajs.s3-20.118.305 (cited on page 104).

[406] L. B. Kreuzer. 'Ultralow Gas Concentration Infrared Absorption Spectroscopy'. In: *Journal of Applied Physics* 42.7 (Dec. 2003), pp. 2934–2943. DOI: 10.1063/1.1660651 (cited on page 104).

[407] Allan Rosencwaig and Allen Gersho. 'Theory of the photoacoustic effect with solids'. In: *Journal of Applied Physics* 47.1 (Aug. 2008), pp. 64–69. DOI: 10.1063/1.322296 (cited on page 104).

[408] Andrew Needles et al. 'Development and initial application of a fully integrated photoacoustic micro-ultrasound system'. In: *IEEE Transactions on Ultrasonics, Ferroelectrics, and Frequency Control* 60 (2013), pp. 888–897. DOI: 10.1109/TUFFC.2013.2646 (cited on page 104).

[409] Maëva Vallet et al. 'Quantitative comparison of PZT and CMUT probes for photoacoustic imaging: Experimental validation'. In: *Photoacoustics* 8 (2017), pp. 48–58. DOI: 10.1016/j.pacs.2017.09.001 (cited on page 104).

[410] Jürgen Glatz et al. 'Blind source unmixing in multi-spectral optoacoustic tomography'. In: *Opt. Express* 19.4 (Feb. 2011), pp. 3175–3184. DOI: 10.1364/OE.19.003175 (cited on pages 104, 105).

[411] Aneline Dolet et al. 'Spatial and spectral regularization to discriminate tissues using multispectral photoacoustic imaging'. In: *EURASIP Journal on Advances in Signal Processing* 39 (1 2018). DOI: 10.1186/s13634-018-0554-8 (cited on page 105).

[412] Aneline Dolet et al. 'In Vitro and In Vivo Multispectral Photoacoustic Imaging for the Evaluation of Chromophore Concentration'. In: *Sensors* 21.10 (May 2021), p. 3366. DOI: 10.3390/s21103366 (cited on page 105).

[413] Krista Jansen et al. 'Lipid detection in atherosclerotic human coronaries by spectroscopic intravascular photoacoustic imaging'. In: *Opt. Express* 21.18 (Sept. 2013), pp. 21472–21484. DOI: 10.1364/OE.21.021472 (cited on page 105).

[414] Srivalleesha Mallidi et al. 'Selective detection of cancer using spectroscopic photoacoustic imaging and bioconjugated gold nanoparticles'. In: *2008 IEEE Ultrasonics Symposium*. 2008, pp. 578–581. DOI: 10.1109/ULTSYM.2008.0139 (cited on page 105).

[415] Aneline Dolet et al. 'In Vitro and In Vivo Multispectral Photoacoustic Imaging for the Evaluation of Chromophore Concentration'. In: *Sensors* 21.10 (May 2021), p. 3366. DOI: 10.3390/s21103366. URL: https://hal.science/hal-03352856 (cited on page 106).

[416] Melanie Schellenberg et al. 'Semantic segmentation of multispectral photoacoustic images using deep learning'. In: *Photoacoustics* 26 (2022), p. 100341. DOI: 10.1016/j.pacs.2022.100341 (cited on page 106).

[417] Michael F. Insana, David G. Brown, and K. Kirk Shung. 'Acoustic scattering theory applied to soft biological tissues'. In: *Ultrasonic scattering in biological tissues*. CRC Press Boca Raton, FL, 1993, pp. 75–124. DOI: `https://doi.org/10.4324/9780203734797` (cited on page 106).

[418] Emilie Franceschini and Régine Guillermin. 'Experimental assessment of four ultrasound scattering models for characterizing concentrated tissue-mimicking phantoms'. In: *The Journal of the Acoustical Society of America* 132.6 (2012). Publisher: Acoustical Society of America, pp. 3735–3747. DOI: `10.1121/1.4765072` (cited on page 106).

[419] Pauline Muleki-Seya and William D. O'Brien. 'Ultrasound Scattering From Cell-Pellet Biophantoms and Ex Vivo Tumors Provides Insight Into the Cellular Structure Involved in Scattering'. In: *IEEE Transactions on Ultrasonics, Ferroelectrics, and Frequency Control* 69.2 (2022). Conference Name: IEEE Transactions on Ultrasonics, Ferroelectrics, and Frequency Control, pp. 637–649. DOI: `10.1109/TUFFC.2021.3130682` (cited on page 107).

[420] Jared McNew, Roberto Lavarello, and William D. O'Brien. 'Sound scattering from two concentric fluid spheres'. In: *The Journal of the Acoustical Society of America* 125.1 (2009). Publisher: Acoustical Society of America, pp. 1–4. DOI: `10.1121/1.3035901` (cited on page 107).

[421] Pauline Muleki-Seya, Aiguo Han, and William D. O'Brien. 'Evaluation of ultrasound scattering models adapted for two types of scatterers to extract scatterer parameters from cell-pellet biophantoms'. In: *2022 IEEE International Ultrasonics Symposium (IUS)*. ISSN: 1948-5727. 2022, pp. 1–4. DOI: `10.1109/IUS54386.2022.9957992` (cited on page 107).

[422] Michael L. Oelze and Jonathan Mamou. 'Review of Quantitative Ultrasound: Envelope Statistics and Backscatter Coefficient Imaging and Contributions to Diagnostic Ultrasound'. In: *IEEE Transactions on Ultrasonics, Ferroelectrics, and Frequency Control* 63.2 (2016). Conference Name: IEEE Transactions on Ultrasonics, Ferroelectrics, and Frequency Control, pp. 336–351. DOI: `10.1109/TUFFC.2015.2513958` (cited on page 107).

[423] Steven C. Lin et al. 'Noninvasive Diagnosis of Nonalcoholic Fatty Liver Disease and Quantification of Liver Fat Using a New Quantitative Ultrasound Technique'. In: *Clinical Gastroenterology and Hepatology* 13.7 (2015), 1337–1345.e6. DOI: `10.1016/j.cgh.2014.11.027` (cited on page 107).

[424] M. C Kolios et al. 'Ultrasonic spectral parameter characterization of apoptosis'. In: *Ultrasound in Medicine & Biology* 28.5 (2002), pp. 589–597. DOI: `10.1016/S0301-5629(02)00492-1` (cited on page 107).

[425] Jonathan Mamou et al. 'Three-Dimensional High-Frequency Backscatter and Envelope Quantification of Cancerous Human Lymph Nodes'. In: *Ultrasound in Medicine & Biology* 37.3 (2011), pp. 345–357. DOI: `10.1016/j.ultrasmedbio.2010.11.020` (cited on page 107).

[426] Cyril Malinet et al. 'Toward cancer characterization using light backscattering spectroscopy and quantitative ultrasound'. In: *Photons Plus Ultrasound: Imaging and Sensing 2023*. Vol. 12379. SPIE, 2023, pp. 39–46. DOI: `10.1117/12.2648087` (cited on page 107).

[427] Wolfgang Bogner, Ricardo Otazo, and Anke Henning. 'Accelerated MR spectroscopic imaging—a review of current and emerging techniques'. In: *NMR in Biomedicine* 34.5 (2021), e4314. DOI: `10.1002/nbm.4314` (cited on page 108).

[428] Jabrane Karkouri et al. 'ACCELERATED SPIRAL CHEMICAL SHIFT IMAGING FOR PROTON DENSITY AND T2*FAT-WATER QUANTIFICATION'. In: *IEEE International Symposium on Biomedical Imaging (ISBI 2019)*. Venice, Italy, Apr. 2019. URL: `https://hal.science/hal-02056801` (cited on page 109).

[429] Jabrane Karkouri et al. 'Time Undersampled Acquisition for Multidimensional Sparse Signals With Application to Magnetic Resonance Spectroscopic Imaging'. In: *IEEE Transactions on Signal Processing* 69 (2021), pp. 5289–5298. DOI: `10.1109/TSP.2021.3112931`. URL: `https://hal.science/hal-03370854` (cited on page 109).

[430] Antoine Naëgel et al. 'Validation of apparent intra-and extra-myocellular lipid content indicator using spiral spectroscopic imaging at 3T'. In: *Annual meeting ESMRMB*. ESMRMB. Basel, Switzerland, Oct. 2023. URL: `https://hal.science/hal-04184268` (cited on page 110).

[431] Antoine Naëgel et al. 'Mapping of apparent Intra-and Extra-myocellular lipid content using spiral spectroscopic imaging and diffusion imaging at 3T'. In: *Annual Meeting ISMRM-ESMRMB*. London, United Kingdom, May 2022. URL: https://hal.science/hal-03770476 (cited on page 110).

[432] CzesĺÍw J Lewa. 'Magnetic resonance imaging in the presence of mechanical waves'. In: *Spectroscopy letters* 24.1 (1991), pp. 55–67 (cited on page 113).

[433] Czeslaw J Lewa and Jacques D de Certaines. 'MR imaging of viscoelastic properties'. In: *Journal of Magnetic Resonance Imaging* 5.2 (1995), pp. 242–244. DOI: 10.1002/jmri.1880050221 (cited on page 113).

[434] R Muthupillai et al. 'Magnetic resonance elastography by direct visualization of propagating acoustic strain waves'. In: *science* 269.5232 (1995), pp. 1854–1857. DOI: 10.1126/science.7569924 (cited on page 113).

[435] Sebastian Hirsch, Jurgen Braun, and Ingolf Sack. *Magnetic resonance elastography: physical background and medical applications*. John Wiley & Sons, 2017 (cited on page 114).

[436] Jin Wang et al. 'New and emerging applications of magnetic resonance elastography of other abdominal organs'. In: *Topics in magnetic resonance imaging: TMRI* 27.5 (2018), p. 335. DOI: 10.1097/RMR.0000000000000182 (cited on page 114).

[437] Pilar Sango Solanas et al. 'Harmonic wideband simultaneous dual-frequency MR Elastography'. In: *NMR in Biomedicine* 34.2 (2021), e4442. DOI: 10.1002/nbm.4442. URL: https://hal.science/hal-03007661 (cited on page 114).

[438] Pauline Lefebvre et al. 'Active Control of the Spatial MRI Phase Distribution with Optimal Control Theory'. In: *Journal of Magnetic Resonance* 281 (2017), pp. 82–93. DOI: 10.1016/j.jmr.2017.05.008. URL: https://hal.science/hal-01528498 (cited on page 114).

[439] Pilar Sango-Solanas et al. 'Ultrashort echo time magnetic resonance elastography for quantification of the mechanical properties of short T2 tissues via optimal control-based radiofrequency pulses'. In: *NMR in Biomedicine* (2024), e5210. DOI: 10.1002/nbm.5210. URL: https://hal.science/hal-04646232v1 (cited on page 115).

[440] Pilar Sango Solanas et al. 'Short echo time dual-frequency MR Elastography with Optimal Control RF pulses'. In: *Scientific Reports* 12.1 (Jan. 2022), p. 1406. DOI: 10.1038/s41598-022-05262-3. URL: https://hal.science/hal-03563413 (cited on page 115).

[441] Mathilde Bigot et al. 'Magnetic Resonance Elastography of Rodent Brain'. In: *Frontiers in Neurology* 9 (2018), p. 1010. DOI: 10.3389/fneur.2018.01010. URL: https://hal.science/hal-01990014 (cited on page 115).

[442] Mathilde Bigot et al. 'The apparent mechanical effect of isolated amyloid-β and α-synuclein aggregates revealed by multi-frequency MRE'. In: *NMR in Biomedicine* 33.1 (2020), e4174. DOI: 10.1002/nbm.4174. URL: https://hal.science/hal-02358712 (cited on page 116).

[443] Lon R Cardon and Hugh Watkins. 'Waiting for the working draft from the human genome project: a huge achievement, but not of immediate medical use'. In: *Bmj* 320.7244 (2000), pp. 1223–1224. DOI: https://doi.org/10.1136/bmj.320.7244.1223 (cited on page 116).

[444] Nicholas J Schork. 'Personalized medicine: time for one-person trials'. In: *Nature* 520.7549 (2015), pp. 609–611. DOI: 10.1038/520609a (cited on page 116).

[445] Seán Walsh et al. 'Decision support systems in oncology'. In: *JCO clinical cancer informatics* 3 (2019), pp. 1–9. DOI: 10.1200/CCI.18.00001 (cited on page 117).

[446] Philippe Lambin et al. 'Radiomics: extracting more information from medical images using advanced feature analysis'. In: *European journal of cancer* 48.4 (2012), pp. 441–446. DOI: 10.1016/j.ejca.2011.11.036 (cited on page 117).

[447] Robert J Gillies, Paul E Kinahan, and Hedvig Hricak. 'Radiomics: images are more than pictures, they are data'. In: *Radiology* 278.2 (2016), pp. 563–577. DOI: 10.1148/radiol.2015151169 (cited on page 117).

[448] Hugo JWL Aerts et al. 'Decoding tumour phenotype by noninvasive imaging using a quantitative radiomics approach'. In: *Nature communications* 5.1 (2014), p. 4006. DOI: `https://doi.org/10.1038/ncomms5006` (cited on page 117).

[449] Benjamin Leporq et al. 'MRI-based radiomics to predict lipomatous soft tissue tumors malignancy: a pilot study'. In: *Cancer Imaging* 20.1 (Dec. 2020), Article number: 78. DOI: `10.1186/s40644-020-00354-7`. URL: `https://hal.science/hal-03107185` (cited on page 117).

[450] Guillaume Fradet et al. 'Prediction of lipomatous soft tissue malignancy on MRI: comparison between machine learning applied to radiomics and deep learning'. In: *European Radiology Experimental* 6.1 (Dec. 2022), p. 41. DOI: `10.1186/s41747-022-00295-9`. URL: `https://hal.science/hal-03773793` (cited on page 117).

[451] Amine Bouhamama et al. 'Prediction of histologic neoadjuvant chemotherapy response in osteosarcoma using pretherapeutic MRI radiomics'. In: *Radiology: Imaging Cancer* 4.5 (2022), e210107. DOI: `10.1148/rycan.210107` (cited on page 118).

[452] Angeline Nemeth et al. 'Multicontrast MRI-based radiomics for the prediction of pathological complete response to neoadjuvant chemotherapy in patients with early triple negative breast cancer'. In: *Magnetic Resonance Materials in Physics, Biology and Medicine* (July 2021). DOI: `10.1007/s10334-021-00941-0`. URL: `https://hal.science/hal-03408526` (cited on page 118).

[453] Khuram Faraz et al. 'Characterization of Breast Tumors from MR Images Using Radiomics and Machine Learning Approaches'. In: *Journal of Personalized Medicine* 13.7 (2023), p. 1062. DOI: `10.3390/jpm13071062`. URL: `https://hal.science/PRIMES_WP2/hal-04209972v1` (cited on page 118).

[454] Amine Bouhamama et al. 'Radiomics combined with transcriptomics to predict response to immunotherapy from patients treated with PD-1/PD-L1 inhibitors for advanced NSCLC'. In: *Frontiers in Radiology* 3 (2023), p. 1168448. DOI: `10.3389/fradi.2023.1168448`. URL: `https://universite-paris-saclay.hal.science/PRIMES_WP2/hal-04209979v1` (cited on page 119).

[455] Emmanuel Mesny et al. 'Intravoxel incoherent motion magnetic resonance imaging to assess early tumor response to radiation therapy: Review and future directions'. In: *Magnetic Resonance Imaging* (2024). DOI: `10.1016/j.mri.2024.02.008`. URL: `https://hal.science/hal-04771740v1` (cited on page 119).

[456] Pietro Caironi et al. 'Lung Opening and Closing during Ventilation of Acute Respiratory Distress Syndrome'. In: *American Journal of Respiratory and Critical Care Medicine* 181.6 (2010), pp. 578–586. DOI: `10.1164/rccm.200905-0787OC` (cited on page 119).

[457] A. Morales Pinzón et al. 'Lung Segmentation by Cascade Registration'. In: *Innovation and Research in BioMedical engineering* 38.5 (Oct. 2017), pp. 266–280. DOI: `10.1016/j.irbm.2017.07.003`. URL: `https://hal.science/hal-01684687` (cited on page 119).

[458] Duván Alberto Gómez Betancur et al. 'Airway Segmentation, Skeletonization, and Tree Matching to Improve Registration of 3D CT Images with Large Opacities in the Lungs'. In: *Computer Vision and Graphics*. Ed. by Leszek J. Chmielewski et al. Cham: Springer International Publishing, 2016, pp. 395–407. DOI: `10.1007/978-3-319-46418-3_35` (cited on page 119).

[459] Alfredo Morales Pinzon et al. 'A tree-matching algorithm: Application to airways in CT images of subjects with the acute respiratory distress syndrome'. In: *Medical Image Analysis* 35 (2017), pp. 101–115. DOI: `10.1016/j.media.2016.06.020`. URL: `https://hal.science/hal-01373998` (cited on page 119).

[460] Maciej Orkisz et al. 'Voxel-wise assessment of lung aeration changes on CT images using image registration: application to acute respiratory distress syndrome (ARDS)'. In: *International Journal of Computer Assisted Radiology and Surgery* 14.11 (Sept. 2019), pp. 1945–1953. DOI: `10.1007/s11548-019-02064-3`. URL: `https://hal.science/hal-02363448` (cited on page 119).

[461] Julien Cohen et al. 'Computed Tomography Registration-Derived Regional Ventilation Indices Compared to Global Lung Function Parameters in Patients With COPD'. In: *Frontiers in Physiology* 13 (2022), p. 862186. DOI: `10.3389/fphys.2022.862186`. URL: `https://hal.science/hal-03679913` (cited on page 119).

[462] Sarah E. Gerard et al. 'Multi-Resolution Convolutional Neural Networks for Fully Automated Segmentation of Acutely Injured Lungs in Multiple Species'. In: *Medical Image Analysis* (2019), p. 101592. DOI: `10.1016/j.media.2019.101592` (cited on page 119).

[463] Ludmilla Penarrubia et al. 'Precision of CT-derived alveolar recruitment assessed by human observers and a machine learning algorithm in moderate and severe ARDS'. In: *Intensive Care Medicine Experimental* 11 (2023), p. 8. DOI: `10.1186/s40635-023-00495-6` (cited on page 119).

[464] Ludmilla Penarrubia et al. 'Improving motion-mask segmentation in thoracic CT with multiplanar U-nets'. In: *Medical Physics* 49.1 (2022), pp. 420–431. DOI: `10.1002/mp.15347`. URL: `https://hal.science/hal-03464276` (cited on page 119).

[465] E.E. Dávila Serrano et al. 'Software for CT-image Analysis to Assist the Choice of Mechanical-ventilation Settings in Acute Respiratory Distress Syndrome'. In: *2020 International Conference on Computer Vision and Graphics (ICCVG 2020)*. Ed. by Leszek J Chmielewski, Ryszard Kozera, and Arkadiusz Orlowski. Vol. 12334. Lecture Notes in Computer Science 5. Varsovie, Poland: Springer Nature, Sept. 2020. DOI: `10.1007/978-3-030-59006-2\_5`. URL: `https://hal.science/hal-02887264` (cited on page 120).

[466] Louis Chauvelot et al. 'Quantitative-analysis of computed tomography in COVID-19 and non COVID-19 ARDS patients: A case-control study'. In: *Journal of Critical Care* 60 (Dec. 2020), pp. 169–176. DOI: `10.1016/j.jcrc.2020.08.006`. URL: `https://hal.science/hal-03149581` (cited on page 120).

[467] J.-C. Richard et al. 'Response to PEEP in COVID-19 ARDS patients with and without extracorporeal membrane oxygenation. A multicenter case-control computed tomography study'. In: *Critical Care* 26.195 (2022), p. 101592. DOI: `10.1186/s13054-022-04076-z` (cited on page 120).

[468] Laurent Bitker et al. 'Validation of a novel system to assess end-expiratory lung volume and alveolar recruitment in an ARDS model'. In: *INTENSIVE CARE MEDICINE EXPERIMENTAL* 9.1 (Dec. 2021), p. 46. DOI: `10.1186/s40635-021-00410-x`. URL: `https://hal.science/hal-03688174` (cited on page 120).

[469] L Bitker et al. 'Non-invasive quantification of macrophagic lung recruitment during experimental ventilation-induced lung injury'. In: *Journal of Applied Physiology* 127.2 (2019), pp. 546–558. DOI: `10.1152/japplphysiol.00825.2018`. URL: `https://hal.science/hal-02274549` (cited on page 120).

[470] L. Bitker et al. 'Non-invasive quantification of acute macrophagic lung inflammation with [11C](R)-PK11195 using a three-tissue compartment kinetic model in experimental acute respiratory distress syndrome.' In: *European Journal of Nuclear Medicine and Molecular Imaging* 49 (2022), pp. 2122–2136. DOI: `10.1007/s00259-022-05713-z` (cited on page 120).

[471] François Dhelft et al. 'Prone position decreases acute lung inflammation measured by [11C](R)-PK11195 positron emission tomography in experimental acute respiratory distress syndrome'. In: *Journal of Applied Physiology* 134.2 (2023), pp. 467–481. DOI: `10.1152/japplphysiol.00234.2022` (cited on page 120).

[472] Hoai-Thu Nguyen et al. 'Quantitative Magnetic Resonance Imaging Assessment of the Quadriceps Changes during an Extreme Mountain Ultramarathon'. In: *Medicine and Science in Sports and Exercise* 53.4 (Apr. 2021), pp. 869–881. DOI: `10.1249/mss.0000000000002535`. URL: `https://hal.science/hal-02998029` (cited on pages 120, 132).

[473] Benjamin Gilles et al. 'Automatic segmentation for volume quantification of quadriceps muscle head: a longitudinal study in athletes enrolled in extreme mountain ultra-marathon'. In: *ISMRM: International Society for Magnetic Resonance in Medicine*. Singapour, Singapore, May 2016. URL: `https://hal-lirmm.ccsd.cnrs.fr/lirmm-01383144` (cited on page 120).

[474] Antoine Naëgel et al. 'Alteration of skeletal muscle energy metabolism assessed by phosphorus-31 magnetic resonance spectroscopy in clinical routine, part 1: Advanced quality control pipeline'. In: *NMR in Biomedicine* 36.12 (2023), e5025. DOI: `10.1002/nbm.5025` (cited on pages 121, 172).

[475] Antoine Naëgel et al. 'Alteration of skeletal muscle energy metabolism assessed by 31P MRS in clinical routine: Part 2. Clinical application'. In: *NMR in Biomedicine* 36.12 (2023), e5031. DOI: `10.1002/nbm.5031` (cited on pages 122, 172).

[476] Olivier Couture et al. ‘Ultrasound Localization Microscopy and Super-Resolution: A State of the Art’. In: *IEEE Transactions on Ultrasonics, Ferroelectrics, and Frequency Control* 65.8 (Aug. 2018), pp. 1304–1320. doi: `10.1109/TUFFC.2018.2850811` (cited on page 122).

[477] Eric Betzig et al. ‘Imaging Intracellular Fluorescent Proteins at Nanometer Resolution’. en. In: *Science* 313.5793 (Sept. 2006), pp. 1642–1645. doi: `10.1126/science.1127344`. url: `https://science.sciencemag.org/content/313/5793/1642` (visited on 11/07/2019) (cited on page 122).

[478] Arthur Chavignon et al. ‘3D Transcranial Ultrasound Localization Microscopy in the Rat Brain with a Multiplexed Matrix Probe’. In: *IEEE Transactions on Biomedical Engineering* (2021). Conference Name: IEEE Transactions on Biomedical Engineering, pp. 1–1. doi: `10.1109/TBME.2021.3137265` (cited on page 122).

[479] Maxime Polichetti et al. ‘A Nonlinear Beamformer Based on p-th Root Compression—Application to Plane Wave Ultrasound Imaging’. en. In: *Applied Sciences* 8.4 (Apr. 2018). Number: 4 Publisher: Multidisciplinary Digital Publishing Institute, p. 599. doi: `10.3390/app8040599`. url: `https://www.mdpi.com/2076-3417/8/4/599` (visited on 04/22/2022) (cited on page 122).

[480] J. Camacho, M. Parrilla, and C. Fritsch. ‘Phase Coherence Imaging’. In: *IEEE Transactions on Ultrasonics, Ferroelectrics, and Frequency Control* 56.5 (2009), pp. 958–974. doi: `10.1109/TUFFC.2009.1128` (cited on page 122).

[481] Tanya Chernyakova et al. ‘iMAP Beamforming for High-Quality High Frame Rate Imaging’. In: *IEEE Transactions on Ultrasonics, Ferroelectrics, and Frequency Control* 66.12 (Dec. 2019). Conference Name: IEEE Transactions on Ultrasonics, Ferroelectrics, and Frequency Control, pp. 1830–1844. doi: `10.1109/TUFFC.2019.2933506` (cited on page 122).

[482] Vincent Perrot et al. ‘So you think you can DAS? A viewpoint on delay-and-sum beamforming’. In: *Ultrasonics* 111 (Mar. 2021), p. 106309. doi: `10.1016/j.ultras.2020.106309`. url: `https://www.sciencedirect.com/science/article/pii/S0041624X20302444` (visited on 09/26/2023) (cited on page 123).

[483] Alexandre Corazza et al. ‘Microbubble Identification Based on Decision Theory for Ultrasound Localization Microscopy’. In: *IEEE Open Journal of Ultrasonics, Ferroelectrics, and Frequency Control* 3 (2023). Conference Name: IEEE Open Journal of Ultrasonics, Ferroelectrics, and Frequency Control, pp. 41–55. doi: `10.1109/OJUFFC.2023.3274512` (cited on page 123).

[484] Clément Daviller et al. ‘Automatic myocardial ischemic lesion detection on magnetic resonance perfusion weighted imaging prior perfusion quantification: A pre-modeling strategy’. In: *Computers in Biology and Medicine* 110 (May 2019), pp. 108–119. doi: `10.1016/j.compbiomed.2019.05.001`. url: `https://hal.science/hal-02135018` (cited on page 123).

[485] Clément Daviller et al. ‘Direct Comparison of Bayesian and Fermi Deconvolution Approaches for Myocardial Blood Flow Quantification: In silico and Clinical Validations’. In: *Frontiers in Physiology* 12 (Apr. 2021). doi: `10.3389/fphys.2021.483714`. url: `https://hal.science/hal-03244361` (cited on page 124).

[486] Matthieu Chourrout et al. ‘Brain virtual histology with X-ray phase-contrast tomography Part II: 3D morphologies of amyloid-β plaques in Alzheimer’s disease models’. In: *Biomedical optics express* 13.3 (2022), pp. 1640–1653. doi: `10.1364/BOE.438890`. url: `https://hal.science/hal-03451419` (cited on page 125).

[487] Matthieu Chourrout et al. ‘Virtual histology of Alzheimer’s Disease: Biometal entrapment within amyloid-β plaques allows for detection via X-ray phase-contrast imaging’. In: *Acta Biomaterialia* 170 (2023), pp. 260–272. doi: `https://doi.org/10.1016/j.actbio.2023.07.046` (cited on page 125).

[488] M. Lapert et al. ‘Exploring the Physical Limits of Saturation Contrast in Magnetic Resonance Imaging’. In: *Scientific Reports* 2.1 (Dec. 2012), p. 589. doi: `10.1038/srep00589` (cited on page 126).

[489] Eric Van Reeth et al. ‘Optimal Control Theory for Applications in Magnetic Resonance Imaging’. In: *Pacific Journal of Mathematics for Industry* 9.1 (Dec. 2017), p. 9. doi: `10.1186/s40736-017-0034-3` (cited on page 126).

[490] Eric Van Reeth et al. 'A Simplified Framework to Optimize MRI Contrast Preparation'. In: *Magnetic Resonance in Medicine* 81.1 (2019), pp. 424–438. DOI: 10.1002/mrm.27417 (cited on page 126).

[491] Benoît Vernier et al. 'MRI CONTRAST ENHANCEMENT OF MAGNETIZATION PREPARED STEADY STATE SEQUENCE: AN OPTIMAL CONTROL FRAMEWORK'. In: *ISBI*. NICE, France, Apr. 2021. URL: https://hal.science/hal-03213076 (cited on page 126).

[492] Hugo Dorez et al. 'Endoluminal high-resolution MR imaging protocol for colon walls analysis in mouse model of colitis'. In: *Magnetic Resonance Materials in Physics, Biology and Medicine* 29.4 (2016), pp. 657–669. DOI: 10.1007/s10334-016-0539-2. URL: https://hal.science/hal-01296355 (cited on page 128).

[493] Hugo Dorez et al. 'In vivo MRS for the assessment of mouse colon using a dedicated endorectal coil: initial findings'. In: *NMR in Biomedicine* 30.12 (Dec. 2017), p. 12. DOI: 10.1002/nbm.3794. URL: https://hal.science/hal-01611564 (cited on page 128).

[494] Paul Nobre et al. 'Optical link as an alternative for MRI receive coils: toward a passive approach'. In: *IEEE Transactions on Biomedical Engineering* (Nov. 2022), pp. 1–7. DOI: 10.1109/TBME.2022.3217822. URL: https://hal.science/hal-03840513 (cited on page 129).

[495] Paul Nobre et al. 'Electric field measurements in preclinical MRI at 11.7 T and 7 T for experimental SAR comparison'. In: *Journal of Magnetism and Magnetic Materials* (2024), p. 171818. DOI: 10.1016/j.jmmm.2024.171. URL: https://udl.hal.science/hal-04771686v1 (cited on page 129).

[496] Michaël Sdika et al. 'Multi-atlas-based fully automatic segmentation of individual muscles in rat leg'. In: *Magnetic Resonance Materials in Physics, Biology and Medicine* 29.2 (2016), pp. 223–235. DOI: 10.1007/s10334-015-0511-6. URL: https://hal.science/hal-01375862 (cited on page 132).

[497] Michaël Sdika. 'Enhancing atlas based segmentation with multiclass linear classifiers'. In: *Medical Physics* 42 (2015), p. 7169. DOI: 10.1118/1.4935946. URL: https://hal.science/hal-01375850 (cited on page 132).

[498] T. Dietenbeck et al. 'Detection of the whole myocardium in 2D-echocardiography for multiple orientations using a geometrically constrained level-set'. In: *Medical Image Analysis* 16.2 (Feb. 2012), pp. 386–401. DOI: 10.1016/j.media.2011.10.003. URL: https://hal.science/hal-00796887 (cited on page 133).

[499] T. Dietenbeck et al. 'Whole myocardium tracking in 2D-echocardiography in multiple orientations using a motion constrained level-set'. In: *Medical Image Analysis* 18.3 (2014), pp. 500–514. DOI: 10.1016/j.media.2014.01.005. URL: https://hal.science/hal-00941827 (cited on page 133).

[500] P. Clarysse and Denis Friboulet. *Traitement et analyse d'images cardiaques*. Ed. by Denis Friboulet Patrick Clarysse. Traitement et analyse d'images cardiaques. Hermès-Lavoisier, 2014. URL: https://hal.science/hal-01117708 (cited on page 133).

[501] Patrick Clarysse and Denis Friboulet. *Multi-modality Cardiac Imaging: Processing and Analysis*. Ed. by Denis Friboulet Patrick Clarysse. Wiley, 2015. URL: https://hal.science/hal-01485985 (cited on page 133).

[502] Sarah Leclerc et al. 'Deep Learning for Segmentation using an Open Large-Scale Dataset in 2D Echocardiography'. In: *IEEE Transactions on Medical Imaging* 38.9 (Mar. 2019), pp. 2198–2210. DOI: 10.1109/TMI.2019.2900516. URL: https://hal.science/hal-02054458 (cited on page 133).

[503] Olivier Bernard et al. 'Deep Learning Techniques for Automatic MRI Cardiac Multi-Structures Segmentation and Diagnosis: Is the Problem Solved?' In: *IEEE Transactions on Medical Imaging* 37.11 (2018), pp. 2514–2525. DOI: 10.1109/TMI.2018.2837502 (cited on page 134).

[504] Pierre-Antoine Ganaye, Michael Sdika, and Hugues Benoit-Cattin. 'Towards Integrating Spatial Localization in Convolutional Neural Networks for Brain Image Segmentation'. In: *2018 IEEE 15th International Symposium on Biomedical Imaging (ISBI 2018)*. Washington, United States: IEEE, Apr. 2018. DOI: 10.1109/ISBI.2018.8363652. URL: https://hal.science/hal-01812045 (cited on page 134).

[505] Matthieu Martin et al. 'Automatic Segmentation and Location Learning of Neonatal Cerebral Ventricles in 3D Ultrasound Data Combining CNN and CPPN'. In: *Computers in Biology and Medicine* (Feb. 2021), p. 104268. DOI: 10.1016/j.compbiomed.2021.104268. URL: https://hal.science/hal-03148181 (cited on page 134).

[506] Matthieu Martin et al. 'Automatic Segmentation of the Cerebral Ventricle in Neonates Using Deep Learning with 3D Reconstructed Freehand Ultrasound Imaging'. In: *2018 IEEE International Ultrasonics Symposium (IUS)*. Kobe, France: IEEE, Oct. 2018, pp. 1–4. URL: https://hal.science/hal-02043054 (cited on page 134).

[507] Pierre-Antoine Ganaye et al. 'Removing Segmentation Inconsistencies with Semi-Supervised Non-Adjacency Constraint'. In: *Medical Image Analysis* 58 (Dec. 2019), p. 101551. DOI: 10.1016/j.media.2019.101551. URL: https://hal.science/hal-02275956 (cited on page 134).

[508] Pierre-Antoine Ganaye, Michaël Sdika, and Hugues Benoit-Cattin. 'Semi-supervised learning for segmentation under semantic constraint'. In: *MICCAI*. Grenada, Spain, Sept. 2018. URL: https://hal.science/hal-01904641 (cited on page 134).

[509] Nathan Painchaud et al. 'Cardiac Segmentation With Strong Anatomical Guarantees'. In: *IEEE Transactions on Medical Imaging* 39.11 (Nov. 2020), pp. 3703–3713. DOI: 10.1109/TMI.2020.3003240. URL: https://hal.science/hal-03119215 (cited on pages 134, 135).

[510] Nathan Painchaud et al. 'Echocardiography Segmentation with Enforced Temporal Consistency'. In: *IEEE Transactions on Medical Imaging* 41.10 (Oct. 2022), pp. 2867–2878. DOI: 10.1109/TMI.2022.3173669. URL: https://hal.science/hal-03672999 (cited on pages 135, 143).

[511] Sophie Carneiro Esteves, Antoine Vacavant, and Odyssée Merveille. 'Learning a reconnecting regularization term for blood vessel variational segmentation'. In: *IEEE-EMBS International Conference on Biomedical and Health Informatics (BHI)*. virtuel, France, July 2021. URL: https://hal.science/hal-03278387 (cited on page 136).

[512] Enyi Chen et al. 'Multiple Sclerosis Clinical Forms Classification Study with Graph Convolutional Networks'. In: *Frontiers in Neuroscience* (2024). DOI: 10.3389/fnins.2023.1268860. URL: https://hal.science/hal-04373468 (cited on page 136).

[513] Ewan Evain et al. 'Motion estimation by deep learning in 2D echocardiography: synthetic dataset and validation'. In: *IEEE Transactions on Medical Imaging* (2022). DOI: 10.1109/TMI.2022.3151606. URL: https://hal.science/hal-03603014 (cited on pages 137, 138).

[514] Michaël Sdika et al. 'Robust real time motion compensation for intraoperative video processing during neurosurgery'. In: *IEEE 13th International Symposium on Biomedical Imaging (ISBI 2016)*. Biomedical Imaging (ISBI), 2016 IEEE 13th International Symposium on. Prague, Czech Republic, Apr. 2016. DOI: 10.1109/ISBI.2016.7493445. URL: https://hal.science/hal-01451713 (cited on page 137).

[515] YI Abel-Aziz and HM Karara. 'Direct linear transformation from comparator coordinates into object space coordinates'. In: *Urbana, IL: American Society of Photogrammetry* (1971), pp. 1–18 (cited on page 138).

[516] Richard I Hartley. 'In defense of the eight-point algorithm'. In: *IEEE Transactions on pattern analysis and machine intelligence* 19.6 (1997), pp. 580–593 (cited on page 138).

[517] Charly Caredda et al. 'Intraoperative Resting-State Functional Connectivity Based on RGB Imaging'. In: *Diagnostics* 11.11 (Nov. 2021), p. 2067. DOI: 10.3390/diagnostics11112067. URL: https://hal.science/hal-03423345 (cited on page 138).

[518] C. Caredda et al. 'Real Time Intraoperative Functional Brain Mapping Based on RGB Imaging'. In: *Innovation and Research in BioMedical engineering* (May 2020). DOI: 10.1016/j.irbm.2020.04.004. URL: https://hal.science/hal-02568247 (cited on page 138).

[519] Charly Caredda et al. 'Optimal Spectral Combination of a Hyperspectral Camera for Intraoperative Hemodynamic and Metabolic Brain Mapping'. In: *Applied Sciences* 10.15 (Aug. 2020), p. 5158. DOI: 10.3390/app10155158. URL: https://hal.science/hal-02908361 (cited on page 138).

[520] Yunyun Sun et al. 'A pipeline for the generation of synthetic cardiac color Doppler'. In: *IEEE Transactions on Ultrasonics, Ferroelectrics and Frequency Control* 69.3 (2022), pp. 932–941. DOI: 10.1109/TUFFC.2021.3136620. URL: https://cnrs.hal.science/hal-03538666 (cited on page 138).

[521] Mathilde Giacalone et al. ‘Robustness of spatio-temporal regularization in perfusion MRI deconvolution: An application to acute ischemic stroke’. In: *Magnetic Resonance in Medicine* 78.5 (2017), pp. 1981–1990. DOI: 10.1002/mrm.26573. URL: https://hal.science/hal-01571763 (cited on page 139).

[522] Noelie Debs et al. ‘Simulated perfusion MRI data to boost training of convolutional neural networks for lesion fate prediction in acute stroke’. In: *Computers in Biology and Medicine* 116 (2020), p. 103579 (cited on page 139).

[523] Noëlie Debs et al. ‘Evaluation of the realism of an MRI simulator for stroke lesion prediction using convolutional neural network’. In: *Simulation and Synthesis in Medical Imaging: 4th International Workshop, SASHIMI 2019, Held in Conjunction with MICCAI 2019, Shenzhen, China, October 13, 2019, Proceedings 4*. Springer. 2019, pp. 151–160 (cited on page 139).

[524] Kannara Mom, Patrick Clarysse, and Nicolas Duchateau. ‘Population-based personalization of geometric models of myocardial infarction’. In: *Proc. FIMH, LNCS*. Vol. 12738. 2021, pp. 3–11 (cited on page 140).

[525] M El Azami et al. ‘Detection of Lesions Underlying Intractable Epilepsy on T1-Weighted MRI as an Outlier Detection Problem’. In: *PLoS ONE* 11.9 (2016), e0161498. DOI: 10.1371/journal.pone.0161498. URL: https://hal.science/hal-01437876 (cited on page 140).

[526] M. El Azami, C. Lartizien, and S. Canu. ‘Robust outlier detection with L0-SVDD’. In: *European Symposium on Artificial Neural Networks, Computational Intelligence and Machine Learning (ESANN) 2014*. Présentation orale. Bruges, Belgium, Apr. 2014. URL: https://hal.science/hal-00956468 (cited on page 140).

[527] M El Azami, Carole Lartizien, and S. Canu. ‘Converting SVDD scores into probability estimates: Application to outlier detection’. In: *Neurocomputing* 268 (2017), pp. 64–75. DOI: 10.1016/j.neucom.2017.01.103. URL: https://hal.science/hal-01592016 (cited on page 140).

[528] Zaruhi Alaverdyan et al. ‘Regularized siamese neural network for unsupervised outlier detection on brain multiparametric magnetic resonance imaging: Application to epilepsy lesion screening’. In: *Medical Image Analysis* 60 (2020). DOI: 10.1016/j.media.2019.101618. URL: https://hal.science/hal-02995591 (cited on page 141).

[529] Daria Zotova, Julien Jung, and Carole Lartizien. ‘GAN-Based Synthetic FDG PET Images from T1 Brain MRI Can Serve to Improve Performance of Deep Unsupervised Anomaly Detection Models’. In: *6th Simulation and Synthesis in Medical Imaging (SASHIMI) workshop held in conjunction with MICCAI 2021*. Vol. 12965. Lecture Notes in Computer Science. Strasbourg, France: Springer International Publishing, Sept. 2021, pp. 142–152. DOI: 10.1007/978-3-030-87592-3_14. URL: https://hal.science/hal-03404479 (cited on page 141).

[530] Nicolas Pinon, Robin Trombetta, and Carole Lartizien. ‘One-Class SVM on siamese neural network latent space for Unsupervised Anomaly Detection on brain MRI White Matter Hyperintensities’. In: *MIDL 2023*. Nashville, United States: MLR Press, July 2023. URL: https://hal.science/hal-04067715 (cited on page 141).

[531] Anthime Flaus et al. ‘Deep-learning predicted PET can be subtracted from the true clinical fluorodeoxyglucose PET co-registered to MRI to identify the epileptogenic zone in focal epilepsy’. In: *Epilepsia Open* 8 (2023), pp. 1440–1451. URL: https://api.semanticscholar.org/CorpusID:261048437 (cited on page 141).

[532] Valentine Wargnier-Dauchelle et al. ‘A Weakly Supervised Gradient Attribution Constraint for Interpretable Classification and Anomaly Detection’. In: *IEEE Transactions on Medical Imaging* (2023). DOI: 10.1109/TMI.2023.3282789. URL: https://hal.science/hal-04110698 (cited on page 142).

[533] Ramprasaath R Selvaraju et al. ‘Grad-cam: Visual explanations from deep networks via gradient-based localization’. In: *Proceedings of the IEEE international conference on computer vision*. 2017, pp. 618–626 (cited on page 142).

[534] Valentine Wargnier-Dauchelle et al. 'A More Interpretable Classifier for Multiple Sclerosis'. In: *International Symposium on Biomedical Imaging (ISBI)*. Nice, France, Apr. 2021. DOI: 10.1109/ISBI48211.2021.9434074. URL: https://hal.science/hal-03212945 (cited on page 142).

[535] Maja Cikes et al. 'Machine learning-based phenogrouping in heart failure to identify responders to cardiac resynchronization therapy'. In: *European Journal of Heart Failure* 21.1 (2019), pp. 74–85. DOI: 10.1002/ejhf.1333. URL: https://hal.science/hal-01912849 (cited on page 143).

[536] Benoit Freiche et al. 'Characterizing myocardial ischemia and reperfusion patterns with hierarchical manifold learning'. In: *Statistical Atlases and Computational Modeling of the Heart (STACOM), MICCAI Workshop*. Strasbourg, France, 2021. URL: https://hal.science/hal-03510191 (cited on page 143).

[537] Maxime Di Folco et al. 'Characterizing interactions between cardiac shape and deformation by non-linear manifold learning'. In: *Medical Image Analysis* 75 (2022), p. 102278. DOI: https://doi.org/10.1016/j.media.2021.102278. URL: https://www.sciencedirect.com/science/article/pii/S1361841521003236 (cited on page 143).

[538] Nathan Painchaud et al. 'Cardiac MRI Segmentation with Strong Anatomical Guarantees'. In: *MICCAI 2019, 22nd International Conference*. Vol. 11765. Lecture Notes in Computer Science book series (LNCS). Shenzhen, China: Springer, Cham, Oct. 2019. DOI: 10.1007/978-3-030-32245-8_70. URL: https://u-bourgogne.hal.science/hal-02318818 (cited on page 143).

[539] Gabriel Bernardino et al. 'Reinforcement learning for active modality selection during diagnosis'. In: *25th International Conference on Medical Image Computing and Computer Assisted Intervention*. Singapore, Singapore, Sept. 2022. URL: https://hal.science/hal-03752018 (cited on page 143).

[540] Peter B Barker and Doris DM Lin. 'In vivo proton MR spectroscopy of the human brain'. In: *Progress in nuclear magnetic resonance spectroscopy* 49.2 (2006), pp. 99–128 (cited on page 143).

[541] Nima Hatami, Michaël Sdika, and Hélène Ratiney. 'Magnetic Resonance Spectroscopy Quantification using Deep Learning'. In: *MICCAI*. Grenada, Spain, Oct. 2018. URL: https://hal.science/hal-01904617 (cited on page 144).

[542] H. Ratiney et al. 'Time-Domain Semi-Parametric Estimation Based on a Metabolite Basis Set'. In: *Nuclear Magnetic Resonance in Biomedicine* 18 (2005). article, pp. 1–13. URL: https://hal.science/hal-00443422 (cited on page 144).

[543] Nima Hatami, Hélène Ratiney, and Michaël Sdika. 'MR SPECTROSCOPY ARTIFACT REMOVAL WITH U-NET CONVOLUTIONAL NEURAL NETWORK'. In: *27th Annual meeting of the ISMRM*. Montreal, Canada, May 2019. URL: https://hal.science/hal-02129946 (cited on page 144).

[544] SA Smith et al. 'Computer simulations in magnetic resonance. An object-oriented programming approach'. In: *Journal of Magnetic Resonance, Series A* 106.1 (1994), pp. 75–105 (cited on page 144).

[545] Brian J Soher et al. 'GAVA: spectral simulation for in vivo MRS applications'. In: *Journal of magnetic resonance* 185.2 (2007), pp. 291–299 (cited on page 144).

[546] Gerardo Rumindo et al. 'In vivo estimation of normal left ventricular stiffness and contractility based on routine cine MR acquisition'. In: *Medical Engineering & Physics* 85 (2020), pp. 16–26. DOI: 10.1016/j.medengphy.2020.09.003. URL: https://hal.science/hal-03093687 (cited on page 144).

[547] Patrick R. Girard et al. 'Dual Hyperquaternion Poincaré Groups'. In: *Advances in Applied Clifford Algebras* 31.2 (2021). DOI: 10.1007/s00006-021-01120-z. URL: https://hal.science/hal-03139597 (cited on page 145).

[548] Kristen M. Meiburger, U. Rajendra Acharya, and Filippo Molinari. 'Automated localization and segmentation techniques for B-mode ultrasound images: A review'. In: *Computers in Biology and Medicine* 92 (2018), pp. 210–235. DOI: 10.1016/j.compbiomed.2017.11.018 (cited on page 145).

[549] G. Zahnd et al. 'Simultaneous extraction of carotid artery intima-media interfaces in ultrasound images - Assessment of wall thickness temporal variation during the cardiac cycle'. In: *International Journal of Computer Assisted Radiology and Surgery* 9.4 (Oct. 2013), pp. 645–658. DOI: 10.1007/s11548-013-0945-0. URL: https://hal.science/hal-00872714 (cited on page 145).

[550] Guillaume Zahnd et al. 'A fully-automatic method to segment the carotid artery layers in ultrasound imaging: Application to quantify the compression-decompression pattern of the intima-media complex during the cardiac cycle'. In: *Ultrasound in Medicine & Biology* 43.11 (2017), pp. 239–257. DOI: `10.1016/j.ultrasmedbio.2016.08.016`. URL: `https://hal.science/hal-01405046` (cited on page 145).

[551] Kristen M. Meiburger et al. 'Carotid Ultrasound Boundary Study (CUBS): An Open Multicenter Analysis of Computerized Intima-Media Thickness Measurement Systems and Their Clinical Impact'. In: *Ultrasound in Medicine & Biology* 47.8 (2021), pp. 2442–2455. DOI: `10.1016/j.ultrasmedbio.2021.03.022` (cited on page 145).

[552] Nolann Lainé et al. 'Carotid artery wall segmentation in ultrasound image sequences using a deep convolutional neural network'. In: *International Conference on Computer Vision and Graphics*. Vol. 598. Lecture Notes in Networks and Systems. Varsovie, Poland, Sept. 2022, pp. 1–12. URL: `https://hal.science/hal-03898051` (cited on page 146).

[553] Kristen Meiburger et al. 'Carotid Ultrasound Boundary Study (CUBS): Technical considerations on an open multi-center analysis of computerized measurement systems for intima-media thickness measurement on common carotid artery longitudinal B-mode ultrasound scans'. In: *Computers in Biology and Medicine* 144 (May 2022), p. 105333. DOI: `10.1016/j.compbiomed.2022.105333`. URL: `https://hal.science/hal-03688169` (cited on page 146).

[554] G. Zahnd et al. 'Evaluation of a Kalman-based block matching method to assess the bi-dimensional motion of the carotid artery wall in B-mode ultrasound sequences'. In: *Medical Image Analysis* 17.5 (July 2013), pp. 573–585. DOI: `10.1016/j.media.2013.03.006`. URL: `https://hal.science/hal-00850540` (cited on page 146).

[555] S. Qorchi et al. 'Kalman-Based Carotid-Artery Longitudinal-Kinetics Estimation and Pattern Recognition'. In: *Innovation and Research in BioMedical engineering* 38.4 (Aug. 2017), pp. 219–223. DOI: `10.1016/j.irbm.2017.06.001`. URL: `https://hal.science/hal-01684662` (cited on page 146).

[556] Guillaume Zahnd et al. 'Progressive Attenuation of the Longitudinal Kinetics in the Common Carotid Artery: Preliminary in Vivo Assessment'. In: *Ultrasound in Medicine & Biology* 41.1 (Jan. 2015), pp. 339–345. DOI: `10.1016/j.ultrasmedbio.2014.07.019`. URL: `https://hal.science/hal-01121159` (cited on page 146).

[557] Sami Qorchi, Didier Vray, and Maciej Orkisz. 'Estimating Arterial Wall Deformations from Automatic Key-Point Detection and Matching'. In: *Ultrasound in Medicine & Biology* 47.5 (Feb. 2021), pp. 1367–1376. DOI: `10.1016/j.ultrasmedbio.2021.01.001`. URL: `https://hal.science/hal-03149555` (cited on page 146).

[558] E.-J. Courtial et al. 'Identifying Hyper-Viscoelastic Model Parameters from an Inflation-Extension Test and Ultrasound Images'. In: *Experimental Mechanics* 55.7 (2015), pp. 1353–1366. DOI: `10.1007/s11340-015-0042-0`. URL: `https://hal.science/hal-01206929` (cited on page 146).

[559] G. Zahnd et al. 'Real-time ultrasound-tagging to track the 2D motion of the common carotid artery wall in vivo'. In: *Medical Physics* 42.8 (2015), pp. 820–830. DOI: `10.1118/1.4905376`. URL: `https://hal.science/hal-01207368` (cited on page 146).

[560] Guillaume Zahnd et al. 'CAROLAB A platform to analyze carotid ultrasound data'. In: *2019 IEEE International Ultrasonics Symposium (IUS)*. Glasgow, United Kingdom: IEEE, Oct. 2019, pp. 463–466. DOI: `10.1109/ULTSYM.2019.8925673`. URL: `https://hal.science/hal-02460951` (cited on page 146).

[561] SW Peterson, D Robertson, and JJPM Polf. 'Optimizing a three-stage Compton camera for measuring prompt gamma rays emitted during proton radiotherapy'. In: *Physics in Medicine & Biology* 55.22 (2010), p. 6841. DOI: `10.1088/0031-9155/55/22/015` (cited on page 153).

[562] Akihisa Omata et al. 'Multi-modal 3D imaging of radionuclides using multiple hybrid Compton cameras'. In: *Scientific reports* 12.1 (2022), p. 2546. DOI: `10.1038/s41598-022-06401-6` (cited on page 153).

[563] Javier Caravaca et al. ‘Compton and Proximity Imaging of Ac In Vivo With a CZT Gamma Camera: A Proof of Principle With Simulations’. In: *IEEE Transactions on Radiation and Plasma Medical Sciences* 6.8 (2022), pp. 904–915. doi: `10.1109/trpms.2022.3166116` (cited on page 153).

[564] Kenichiro Ogane et al. ‘Simultaneous measurements of single gamma ray of 131I and annihilation radiation of 18F with Compton PET hybrid camera’. In: *Applied Radiation and Isotopes* 176 (2021), p. 109864. doi: `10.1016/j.apradiso.2021.109864` (cited on page 153).

[565] Emily Frame et al. ‘Coded aperture and Compton imaging for the development of 225Ac-based radiopharmaceuticals’. In: *Medical Physics* 50.10 (2023), pp. 6454–6468. doi: `10.1002/mp.16717` (cited on page 153).

[566] Takashi Nakano et al. ‘Imaging of 99mTc-DMSA and 18F-FDG in humans using a Si/CdTe Compton camera’. In: *Physics in Medicine & Biology* 65.5 (2020), 05LT01. doi: `10.1088/1361-6560/ab33d8` (cited on page 153).

[567] Fatma Terzioglu, Peter Kuchment, and Leonid Kunyansky. ‘Compton camera imaging and the cone transform: a brief overview’. In: *Inverse Problems* 34.5 (2018), p. 054002. doi: `10.1088/1361-6420/aab0ab` (cited on page 153).

[568] Markus Haltmeier and Daniela Schiefeneder. ‘Variational regularization of the weighted conical Radon transform’. In: *Inverse problems* 34.12 (2018), p. 124009. doi: `10.1088/1361-6420/aae9a3` (cited on page 153).

[569] Mirela Frandes et al. ‘A Tracking Compton-Scattering Imaging System for Hadron Therapy Monitoring’. In: *IEEE Transactions on Nuclear Science* 57.1 (2010), pp. 144–150. doi: `10.1109/TNS.2009.2031679` (cited on page 154).

[570] Andreas Zoglauer, R Andritschke, and F Schopper. ‘MEGAlib–the medium energy gamma-ray astronomy library’. In: *New Astronomy Reviews* 50.7-8 (2006), pp. 629–632. doi: `10.1016/j.newar.2006.06.049` (cited on page 154).

[571] Voichiţa Maxim, Mirela Frandeş, and Rémy Prost. ‘Analytical inversion of the Compton transform using the full set of available projections’. In: *Inverse Problems* 25.9 (2009), p. 095001. doi: `10.1088/0266-5611/25/9/095001` (cited on page 154).

[572] Mai K. Nguyen et al. ‘On a Novel Approach to Compton Scattered Emission Imaging’. In: *IEEE Transactions on Nuclear Science* 56.3 (2009), pp. 1430–1437. doi: `10.1109/TNS.2009.2018106` (cited on page 154).

[573] Voichiţa Maxim. ‘Filtered Backprojection Reconstruction and Redundancy in Compton Camera Imaging’. In: *IEEE Transactions on Image Processing* 23.1 (2014), pp. 332–341. doi: `10.1109/TIP.2013.2288143` (cited on page 154).

[574] Voichiţa Maxim. ‘Enhancement of Compton camera images reconstructed by inversion of a conical Radon transform’. In: *Inverse Problems* 35.1 (2018), p. 014001. doi: `10.1088/1361-6420/aaecdb`. url: `https://dx.doi.org/10.1088/1361-6420/aaecdb` (cited on page 154).

[575] Arthur P Dempster, Nan M Laird, and Donald B Rubin. ‘Maximum likelihood from incomplete data via the EM algorithm’. In: *Journal of the royal statistical society: series B (methodological)* 39.1 (1977), pp. 1–22. doi: `10.1111/j.2517-6161.1977.tb01600.x` (cited on page 154).

[576] Voichita Maxim et al. ‘Probabilistic models and numerical calculation of system matrix and sensitivity in list-mode MLEM 3D reconstruction of Compton camera images’. In: *Physics in Medicine & Biology* 61.1 (2015), p. 243. doi: `10.1088/0031-9155/61/1/243`. url: `https://dx.doi.org/10.1088/0031-9155/61/1/243` (cited on page 154).

[577] Xavier Lojacono et al. ‘Low Statistics Reconstruction of the Compton Camera Point Spread Function in 3D Prompt-$gamma$ Imaging of Ion Beam Therapy’. In: *IEEE Transactions on Nuclear Science* 60.5 (2013), pp. 3355–3363. doi: `10.1109/TNS.2013.2275200`. url: `https://inria.hal.science/hal-00872700/` (cited on page 154).

[578] Xavier Lojacono, Voichita Maxim, and Rémy Prost. ‘Calcul de la matrice des probabilités de transfert en imagerie compton 3d’. In: *XXIIIe Colloque GRETSI-Traitement du Signal et des Images (GRETSI’11)*. 2011 (cited on page 154).

[579] Estelle Hilaire et al. ‘Proton therapy monitoring by Compton imaging: influence of the large energy spectrum of the prompt-γ radiation’. In: *Physics in Medicine & Biology* 61.8 (2016), p. 3127. DOI: `10.1088/0031-9155/61/8/3127`. URL: `https://dx.doi.org/10.1088/0031-9155/61/8/3127` (cited on page 154).

[580] Voichiţa Maxim et al. ‘Tomographic reconstruction from Poisson distributed data: a fast and convergent EM-TV dual approach’. In: *Numerical Algorithms* (2023), pp. 1–31. DOI: `10.1007/s11075-023-01517-w`. URL: `https://hal.science/hal-01892281v1` (cited on pages 154, 155).

[581] Yuemeng Feng et al. ‘3-D Reconstruction Benchmark of a Compton Camera Against a Parallel-Hole Gamma Camera on Ideal Data’. In: *IEEE Transactions on Radiation and Plasma Medical Sciences* 4.4 (2020), pp. 479–488. DOI: `10.1109/TRPMS.2019.2955745` (cited on pages 154, 155).

[582] Yuemeng Feng et al. ‘Influence of Doppler broadening model accuracy in Compton camera list-mode MLEM reconstruction’. In: *Inverse Problems in Science and Engineering* 29.13 (2021), pp. 3509–3529. DOI: `10.1080/17415977.2021.2011863`. URL: `https://hal.science/hal-03481082v1` (cited on page 155).

[583] Yuemeng Feng. ‘Modeling and regularization in tomographic reconstruction for Compton camera imaging’. PhD thesis. Université de Lyon, 2019. URL: `https://theses.hal.science/tel-02900652v1` (cited on page 155).

[584] Théo Leuliet, Voichita Maxim, and Bruno Sixou. ‘Reconstruction tomographique et déconvolution aveugle en TEP: une méthode d’apprentissage profond hybride’. In: *XXVIIIème Colloque Francophone de Traitement du Signal et des Images (Gretsi 2022)*. 2022. URL: `https://hal.science/hal-03706239/` (cited on page 155).

[585] B. M. Asl, A. Mahloojifar, and A. Mahloojifar. ‘Contrast enhancement and robustness improvement of adaptive ultrasound imaging using forward-backward minimum variance beamforming’. In: *IEEE Transactions on Ultrasonics, Ferroelectrics, and Frequency Control* 58.4 (2011), pp. 858–867. DOI: `10.1109/TUFFC.2011.1880` (cited on page 156).

[586] C. I. C. Nilsen and S. Holm. ‘Wiener beamforming and the coherence factor in ultrasound imaging’. In: *IEEE Transactions on Ultrasonics, Ferroelectrics, and Frequency Control* 57.6 (2010), pp. 1329–1346. DOI: `10.1109/TUFFC.2010.1553` (cited on page 156).

[587] J.-F. Synnevag et al. ‘Benefits of minimum-variance beamforming in medical ultrasound imaging’. In: *IEEE Transactions on Ultrasonics, Ferroelectrics, and Frequency Control* 56.9 (2009), pp. 1868–1879. DOI: `10.1109/TUFFC.2009.1263` (cited on page 156).

[588] L. Tong et al. ‘Multi-Transmit Beam Forming for Fast Cardiac Imaging—Experimental Validation and In Vivo Application’. In: *IEEE Transactions on Medical Imaging* 33.6 (2014), pp. 1205–1219. DOI: `10.1109/TMI.2014.2302312` (cited on page 156).

[589] Jian-Yu Lu. ‘2D and 3D high frame rate imaging with limited diffraction beams’. In: *IEEE Transactions on Ultrasonics, Ferroelectrics, and Frequency Control* 44.4 (1997), pp. 839–856. DOI: `10.1109/58.655200` (cited on pages 156, 157).

[590] G. Montaldo et al. ‘Coherent plane-wave compounding for very high frame rate ultrasonography and transient elastography’. In: *IEEE Transactions on Ultrasonics, Ferroelectrics and Frequency Control* 56.3 (2009), pp. 489–506. DOI: `10.1109/TUFFC.2009.1067` (cited on page 156).

[591] A. Besson et al. ‘Ultrafast Ultrasound Imaging as an Inverse Problem: Matrix-Free Sparse Image Reconstruction’. In: *IEEE Transactions on Ultrasonics, Ferroelectrics, and Frequency Control* 65.3 (2018), pp. 339–355. DOI: `10.1109/TUFFC.2017.2768583` (cited on pages 156, 157).

[592] G. David et al. ‘Time domain compressive beam forming of ultrasound signals’. In: *The Journal of the Acoustical Society of America* 137.5 (2015), pp. 2773–2784. DOI: `10.1121/1.4919302` (cited on pages 156, 157).

[593] E. Ozkan et al. ‘Inverse Problem of Ultrasound Beamforming With Sparsity Constraints and Regularization’. In: *IEEE Transactions on Ultrasonics, Ferroelectrics, and Frequency Control* 65.3 (2018), pp. 356–365. DOI: `10.1109/TUFFC.2017.2757880` (cited on page 156).

[594] M. Schiffner et al. 'Compressed Sensing for Fast Image Acquisition in Pulse-Echo Ultrasound'. In: *Biomedical Engineering* 57.SI-1 (2012), pp. 192–195. DOI: `10.1515/bmt-2012-4142` (cited on page 156).

[595] T. Szasz et al. 'Beamforming Through Regularized Inverse Problems in Ultrasound Medical Imaging'. In: *IEEE Transactions on Ultrasonics, Ferroelectrics, and Frequency Control* 63.12 (2016), pp. 2031–2044. DOI: `10.1109/TUFFC.2016.260893`. URL: `https://hal.science/hal-01474905v1` (cited on page 156).

[596] H. Liebgott, R. Prost, and D. Friboulet. 'Pre-beamformed RF signal reconstruction in medical ultrasound using compressive sensing'. In: *Ultrasonics* 53.2 (Feb. 2013), pp. 525–533. DOI: `10.1016/j.ultras.2012.09.008`. URL: `https://hal.science/hal-00798017` (cited on page 157).

[597] Oana Lorintiu et al. 'Compressed sensing reconstruction of 3D ultrasound data using dictionary learning and line-wise subsampling'. In: *IEEE Transactions on Medical Imaging* 34.12 (2015), pp. 2467–2477. DOI: `10.1109/TMI.2015.2442154`. URL: `https://hal.science/hal-01180189` (cited on page 157).

[598] Oana Lorintiu et al. 'Compressed sensing Doppler ultrasound reconstruction using block sparse Bayesian learning'. In: *IEEE Transactions on Medical Imaging* 35 (2016), pp. 978–987. DOI: `10.1109/TMI.2015.2504240`. URL: `https://hal.science/hal-01274672` (cited on page 157).

[599] Maxime Gasse et al. 'High-Quality Plane Wave Compounding using Convolutional Neural Networks'. In: *IEEE Transactions on Ultrasonics, Ferroelectrics and Frequency Control* 64.10 (2017), pp. 1637–1639. DOI: `10.1109/TUFFC.2017.2736890`. URL: `https://hal.science/hal-01596034` (cited on pages 157, 158).

[600] D. Friboulet et al. 'Compressive sensing for raw RF signals reconstruction in ultrasound'. In: *IEEE International Ultrasonics Symposium*. 2010, pp. 367–370. DOI: `10.1109/ULTSYM.2010.5935766` (cited on page 157).

[601] J. Richy et al. 'Blood Velocity Estimation Using Compressive Sensing'. In: *IEEE Transactions on Medical Imaging* 32.11 (June 2013), pp. 1979–1988. DOI: `10.1109/TMI.2013.2266871`. URL: `https://hal.science/hal-00839213` (cited on page 157).

[602] D. Garcia et al. 'Stolt's f-k migration for plane wave ultrasound imaging'. In: *IEEE Transactions on Ultrasonics, Ferroelectrics and Frequency Control* 60.9 (2013), pp. 1853–1867. DOI: `10.1109/TUFFC.2013.2771` (cited on page 157).

[603] Olivier Bernard et al. 'Ultrasound Fourier slice imaging: a novel approach for ultrafast imaging technique'. In: *IEEE International Ultrasonics Symposium (IUS) 2014*. Ultrasonics Symposium (IUS), 2014 IEEE International. Chicago, United States: IEEE, Sept. 2014, pp. 129–132. DOI: `10.1109/ULTSYM.2014.0033`. URL: `https://hal.science/hal-01117623` (cited on page 157).

[604] Miaomiao Zhang et al. 'Extension of Fourier-Based Techniques for Ultrafast Imaging in Ultrasound With Diverging Waves'. In: *IEEE Transactions on Ultrasonics, Ferroelectrics and Frequency Control* 63.12 (2016), pp. 2125–2137. DOI: `10.1109/TUFFC.2016.2616300`. URL: `https://hal.science/hal-01433038` (cited on page 158).

[605] F. Nicolet et al. 'Simultaneous Coded Plane-Wave Imaging Using an Advanced Ultrasound Forward Model'. In: *Applied Sciences* 12.24 (2022). DOI: `10.3390/app122412809` (cited on page 158).

[606] Hervé Liebgott et al. 'Plane-Wave Imaging Challenge in Medical Ultrasound'. In: *IEEE International Ultrasonics Symposium*. Tours, France, 2016, pp. 1–4. DOI: `10.1109/ULTSYM.2016.7728908` (cited on page 158).

[607] Jingfeng Lu et al. 'Reconstruction for Diverging-Wave Imaging Using Deep Convolutional Neural Networks'. In: *IEEE Transactions on Ultrasonics, Ferroelectrics and Frequency Control* 67.12 (Apr. 2020), pp. 2481–2492. DOI: `10.1109/TUFFC.2020.2986166`. URL: `https://hal.science/hal-02919384` (cited on page 158).

[608] Jingfeng Lu et al. 'Complex Convolutional Neural Networks for Ultrafast Ultrasound Imaging Reconstruction from In-Phase/Quadrature Signal'. In: *IEEE Transactions on Ultrasonics, Ferroelectrics and Frequency Control* 69.2 (2022), pp. 592–603. DOI: `10.1109/TUFFC.2021.3127916`. URL: `https://cnrs.hal.science/hal-03538669` (cited on page 158).

[609] M.F. Duarte et al. 'Single-Pixel Imaging via Compressive Sampling'. In: *Signal Processing Magazine, IEEE* 25.2 (Mar. 2008), pp. 83–91. DOI: `10.1109/MSP.2007.914730` (cited on page 158).

[610] Antonio Lorente Mur et al. 'Single-Pixel Image Reconstruction from Experimental Data Using Neural Networks'. In: *Optics Express* 29.11 (May 2021), p. 17097. DOI: 10.1364/OE.424228. URL: https://hal.science/hal-03202353 (cited on page 159).

[611] Antonio Lorente Mur, Françoise Peyrin, and Nicolas Ducros. 'Deep expectation-maximization for single-pixel image reconstruction with signal-dependent noise'. working paper or preprint. Jan. 2022. URL: https://hal.science/hal-03522038 (cited on page 159).

[612] S. Basu and Y. Bresler. 'Feasibility of tomography with unknown view angles'. In: *IEEE Trans. Signal Process.* 9.6 (June 2000), pp. 1107–1122. DOI: 10.1109/83.846252 (cited on page 160).

[613] A. Aichert et al. 'Epipolar Consistency in Transmission Imaging'. In: *IEEE Trans. Med. Imag.* 34.11 (2015), pp. 2205–2219. DOI: 10.1109/TMI.2015.2426417 (cited on page 160).

[614] S. Abdurahman et al. 'Beam hardening correction using cone beam consistency conditions'. In: *IEEE Trans. on Med. Imag.* 37.10 (Oct. 2018), pp. 2266–2277. DOI: 10.1109/TMI.2018.2840343 (cited on page 160).

[615] T. Würfl et al. 'Calibration-free beam hardening reduction in x-ray CBCT using the epipolar consistency condition and physical constraints'. In: *Med Phys* 46 (12 Dec. 2019), e810–e822. DOI: 10.1002/mp.13625 (cited on page 160).

[616] C. Kim et al. 'Data consistency-driven scatter kernel optimization for x-ray cone-beam CT'. In: *Phys Med Biol* 60.15 (Aug. 2015), pp. 5971–5994. DOI: 10.1088/0031-9155/60/15/5971 (cited on page 160).

[617] Y. Wei, H. Yu, and G. Wang. 'Integral Invariants for Computed Tomography'. In: *"IEEE Signal Process. Lett.* 13.9 (2006), pp. 549–552. DOI: 10.1109/LSP.2006.874452. URL: http://ieeexplore.ieee.org/stamp/stamp.jsp?arnumber=1673417 (cited on page 160).

[618] H. Yu and G. Wang. 'Data consistency based rigid motion artifact reduction in fan-beam CT'. In: *IEEE Trans. on Med. Imag.* 26.2 (2007), pp. 249–250. DOI: 10.1109/TMI.2006.889717 (cited on page 160).

[619] J. Lesaint et al. 'GCC and FBCC for linear tomosynthesis'. In: *Sixth international conference on image formation in X-ray computed tomography*. Salt Lake City, USA, Unknown Region, 2018, pp. 114–118. URL: https://hal.science/hal-01967288 (cited on page 160).

[620] Jerome Lesaint et al. 'Calibration for Circular Cone-Beam CT Based on Consistency Conditions'. In: *IEEE Transactions on Radiation and Plasma Medical Sciences* 1.6 (Nov. 2017), pp. 517–526. DOI: 10.1109/TRPMS.2017.2734844. URL: https://hal.science/hal-01686646 (cited on page 160).

[621] David Rousseau et al. 'Plateforme didactique mutualisée de travaux pratiques en instrumentation et imagerie biomédicale'. In: *12ème édition du colloque du Club EEA consacré à l'Enseignement des Technologies de l'Information et des Systèmes - CETSIS 2017*. Le Mans, France, May 2017. URL: https://hal.science/hal-01598498 (cited on page 160).

[622] Mélanie Mouchet, Simon Rit, and Jean Michel Létang. 'Motion detection in helical CT using data consistency conditions'. In: *2020 IEEE Nuclear Science Symposium and Medical Imaging Conference (NSS/MIC)*. Boston, United States: IEEE, Oct. 2020, pp. 1–3. DOI: 10.1109/NSS/MIC42677.2020.9507979. URL: https://hal.science/hal-03511400 (cited on page 160).

[623] Mélanie Mouchet et al. 'Cone-beam pair-wise data consistency conditions in helical CT'. In: *IEEE Transactions on Medical Imaging* (2023). DOI: 10.1109/TMI.2023.3265812. URL: https://hal.science/hal-04072471 (cited on page 160).

[624] Jérome Lesaint and Simon Rit. 'Consistency-based auto-calibration of the spectral model in dual-energy CT'. In: *Seventh International Conference on Image Formation in X-Ray Computed Tomography*. Vol. 12304. Proceedings of SPIE. Baltimore, United States: SPIE, June 2022, p. 47. DOI: 10.1117/12.2646526. URL: https://hal.science/hal-03821856 (cited on page 160).

[625] A.M. Cormack. 'Representation of a Function by Its Line Integrals, with Some Radiological Applications'. In: *Journal of Applied Physics* 34.9 (1963), pp. 2722–2727. DOI: 10.1063/1.1729798 (cited on page 161).

[626] R. W. Schulte et al. 'A maximum likelihood proton path formalism for application in proton computed tomography.' In: *Med Phys* 35.11 (2008), pp. 4849–4856. DOI: 10.1118/1.2986139 (cited on page 161).

[627] S. Rit et al. 'Distance-driven binning for proton CT filtered backprojection along most likely paths'. In: *Second International Conference on Image Formation in X-Ray Computed Tomography*. Salt Lake City, United States, June 2012, p. 382. URL: `https://hal.science/hal-00829634` (cited on page 161).

[628] S. Rit et al. 'Filtered backprojection proton CT reconstruction along most likely paths'. In: *Medical Physics* 40.3 (Feb. 2013), p. 031103. DOI: `10.1118/1.4789589`. URL: `https://hal.science/hal-00796949` (cited on pages 161, 162).

[629] G. Dedes et al. 'Spatial resolution and electron density study for proton computed tomography (pCT), using a curved proton track reconstruction algorithm'. In: *52nd Annual Conference of the Particle Therapy Co-Operative Group*. Essen, Germany, June 2013. URL: `https://hal.science/hal-00838489` (cited on page 161).

[630] Simon Rit et al. 'List-mode proton CT reconstruction using their most likely paths via the finite Hilbert transform of the derivative of the backprojection'. In: *The 13th International Meeting on Fully Three-Dimensional Image Reconstruction in Radiology and Nuclear Medicine*. Fully3D 2015 Conference Proceedings. Newport, Rhode Island, United States, May 2015, pp. 324–327. URL: `https://hal.science/hal-01272941` (cited on page 161).

[631] David Hansen, Thomas Sangild Sørensen, and Simon Rit. 'Fast reconstruction of low dose proton CT by sinogram interpolation'. In: *Physics in Medicine and Biology* 61.15 (2016), p. 5868. DOI: `10.1088/0031-9155/61/15/5868`. URL: `https://hal.science/hal-01375690` (cited on page 162).

[632] Feriel Khellaf et al. '2D directional ramp filter'. In: *Physics in Medicine and Biology* 65.8 (Apr. 2020), 08NT01. DOI: `10.1088/1361-6560/ab7875`. URL: `https://hal.science/hal-02486620` (cited on page 162).

[633] Feriel Khellaf et al. 'A comparison of direct reconstruction algorithms in proton computed tomography'. In: *Physics in Medicine and Biology* 65.10 (2020), p. 105010. DOI: `10.1088/1361-6560/ab7d53`. URL: `https://hal.science/hal-02502179` (cited on page 162).

[634] Feriel Khellaf et al. 'Projection deconvolution for proton CT using the spatially variant path uncertainty'. In: *IEEE Transactions on Radiation and Plasma Medical Sciences* 6.8 (Nov. 2022), pp. 847–858. DOI: `10.1109/TRPMS.2022.3167334`. URL: `https://hal.science/hal-03656408` (cited on page 162).

[635] Feriel Khellaf et al. 'Monte Carlo simulation of the most likely path of protons through a transverse heterogeneity'. In: *IEEE Nuclear Science Symposium and Medical Imaging Conference (NSS/MIC)*. Sydney, Australia, Nov. 2018. URL: `https://hal.science/hal-02330901` (cited on page 162).

[636] Feriel Khellaf et al. 'Effects of transverse heterogeneities on the most likely path of protons'. In: *Physics in Medicine and Biology* 64 (Mar. 2019), p. 065003. DOI: `10.1088/1361-6560/ab02a8`. URL: `https://hal.science/hal-02023848` (cited on page 162).

[637] Nils Krah et al. 'Energy-adaptive calculation of the most likely path in proton CT'. In: *Physics in Medicine and Biology* 66 (2021), 20NT02. DOI: `10.1088/1361-6560/ac2999`. URL: `https://hal.science/hal-03353954` (cited on page 162).

[638] C.T. Quinones, J. M. Létang, and S. Rit. 'Filtered back-projection reconstruction for attenuation proton CT along most likely paths'. In: *Physics in Medicine and Biology* 61.9 (2016), pp. 3258–3278. DOI: `10.1088/0031-9155/61/9/3258`. URL: `https://hal.science/hal-01375745` (cited on page 162).

[639] Ahmad Addoum et al. 'Proton scatter radiography with integration-mode detectors by exploiting the West-Sherwood effect'. In: *2019 IEEE Nuclear Science Symposium and Medical Imaging Conference (NSS/MIC)*. Manchester, United Kingdom, Oct. 2019. URL: `https://hal.science/hal-03126835` (cited on page 162).

[640] Nils Krah et al. 'Scattering proton CT'. In: *Physics in Medicine and Biology* 65.22 (Nov. 2020), p. 225015. DOI: `10.1088/1361-6560/abbd18`. URL: `https://hal.science/hal-02959263` (cited on page 162).

[641] George Dedes et al. 'The role of Monte Carlo simulation in understanding the performance of proton computed tomography'. In: *Zeitschrift fur Medizinische Physik* 32 (2022), pp. 23–38. DOI: `10.1016/j.zemedi.2020.06.006`. URL: `https://hal.science/hal-02920133` (cited on page 162).

[642] N. Arbor et al. 'Monte Carlo evaluation of X-ray and proton CT for the prediction of the range of proton therapy beams'. In: *3rd ESTRO Forum 2015*. Vol. 115. Radiotherapy & Oncology: journal of the european society of Radiotherapy and Oncology Suppl 1. Barcelona, Spain, Apr. 2015, p87 PD–0139. URL: https://hal.science/hal-01279593 (cited on page 162).

[643] N. Arbor et al. 'Monte Carlo comparison of x-ray and proton CT for range calculations of proton therapy beams'. In: *Physics in Medicine and Biology* 60.19 (2015), pp. 7585–7599. DOI: 10.1088/0031-9155/60/19/7585. URL: https://hal.science/hal-01205940 (cited on page 162).

[644] N. Arbor et al. 'In-silico comparison of X-ray and proton computed tomography for proton therapy dose simulation with a full Monte Carlo treatment planning'. In: *IEEE Nuclear Science Symposium & Medical Imaging Conference*. Seattle, United States, Nov. 2014. URL: https://hal.science/hal-01054233 (cited on page 162).

[645] Georgios Dedes et al. 'Experimental comparison of proton CT and dual energy X–ray CT for relative stopping power estimation in proton therapy'. In: *Physics in Medicine and Biology* 64.16 (Aug. 2019), p. 165002. DOI: 10.1088/1361-6560/ab2b72. URL: https://hal.science/hal-02171164 (cited on page 162).

[646] G. Dedes et al. 'Comparative accuracy and resolution assessment of two prototype proton computed tomography scanners'. In: *Medical Physics* (Apr. 2022). DOI: 10.1002/mp.15657. URL: https://hal.science/hal-03637368 (cited on page 162).

[647] Nils Krah et al. 'A theoretical comparison of different proton imaging set-ups'. In: *The 4th Loma Linda workshop*. Loma Linda, United States, Aug. 2018. URL: https://hal.science/hal-02048665 (cited on page 162).

[648] Nils Krah et al. 'Which proton imaging set-up should we use in a proton therapy facility?' In: *57th Annual Meeting of the Particle Therapy Cooperative Group (PTCOG)*. Cincinnati, United States, May 2018. URL: https://hal.science/hal-02050814 (cited on page 162).

[649] N. Krah et al. 'A comprehensive theoretical comparison of proton imaging set-ups in terms of spatial resolution'. In: *Physics in Medicine and Biology* 63.13 (July 2018). DOI: 10.1088/1361-6560/aaca1f. URL: https://hal.science/hal-01909706 (cited on page 162).

[650] Felix Ulrich-Pur et al. 'Feasibility study of a proton CT system based on 4D-tracking and residual energy determination via time-of-flight'. In: *Physics in Medicine and Biology* 67.9 (Apr. 2022), p. 095005. DOI: 10.1088/1361-6560/ac628b. URL: https://hal.science/hal-03625782 (cited on page 162).

[651] Nils Krah et al. 'Relative stopping power resolution in time-of-flight proton CT'. In: *Physics in Medicine and Biology* 67.16 (2022), p. 165004. DOI: 10.1088/1361-6560/ac7191. URL: https://hal.science/hal-03677847 (cited on page 162).

[652] F. Ulrich-Pur et al. 'Novel ion imaging concept based on time-of-flight measurements with low gain avalanche detectors'. In: *23rd International Workshop on Radiation Imaging Detectors*. Vol. 18. 02. Riva del Garda, Italy, June 2022, p. C02062. DOI: 10.1088/1748-0221/18/02/C02062. URL: https://hal.science/hal-03815221 (cited on page 162).

[653] Vicente Micó et al. 'Resolution enhancement in quantitative phase microscopy'. EN. In: *Advances in Optics and Photonics* 11.1 (Mar. 2019), pp. 135–214. DOI: 10.1364/AOP.11.000135. URL: https://www.osapublishing.org/aop/abstract.cfm?uri=aop-11-1-135 (visited on 05/10/2019) (cited on page 163).

[654] D. GABOR. 'A New Microscopic Principle'. En. In: *Nature* 161 (1948), pp. 777–778. DOI: 10.1038/161777a0. URL: https://www.nature.com/articles/161777a0 (visited on 07/18/2019) (cited on page 163).

[655] Jianwei Miao et al. 'Extending the methodology of X-ray crystallography to allow imaging of micrometre-sized non-crystalline specimens'. en. In: *Nature* 400.6742 (July 1999). Number: 6742 Publisher: Nature Publishing Group, pp. 342–344. DOI: 10.1038/22498. URL: https://www.nature.com/articles/22498 (visited on 08/21/2023) (cited on page 163).

[656] P. D. Nellist, B. C. McCallum, and J. M. Rodenburg. 'Resolution beyond the 'information limit' in transmission electron microscopy'. en. In: *Nature* 374.6523 (Apr. 1995). Number: 6523 Publisher: Nature Publishing Group, pp. 630–632. DOI: `10.1038/374630a0`. URL: `https://www.nature.com/articles/374630a0` (visited on 08/21/2023) (cited on page 163).

[657] O. Haeberlé et al. 'Tomographic diffractive microscopy: basics, techniques and perspectives'. In: *Journal of Modern Optics* 57.9 (May 2010), pp. 686–699. DOI: `10.1080/09500340.2010.493622`. URL: `http://dx.doi.org/10.1080/09500340.2010.493622` (visited on 10/21/2016) (cited on page 163).

[658] Mohendra Roy et al. 'A review of recent progress in lens-free imaging and sensing'. In: *Biosensors and Bioelectronics*. Special Issue Selected papers from the 26th Anniversary World Congress on Biosensors (Part I) 88 (Feb. 2017), pp. 130–143. DOI: `10.1016/j.bios.2016.07.115`. URL: `http://www.sciencedirect.com/science/article/pii/S0956566316307461` (visited on 06/05/2019) (cited on page 163).

[659] Fabien Momey et al. 'From Fienup's phase retrieval techniques to regularized inversion for in-line holography: tutorial'. EN. In: *JOSA A* 36.12 (Dec. 2019), pp. D62–D80. DOI: `10.1364/JOSAA.36.000D62`. URL: `https://www.osapublishing.org/josaa/abstract.cfm?uri=josaa-36-12-D62` (visited on 01/06/2020) (cited on pages 163, 165).

[660] R.W. Gerchberg and W.O. Saxton. 'A practical algorithm for the determination of phase from image and diffraction plane pictures'. EN. In: *Optik* 35.2 (1972), pp. 237–246. URL: `https://api.semanticscholar.org/CorpusID:55691159` (cited on page 164).

[661] J. R. Fienup. 'Reconstruction of an object from the modulus of its Fourier transform'. EN. In: *Optics Letters* 3.1 (July 1978), pp. 27–29. DOI: `10.1364/OL.3.000027`. URL: `https://www.osapublishing.org/abstract.cfm?uri=ol-3-1-27` (visited on 03/27/2017) (cited on page 164).

[662] J. R. Fienup. 'Phase retrieval algorithms: a comparison'. EN. In: *Applied Optics* 21.15 (Aug. 1982), pp. 2758–2769. DOI: `10.1364/AO.21.002758`. URL: `https://www.osapublishing.org/abstract.cfm?uri=ao-21-15-2758` (visited on 03/27/2017) (cited on page 164).

[663] Heinz H. Bauschke, Patrick L. Combettes, and D. Russell Luke. 'Hybrid projection–reflection method for phase retrieval'. EN. In: *JOSA A* 20.6 (June 2003), pp. 1025–1034. DOI: `10.1364/JOSAA.20.001025`. URL: `https://www.osapublishing.org/josaa/abstract.cfm?uri=josaa-20-6-1025` (visited on 06/03/2019) (cited on page 164).

[664] Tatiana Latychevskaia and Hans-Werner Fink. 'Solution to the Twin Image Problem in Holography'. In: *Physical Review Letters* 98.23 (June 2007), p. 233901. DOI: `10.1103/PhysRevLett.98.233901`. URL: `https://link.aps.org/doi/10.1103/PhysRevLett.98.233901` (visited on 06/05/2019) (cited on page 164).

[665] Ferréol Soulez et al. 'Proximity operators for phase retrieval'. EN. In: *Applied Optics* 55.26 (Sept. 2016), pp. 7412–7421. DOI: `10.1364/AO.55.007412`. URL: `https://www.osapublishing.org/abstract.cfm?uri=ao-55-26-7412` (visited on 11/23/2017) (cited on page 164).

[666] Corinne Fournier et al. 'Pixel super-resolution in digital holography by regularized reconstruction'. In: *Applied optics* 56.1 (Jan. 2017), pp. 69–77. DOI: `10.1364/AO.56.000069`. URL: `https://hal-ujm.archives-ouvertes.fr/ujm-01575914` (cited on pages 164, 165).

[667] Anthony Berdeu et al. 'Joint reconstruction of an in-focus image and of the background signal in in-line holographic microscopy'. In: *Optics and Lasers in Engineering* 146 (Nov. 2021), p. 106691. DOI: `10.1016/j.optlaseng.2021.106691`. URL: `https://hal.science/hal-03270308` (cited on pages 164, 165).

[668] Dylan Brault et al. 'Accurate unsupervised estimation of aberrations in digital holographic microscopy for improved quantitative reconstruction'. In: *Opt. Express* 30.21 (Oct. 2022), pp. 38383–38404. DOI: `10.1364/OE.471638`. URL: `https://opg.optica.org/oe/abstract.cfm?URI=oe-30-21-38383` (cited on pages 164, 165).

[669] L. Denneulin et al. 'GSURE criterion for unsupervised regularized reconstruction in tomographic diffractive microscopy'. In: *J. Opt. Soc. Am. A* 39.2 (Feb. 2022), A52–A61. DOI: `10.1364/JOSAA.444890`. URL: `https://opg.optica.org/josaa/abstract.cfm?URI=josaa-39-2-A52` (cited on pages 164, 165).

[670] Ferréol Soulez et al. 'Inverse-problem approach for particle digital holography: accurate location based on local optimization'. en. In: *Journal of the Optical Society of America A* 24.4 (Apr. 2007), p. 1164. DOI: `10.1364/JOSAA.24.001164`. URL: `https://www.osapublishing.org/abstract.cfm?URI=josaa-24-4-1164` (visited on 09/15/2016) (cited on page 165).

[671] Ferréol Soulez et al. 'Inverse problem approach in particle digital holography: out-of-field particle detection made possible'. en. In: *Journal of the Optical Society of America A* 24.12 (Dec. 2007), p. 3708. DOI: `10.1364/JOSAA.24.003708`. URL: `https://www.osapublishing.org/abstract.cfm?URI=josaa-24-12-3708` (visited on 09/15/2016) (cited on page 165).

[672] Loïc Denis et al. 'Inline hologram reconstruction with sparsity constraints'. en. In: *Optics Letters* 34.22 (Nov. 2009), p. 3475. DOI: `10.1364/OL.34.003475`. URL: `https://www.osapublishing.org/abstract.cfm?URI=ol-34-22-3475` (visited on 09/15/2016) (cited on page 165).

[673] Frédéric Jolivet et al. 'Regularized reconstruction of absorbing and phase objects from a single in-line hologram, application to fluid mechanics and micro-biology'. EN. In: *Optics Express* 26.7 (Apr. 2018), pp. 8923–8940. DOI: `10.1364/OE.26.008923`. URL: `https://www.osapublishing.org/oe/abstract.cfm?uri=oe-26-7-8923` (cited on page 165).

[674] Anthony Berdeu et al. 'Reconstruction of in-line holograms: combining model-based and regularized inversion'. In: *Optics Express* 27.10 (May 2019), p. 14951. DOI: `10.1364/OE.27.014951`. URL: `https://hal.science/hal-02125177` (cited on page 165).

[675] Dylan Brault et al. 'Automatic numerical focus plane estimation in digital holographic microscopy using calibration beads'. In: *Applied optics* 61.5 (Jan. 2022), B345. DOI: `10.1364/AO.444996`. URL: `https://hal-ujm.archives-ouvertes.fr/ujm-03571296` (cited on page 165).

[676] Olivier Flasseur et al. 'Self-calibration for lensless color microscopy'. In: *Applied optics* 56.13 (Apr. 2017). DOI: `10.1364/AO.56.00F189`. URL: `https://hal-ujm.archives-ouvertes.fr/ujm-01577888` (cited on page 165).

[677] Laurence Denneulin, Fabien Momey, and Dylan Brault. 'GSURE criterion for unsupervised regularized reconstruction in Tomographic Diffractive Microscopy'. In: *OSA Imaging and Applied Optics Congress 2021 (3D, COSI, DH, ISA, pcAOP), Digital Holography and Three-Dimensional Imaging 2021*. Virtual Event, United States, July 2021. URL: `https://hal.science/hal-03376992` (cited on page 165).

[678] Lorena A. Barba. *Terminologies for Reproducible Research*. 2018 (cited on page 167).

[679] Jon F. Claerbout and Martin Karrenbach. 'Electronic documents give reproducible research a new meaning'. In: *SEG Technical Program Expanded Abstracts 1992*. 2005, pp. 601–604. DOI: `10.1190/1.1822162`. URL: `https://library.seg.org/doi/abs/10.1190/1.1822162` (cited on page 167).

[680] Roger D. Peng. 'Reproducible research in computational science'. In: *Science* (Dec. 2011), pp. 1226–1227. URL: `https://doi.org/10.1126/science.1213847` (cited on page 167).

[681] Victoria Stodden. *Reproducibility*. 2014. URL: `https://www.edge.org/response-detail/25340` (cited on page 167).

[682] Fabien C. Y. Benureau and Nicolas P. Rougier. 'Re-run, Repeat, Reproduce, Reuse, Replicate: Transforming Code into Scientific Contributions'. In: *Frontiers in Neuroinformatics* 11 (Jan. 2018). DOI: `10.3389/fninf.2017.00069`. URL: `https://inria.hal.science/hal-01577578` (cited on page 168).

[683] Gregory Kiar et al. 'Numerical uncertainty in analytical pipelines lead to impactful variability in brain networks'. In: *PLOS ONE* 16.11 (Nov. 2021), pp. 1–16. DOI: `10.1371/journal.pone.0250755`. URL: `https://doi.org/10.1371/journal.pone.0250755` (cited on page 168).

[684] Nicolas Vallet, David Michonneau, and Simon Tournier. 'Toward practical transparent verifiable and long-term reproducible research using Guix'. In: *Scientific Data* (2022). URL: `https://doi.org/10.1038/s41597-022-01720-9` (cited on page 169).

[685] Guiomar Niso et al. ‘Open and reproducible neuroimaging: From study inception to publication’. In: *NeuroImage* 263 (2022), p. 119623. DOI: https://doi.org/10.1016/j.neuroimage.2022.119623. URL: https://www.sciencedirect.com/science/article/pii/S1053811922007388 (cited on page 169).

[686] Morgane Des Ligneris et al. ‘REPRODUCIBILITY OF TUMOR SEGMENTATION OUTCOMES WITH A DEEP LEARNING MODEL’. In: *International Symposium on Biomedical Imaging (ISBI)*. Cartagena de Indias, Colombia, Apr. 2023. URL: https://hal.science/hal-04006057 (cited on page 169).

[687] Spyridon Bakas et al. ‘The University of Pennsylvania glioblastoma (UPenn-GBM) cohort: advanced MRI, clinical, genomics, & amp; radiomics’. In: *Scientific data* 9.1 (July 2022), p. 453. DOI: 10.1038/s41597-022-01560-7. URL: https://europepmc.org/articles/PMC9338035 (cited on page 169).

[688] T. Glatard et al. ‘Reproducibility of neuroimaging analyses across operating systems’. In: *Frontiers in Neuroinformatics* (2015), pp. 1–14. DOI: 10.3389/fninf.2015.00012. URL: https://hal.science/hal-01207394 (cited on page 169).

[689] Gaël Vila et al. ‘The Impact of Hardware Variability on Applications Packaged with Docker and Guix: a Case Study in Neuroimaging’. Submitted at https://acm-rep.github.io/2024/. Feb. 2024. URL: https://hal.science/hal-04480308 (cited on page 170).

[690] Kevin Tse Ve Koon et al. ‘Comparison of high-resolution magnetic resonance imaging and micro-computed tomography arthrography for in-vivo assessment of cartilage in non-human primate models’. In: *Quantitative Imaging in Medicine and Surgery* 11.8 (Aug. 2021), pp. 3431–3447. DOI: 10.21037/qims-20-116. URL: https://hal.science/hal-03340039 (cited on page 170).

[691] Małgorzata Marjańska et al. ‘Results and interpretation of a fitting challenge for MR spectroscopy set up by the MRS study group of ISMRM’. In: *Magnetic Resonance in Medicine* 87.1 (2022), pp. 11–32. DOI: https://doi.org/10.1002/mrm.28942. URL: https://onlinelibrary.wiley.com/doi/abs/10.1002/mrm.28942 (cited on page 172).

[692] Jiqing Huang et al. ‘Diffusion-Weighted MRI of the Liver in Patients With Chronic Liver Disease: A Comparative Study Between Different Fitting Approaches and Diffusion Models’. In: *Journal of Magnetic Resonance Imaging* 59 (), pp. 894–906. DOI: https://doi.org/10.1002/jmri.28826. URL: https://onlinelibrary.wiley.com/doi/abs/10.1002/jmri.28826 (cited on page 173).